Betatron radiation in beam-driven plasma wakefield acceleration and ultra-relativistic beam-plasma instabilities

Pablo San Miguel

To cite this version:

Pablo San Miguel. Betatron radiation in beam-driven plasma wakefield acceleration and ultra-relativistic beam-plasma instabilities. Mechanics of materials [physics.class-ph]. Institut Polytechnique de Paris, 2021. English. NNT : 2021IPPAE016 . tel-03544110

HAL Id: tel-03544110
https://theses.hal.science/tel-03544110v1

Submitted on 26 Jan 2022

HAL is a multi-disciplinary open access archive for the deposit and dissemination of scientific research documents, whether they are published or not. The documents may come from teaching and research institutions in France or abroad, or from public or private research centers.

L'archive ouverte pluridisciplinaire **HAL**, est destinée au dépôt et à la diffusion de documents scientifiques de niveau recherche, publiés ou non, émanant des établissements d'enseignement et de recherche français ou étrangers, des laboratoires publics ou privés.

INSTITUT
POLYTECHNIQUE
DE PARIS

NNT : 2021IPPAE016

Thèse de doctorat

Betatron radiation in beam-driven plasma wakefield acceleration and ultra-relativistic beam-plasma instabilities

Thèse de doctorat de l'Institut Polytechnique de Paris
préparée à Laboratoire d'Optique Appliquée

École doctorale n°626 École doctorale de l'Institut Polytechnique de Paris (EDIPP)
Spécialité de doctorat : Physique

Thèse présentée et soutenue à Palaiseau, le 17 Décembre 2021, par

PABLO SAN MIGUEL CLAVERIA

Composition du Jury :

Caterina Riconda Professeure, Sorbonne Université	Présidente
Jorge Vieira Assistant professor, Instituto Superior Tecnico	Rapporteur
Fabien Dorchies Directeur de recherche, CNRS	Rapporteur
Olle Lundh Senior Lecturer, Lund University	Examinateur
Victor Malka Professeur, Weizmann Institute of Science	Examinateur
Sebastien Corde Professeur, Institut Polytechnique de Paris	Directeur de thèse

ACKNOWLEDGEMENTS

An incredible amount of incredible people have helped me, supported me and motivated me through this PhD adventure. I would like to thank all these people, thanks to whom this manuscript has become real. Tout d'abord je tiens à remercier énormement mon encadrant Sébastien Corde, qui m'a tellement apporté, aussi à moi qu'à mon travail, depuis la première minute où j'ai rejoint son équipe. Sa pédagogie et sa patiente font de Sébastien un encadrant examplaire. Après trois ans sous sa direction, je n'ai que des mots d'admiration et de respect pour lui.

I would also like to give special thanks to two people that have played an important leading role in the work presented in this manuscript. Thanks to Mark Hogan for giving me the opportunity to join his team at SLAC, I am grateful to have discovered in first person his many attributes as a physicist and as a person. Et merci à Laurent Gremillet pour son savoir-faire, sa rigueur et sa passion, et pour avoir partagé tout cela avec moi. Similarly, I would like to thank the jury of the defence for all the fruitful remarks and comments on the manuscrit as well as during the defence.

During my PhD I mainly had three workplaces: le Laboratoire d'Optique Appliquée, SLAC National Accelerator Laboratory and chez-moi (yes, pandemic times were part of this thesis...). But these places are nothing without the people that they host. In each of them I have been surrounded by wonderful people that have played an important role for me to complete my thesis, and I would like express my gratitude to them.

Au LOA, I need to give a big thanks to Lena for making me discover the world of plasma wakefield acceleration. Together with Gaurav and Siyi, you made my first days at LOA (and outside) simple and easy-going. Thank you for that. During these early times I also had the chance to share the office with Slava, with whom I spent an unforgettable time in the CERN summer-school. Y por supuesto mil gracias a Isa, por todas esas conversaciones de café y esa simpatía natural que te acompaña. Merci à Kosta et à Ginevra pour être les co-doctorant.es parfait.es, ainsi qu'à Neil et JB pour tous les moments ensemble. Thanks to Alex, Max and Yuliia for everything they taught me. Merci à Xavier pour être mon mentor des codes PIC et pour toute l'aide qu'il m'a apportée pendant ces trois ans. Et un grand merci aux nouveaux arrivants Aimé et Thomas, qui ont dernièrement dynamisé la vie du bureau et auxquels je souhaite (et prévois) une belle aventure pour la thèse qu'ils commencent. En dernier point, mais non le moindre, je tiens à remercier tout le personnel du LOA, secretaires, technicien.nes et chercheur.ses, grâce auxquels je me suis toujours senti si bien accueilli au laboratoire.

At SLAC, I need to thank Doug for all the help and support he provided since we started working together. It has been a real pleasure to work and learn from you. Thanks also to all the team, Spencer, Andy, Mike, Henrik, Claudio, Christine, Brendan, James and Lauren for the welcoming atmosphere and the after-work events. And thanks to all the E300, E305 and E320 collaborators.

And chez-moi I've been supported by many people. Estoy enormemente agradecido a mis padres, hermano y familia. Siempre han sido un apoyo constante, y sin ellos nunca habría podido llegar hasta aquí. A mis amigos del pueblo, en especial a Manuel por haberme acompañado durante gran parte de mi estancia en París, y a los de Madrid por siempre haberme acogido en sus brazos como si nunca me hubiera ido. To Giulio et Guillaume, for the times and experiences shared together, y a Ceci por todos los viajes de carretera y manta. Et à Antoine, Annabel, Momo, Agnès et Laurent, pour m'avoir appris à gérer la vie parisienne.

En dernier place, je tiens à remercier Aurore, simplement pour avoir existé pendant tout ce temps dans ma vie.

RÉSUMÉ SUBSTANTIEL EN LANGUE FRANÇAISE

Le rôle des plasmas s'étend actuellement sur de nombreux domaines de la physique, autant fondamentale qu'appliquée. Ce qui rend le plasma unique et central dans les phénomènes physiques où il est présent c'est sa réponse collective à des perturbations électromagnétiques. Ceci est notamment important dans le cas des plasmas chauds, où ce comportement caractéristique des plasmas permet d'atteindre des conditions extrêmes similaires aux environnements astrophysiques associés aux évènements les plus énergétiques de l'univers. Avoir une bonne compréhension de ces mécanismes permet d'améliorer les modèles astrophysiques, mais aussi de poser les bases de nouvelles techniques expérimentales qui pourraient avoir un impact ultérieur sur des applications industrielles et sociétales.

Dans un laboratoire, reproduire et étudier ces phénomènes nécessite la production de plasmas très énergétiques de telle sorte que des diagnostiques puissent être implantés pour les caractériser. Pour cela des installations délivrant des faisceaux laser ou des particules sont souvent utilisées. Ces faisceaux peuvent transférer leur énergie au plasma, excitant ainsi des phénomènes extrêmes dont les mécanismes subjacentes peuvent être étudiés expérimentalement. Les résultats présentés dans ce manuscrit portent sur deux de ces phénomènes physiques: l'accélération de particules par onde de sillage plasma et les instabilités faisceau-plasma.

La technique d'accélération par champ de sillage piloté par faisceau est aujourd'hui l'une des alternatives les plus prometteuses aux accélérateurs conventionnels. Avec des gradients d'accélération jusqu'à quatre ordres de grandeur plus importants que dans une cavité radio-fréquence, cette technique pourrait réduire considérablement la taille et le coût des accélérateurs de particules à haute énergie. Pourtant, plusieurs étapes expérimentales doivent être franchies pour démontrer que cette technique d'acceleration peut fonctionner au niveau requis de reproductibilité, contrôle et qualité du faisceau, notamment pour des applications en physique des hautes énergies. Dans ce manuscrit, nous proposons via des simulations une nouvelle méthode non destructive basée sur le rayonnement pour diagnostiquer les dynamiques d'un faisceau relativiste dans une onde de sillage plasma qui sont préjudiciables à la qualité du faisceau accéléré. Cet étude s'inscrit dans le contexte des expériences d'accélération plasma sur la nouvelle installation expérimentale FACET-II, qui délivrera des faisceaux d'électrons dans une gamme de paramètres optimale pour l'accéleration plasma jamais explorée auparavant.

Autour de cette même installation une nouvelle campagne expérimentale a été crée pour étudier les instabilités faisceau-plasma, parfois dites de filamentation, qui surviennent pendant la propagation d'un faisceau de particules chargées dans un plasma. Ces instabilités sont souvent modelisées pour des systèmes non bornés. Dans la limite ultra-relativiste, ces modèles prévoient que l'instabilité oblique, dont le vecteur d'onde est oblique par rapport à la vitesse du faisceau, domine le stade précoce de l'interaction faisceau-plasma. Dans ce manuscrit, les effets d'un système borné sur les modes obliques instables sont étudiés. Tenir compte de la taille finie du faisceau fait apparaitre le caractère spatio-temporel dans le développement de l'instabilité, en contraste avec l'évolution purement temporelle décrite par les théories non-bornées. Un

nouveau modèle analytique est développé pour décrire la croissance spatio-temporelle associée à la phase linéaire de l'instabilité, en très bon accord avec des simulations numériques. D'un autre côté, les champs de sillage plasma excités par un faisceau de taille finie ont aussi un effet dans la propagation du faisceau dans le plasma, pouvant impacter le développement des instabilités. Pour les paramètres expérimentaux de FACET-II, l'auto-focalisation d'un faisceau d'électrons induit par les champs de sillage peut avoir un effet important sur l'évolution de l'instabilité, et même supprimer complètement cette dernière. Dans ce manuscrit, la compétition entre l'auto-focalisation et l'instabilité est analysée, ainsi que les répercussions sur les systèmes expérimentaux visant à étudier ces instabilités dans le régime ultra-relativiste.

Enfin, ce manuscrit présente des résultats expérimentaux obtenus sur une plateforme laser visant à étudier les instabilités plasma excitées dans l'interaction d'une impulsion laser femtoseconde avec une cible solide. Dans cette campagne expérimentale réalisée au Laboratoire d'Optique Appliquée, l'interaction d'un faisceau laser "pompe" avec la cible solide est sondée par un paquet d'électrons rélativistes créé par accélération laser-plasma. Ce paquet d'électrons "sonde" voit les champs électromagnétiques excités par le faisceau laser "pompe" à la surface et à l'intérieur de la cible, ce qui modifie les proprietés du faisceau sonde. Deux types d'observations sont presentés dans ce manuscrit. Avec un désalignement spatial entre les faisceaux pompe et sonde, des déviations dans le pointé du faisceau sonde sont mesurées. Ces déviations pourraient être associées aux champs magnétiques dites "TNSA" (*Target Normal Sheath Acceleration*) excités sur les surfaces de la cible solide. Par ailleurs, quand les faisceaux sont alignés une perturbation plus importante sur le faisceau sonde est observée. Ceci pourrait être associé aux instabilités de filamentation excités dans la cible pendant la propagation des électrons chauds du plasma à travers la cible solide. Grâce au controle temporel très précis entre les faisceaux "pompe" et "sonde", l'évolution temporelle de ces observations est mesurée, avec un accord raisonnable avec ce qui est attendu pour les phénomènes du TNSA et des instabilités de filamentation.

CONTENTS

INTRODUCTION

Scientific context

One of the most successful theories in the history of Physics is the Standard Model of particle physics, which so far has been able to reproduce all the observations measured by the dedicated experiments. There are though strong reasons to believe that this model might not be valid at higher energies than what can be achieved currently in the largest particle colliders. Being able to increase the center of mass energy available in particle collision will not only help to find the break-down, if there is such, of the Standard Model, but it will also get us closer to the initial conditions of our Universe. Such objectives are behind the new proposal of the Future Circular Collider at CERN [1], for which a new acceleration ring of 100 km in circungerence is currently under design.

Nevertheless, building such an accelerator is going to require a big international effort, without clear guarantees that it will enable the discovery of new particles or interactions. Given the complexity and challenges of building high energy particle colliders, several physicists started to search for other sources of high energy elementary particles. Based on astronomical observations such as the discovery of neutrino oscillations [2], one of the most popular alternatives to particle colliders are the energetic particles of astronomical origin. This scission of particle physics, often referred to as astroparticle physics, brought together several fields of physics, such as detector physics, astronomy, cosmology or plasma physics. In this new field, one of the important questions that still remains speculative is the acceleration mechanisms that lead to the measured particle energies, which can be orders of magnitude higher than at state-of-the-art particle accelerators. In most of the astrophysical models, plasmas, which represent 99% of the visible matter in the universe, play an important role in these energetic acceleration mechanisms. In this ionised state, matter can respond collectively to electromagnetic phenomena, being able to sustain strong electromagnetic fields that could be responsible for the particle acceleration.

Plasmas started to be studied around a century ago in laboratories, and have become nowadays not only an important topic of research in many academic institutions but also a source of new techniques with strong implications in industry and societal applications. Some examples where plasmas play a central role are nuclear fusion, high power laser technologies, and of course astrophysics. Remarkably one of the applications of plasmas, first proposed around 40 years ago, is the so-called plasma wakefield acceleration [3]. By means of the collective plasma response to electromagnetic perturbations, an electromagnetic mode can be excited in a plasma, similarly to the accelerating modes of the metallic cavities of the CERN collider, which can be used to accelerate charged particles. Despite not being the best candidate for the astrophysical origin of cosmic rays, this process can lead to extremely high acceleration gradients and ultimately result in large energy gains over very short time-scales.

The plasma wakefield acceleration concept has been developed over the years with the goal to provide a new laboratory source of high energy particles, and currently acceleration gradient of 10's of GigaVolts per meter have been measured in dedicated experiments. These gradients, several orders of magnitude larger than metallic cavities, have been successfully used to accelerate electrons to GeV energies in cm-scale long plasmas. There are however several challenges to overcome in order to use plasma wakefield accelerators as the main accelerating component of a particle collider. Namely, actual plasma-based accelerators need to improve in terms of reproducibility, stability and beam quality. For this purpose, a new experimental facility is being commissioned at SLAC National Accelerator Laboratory, called Facility for Advanced Accelerator Experimental Tests II (FACET-II) [4], to overcome and study the current limitations of the plasma wakefield acceleration concept. The work of my PhD has been mostly carried out in the context of FACET-II. The results produced at this facility are expected to pave the way towards the demonstration of the required performance for an acceleration technology, which will ultimately reduce the overall size and cost of the accelerator infrastructures, not only for particle colliders but also for other applications requiring high energy particle beams and/or compactness such as medicine or light sources.

This new FACET-II facility is one of the only places in the world where the interaction between a high energy particle beam, accelerated by a conventional accelerator, and plasmas can be studied. This interaction is not only relevant for plasma-based acceleration but also for astrophysical scenarios in which streams of charged particles and plasmas interact with each other. For instance it is known that plasma streaming instabilities arising under such conditions can generate a large amount of electromagnetic radiation and potentially play a role in the unknown origin of Gamma-Ray Bursts (GRB). Being able to characterise the onset of these instabilities in a laboratory allows on the one hand to refine the astrophysical models in which these processes are relevant, and on the other hand to harness the intrinsic physical mechanisms to create new sources of energetic particles or electromagnetic radiation in laboratories.

The interaction of relativistic streams of charged particles is also being explored in laser facilities thanks to the advent of ultrahigh power laser systems. These laser pulses carry a large amount of energy that can be quickly deposited on a small amount of matter, allowing to study matter in extreme conditions similar to the environment in the planetary or stelar medium. These experiments are at the intersection between High Energy Density Science and Laboratory Astrophysics, and are becoming nowadays a new pathway to assess the underlying physical process of the most energetic electromagnetic events in the Universe.

Scope of the work

Most of the work presented in this manuscript falls within the research programs surrounding the new Facility for Advanced Accelerator Tests II (FACET-II) at SLAC National Accelerator Laboratory. This accelerator facility will deliver 10 GeV electron beams (and possibly positron beams [4]) with unprecedented beam parameters in terms of peak current and emittance, allowing to take one step further the experimental progress of plasma wakefield acceleration. Furthermore these extreme beam parameters, together with the capability of implementing a plasma target in an accelerator beamline, open up new opportunities to study different aspects of the interaction of an ultra-relativistic particle beam with plasmas. With strong implications in astrophysics as well as in gamma-ray generation, a new experimental program has been developed to explore the ultra-relativistic regime of beam-plasma instabilities using the high energy particle beams delivered by the FACET-II accelerator.

One of the next experimental milestones in the field of beam-driven plasma wakefield acceleration is the emittance preservation of the accelerated trailing beam. Via simulations, several processes have been identified to be responsible for the emittance growth of the trailing beam in a plasma wakefield acceleration stage. However it is not clear how to diagnose each process separately in an experiment, which would require a very precise control of the trailing beam dynamics at the entrance of the plasma stage and high resolution and complex beam diagnostics to measure the accelerated beam phase-space distributions. In this manuscript, a new non-destructive diagnostic is proposed to assess several of these processes that lead to the degradation of the trailing beam emittance. This new diagnostic is based on the emitted betatron radiation, which allows to retrieve information about the beam dynamics that are ultimately leading to the emittance growth during the plasma acceleration stage. Furthermore, the design, implementation and commissioning of the required radiation diagnostics at the experimental facility is presented.

In terms of the beam-plasma instabilities, historically these instabilities have been studied in unbounded systems [5]. The Particle-In-Cell simulations, successfully used to reproduced the existing theoretical models, are often run with periodic boundary conditions, which effectively corresponds to the unbounded geometry of the models. Nonetheless, the predictions of the unbounded theory do not necessarily hold under experimental conditions involving finite extent systems. In this manuscript we analyse the effect of considering the spatial boundaries of the different elements on the development of beam-plasma instabilities. Namely, a novel spatiotemporal model of the dominant beam-plasma instability in the diluted ultra-relativistic beam regime is presented. The results from these analysis bear significant implications for the experimental program of FACET-II devoted to beam-plasma instabilities.

These two processes arising in beam-plasma interactions (beam-driven plasma wakefield acceleration and beam plasma instabilities) have been mainly developed in parallel. Even if it was known that for large beams ($k_p\sigma_r \gg 1$) the beam-plasma instabilities could set an important limitation to the efficient excitation of linear wakefields [6], once the non-linear or "blow-out" scenario revealed itself as the best regime for electron acceleration, the two processes were investigated separately. However it is worth noticing that in the plasma wakefield concept the boundaries of the electron beam (and also of the plasma) are essential, and the formalism used to model this process naturally accounts for these boundaries. This manuscript also represents a first step towards a new formalism at the intersection of both phenomena, in which the quasi-static approximation largely used for wakefields could be applied up to some level of accuracy to model the beam-plasma instabilities in the ultra-relativistic regime.

In a different context from the FACET-II facility, results of an experimental campaign at Laboratoire d'Optique Appliquée (LOA) aiming at probing the electromagnetic fields excited in the interaction of a femtosecond high-power laser pulse with a solid density plasma are presented. Using a laser-wakefield accelerated electron beam as a probe, the temporal evolution of these electromagnetic fields is measured. The observed features of the probe presumably show that two phenomena dominate the probed laser-solid interaction: the Target Normal Sheath Acceleration magnetic fields and the Current Filamentation Instability.

Organisation of the manuscript

The manuscript is divided in three in parts. Part I is devoted to the plasma wakefield acceleration experimental program at FACET-II. Part II focuses on the ultra-relativistic regime of beam-plasma instabilities, while Part III presents the experimental results of the laser-solid interaction experiment carried out at LOA.

Part I is divided in three chapters. Chapter 1 serves as an introduction to the theory of plasma wakefield acceleration and the associated relevant beam dynamics that lead to the beam quality degradation, Chap. 2 presents the working principle and simulations of the betatron-radiation-based diagnostic to assess conditions susceptible to emittance growth, and Chap. 3 discusses the design, implementation and comissionning of the radiation diagnostics at FACET-II.

Part II is also divided in three chapters. Chapter 4 gives an overview of the state-of-the-art of beam-plasma instabilities and introduces the mathematical formalism used to model these instabilities. Chapter 5 presents an exhaustive analysis of the boundary and finite-size effects in the ultra-relativistic regime of beam-plasma instabilities, and Chap. 6 shows simulation results of the beam-plasma instability with the expected beam-plasma parameters at FACET-II.

Finally Part III (Chap. 7) presents the results of the experimental campaign carried out at LOA on high power laser-solid interaction, with an introduction to the facility, the relevant mechanisms in the laser-solid interaction under the considered experimental conditions and the designed experimental set-up.

Part I

BEAM-DRIVEN PLASMA-BASED ACCELERATION

1. INTRODUCTION TO BEAM-DRIVEN PLASMA WAKEFIELD ACCELERATION

Plasma-based particle acceleration has been one of the main research topics that I have worked on during my PhD. This chapter serves as an introductory overview of the relevant aspects of the subject to contextualise the results presented in the following chapters. As will be explained soon in the first section of the chapter, the Plasma-Based Acceleration (PBA) concept has been historically developed in two parallel pathways: the Laser WakeField Acceleration (LWFA) and the beam driven Plasma WakeField Acceleration (PWFA). During my PhD I have mainly worked on the beam-driven concept, but being based in a laser laboratory (Laboratoire d'Optique Appliquée, LOA) I also had the chance to work on the laser-driven side (see for instance Chap. 7). Both scenarios are discussed in this introductory chapter, but a more exhaustive overview of the PWFA concept is provided.

The first section gives a brief historical outline, highlighting the main motivations that lead to the main scientific advances in both LWFA and PWFA. The second section deals with the theory and modelling of the plasma wakefields, introducing the most important plasma-related concepts needed to understand the following chapters. The third section serves as an introduction to the relevant beam dynamics in PWFA and to the mathematical formalism used to model these dynamics. Finally the fourth section gives an overview of the betatron radiation emission together with some characteristic features of this radiation mechanism.

1.1 Plasma-Based Acceleration: Motivations, History and Limits

Plasma-based acceleration was initially envisioned as an alternative technique to accelerate charged particles thanks to the high amplitude electromagnetic fields that can be sustained inside the plasma. Before entering into the details of PBA, it is worth explaining the principles of particle acceleration as well as the outstanding discoveries that came along with the development of particle accelerators.

Historically the acceleration of charged particles was conceived by means of electromagnetic (EM) fields implemented in a vacuum chamber, so that when particles are injected in the vacuum chamber the EM fields provide the accelerating and guiding force. The vacuum requirement partially responded to the need of having the particle motion only dictated by the EM fields and not interacting with any background matter. Following this concept, from the first cathodic tube 130 years ago to the current high-energy particle accelerators, this technology has gained over the years in efficiency and performance, delivering particles beams with higher energy and better quality used in a wide variety of applications. The development of this "under-vacuum" acceleration technique over the last century has gone hand-in-hand with the scientific progress in probing matter at smaller and faster scales. Two clear examples of this hand-in-hand evolution are High Energy Physics (HEP) particle accelerators, e.g. the Large Hadron Collider at CERN, where the extremely large beam energies enable us to probe the Standard Model of particle physics [7, 8], and Free Electron Lasers (FEL), e.g. the Linac Coherent Light Source LCLS at SLAC, where the produced femtosecond X-ray pulses enable us to study ultra-fast phenomena such as DNA structure evolution or ultrafast chemistry [9]. Moreover, particle accelerators are also used in medicine for cancer therapy and in industry for non-destructive inspection or electron cutting.

Nowadays most of the particle accelerators are based on Radio-Frequency (RF) cavities: metallic cavities with vacuum inside that are electrically powered to excite the resonant EM modes in the frequency domaine of radio waves. When a charged particle passes through the cavity, it experiences the EM fields and if it is placed on the right phase of the RF wave it gets accelerated. This technique, sometimes referred to as conventional acceleration, has been developed over the years and is nowadays considered to be reliable and controllable, specially in terms of beam energy and quality. Furthermore RF-based accelerators, together with other beam-optics elements, offer a significant flexibility in terms of the beam parameter space that can be achieved, making them suitable for many societal applications.

However, the cost and size of these machines limits their worldwide implementation and use, specially when high particle energies are required. Since these cavities are limited in terms of the maximum EM field amplitude that they can sustain, the particle needs to go through several of them in order to reach relativistic energies. The higher the required beam energy, the more cavities are needed and the larger the accelerator needs to be. The limit on the EM amplitude sustained by a metallic cavity is imposed by the electrical breakdown of the walls of the cavity, i.e. at a certain amplitude the EM fields start to pull electrons out of the metallic wall, which contaminates the vacuum inside the cavity and damages the cavity wall, deteriorating its performance. This limit typically set the maximum acceleration gradient that RF-cavities can provide to 10's or 100 MV/m. To overcome this limited acceleration gradient and build shorter (and cheaper) accelerators that can reach high beam energies, Plasma-Based Accelerators represent, as of today, a promising alternative.

As stated before, plasmas can sustain very high amplitude EM fields, and therefore could provide large acceleration gradients. Let us briefly discuss the qualitative characteristics that make plasmas suitable for particle acceleration. We say that matter turns into plasma when the electrons, usually bounded in the atoms, are released from the atomic unit and interact with the environment as individual charged particles (electrons are negatively charged and ions are positively charged). In other words, plasma is a state of matter, sometimes called the forth state of matter, in which the atoms are ionised and therefore matter can respond collectively to EM phenomena. The plasma wave excitation, which is the fundamental process of PBA (see Sec. 1.2), is one of these collective EM phenomena that arise in plasmas. It results in the excitation of large amplitude EM fields (up to 100s of GV/m) that can then be used for particle acceleration. In other words, since plasmas are electronically "broken-down" matter they can sustain EM fields of amplitudes that are several orders of magnitude higher than non-ionised matter, making them suitable to build smaller particle accelerators that can still provide high particle energies.

Even if plasma can indeed sustain high amplitude EM fields thanks to its collective response to EM perturbations, there needs to be a way to "pump" the system, same as EM-modes in the RF-cavities are externally powered. In other words, the energy gained by the accelerated particle beam needs to be somehow provided to the system. Two scenarios were initially proposed: Tajima and Dawson [3] came up with the idea to use a laser pulse to create the accelerating fields in the plasma (LWFA), and 6 years later Chen and Dawson [10] realised that

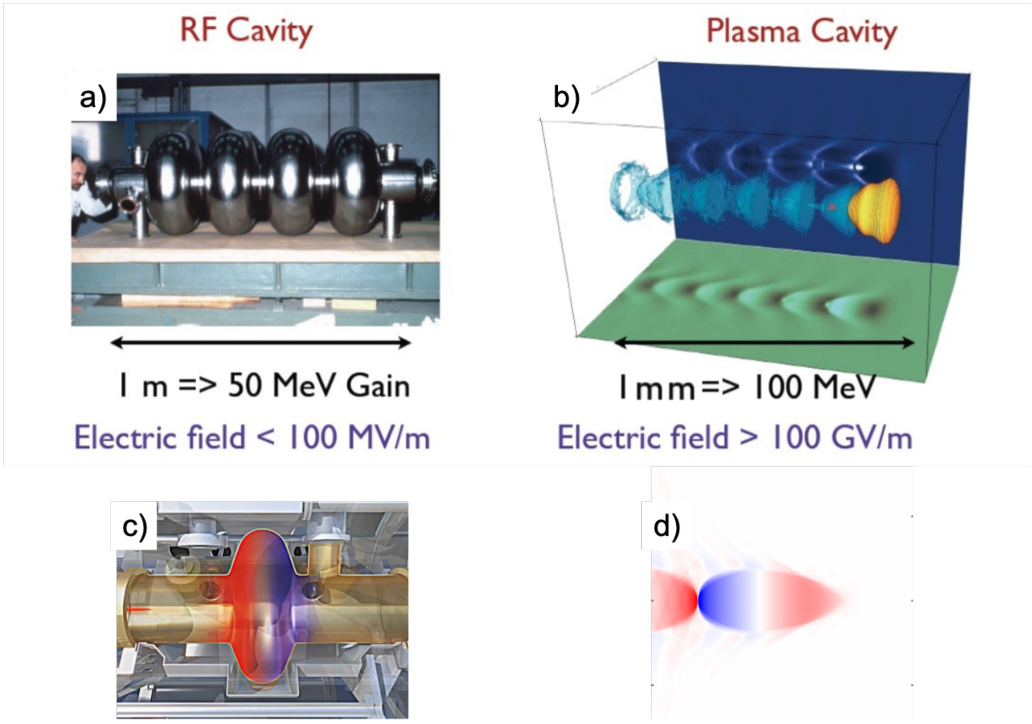

Fig. 1.1: Schematic comparison of a RF-cavity accelerating structure and a PBA accelerating structure. (a) Picture of an RF cavity. (b) Simulated image of a plasma wave. (c) RF-cavity with snapshot of the associated longitudinal electric mode. (d) Snapshot of the longitudinal electric field in a PBA. Figure (a) and (b) from Ref. [11].

an electron bunch could be used for the same purpose (PWFA). In both scenarios the laser (in LWFA) and the electron bunch (in PWFA) are used to excite a electronic plasma wave whose associated EM fields, also called wakefields, can be up to four orders of magnitude higher than the maximum EM amplitude sustained in a RF-cavity. Similarly to what happens in the RF-cavity scenario, if electrons are injected in the right phase of the plasma wave they will experience the accelerating fields and gain energy. An energy-flow analysis of this PBA scenario tells us that the plasma acts as the accelerating medium by taking the energy out of the "driver" (laser pulse in LWFA, electron beam in PWFA) and transfers it to the "witness" electrons by means of the plasma wave and the associated high amplitude EM fields (see Fig. 1.2). A schematic comparison of a RF-cavity accelerating structure and a PBA accelerating structure is shown in Fig. 1.1. A more rigorous and accurate description of the physical processes involved in PBA is given in the Sec. 1.2.

Since the publication of these precursory studies, a lot of efforts have been made towards their experimental realisation, and many challenges had to be overcome. For the laser-driven PBA, the first experiments were carried out at the beginning of the 1990s, showing acceleration of electrons up to relatively low energies and with broad spectra. Even if these first experimental results were far from fulfilling the beam requirements for applications, they were the first proof-of-principle experiments, and they showed how a laser facility could potentially one day replace a particle accelerator [12]. It was not until the advent of Chirped Pulse Amplification [13] (CPA) femtosecond laser systems and the development of new injection and guiding techniques that the LWFA experiments were able to produce quasi-monoenergetic high energy ($> 50\,\mathrm{MeV}$)

electrons bunches [14, 15, 16].

For the beam-driven concept, a conventional accelerator is required to pre-accelerate the charged particle beam that drives the plasma wave. In this sense, the PWFA scenario acts more like a transformer since it provides a mechanism to extract the energy of a pre-accelerated beam and transfer it, via a plasma wave, to a second beam (see Fig. 1.2). Due to the lack of particle accelerators that can deliver suitable electron beams for PWFA, there are fewer experimental studies of PWFA compared to LWFA. The first proof-of-principle experiment of beam-driven PWFA happened at the Argonne Wakefield Accelerator Facility [17]. Shortly afterwards, the HEP Linear Accelerator (LINAC) of SLAC National Accelerator Laboratory started to perform the first PWFA experiments using long 42 GeV electron bunches, studies done in parallel with the last for HEP e^+e^- collisions experiments at the facility. Using a single bunch to ionise the plasma source, drive the plasma wave and experience the plasma wakefields, they showed that while the front of the beam was loosing energy, some of the electrons sitting at the rear of the bunch doubled their energy (i.e. 84 GeV) after the propagation in the plasma [18]. All this in a 85 cm long plasma target, in contrast with the 3 km of RF-cavity-based LINAC to reach the pre-accelerated 42 GeV. The overall efficiency of the acceleration was very poor though, since it was only a minor part of the beam charge that was accelerated to these very high energies and it resulted in a continuum energy spectrum of accelerated particles.

It is worth noticing that the so-called linear theory developed for the original LWFA and PWFA scenarios was not valid (see Sec. 1.2) for the intense drivers used in some of these pioneering LWFA and PWFA experiments. Instead, a new non-linear theory was needed to reproduce and understand these experiments. Initially, an analytical model was derived to describe the one dimensional non-linear plasma oscillations [19]. Before the development of a model accounting for the transverse component of the non-linear plasma oscillations [20], Particle-in-Cell (PIC, see App. A) simulations were used to assess the multidimensional non-linear regime [21, 22] showing an overall good agreement with the experimental results.

After this first set of PWFA experiments at SLAC, part of the LINAC was redesigned to host the first PWFA experiments in the two bunch configuration, i.e. a first bunch (driver) who drives the plasma waves and looses its energy and a second bunch (trailing) propagating right behind the driver to experience the large amplitude plasma wakefields and therefore gain energy (see Fig. 1.2). This configuration allowed to decouple the driving process and the acceleration process, and enable the measurement of the non-linear accelerating structure [23]. Furthermore, quasi-monochromatic acceleration of ≈ 9 GeV was achieved in a meter-scale plasma [24].

In the more recent years, a new PWFA facility called FlashForward has come online in Hamburg, where the beam-loading [25] process in PWFA has been accurately measured [26] and low energy spread and high transfer efficiency were simultaneously achieved [27]. Also at CERN a PWFA experiment is currently taking place using a proton bunch as a driver, which after undergoing the Self-Modulation Instability [28] is capable of accelerating electron beams from several MeV to 2 GeV in a 10 meters long plasma [29].

One of the next milestones for electron acceleration in PWFA is the beam quality. As mentioned above, several experiments have succeeded in demonstrating the high acceleration gradients, and have studied mechanisms to improve the monochromaticity of the accelerated bunches. Yet the out-coming transverse beam quality has been so far either severely degraded in most experiments when compared to the incoming beam quality, or not characterized. This, together with the not-yet-reached monochromaticity makes, the PWFA technique not capable to perform as good as RF-based accelerators in terms of beam parameters and limits its potential

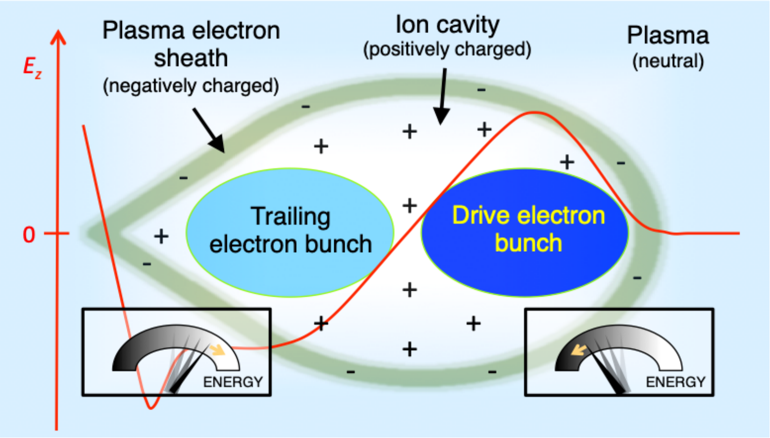

Fig. 1.2: Schematics of a PWFA (Courtesy of S. Corde).

applications. On the other hand, theory and simulations predict that the PBAs have most of the required features to perform similarly to RF-cavities. The upcoming experimental programs are planning to tackle these limitations and assess the remaining challenges. For instance, the SLAC LINAC has undergone a new reconfiguration which will enable the production of even more suitable beams for achieving the best expected performance of PWFA, building the upgraded Facility for Advance Accelerator Tests (FACET-II). In the context of this new facility, part of my PhD work has been dedicated to the transverse beam quality preservation.

As a hand-waving argument, the poorer performance that PBAs offer compared to RF-Cavities in terms of beam quality can be understood from the relevant spatial and temporal scales over which each technique occurs (see Fig. 1.1). The EM-modes excited in RF-cavities have typically meter long wavelengths, so as long as the beam longitudinal size is of the order of or smaller than a centimetre, all beam electrons will sit in the same phase of the mode and will be accelerated uniformly. For PBAs, the typical wavelengths of the plasma mode range from the millimeter to several micrometers, therefore requiring even smaller beams which are not trivial to produce in conventional accelerators. This explains why the first PWFA experiments at SLAC with the long 42 GeV electron beam had a very broad energy spectrum after the propagation in the plasma, since the beam longitudinal size was of the order of the plasma wavelength and therefore the beam electrons experienced all the phases, accelerating and decelerating, of the plasma wave.

In LWFA, since the electron beams are produced (injected) in-situ in the plasma wave, the beam quality is not analyzed from the perspective of preservation but rather from the production perspective. It is noteworthy that despite producing electron beams with parameters not as good as conventional accelerators in some aspects, it has been recently shown that an LWFA can also produce FEL-like radiation [30], process that requires an excellent beam quality and that so far was only achieved in high energy conventional accelerators. Nevertheless, the LWFA concept suffers from a phenomenon that does not occur in beam-driven PWFA, the dephasing of the accelerated beam: since the laser pulse propagates in the plasma at a slower velocity than relativistic electrons due to the index of refraction of the plasma, the accelerated electrons tend to dephase with respect to the plasma wave, ultimately quenching the acceleration. Innovating propositions to overcome this limitations in LWFA are being developed and GeV electrons bunches are currently produced in less than 10 cm in LWFA experiments

[31, 32].

To finish this section, I would like to briefly introduce two sub-topics of the field of PBAs that I have been able to follow closely during my PhD. The first one is positron acceleration. So far all the results presented in this section are related to electron acceleration in LWFA/PWFA. If at some point PBAs want to be the alternative to conventional accelerators in HEP colliders, they need to be able to also accelerate positrons. However plasmas are not exactly symmetric in terms of charge, since the positive component of plasmas (the ions) are heavier than the negative part, so they don't respond equally. Different techniques and scenarios have been proposed, but there is generally a tradeoff between energy efficiency and beam quality [33], and accelerating positrons with the same quality as electrons will likely result in a smaller energy efficiency.

The second topic is the so-called Hybrid Acceleration (or LPWFA), which consists on using a LWFA produced electron bunch to drive a PWFA stage [34]. The interest of this combination is that PWFAs are thought to be more stable and colder than LWFA, and therefore the PWFA could produce better quality electron beams than in a single LWFA stage [35]. Furthermore, it allows to probe the physics of PWFA in a laser laboratory, which has enabled for instance the optical measurement of plasma waves driven by a particle bunch [36].

1.2 Theory of Plasma Wakefield Acceleration

In this section the basic formalism and concepts used to model the plasma wakefield are introduced. We start with a qualitative description of the plasma wave and then the linear and non-linear models of the PWFA are discussed. The basic derivations presented in this chapter allow to describe the underlying physical processes of the plasma-based acceleration concept.

1.2.1 Electronic plasma wave

The electronic plasma wave is one of the collective EM phenomena that are characteristic of plasmas. It originates from an electronic density perturbation in an equilibrium plasma, which excites an electronic density wave. An illustrative analogy of this process are the waves produced in a lake when the surface equilibrium is perturbed. The excitation of an electronic plasma wave is schematically represented in Fig. 1.3. Figure 1.3(a) shows an equilibrium plasma with an equal amount of positive and negative charges, where positive charges (ions) are much heavier than negative charges (electrons). In such a system the time scale of the motion of positive charges is greater than that of the negatives, so as a first approximation we can consider positive charges as immobile during the motion of negative charges.

Let us now displace all negative charges from the position ξ_0 to the position $\xi_0 + \xi$ as indicated in Fig. 1.3(b). The system is not anymore is equilibrium and the displaced charges feel an electric force F_e towards the left due to the charge separation. The negative charges will thus start an oscillatory motion. Mathematically we can express the electric field seen by the displaced particles using Poisson equation as

$$E(\xi_0 + \xi) = \frac{n_0 e}{\epsilon_0}\xi \tag{1.1}$$

where n_0 is the particle density of ions (or equivalently that of unperturbed electrons), e is the electron charge and ϵ_0 is the vacuum permittivity. If we now insert this electric field in the

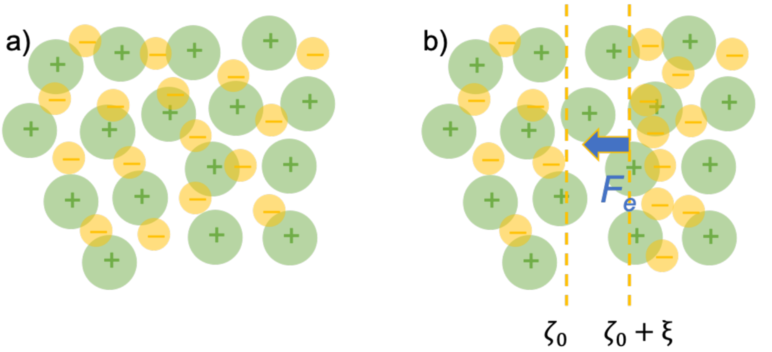

Fig. 1.3: Schematics of a plasma electronic perturbation leading to an electronic plasma wave. Yellow circles represent electrons and green circles ions. (a) Unperturbed plasma in equilibrium. (b) Perturbed plasma by an horizontal displacement of all plasma electron between the two yellow dashed lines.

equation of motion of a displaced electron we have

$$d_t^2\xi = -\frac{e}{m_e}E = -\frac{e^2 n_0}{m_e \epsilon_0}\xi \tag{1.2}$$

where m_e is the electron mass. The solution of this equation is an oscillatory solution of frequency $\omega_p = \sqrt{\frac{e^2 n_0}{m_e \epsilon_0}}$, the so-called plasma frequency. Another typical quantity often used in plasmas, the plasma skin-depth, can be expressed as $k_p^{-1} = c/\omega_p$ and represents the distance over which the plasma electrons can respond collectively.

The electric field experienced by the perturbed electrons is proportional to the plasma density and the frequency is proportional to the square root of the plasma density, so higher plasma densities can sustain larger fields at higher oscillation frequencies.

This simple description of the plasma wave allows us to estimate the maximum field amplitude that can be sustained in a plasma wave: the cold wave-breaking limit. It corresponds to having all plasma electrons displaced over a plasma skin depth, i.e. $E_0 = m_e c\omega_p/e$.

1.2.2 Linear fluid theory

The linear fluid model of PWFA describes the electronic plasma wave excited by a charged particle bunch propagating in a neutral plasma by applying a first order perturbative treatment to the plasma fluid equation of motion and taking the particle bunch as the initial source of the perturbation. Indeed, introducing a charged particle beam in an equilibrium plasma increases locally the charge density, which breaks the equilibrium. Plasma electrons react to this perturbation by moving away from the location with the excess of charge, same as in a conductor electrons tend to screen the fields of an external charge. If the electron bunch is then suddenly removed from that position in the plasma, there will be a positively charged area where the electron beam was placed, which will onset the electron plasma oscillation.

As will be clear later, the fact that the electron beam is treated as a perturbation means that its density needs to be much smaller than the plasma density, so that indeed the resulting plasma density perturbation is small compared to its unperturbed value. Ions are considered a steady neutralising background, so in this model the fluid quantities refer to the plasma electron specie. Let n_0 denote the equilibrium plasma density and n_1 the perturbed plasma density, so that $n_p(\mathbf{r},t) = n_0 + n_1(\mathbf{r},t)$ where $n_1(\mathbf{r},t) \ll n_0$. Similarly, the equilibrium and perturbed plasma fluid velocities are $v_0(\mathbf{r},t) = 0$ and $v_1(\mathbf{r},t)$ respectively. Note that since there are not electromagnetic fields in equilibrium ($E_0(\mathbf{r},t) = B_0(\mathbf{r},t) = 0$), at first order only electrostatic forces act on the plasma.

Let us start by deriving the equation describing the plasma density oscillations. Under these conditions, the fluid equation of motion and the continuity equation for plasma electrons read, at first order:

$$\partial_t \mathbf{p}(\mathbf{r},t) = m_e \partial_t \mathbf{v}_1(\mathbf{r},t) = -e\mathbf{E}_1(\mathbf{r},t) \tag{1.3}$$

$$\partial_t n_1(\mathbf{r},t) = -\nabla(n_p(\mathbf{r},t)\mathbf{v_p}(\mathbf{r},t)) = \nabla(n_0 \mathbf{v_1}(\mathbf{r},t)) \tag{1.4}$$

Merging both equations gives

$$\partial_t^2 n_1(\mathbf{r},t) = -\frac{n_0 e}{m_e} \nabla \cdot \mathbf{E_1}(\mathbf{r},t) \tag{1.5}$$

We can now use Maxwell-Gauss equation to express $\mathbf{E_1}$ as a function of the charged density of the system $-en(\mathbf{r},t)$

$$\nabla \cdot \mathbf{E}(\mathbf{r},t) = -\frac{e\,n(\mathbf{r},t)}{\epsilon_0} \tag{1.6}$$

Since the unperturbed plasma is charge neutral, the only perturbations in the system are $n_1(\mathbf{r},t)$ and the beam density $n_b(\mathbf{r},t)$, so we have $n(\mathbf{r},t) = n_1(\mathbf{r},t) + n_b(\mathbf{r},t)$. Introducing this in eq. (1.5) we obtain

$$\partial_t^2 n_1(\mathbf{r},t) = -\frac{n_0 e^2}{m_e \epsilon_0}(n_1(\mathbf{r},t) + n_b(\mathbf{r},t)) \tag{1.7}$$

which is the equation of an harmonic oscillator for $n_1(\mathbf{r},t)$ and therefore describes the electronic plasma waves. In the absence of beam, i.e. $n_b = 0$, $n_1(\mathbf{r},t) = 0$ is a valid solution of eq. (1.7), which means that indeed the beam is the source of the excitation of the electronic plasma density wave. The EM fields associated to this density wave, i.e. the plasma wakefields, can be derived using Maxwell equations under the quasi-static approximation. We start with the wave equation of the electric field in the Lorentz gauge

$$\left(\boldsymbol{\nabla}^2 - \frac{1}{c^2}\partial_t^2\right)\mathbf{E} = \mu_0 \partial_t \mathbf{j} + \frac{\boldsymbol{\nabla}\rho_{\text{tot}}}{\epsilon_0} \tag{1.8}$$

where $\mathbf{j}$ is the current density and ρ_{tot} is the total charge density of the system. To remove complexity in the notation, the spatial ($\mathbf{r}$) and temporal (t) dependences of the system variables are not explicitly written. As before, plasma electrons are denoted with subindex p. Beam electrons, denoted with subindex b, will be considered to be rigid, i.e. only have a fixed longitudinal velocity v_b in the z direction. This last assumption of the rigid beam can be justified by the relativistic component of the motion of beam electrons, which implies that they evolve over timescales longer than that of the non-relativistic plasma electrons.

Using the generalised Ohm's law of a collisionless plasma with a linear non-relativistic response

$$\mathbf{E} = \frac{m_e}{n_p e^2}\partial_t \mathbf{j_p} \tag{1.9}$$

we can get rid of the plasma current source of eq (1.8) and get

$$\left(\boldsymbol{\nabla}^2 - \frac{\omega_p^2}{c^2} - \frac{1}{c^2}\partial_t^2\right)\mathbf{E} = \mu_0 \partial_t \mathbf{j_b} + \frac{\boldsymbol{\nabla}\rho_{\text{tot}}}{\epsilon_0} \tag{1.10}$$

Using Faraday's law a similar equation is obtained for the magnetic field

$$\left(\boldsymbol{\nabla}^2 - \frac{\omega_p^2}{c^2} - \frac{1}{c^2}\partial_t^2\right)\mathbf{B} = -\mu_0 \boldsymbol{\nabla} \times \boldsymbol{j_b} \tag{1.11}$$

A first remark is that the only source of magnetic field is the beam current, which means that as showed before the plasma density wave itself is purely electrostatic. Yet, the magnetic field of the system is not the same with and without plasma, due to the current screening response of the plasma. We now apply the quasi-static approximation. For that, we define the co-moving longitudinal coordinate $\xi = v_b t - z$, and then we assume that all longitudinal and temporal dependencies enter only through this co-moving variable ξ. This mean that we can replace $\partial_t \rightarrow v_b \partial\xi$ and $\partial_z \rightarrow -\partial_\xi$. Under the quasi-static approximation and in cylindrical coordinates the equation of the EM fields can be rewritten as

$$\left(\triangle^2 - \frac{\omega_p^2}{c^2} - \frac{1}{\gamma^2}\partial_\xi^2\right)\mathbf{E} = -\mathbf{e}_z \frac{1}{\epsilon_0}\partial_\xi \left(\frac{\rho_b}{\gamma^2} + \rho_p\right) + \mathbf{e}_r \frac{1}{\epsilon_0}\partial_r \left(\rho_b + \rho_p\right) \tag{1.12}$$

$$\left(\triangle^2 - \frac{\omega_p^2}{c^2} - \frac{1}{\gamma^2}\partial_\xi^2\right)\mathbf{B} = -\mathbf{e}_\theta \mu_0 v_b \partial_r \rho_b \tag{1.13}$$

where we have defined $\triangle^2 = \boldsymbol{\nabla}^2 - \partial_z^2$ and γ is the relativistic Lorentz factor of the beam.

Note that if $\rho_b = -\rho_p$, which is just the beam charge neutralisation by the plasma, the radial electric field vanishes. Therefore if the plasma is able to neutralise the beam charge only the magnetic field B_θ can affect the beam transverse dynamics. This, which is relevant to understand the beam transverse dynamics in PWFA that will be discussed at a later point in this manuscript, means that it is the magnetic field that is responsible for the beam self-focusing under linear wakefields (see Sec. 5.2). The transverse beam dynamics in a PWFA is discussed in Sec. 1.3.

Finding the solutions of eq. (1.12) and (1.13) requires to first do a Fourier transform in ξ, use eq. (1.7) to express the Fourier transform of ρ_p as a function of the Fourier transform of ρ_b, solve the radial component of the differential equation (in cylindrical coordinates it is a Bessel-like differential equation) and then do the inverse Fourier transform in ξ. The calculation, especially the inverse Fourier transform, largely simplifies if one takes the ultra-relativistic approximation $\gamma \gg 1$. A detailed derivation can be found in [6], resulting in the following solution for a azimuthally symmetric system under the ultra-relativistic approximation in cylindrical coordinates:

$$E_z(r,\xi) = -\frac{k_p^2}{\epsilon_0}\int_0^\infty dr' I_0(k_p r_<) K_0(k_p r_>) \int_{-\infty}^{\xi} d\xi' \rho_b(r',\xi') \cos k_p(\xi - \xi') \tag{1.14}$$

$$E_r(r,\xi) = \frac{k_p}{\epsilon_0}\int_0^\infty dr' I_1(k_p r_<) K_1(k_p r_>) \int_{-\infty}^{\xi} d\xi' \partial_{r'} \rho_b(r',\xi') \sin k_p(\xi - \xi') \tag{1.15}$$

$$B_\theta(r,\xi) = k_p \mu_0 v_b \int_0^\infty dr' I_1(k_p r_<) K_1(k_p r_>) \int_{-\infty}^{\xi} d\xi' \partial_{r'} \rho_b(r',\xi') \sin k_p(\xi - \xi') \tag{1.16}$$

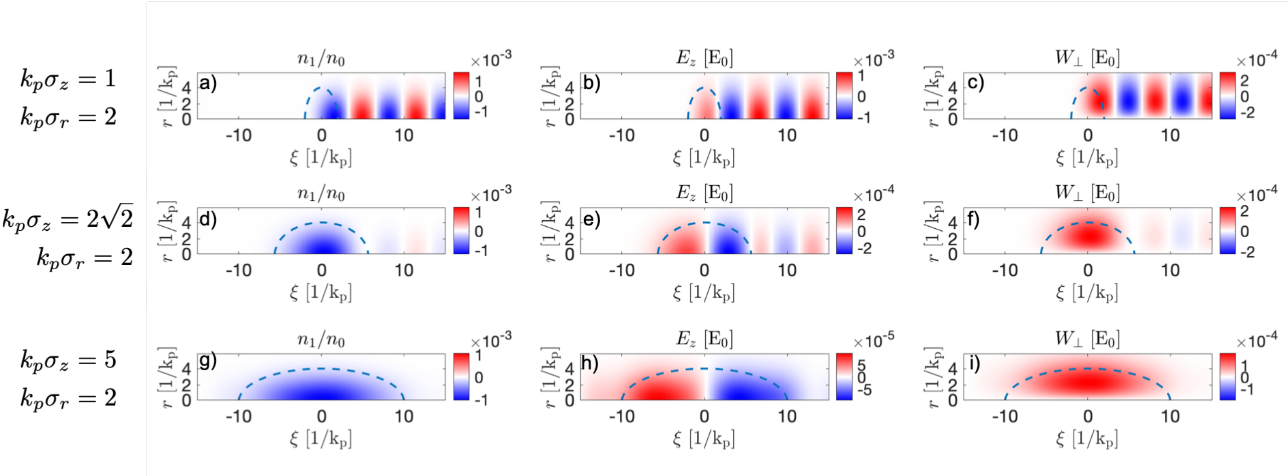

Fig. 1.4: Linear density perturbations (a,d,g) and linear wakefields (b,c,e,f,h,i) driven by a gaussian beam of peak density $n_b = 0.001n_p$ and different sizes. Dashed lines show the 2σ contour of the beam density.

where $I_{0(1)}$ and $K_{0(1)}$ represent the modified Bessel functions of zero (first) order, and $r_<$ ($r_>$) is the minimum (maximum) of between r and r'). The integral $\int_{-\infty}^{\xi}$ indicates that at a longitudinal position ξ only what happens "before", i.e. from $-\infty$ to ξ, matters (note that in the co-moving coordinates the beam propagates towards negative ξ). 2D maps of these solutions, together with the associated plasma density perturbation computed from eq. (1.7), are plotted in Fig. 1.4 for a gaussian beam of R.M.S. length σ_z and R.M.S. transverse size σ_r placed at $\xi = 0$. The peak beam density is set to $n_b = 0.001n_p$ in order to satisfy $n_b \ll n_p$. The third column shows the transverse force as experienced by an electron moving at the speed of the driver $W_\perp = E_r - v_b B_\theta$. The beam, whose 2σ contour is indicated by the blue dashed lines, propagates towards the left of the pictures.

For $k_p\sigma_z = 1$ (Fig. 1.4(a-c)) we observe the typical plasma wave left behind the beam, with the expected order of magnitude comparable to the beam-to-plasma density ratio (in normalized units). The plasma responds to the beam by trying to neutralise its charge, which due to the short duration of the beam (compared to the plasma period) is not effective at the front. Furthermore the short beam pulse duration leaves the plasma electron with some inertia after its passage, which onsets the electronic plasma oscillation. In terms of the wakefields, we observe that transverse and longitudinal wakefields are out of phase by a $\pi/2$ shift. In this short beam scenario, most of the beam electrons sit in the same phase of the wave, i.e. decelerating and focusing.

As the beam gets longer, the plasma electrons start to respond adiabatically, in other words, they have time to "accommodate" and screen the beam charge smoothly. For $k_p\sigma_z = 2\sqrt{2}$ we observe a weak plasma wave behind the driver, and for $k_p\sigma_z = 5$ no plasma wave is observed behind. The beam electrons experience a focusing transverse force, and the beam sees both the decelerating phase at the front and the accelerating phase at the rear. Note that the peak amplitude of the wakefields is decreased even if the plasma density perturbation is the same. An interesting interpretation of the long beam scenario is that the beam recovers most of the energy that it gives to the plasma (the front is decelerated but the rear is accelerated), so that the plasma has no energy left for the wave after the beam passage.

This analysis allows to do optimisation studies of the plasma wave excitation process to improve the performance of a PWFA. So far we are only including a drive beam, which will always in average lose energy to the plasma wave, but one can still optimise the peak wakefield amplitude at which a second electron beam (the trailing beam) will be placed. It can be shown that for gaussian beams and for a fixed beam-to-plasma density ratio, the maximum beam-plasma coupling efficiency is obtained for $k_p\sigma_z \approx \sqrt{2}$.

One advantage of the linear model is that the interference of two plasma waves can be described by a simple wave superposition. This is relevant when adding a second trailing bunch in the plasma wave excited by the drive beam: this second bunch is going to drive its own plasma wave, which is going to interfere with the original wave. This phenomenon is known as beam-loading. Similar to the long beam case, we want the trailing beam to extract most of the energy of the plasma wake, i.e. we want destructive interference. It turns out though, that due to geometrical constrains one cannot extract all the energy of a linear wake in 3D by destructive interference if drive and trailing have different beam sizes. It should also be noted that so far we have only mentioned electron bunches, but if this was a positively charged beam (positrons or protons) the wave would have the same shape but with the opposite amplitude.

It is important to keep in mind that this model is only valid if $n_b \ll n_p$ and does not describe the beam evolution. Yet, the transverse wakefields have a focusing effect on the driving beam, for either electrons and positrons. On the one hand, this focusing force helps to drive the wakefields over long propagation distances since it prevents the beam from diverging. On the other hand, unless the beam emittance term (see Sec. 1.3) compensate the focusing effect in the beam envelope equation (eq. (1.23)), the focusing effect naturally results in an increase of the beam density, and thus after some propagation the condition $n_b \ll n_p$ may no longer hold and a different non-linear formalism is required. As will be presented later in Chap. 5, this can bear important consequences for several processes.

Finally we would like to briefly discuss the linear formalism of the LWFA. Instead of having a n_b source term in the equations, the laser pulse can be described as first order EM fields via the vector potential $\mathbf{A_1}$. The linear plasma wave formalism then applies when the normalized vector potential $a_0 = \frac{eE}{m_e c\omega} \ll 1$ (where E is the electric field amplitude of the laser and ω the laser frequency). It turns out though that a linear perturbation $\mathbf{A_1}$ cannot excite a plasma wave (same as a when charged particle sees the EM fields of plane wave does not gain energy). It is actually through a second order term, the ponderomotive term ∇A_1^2, that a laser pulse can excite a plasma wave.

1.2.3 Non-linear theory

One of the pioneer theoretical studies of non-linear plasma electron oscillations was carried out by Dawson [37] in 1D back in 1959, showing that larger acceleration gradients could be achieved in this non-linear regime. The main limitation to extend this model to more than one dimension is that if electrons undergo non-linear oscillations particle crossing occurs and simple fluid theory breaks down. PIC simulations were initially used to assess this regime in more than 1D, which allowed to infer some basic scalings and properties of non-linear plasma wakes driven by high intensity beams ($n_b \geq n_p$ for electron beams and $a_0 \geq 1$ for laser pulses). Although several models of non-linear plasma wakes were derived at the beginning of the 2000's [38, 39], the most successful model was carried by Lu *et al* [40] in 2006. In the following we will briefly discuss the main elements of the so-called "blow-out" model without writing the explicit derivation, which can be found in Ref. [20].

This model assumes that an intense driver (either electron beam or laser pulse) expels all plasma electrons out, which can be interpreted as an extrapolation of the linear theory result that states that the amplitude of plasma density perturbation is of the order of the driver density. Therefore the driver creates an ion cavity void of plasma electrons. After the passage of the intense driver, the expelled electrons feel the attractive force of the ions and are then pulled back towards the center of the ion cavity, onsetting non-linear electron oscillations (see Fig. 1.2).

In the original paper by Lu *et al.* [20] it is shown that the formation of this ion cavity is tightly related with the onset of particle crossing in the blown-out plasma electrons, and conditions on the driver beam parameters are given to create an ion cavity, namely that it is the beam driver current and not the density the relevant parameter for the onset of non-linear plasma wakes. This particle crossing prevents a self-consistent fluid theory to relate the plasma electron trajectories with the EM fields, so a different formalism is required. The blow-out model assumes that the blown-out plasma electrons create a sheath of particles around the ion cavity, so that radially the plasma can be divided in three regions. For small radius only (immobile) ions are present. Then there is a thin sheath (thinner than the outer ion cavity radius) of blown-out plasma electrons whose radial coordinate is given by $r_b(\xi)$ (sub-index b stands for blow-out and ξ is the longitudinal co-moving coordinate), which defines the ion cavity shape. Finally for large radius (far from the driver) plasma electrons respond linearly, but this contribution (presumably small) is not described in the original paper.

The plasma response in this model is described by the blow-out sheath $r_b(\xi)$, i.e. only one trajectory. In this way the model can provide a description that is self-consistent with respect to the plasma motion and the electromagnetic fields. This model shows an excellent agreement with PIC simulation results, and allows to describe the EM fields inside the ion cavity.

Despite the higher amplitude of the non-linear wakefields predicted by this model, which are comparable to the cold wave-breaking field amplitude, the structure of these non-linear wakefields inside the ion cavity has some similarities with the linear model: the longitudinal electric field is decelerating at the front of the cavity (i.e. where the driver sits), vanishes and changes sign around the central longitudinal slice of the cavity (where $\partial_\xi r_b(\xi) = 0$) and reaches its maximum amplitude (accelerating for electrons) near the rear the ion cavity, where the cavity closes itself. Furthermore the transverse force has the same sign (focusing for electrons) all over the cavity, as in the linear regime. However the non-linear character of the plasma oscillations make the field spatial structure less sinusoidal, the longitudinal and transverse force having respectively a linear dependency on the longitudinal and transverse coordinate in the central region of the cavity. Furthermore, unlike in the linear case, the longitudinal electric field is transversely homogenous in the cavity, which implies that all electrons sitting in the same longitudinal position but at different radial positions in the cavity experience the same accelerating field. Similarly, as a consequence of the Panofsky-Wenzel theorem [41], the transverse force is longitudinally uniform. The larger amplitude, the linear spatial structure and the higher degree of uniformity of these fields make the non-linear "blow-out" regime of plasma wakefields much more suitable for electron acceleration than the linear regime.

One of the inconveniences of the non-linear model is that it is not symmetric for positive and negative charges, and thus cannot be extended to positron acceleration straightforwardly. The transverse wakefields inside the ion cavity are defocusing for positrons, and the accelerating fields are at the front of the cavity. Furthermore the non-linear waves excited by a intense positron bunch are very different to that driven by electrons [42] since plasma electrons are rather "suck-in" than blown-out. Acceleration has been nevertheless shown for positrons in the non-linear regime [43], but with a lower acceleration gradient compared to the electron case.

To finish this brief discussion of the non-linear plasma blow-out regime, I would like to illustrate with a recent example its validity. This model can also describe the beam-loading, i.e. the effect of adding a second electron bunch in the ion cavity [25]. It predicts that the length of the ion cavity is increased and the accelerating longitudinal field in the position of the beam tends to flatten, which further reduces the energy spread of the trailing beam. A recent experimental campaign at FlashForward showed an excellent agreement with this theory by changing the trailing bunch length [26, 27] and observing the predicted trends in terms of trailing final energy and energy spread.

1.3 Introduction to beam dynamics in a Plasma-Based Accelerator

This section is a brief introduction to the beam parameters and beam dynamics that are relevant for the results presented in this manuscript. The main focus is on the transverse beam parameters and their evolution, which allow to quantify the so-called transverse beam quality. Preserving the transverse beam quality in PWFA accelerators is one of the next milestones that need to be achieved to prove that PBAs can be a feasible alternative to conventional RF-based accelerators. Unlike for the longitudinal beam quality (energy spread), not many experimental campaigns have been dedicated to the transverse beam quality and the promising theoretical predictions still need to be confirmed in experiments.

1.3.1 Beam parameters

The motion of a point-like particle at a given time can be defined by the 6 phase-space coordinates (x, y, z, p_x, p_y, p_z). For ultra-relativistic particles moving with a relativistic velocity along one specific direction (z), it is often useful to perform the following change of variables:

$$(x, y, z, p_x, p_y, p_z) \rightarrow \left(x, y, z, x' = \frac{p_x}{p_z} = \frac{dx}{dz}, y' = \frac{p_y}{p_z} = \frac{dy}{dz}, \gamma \right) \tag{1.17}$$

where γ is the relativistic Lorentz factor of the particle. In this case we use the transverse angle x' with respect to the longitudinal axis to describe the transverse motion: for the same energy, free particles with larger angles will diverge faster from the longitudinal axes. Instead of phase-space, this new 6D space is sometimes referred to as trace-space.

In order to describe the motion of a particle beam, collective variables are needed. In the case of a cylindrically symmetric beam, the transverse motion is only defined by the radial trace-space (r, r'). Yet it should be noted that conventional accelerator beam optics (quadrupoles or sextupoles) are not cylindrically symmetric, i.e. they do not produce symmetric beams. For the collective variables, accelerator physicists typically use root-mean-squared (RMS) values, so that one can define the beam radius $\sigma_r = \sqrt{\langle r^2 \rangle}$ or divergence $\sigma'_r = \sqrt{\langle r'^2 \rangle}$ where $\langle \cdot \rangle$ represents the mean value.

One of the most relevant transverse beam parameters is the geometrical emittance, which quantifies the transverse trace-space area occupied by the beam particle distribution. It is often denoted $\tilde{\epsilon}$, and can be computed as $\tilde{\epsilon}_r = \sqrt{\langle r^2 \rangle \langle r'^2 \rangle - \langle r\, r' \rangle^2}$. Since the divergence $\sigma_{r'}$ naturally decreases as the beam gains energy, in order to compare the transverse emittance of beams with

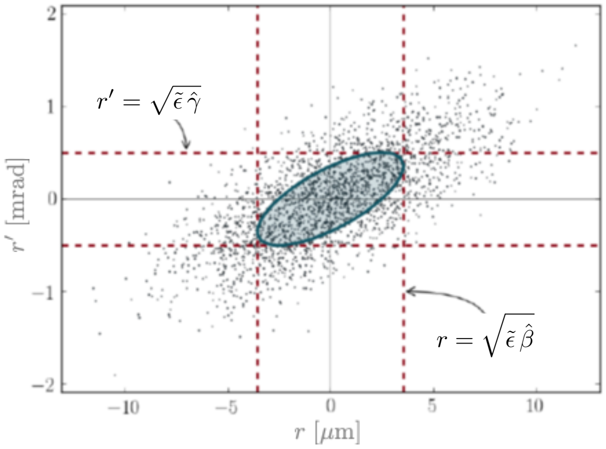

Fig. 1.5: Trace-space distribution of a particle beam. Individual particles are represented by the dots, and the shaded area represents the R.M.S. ellipse whose area is the geometrical emittance. Figure from Ref. [44].

different energies the normalized emittance is defined as $\tilde{\epsilon}_{r,n} = \gamma\beta\tilde{\epsilon}$ where β is the normalized beam mean velocity. A schematic representation of the trace-space of a particle beam is shown in Fig. 1.5, where the shaded area is proportional to the beam emittance. It should be noted that this manuscript sometimes deals with transversely asymmetric beams, for which the four dimensional normalized emittance is computed as $\tilde{\epsilon}_{4\mathrm{D},n} = \tilde{\epsilon}_{x,n}\tilde{\epsilon}_{y,n}$ where x and y denote the two transverse coordinates.

Sometimes the concept of beam emittance is compared to the concept of entropy. The underlying idea is that, even if there exists methods to decrease the emittance of a beam, under most circumstances the normalized emittance always tends to increase as the beam evolves. As it will be explained later, the emittance sets the limit of the minimum transverse size down to which the beam can be focused in a given transport system, so for most applications one wants to design an accelerator where the emittance does not significantly grow during the acceleration.

The beam evolution in an accelerator is usually described by the Twiss parameters. Denoted $\hat{\alpha}$, $\hat{\beta}$ and $\hat{\gamma}$, they are defined in each transverse plane (x, y) as the second order momenta:

$$\hat{\alpha}_x = -\frac{\langle x\,x' \rangle}{\tilde{\epsilon}} \tag{1.18}$$

$$\hat{\beta}_x = \frac{\langle x^2 \rangle}{\tilde{\epsilon}} \tag{1.19}$$

$$\hat{\gamma}_x = \frac{\langle x'^2 \rangle}{\tilde{\epsilon}} \tag{1.20}$$

and equivalently for y. Also called "the beta function", $\hat{\beta}_x$ is equivalent to the Rayleigh length of a laser, i.e. the typical propagation distance over which the beam exapands. $\hat{\gamma}_x$ is the normalized beam divergence (see Fig. 1.5). Finally $\hat{\alpha}_x$ measures the correlation between the space and the angle coordinates. Note that $\hat{\beta}_x\hat{\gamma}_x - \hat{\alpha}_x = 1$ and $\partial_z\hat{\beta}_x = -2\hat{\alpha}_x$.

Typically the transverse trace-space distribution of a particle beam is an ellipse centered at the origin. A positively tilted trace-space ellipse ($\hat{\alpha} < 0$) represents a diverging beam, a negatively tilted ellipse ($\hat{\alpha} > 0$) represents a converging beam, and an up-right ellipse ($\hat{\alpha} = 0$) represents a beam at waist.

There are two main processes for a charged particle beam to diverge: at low energies ($v < c$) the space-charge force (Coulomb repulsion) push charged particles away from each other. At relativistic energies ($v \approx c$) the magnetic field of the beam almost completely compensates the electric force down to $1/\gamma^2$, and then the main source of divergence is the inner pressure (transverse momentum spread) of the beam.

As a consequence, a particle beamline requires focusing elements to prevent the beam from expanding too much. In conventional particle accelerators this is usually done via the so-called FODO lattices (magnetic quadrupoles) [45]. These elements are inserted in between RF-cavities sections to refocus the beam and control the particle beam size and divergence. In the particle transverse trace-space, this refocusing leads to ellipsoidal trajectories. For the trace-space ellipse it results in a rotation, evolving from positively tilted to negatively tilted and vice-versa. It should be noted that, as a consequence of Liouville's theorem, as long as the transverse forces are linear in the radial coordinate and in the absence of collisions the ellipse rotation does not lead to any normalized emittance growth, i.e. the phase-space ellipse area are remains constant.

Before moving to the beam dynamics in PWFA, let us briefly describe in terms of the beam parameters that we have defined in this section the evolution of a monochromatic (zero energy spread) relativistic particle beam free propagating from the exit of a focusing element of a given focusing strength. Initially the beam will be converging, and so the corresponding trace-space ellipse will be negatively tilted. Individual particles will only move horizontally in the trace-space $x - x'$ ($\hat{\gamma}$ is constant) and the trace-space ellipse evolves towards the up-right position. In terms of beam parameters this means that $\hat{\beta}$ decreases as $\partial_z \hat{\beta} = -2\hat{\alpha}$. When the ellipse gets to its up-right position, corresponding to the waist, $\hat{\alpha} = 0$ and $\hat{\beta}$ reaches its minimum value $\hat{\beta}^* = (\hat{\gamma}^*)^{-1}$, where the star refers to the values at waist. Note that for a given initial beam size $\sigma_{r0} = \sqrt{\langle r_0^2 \rangle}$ and focusing strength element, a smaller emittance results in a smaller beam size at waist. After the waist, the beam diverge and $\hat{\beta}$ increase. In this process (free drift), the evolution of the beta function with respect its waist value can be computed as

$$\hat{\beta}_x(z) = \hat{\beta}_x^* \left(1 + \hat{\alpha}_x^2(z)\right) = \hat{\beta}_x^* \left(1 + \left(\frac{z - z^*}{\hat{\beta}_x^*}\right)^2\right) \tag{1.21}$$

1.3.2 Beam matching

As stated before, one of the main advantages of the blow-out regime of PWFA is that the focusing force is linear in r. Therefore a mono-energetic electron beam propagating inside the ion cavity will be continuously focused without emittance growth. The transverse equation of motion of a single particle can be written as

$$\partial_z^2 r + k_\beta^2 r = 0 \tag{1.22}$$

where $k_\beta = \frac{1}{\sqrt{2\gamma \partial_r F_\perp}}$ is the betatron wave number and $\frac{F_\perp(r)}{eE_0} = \frac{-k_p r}{2}$ is the radial force inside the ion cavity [40]. The solution to this equation is an oscillating trajectory which is represented in trace-space as a closed elliptical trajectory, which when accounting for a particle distribution leads to the aforementioned trace-space ellipse rotation at the betatron frequency $\omega_\beta = ck_\beta$.

After some algebra, a similar equation can be derived from eq. (1.22) for the beam radius $\sigma_r = \sqrt{\langle r^2 \rangle}$

$$\partial_z^2\sigma_r + k_\beta^2\sigma_r = \frac{\tilde{\epsilon}_r^2}{\sigma_r^3} \tag{1.23}$$

often referred as the beam-envelope equation. The solutions to this equation are the so-called beam-envelope oscillations: when $k_\beta\sigma_r^2 \neq \tilde{\epsilon}_r$ the envelope perform oscillations at $2\omega_\beta$, but when $k_\beta\sigma_r^2 = \tilde{\epsilon}_r$ the right hand side emittance term of the eq. (1.23) compensates the focusing term and $\sigma_r = \mathrm{cte}$ is a valid solution. Once again, we observe here the limiting effect of the emittance as it opposes to the focusing and therefore play a key role in the minimum beam size that can be achieved.

So far we have only discussed mono-chromatic beams. It is known though that it is challenging to produce mono-chromatic beams in a PWFA due to the typical small size of the accelerating structure. For most of the relevant experimental conditions, in the two-bunch PWFA configuration even if the injected trailing beam is initially mono-chromatic the accelerating field is not totally flatten over the whole length of the beam, which results in the beam experiencing different accelerating fields at different longitudinal positions and thus induces a certain degree of energy spread.

Since the betatron frequency of each particle depends on the energy ($\omega_\beta \propto \gamma^{-1/2}$), a non-monochromatic beam will experience different envelope evolutions and trace-space ellipse rotations at each energy. This can lead to an increase of the trace-space area occupied by the beam particles as illustrated in Fig. 1.6 (a), even if the area of a single-energy trace-space ellipse does not increase during the ellipse rotation. In this figure, each color represents one particle energy. This emittance growth due to chromaticity spread is thought to be an important source of emittance growth in PWFA, and its mitigation is one of the main challenges to overcome in order to demonstrate the trailing beam emittance preservation.

The most straightforward solution is to have completely monochromatic beams during all the acceleration process, i.e. inject a monochromatic trailing beam which perfectly flattens the accelerating field over its full length. This scenario, though being theoretically possible [47], requires a high control on the beam current profile which is currently not achievable experimentally with the high peak current beams required to drive a PWFA.

The second solution to suppress the emittance growth due to chromaticity spread, which does not require a zero beam energy spread, is called beam matching. Intuitively, the beam matching scenario consists in making the beam trace-spaces ellipses "round" so that even if different energy ellipses rotate at different rates the overall trace-space area remains constant. In this definition the roundness of the trace-space ellipse should be measured in the normalized coordinates ($\hat{x} = k_\beta x, x'$). A round trace-space ellipse further leads to a non-evolving beam envelope, and it can be easily shown that in the normalized coordinates the roundness condition implies that $\sigma_r = \sqrt{\tilde{\epsilon}_r k_\beta^{-1}}$, which as expected cancels the second term of the left hand side with the right hand side of eq. (1.23). In terms of Twiss parameters, the beam matching conditions can be expressed as $\hat{\alpha}_\mathrm{m} = -\partial_z\hat{\beta}_\mathrm{m}/2 = 0$ and $\hat{\beta}_\mathrm{m} = k_\beta^{-1}$ where the subindex m denotes the matched parameters. The degree of mismatch is sometimes expressed via the emittance magnification factor β_mag [48]. For a matched system $\beta_\mathrm{mag} = 1$, and this value increases as the system gets a larger degree of mismatch. In the limit of a large mismatch $\beta_\mathrm{mag} \approx \frac{1}{2}\frac{\hat{\beta}_\mathrm{max}}{\hat{\beta}_\mathrm{m}}$. Furthermore, it should be noted that a small non-linearity of $F_\perp$ with respect to the radial coordinate a matched propagation also lead to a minimum emittance growth, even with a mono-energetic beam.

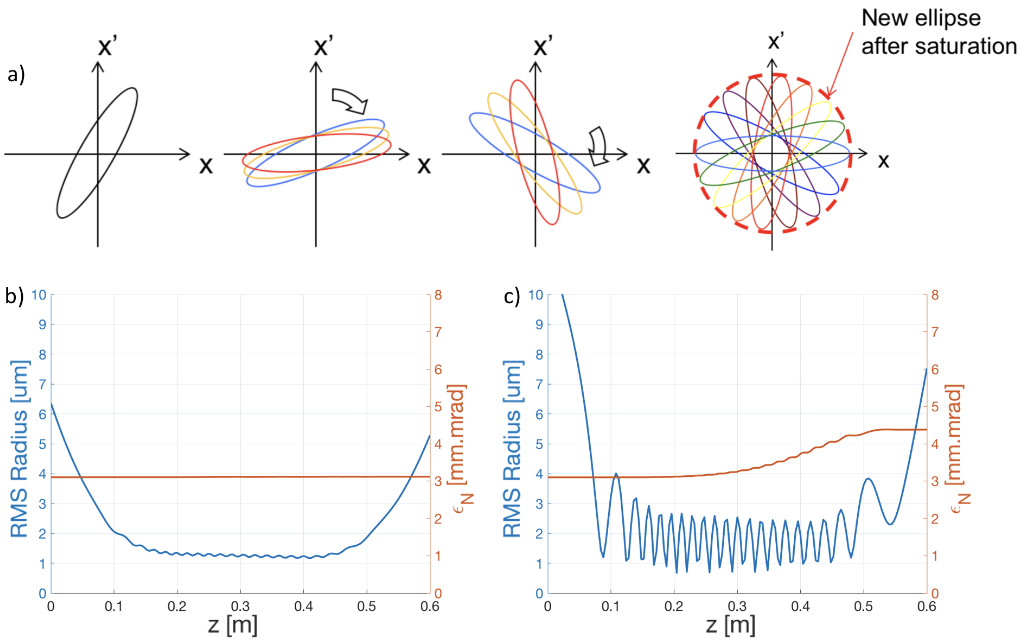

Fig. 1.6: (a) Schematics of emittance growth due to chromaticity spread under a linear focusing force. Each particle energy is represented by one color. (b) and (c) show the trailing beam envelope (blue) and normalized emittance (orange) evolution for a PWFA in FACET-II-like configuration (see Chap. 2) under beam matching conditions (b) and without matching conditions (c). Figure from Ref. [46].

An example of a matched PWFA and a mismatched PWFA is shown in Fig. 1.6 (b) and (c) respectively as extracted from QuickPIC simulations [49, 50]. The trailing beam envelope (blue) and normalized emittance (orange) are plotted as a function of the propagation distance. The plasma has 20 cm long semi-gaussian ramps at the entrance and at the exit, which dictates the initial and final beam envelope evolutions (see Fig. 2.1(a)). In both cases the bi-gaussian trailing beam has zero initial energy spread, but the wake not being completely loaded some energy spread grows as the beam propagates in the plasma. In both cases the final energy spread is ≈ 10%. The only difference between the two cases is the initial trailing Twiss parameters. In the matched case almost no beam envelope oscillations are observed, and the normalized emittance is constant throughout the plasma. The slight decrease of the trailing beam envelope is related to the trailing energy gain in the plasma. In the mismatched case beam envelop oscillation are present and as the beam energy spread grows the normalized emittance also increases. These two examples of beam matching in a PWFA are part of a more extensive simulation study that is presented in the Chap. 2, but they are shown here for illustrative purposes.

It should be noted that the concept of beam matching also exists in conventional accelerators in the focusing sections. As in PWFA, in order to achieve the matching conditions experimentally one needs to inject the initially monochromatic beam in the focusing section with the right beam radius and angular spread. However in the PWFA scenario the presence of plasma density gradients at the plasma entrance, for which tracking the beam evolution is a non-trivial task, make achieving the beam matching conditions a very challenging process. This non-trivial beam dynamics in a plasma density gradient can be observed at the beginning of the beam propagation in the beam envelope evolution (blue curves) plotted in Fig. 1.6 (b) and (c): whereas a smooth focusing is observed in the matched case, several varying amplitude oscillations are observed before the beam enters the uniform region (at $z = 20\,\mathrm{cm}$). Predicting the matching conditions for a given initial beam parameters needs to account for this non-trivial evolution, which further requires a precise knowledge of the density gradient, task that also present several experimental challenges. Yet, theoretical and simulation studies show that under the right assumptions or using specific plasma density profiiles the trailing beam evolution can be computed and controlled to reach the matching conditions in the flat-top region of the plasma [51, 52]. The technique that will be used in this manuscript to study different beam matching conditions with a plasma profile that includes density gradients is to vary the initial beam parameters at the plasma entrance in such a way that is equivalent to a longitudinal shift of the waist position of the particle beams. Using this procedure, a new experimental technique to asses beam matching non-destructively is presented in Chap. 2.

1.3.3 Centroid oscillations and hosing instability

Beam centroid oscillations are expected to arise when a beam propagates in a steady ion channel with a transverse offset with respect to the central axis of the channel. However if we also consider the electrostatic response of the channel boundaries (plasma electrons placed at the ion channel boundary) to these beam centroid oscillations, the so called "hosing instability" can be onset. This instability refers to the beam centroid oscillations whose amplitude grows exponentially, and that results from the coupling of the beam transverse displacement with the plasma electrons placed at the boundary of the ion cavity. This mechanism leads to a severe disruption of the beam propagation, especially when the beam electron trajectories start to reach the ion cavity walls. A beam profile disrupted by the hosing instability is shown in Fig. 1.7(a).

The existing theories [53, 54] predict a rapid growth of the instability for experimentally relevant beam-plasma parameters, which would set an important limitation to the PWFA concept. Nevertheless several mitigation effects have been identified [55], which could potentially explain the fact that no clear experimental signature has been found so far in a PWFA experiment.

Nevertheless, in the two-bunch configuration of PWFA, an initial misalignment between the driving and trailing beams would onset the beam centroid oscillations and, unless suppressed, the growth of the hosing instability. Both processes would anyway lead to a non-negligible amount of emittance growth, as shown in Fig. 1.7(b). This figure shows the simulated trailing beam centroid and the emittance growth of a matched FACET-II beam-plasma configuration (see Sec. 2.1) to which a transverse initial offset of the order of the beam size is introduced along one of the transverse direction. The solid lines correspond to the beam parameters along the direction to which the offset is introduced, showing a significant emittance growth caused by the beam centroid oscillations (no clear hosing instability development is observed). In contrast, the dashed lines, which correspond to the beam parameters along the centered transverse direction, do not show significant centroid oscillations and no emittance growth is observed along this direction.

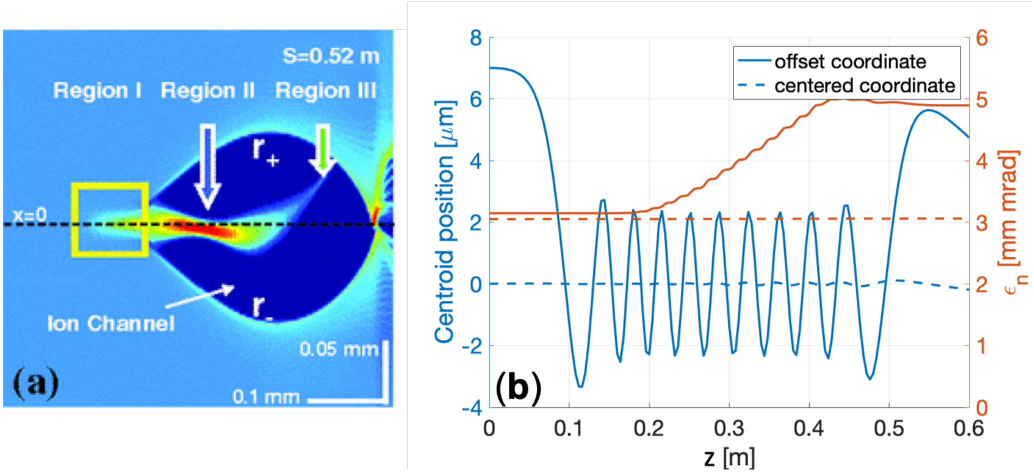

Fig. 1.7: (a) Simulated beam density and plasma density profile after the development of the hosing instability (figure from Ref. [54]). (b) QuickPIC simulation results (see App. A) of the FACET-II matched configuration (see next chapter) with an initial transverse offset in the trailing beam centroid position. Trailing beam centroid position (blue) and normalized emittance (orange) as a function of the propagation distance in the two transverse directions: solid lines correspond to the transverse direction along which the initial offset is introduced and dashed lines correspond to the centered transverse direction.

1.4 *Betatron radiation in Plasma-Based Accelerators*

When charged particles are accelerated they emit electromagnetic radiation. The betatron radiation refers to the radiation produced by the beam particles in a PBA due to their transverse motion. From the resulting oscillatory trajectories $\mathbf{r}(t)$ of individual beam particles, the angular and spectral distribution of the emitted radiation in a direction $\mathbf{n}$ can be computed from the Liénard-Wiechert fields as [56]

$$\frac{d^2 I}{d\Omega d\omega} = \frac{e^2}{16\pi^3 \epsilon_0 c} \times \left| \int_{-\infty}^{\infty} e^{i\omega(t-\mathbf{n}\cdot\mathbf{r}(t)/c)} \frac{\mathbf{n} \times \left[(\mathbf{n} - \boldsymbol{\beta}) \times \dot{\boldsymbol{\beta}} \right]}{(1 - \mathbf{n}\cdot\boldsymbol{\beta})^2} dt \right|^2 \tag{1.24}$$

where $\boldsymbol{\beta}$ is the normalized velocity of the particle. This general formula contains all the physics of the radiation emission, and an interesting qualitative analysis of this formula can be found in Ref. [57]. In the same reference the authors show a detailed derivation, starting from this formula, of the main features of betatron radiation in PBAs. In this section we will only highlight the main points of this derivation to then apply the results to our analysis.

The beam electron trajectories in a PBA have a relativistic longitudinal component ($\beta_z \approx 1$) and perform sinusoidal transverse oscillation ($r(t) \propto \sin(\omega_\beta t)$). For such trajectories it can be shown that the radiation is mostly emitted in the direction of the velocity $\boldsymbol{\beta}$, i.e. mainly in the forward direction, with a typical opening angle of $1/\gamma$.

For these trajectories there exist two radiation regimes: the wiggler and the undulator. The parameter that defines in which regime the radiation emission happens is the K-parameter (or strength paremeter) $K = \gamma\psi$, where ψ denotes the maximum transverse angle x' of the trajectory. As illustrated in Fig. 1.8, the K-parameter quantifies the ratio of the particle angle and radiation aperture angle: if $K \ll 1$ the radiation emitted at different points of the

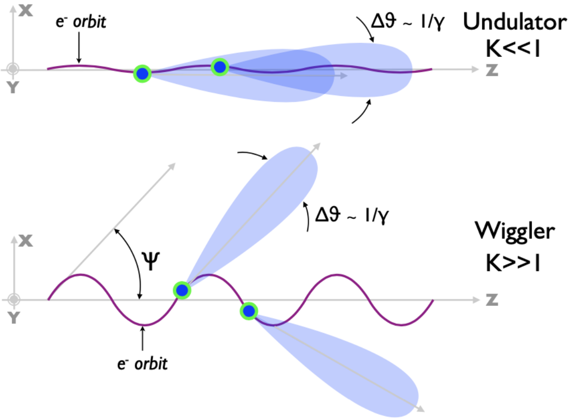

Fig. 1.8: Illustration of two electron trajectories in the undulator (top) and wiggler (bottom) regimes. Shaded areas represent the angular distribution of the emitted radiation. Figure from Ref. [57].

trajectory overlap, which is called the undulator regime, whereas if $K \gg 1$ different points of the trajectories radiate in different directions, which is called the wiggler regime. This difference leads to two different radiation features, in terms of the spectral and angular distributions. The undulator motion leads to monochromatic radiation around the fundamental doppler-shifted wavelength

$$\lambda = \frac{\lambda_u}{2\gamma^2}(1 + \frac{K^2}{2} + \gamma^2\theta^2) \tag{1.25}$$

where λ_u is the trajectory period and θ is the angle of observation with respect to the longitudinal axis. In contrast, the wiggler motion regime leads to a continuous spectrum referred to as synchrotron spectrum, characterized by a critical frequency $\omega_c = \frac{3}{2}\gamma^3 \times \frac{c}{\rho}$ where ρ denotes the curvature of the trajectory, and leads to the following power spectrum

$$\frac{dP}{d\omega} = \frac{2e^2}{27\pi\epsilon_0 c\gamma^2}\frac{9\sqrt{3}}{8\pi}\omega\int_{\omega/\omega_c}^{\infty} K_{5/3}(\xi)d\xi \tag{1.26}$$

where $K_{5/3}$ denotes the modified Bessel function of second kind. Examples of a synchrotron-like spectrum with a critical frequency $\omega_c \approx 300$ keV are plotted in Fig. 2.1 (b) (see Sec. 2.1 for further details on the plotted spectra).

So far we have only discussed single particle emission, but in reality all beam particles contribute to the emitted radiation. Disregarding coherence effects, which are not expected to play an important role in most PBAs, the total radiation can be computed as an incoherent superposition of individual particle emissions (summing intensities). In order to get simple estimations, back-of-the-envelope calculations can be carried out for a given system, relying on the fact that the main contribution to the total radiation originates from those particles who experience the largest transverse forces (typically the outer most particles) and that have the largest Lorentz factor (typically close the end of the acceleration stage).

The first experimental measurement of betatron radiation was carried out at SLAC in a beam-driven PWFA [58]. In this experiment, as in most PBAs operating in the blow-out regime, the betatron radiation is dominated by the wiggler motion, and a synchrotron-like radiation is produced. Most of the experimental studies of betatron radiation have been carried out in the context of LWFA [57], where it can be used as a mechanism to transform an optical laser system into an X-ray source [59]. Moreover the betatron radiation produced in LWFA has been proposed as an electron beam diagnostic to retrieve information on beam dynamics, injection and emittance [60, 61, 62, 46]. As a recent example of the state-of-art of the betatron studies in LWFA, a original experimental method has been proposed [63] to boost the X-ray yield of a LWFA by increasing the transverse displacement of the beam electron trajectories inside the ion cavity.

In the PWFA community, much fewer studies of betatron radiation have been published in the recent years. Moreover, these recent studies are mainly of theoretical and simulation nature [64, 65], emphasising the lack of designed experiments to explore the underlying physics behind this process. In the next chapter simulation results of the betatron radiation emitted with the expected FACET-II beam-plasma parameters are presented, showing how the betatron radiation can provide a precious insight into the beam dynamics and help the accomplishment of the next PWFA milestones and their experimental demonstration, in particular the emittance preservation.

2. BETATRON RADIATION AND BEAM DYNAMICS IN PWFA

The second chapter of this manuscript presents simulation results that show the correlation between the beam dynamics and the characteristics of the emitted betatron radiation in a PWFA stage. Namely, a new experimental technique to assess the matching dynamics of the trailing beam in a PWFA is proposed. The signatures of beam centroid oscillations and asymmetrical transverse beam dynamics on the betatron radiation features are also discussed. Since this study was carried out in the context of the FACET-II facility, the first section describes typical beam-plasma parameters available at the facility as well as the associated betatron radiation properties. The second section shows via simulations the working principle of the proposed experimental technique to assess non-destructively the beam matching conditions. Finally the third section discusses the effect of beam centroid oscillation on the emitted betatron radiation, relevant for hosing instability studies.

2.1 Betatron radiation at FACET-II

FACET-II is a new facility with the unique capability to develop advanced acceleration and radiation techniques with high-energy electron and positron beams [66]. It inherits the second half of the FACET LINAC, i.e. about 1 kilometer of LINAC, to accelerate electrons up to 13 GeV. Furthermore a new photocathode has been installed as the injector, in contrast to the thermionic gun that was used in the previous FACET facility. This new electron gun, together with a new design of the beamline, enable FACET-II to deliver beams with unprecedented beam peak currents and low emittances. This choice of beam parameters is strongly motivated by the optimum parameters for a PWFA stage: the high peak current allows to drive strongly non-linear wakefields and the small emittances allow to strongly focus the beams to fit them transversely inside the ion cavity. Further information about the FACET-II accelerator and experimental area is presented in Sec. 3.1.

Particle tracking simulations of the FACET-II accelerator have been used to give estimates of the optimum beam parameters that will be achieved. For PWFA experiments, the nominal beam parameters in the two bunch configuration that FACET-II is expected to deliver are summarised in table 2.1. The nomenclature used, which follows the same convention as before, is defined in the table caption. It should be noted that these beam parameters are given at the trailing waist, which does not correspond to the drive waist location due to the slightly different energies of each beam, originating from the optimisation of the trailing beam parameters.

In terms of plasma target, the same lithium oven as in FACET will be used [67]. The typical working conditions of this oven provide the plasma density profile shown in Fig. 2.1(a): semi-gaussian up and down ramps of ≈ 20 cm of length and a plateau density of $n_p = 4 \times 10^{16}\,\mathrm{cm}^{-3}$ and length ≈ 20 cm. Remarkably, the first simulations performed with these expected beam-plasma parameters showed excellent results in terms of energy transfer efficiency, reaching drive beam energy depletion, and in terms of trailing beam energy spread and emittance [68].

	Drive Beam	Trailing Beam
$\hat{\alpha}_{x,y}$	4.2, 1.6	0, 0
$\hat{\beta}_{x,y}$ [m]	0.7, 0.7	0.05, 0.05
Q [nC]	1.6	0.5
σ_z [μm]	6.4	2.8
E [GeV]	10	10
$\tilde{\epsilon}_{n_{x,y}}$ [mm·mrad]	3.4, 3.0	3.2, 3.2
Δz [μm]	150	
$\Delta W_{x,y}$ [cm]	16, 31	

Tab. 2.1: Relevant beam parameters at the location of the x and y trailing waist used in the simulations: α and β are the Twiss parameters, Q is the beam charge, σ_z is the R.M.S. bunch length, E is the energy, $\epsilon_{N_{x,y}}$ is the normalized emittance, Δz is the longitudinal separation distance between the bunches and $\Delta W_{x,y}$ is the distance between locations of the drive waist and the trailing waist (ΔW_x for x waist, ΔW_y for y waist).

However it was soon pointed out that such extreme beam parameters are not only able to ionise lithium (which will be pre-ionised with a laser pulse) but also the buffer gas (He) placed at the entrance and exit of the heated lithium, creating a non-desired He plasma density that disturbs the beam ballistic propagation towards the lithium plasma. This issue was found to set a non-zero lower limit in the achievable emittance growth, i.e. if the beam ionises the buffer gas the trailing emittance cannot be preserved in the PWFA stage. For the first PWFA experiments, the normalized emittance will be increase to ≈ 30mm mrad, but in order to work at lower emittance values a hydrogen plasma target is being designed.

Using the beam-plasma parameters of Tab. 2.1 it is possible to numerically compute the betatron radiation that will be produced at FACET-II. The numerical calculation is carried out in two steps:

- The quasi-static PIC code QuickPIC [50, 49] (see App. A) is used to self-consistently simulate the beam propagation in the plasma in a 3D geometry with a moving window. An interesting feature of QuickPIC is the beam initialisation via the Twiss parameters, which allows to easily reproduce experimental beam conditions. The plasma is initialised as Li^{1+} with the expected longitudinal profile shown in Fig. 2.1. Since the ionisation is not modelled in these simulations the He buffer gas is not simulated. In addition to the density and field maps, full 6D phase-space coordinates of beam macro-particules are extracted with a high enough dumping frequency to resolve the individual macro-particles trajectories.

- A post-processing code based on the Lienard-Wiechert potentials and the formulas given in Sec. 1.4 is used to compute the radiation angular and spectral distribution emitted by each individual trajectory, which are afterwards incoherently summed and rescaled to the total number of real electrons in the beam. Due to the strongly non-linear wakefields excited under the FACET-II experimental conditions ($K \gg 1$) the following simplification, sometimes referred to as synchrotron approximation, is adopted: instead of computing the numerically expensive eq. (1.24), one can assume that at a given time-step the particle radiates in the direction of the particle velocity with a synchrotron spectrum (eq. (1.26)). This approximation reduces significantly the computational cost of the radiation calcula-

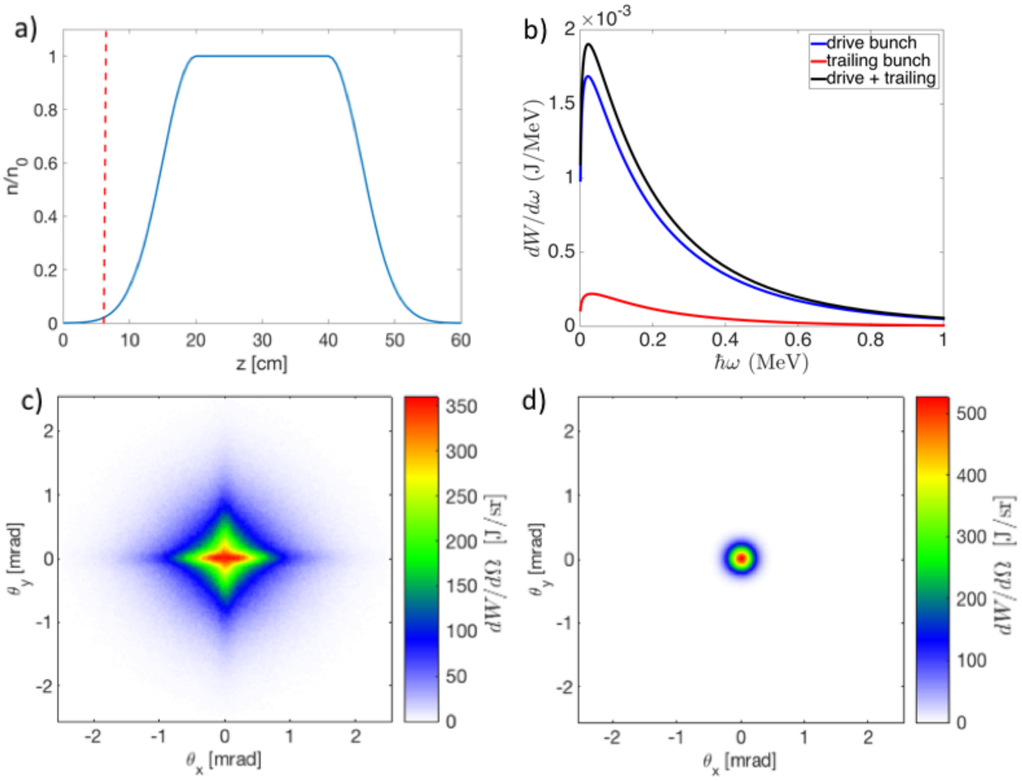

Fig. 2.1: a) Plasma density profile used for QuickPIC simulations ($n_0 = 4 \cdot 10^{16}$ cm^{-3}). Red-dashed line shows the position of the focal plane of the trailing bunch for the matched conditions. b) Photon energy spectrum of the radiation emitted by the trailing bunch (red), drive bunch (blue) and both (black). c) Radiation angular distribution of the drive bunch (J/sr). d) Radiation angular distribution of the trailing bunch (J/sr). Figure from Ref. [46].

tion and provides good agreement with the exact calculation under the studied conditions. It should be noted that if the only desired quantity is the integrated radiated energy and not the spatial or spectral distributions, the Larmor formula [56] provides a faster method to do the calculation without any simplifying assumption.

Following this procedure, the simulated spectrum and transverse profile of the betatron radiation emitted by each bunch under FACET-II conditions are shown in Fig. 2.1(b,c,d). For this simulation the waist position of the trailing beam is set at $z = 6.3$ cm (red dashed line in Fig. 2.1(a), $z = 0$ being the beginning of the ramp and of the simulation), which corresponds to the trailing matching conditions as will be shown later. The drive beam emits a total radiated energy of ≈ 0.46 mJ with a ≈ 1 mrad divergence, whereas the trailing beam emits ≈ 0.06 mJ with a sub-mrad divergence. The energy spectra have a synchrotron-like distribution with a critical frequency of ≈ 150 keV for the drive betatron spectrum and ≈ 300 keV for the trailing betatron spectrum.

The relative difference between the betatron radiation features of each bunch comes from the different beam dynamics of each bunch. First of all it should be noted that to have a good energy transfer efficiency and optimum beam loading the drive beam has more charge (more electrons) than the trailing beam, which already sets a significant factor (≈ 3) difference in the integrated radiated energy. On the other hand, the difference in the radiated spectrum comes from the fact that during the propagation in the plasma the trailing beam gains energy, leading to the radiation shifting towards higher photon energies, whereas the drive beam looses energy, leading to the radiation shifting towards lower photon energies. Concerning the angular distribution of the betatron radiation, the difference cannot be explained by the beam emittances since both beams have similar values. The divergence difference actually originates from the different matching dynamics of each bunch. As stated before, in this beam-plasma configuration the trailing beam is matched to the plasma, which means that the trailing electron trajectories are confined radially in a constant beam envelope. In contrast, the drive beam is not matched due to the different waist position and therefore drive beam electrons can reach higher trajectory amplitudes and therefore radiate at larger angles. This difference in matching conditions also leads to different integrated radiated energies, but in this case the difference is mainly dominated by the different total charges of each bunch.

Another striking feature is the cylindrical asymmetry in the drive betatron profile, which shows a cross pattern on the top of a diamond-like profile in contrast with the circular profile of the trailing beam radiation. In order to understand the formation of such an asymmetric angular distribution, we have computed the radiation produced at different consecutive time-steps of the trajectory by the drive beam particles. The associated angular distribution are plotted in Fig. 2.2 over one betatron period $2\pi/\omega_\beta$. This figure shows that the formation of the diamond pattern originates from a superposition of the two out-of-phase transverse dynamics in each transverse direction x and y. When the beam envelope oscillations reach their maximum in the x direction the outer most particles experience the largest restoring force in the x direction and radiate mainly along this direction. Since the transverse envelope oscillations are out-of-phase, the maximum amplitude in x does not coincide with the maximum amplitude in the y direction and therefore significantly less radiation is emitted along the y direction (see Fig. 2.2(c)). The same reasoning applies when the envelope oscillations reach the maximum in the y direction (see Fig. 2.2(e)). Note this out-of-phase transverse motion does not mean that there are no particles oscillating in other azimuthal planes than the preferred x and y directions, but their amplitude of oscillation is smaller than along the preferred directions and therefore their contribution to the total betatron radiation is minor.

2.2 Emittance preservation and betatron radiation

It is clear from last section that the betatron radiation encloses considerable information about the beam dynamics in the plasma. In this second section some particular aspects of the beam dynamics will be correlated with specific features of the emitted betatron radiation, with the ultimate goal of developing experimental diagnostics to asses the considered beam dynamics. In particular, two beam dynamics that lead to transverse emittance growth will be analyzed: beam mismatch and beam centroid oscillations (related to hosing instability).

2.2.1 Beam matching and betatron radiation

As already mentioned in Sec. 1.3.2, chromaticity spread due to mismatch propagation is thought to be the main cause of emittance growth in actual beam-driven plasma-based accelerators. Hence, achieving trailing emittance preservation requires the trailing beam to be matched in and out of the plasma. In the same section it was discussed that the presence of plasma density gradients increases the complexity of the beam matching dynamics, and therefore under realistic

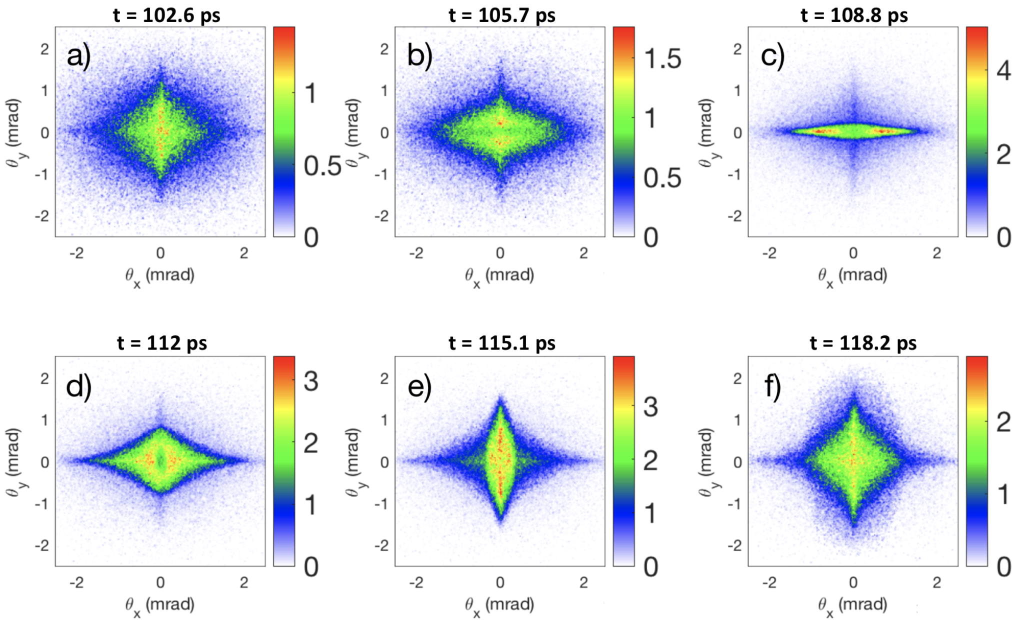

Fig. 2.2: Betatron radiation angular distributions in J/sr emitted by the drive bunch at 6 consecutive timesteps. The timesteps represented here are $t = 102.6, 105.7, 108.8, 112, 115.1$ and 118.2 ps, corresponding to the beginning of the plateau region ($z = 20$ cm). In this simulation the trailing focal plane position is at $z_{\text{trailing}} = 12$ cm, the x drive focal plane position is at $z_{\text{drive},x} = z_{\text{trailing}} + \Delta W_x = 28$ cm and the y drive focal plane position is at $z_{\text{drive},y} = z_{\text{trailing}} + \Delta W_y = 43$ cm. Figure from Ref. [46].

conditions it is necessary to have an experimental measurement sensitive to these matching dynamics. One possibility to diagnose these dynamics is to measure directly the trailing beam emittance: if with a certain degree of energy spread the normalized emittance is preserved, the trailing beam must be matched to the plasma. Two main problems arises with this approach: first, if there is another source of emittance growth this method would naturally fail. Secondly, emittance diagnostics with enough resolution at the ultra-low emittance levels required for some applications are very hard to achieve and rely typically on multi-shot techniques or require doing assumptions on the beam parameters (for example the "butterfly" method [69] assumes $\hat{\alpha}$, $\hat{\beta}$ and emittance to be independent of the energy). Multi-shot techniques require a very stable and reproducible acceleration process, at a degree that has been difficult to achieve so far in PBAs.

An alternative solution to diagnose the matching dynamics is to use the betatron radiation. The idea is very similar to what was explained in the last section, but instead of comparing the drive and trailing betatron radiation, the underlying concept is applied to different trailing matching conditions. Under matching conditions the beam envelope is constant and thus the average amplitude of the particle trajectories is also constant during the propagation (apart from the $\gamma^{-1/4}$ adiabatic evolution of the amplitude during acceleration). For a certain degree of mismatch $\beta_{\text{mag}} > 1$, the beam envelope oscillations are related to higher average amplitude of the particle trajectories, which ultimately leads to an increase of the betatron radiated energy. Thus it would be intuitively expected that the larger the degree of mismatch the more energy is radiated.

In order to scan different matching conditions the approach followed here is to shift the

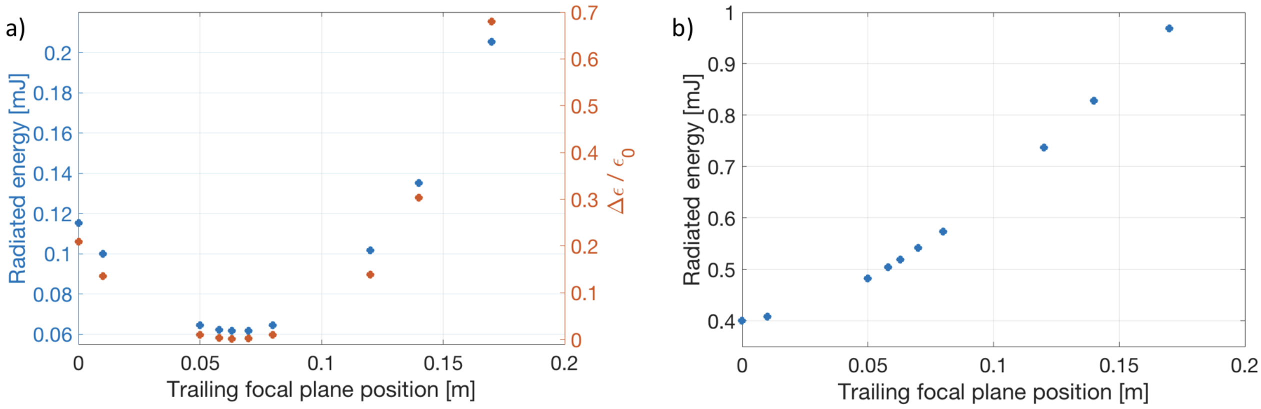

Fig. 2.3: a) Total radiated energy (blue) and relative emittance growth (orange) from the trailing bunch as a function of the focal plane position of the trailing bunch. b) Total radiated energy from the trailing and drive bunches. Figure from Ref. [46].

waist position of the beams in the plasma. This procedure, which can be easily applied in an accelerator facility just by changing the strength of the final focus (FF) quadrupoles, is equivalent to the change of the initial beam parameters at the entrance of the plasma. As long as the plasma gradients are adiabatic (the length scale of the gradient is larger than the betatron period) there should be an optimum waist position for which the beam parameters are matched in and out of the plasma, and it is precisely at this waist position that the betatron radiated energy should be minimum.

A set of QuickPIC simulations were run under FACET-II experimental conditions scanning the trailing waist position. Figures 1.6 (b) and (c) show the trailing beam evolution of two of these simulations: Fig. 1.6 (b) corresponds to a simulation with the trailing waist position at $z = 6.3$ cm and a matched propagation, and Fig. 1.6 (c) corresponds to a simulation with the trailing waist position at $z = 12$ cm and a mismatched propagation. In this set of simulations the uniform plasma starts at $z = 20$ cm (see Fig. 2.1 (a)). These two cases confirm that indeed changing the waist position in the plasma modifies the matching conditions.

In order to simulate the experimental conditions, the drive waist position was shifted consistently by the same amount as the trailing beam. This does not have a significant impact in the trailing dynamics since the strongly non-linear blow-out wakefield driven by the drive is not sensitive to the variations of the driving parameters over the considered waist positions. However it does have an impact on the betatron radiation emitted by the driver as will be shown later.

Computing the betatron radiation as explained in Sec. 2.1, the final trailing emittance growth normalized to its initial value and the total radiated energy of the trailing bunch is plotted in Fig. 2.3(a) for different waist positions. A clear correlation is observed between the normalized emittance growth and the computed betatron radiation energy, showing how both quantities reach the minimum value at the same waist position. The waist positions considered here correspond to β_{mag} values ranging from 1 to 3.2, and for these values the corresponding radiated energy increases up to a factor of 3.5. This indicates that these variations in the betatron radiation should be detectable in an experiment with the appropriate diagnostics, which are discussed in the Chap. 3.

So far only the trailing radiation has been considered. Yet, as it has been already discussed, the drive beam emits a larger amount of radiation due to its higher charge, and experimentally it is not possible to separate the betatron signal of the trailing beam from that of the drive in a single shot measurement. In Fig. 2.3(b) the addition of the radiated energy of both drive and trailing beam is plotted as a function of the trailing waist position from the same set of simulations, showing how the trend of the trailing matching are not evident from the integrated signal of both beams. As expected it is now the drive dynamics (not shown here) that dictate the betatron energy, and the total radiated energy is found to be minimum for a trailing waist located at $z \approx 0$. A solution to this experimental constraint consists on sending only the drive beam to the plasma, measuring the "drive-only" emitted radiation and then subtract this value to the total radiation measured when both drive and trailing bunches are sent to the plasma. Since the presence of a trailing beam does not alter the drive dynamics, this method should correctly retrieve the trailing betatron radiation.

2.2.2 Beam centroid oscillations and betatron radiation

We now consider the effect of centroid oscillations due to drive-trailing misalignments and analyze the resulting betatron radiation. Similarly to the relation between the matching dynamics and the betatron radiation, the trailing centroid oscillations lead to larger amplitude particle trajectories and thus to an enhancement of the betatron radiation. In order to simulate this process, the trailing beam is initialised with a transverse offset Δx in one direction in the QuickPIC simulations. For a transverse offset of 7 μm under FACET-II experimental conditions, the evolution of the trailing centroid position and normalized emittance are plotted in Fig. 1.7(b), evidencing the detrimental effect of the centroid oscillations on the emittance as discussed in Sec. 1.3.3.

A set of QuickPIC simulations was run under matching conditions (trailing waist at $z = 6.3$ cm) with different drive-trailing transverse offsets, from which the beam particle trajectories were extracted to compute the angular and spectral distributions of the betatron radiation. These calculations confirmed that the trailing centroid oscillations lead to an enhancement of the betatron radiation emitted by the trailing bunch, and that as the initial offset is increased the integrated betatron radiated energy is consequently enhanced. It should be noted that, in contrast to the waist position scan showed in the last section, this type of study might not be easily feasible in an experimental facility such as FACET-II due to the complexity of controlling the transverse offset between the two beams with the required precision.

The computed angular distributions of the trailing beam showed an elongated profile along the offset direction, which was also confirmed by a new set of simulations where the transverse offset was introduced in different azimuthal directions. Furthermore, for large enough offsets, this elongated profile was clearly visible in the angular profile of the betatron radiation emitted by both beams as shown in Fig. 2.4(a) and (b). In terms of spectral distributions, an enhancement at high energy tails of the spectra is observed as the initial transverse offset is increased (see Fig. 2.4(c)). As will be shown in Chap. 3, a thoughtful design of the experimental diagnostics can enable a sensitive measurement of this high energy part of the spectrum, which could ultimately be related to transverse offsets between the drive and trailing beams.

It should be noted being able to measure a transverse offset between the drive and trailing beams can be crucial to mitigate the hosing instabilities. Even if for FACET-II beam-plasma parameters our simulations reveal that no significant hosing instability develops in the system, hosing instabilities could represent a severe limitation for parameters required for particle col-

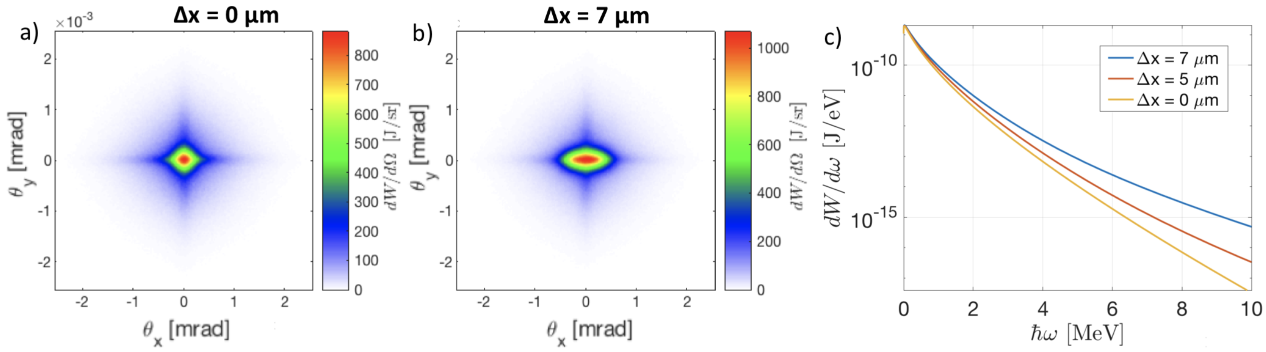

Fig. 2.4: a) Angular distribution (J/sr) of the betatron radiation emitted by both beams when no offset in the trailing is introduced. b) Angular distribution (J/sr) of the betatron radiation emitted by both beams when an offset of $\Delta x = 7\,\mu$m is introduced along the x axis for the trailing bunch. c) Energy spectrum of the betatron radiation emitted by both bunches for three different offset values. Figure from Ref. [46].

liders [70]. These transverse offset could seed the hosing instability and lead to a faster growth, so minimising its effect can be an important achievement for the community.

To summarise this chapter, we have set the basis and principles of a new experimental technique to assess the beam dynamics responsible of emittance degradation in current state-of-art PWFA, namely beam matching and hosing instability, based on the emitted betatron radiation. Furthermore, the non-destructive nature of this technique makes it suitable not only to achieve the experimental milestone of emittance preservation but also for the staging of several plasma-based accelerators, allowing to monitor on-line the matching in and out of the plasma of the accelerated beam. The main limitation of this technique, apart from the need of specifically designed diagnostics to be sensitive to the relevant features of the betatron radiation, is the fact that the trailing betatron radiation that has the relevant information is hidden "behind" the dominant betatron radiation emitted by the drive beam. Solutions to this issue have been proposed, specifically to subtract the drive radiation, but the implementation of this method might depend on the relative trailing-to-drive parameters and the sensitivity of the detectors. The design of the appropriate X-ray and gamma radiation detectors to carry out this measurement at FACET-II is discussed in Chap. 3.

3. GAMMA-RAY DIAGNOSTICS AT FACET-II

The FACET-II facility has been designed to deliver high-energy particles beams (electrons and positrons) with unprecedented peak beam currents and low emittances. These beam parameters will allow to study extreme beam-matter interactions relevant not only to the field of advanced accelerators but also to other fields of science such as astrophysics or Quantum Electro Dynamics (QED). During my PhD I have assisted to the birth and development of several of the scientific programs surrounding this facility, and actively participated in some of them. Namely, I have been involved in the design and development of the gamma-ray diagnostics produced in the interaction of the relativistic FACET-II beam with different types of light and matter. Furthermore, during a significant part of my PhD I was based at the facility to carry out the main construction and installation work of these diagnostics. Finally, during the last months of my PhD I have been able to remotely participate in the commissioning phase of these diagnostics, using the first FACET-II electron beams to produce gamma rays and commission the gamma diagnostics.

This chapter is divided in three sections. The first section gives an overview of the FACET-II experimental area, as well as of the main experiments that will be performed during the first years of operation. In the second section an overview of the design process and installation of the gamma diagnostics at FACET-II is presented, together with some simulation results of the expected performance and information retrieval for different experiments. Finally the first experimental data taken with the gamma-ray diagnostics will be shown together with some preliminary analyzes that were carried out for commissioning purposes.

3.1 FACET-II facility overview

The Facility for Advanced Accelerator Experimental Tests FACET-II heritages the last kilometer from the beamline of the precedent facility FACET, while the first kilometer is under transformation into a superconducting LINAC for the new Linac Coherent Light Source beamline (see top Fig. 3.1). The decrease of accelerator length from FACET to FACET-II translates into lower energy particle beams, from the $\approx 20\,\mathrm{GeV}$ of FACET to $\approx 10\,\mathrm{GeV}$ of FACET-II. However, as already explained in the last section, a major upgrade has been done in the particle gun, going from a thermionic gun to a photocathode, which significantly reduces the delivered beam transverse emittance. The rest of the LINAC consists on 3 alternating acceleration and compression sections that bring the accelerated particles to the experimental area (see bottom of Fig. 3.1).

An overview of the experimental area is shown in Fig. 3.2. In this figure the beam comes from the left. The first triplet of quadrupoles, also called the Final Focus system, focus the beam into the interaction point. The main interaction happens in what is labelled as "Interaction region" in Fig. 3.2. Two main elements are hosted the interaction region: the first, starting from the left, is the so-called Picnic Basket, a vacuum chamber where the relevant interaction happens

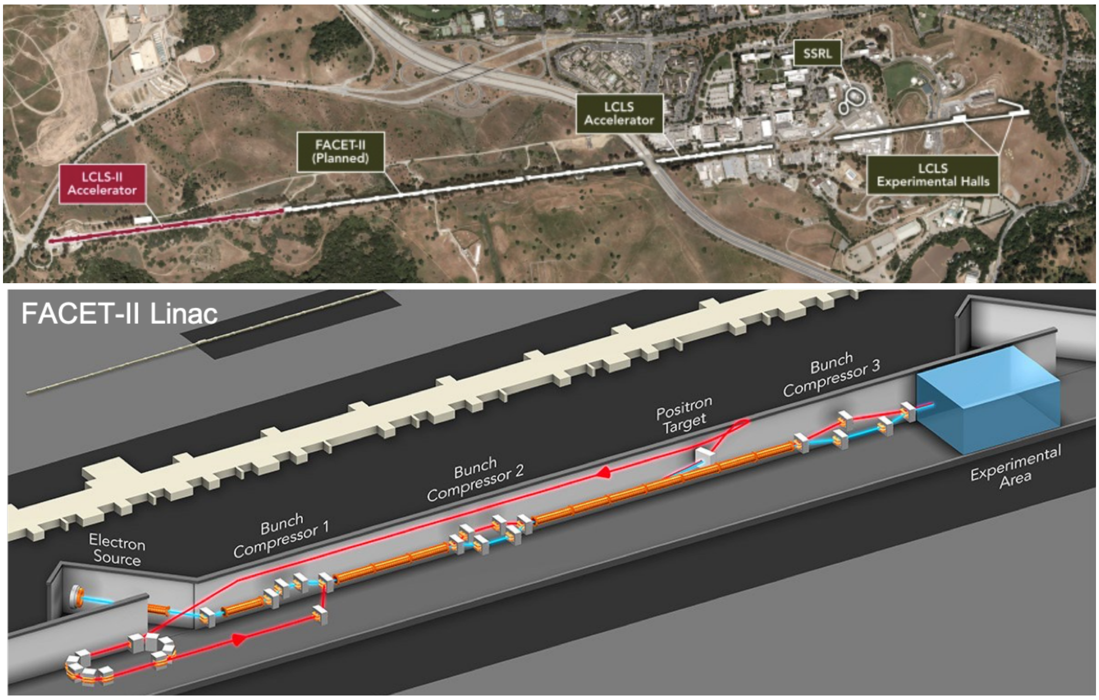

Fig. 3.1: Top: Aerial view of SLAC accelerator showing its division in three parts corresponding to the three different facilities LCLS-II, FACET-II and LCLS. Bottom: sketch of the FACET-II LINAC.

for most experiments. In particular, the gas and solid targets of the "Beam-filamentation" E305 experiment as well as the beam-laser interaction of the "Strong-Field QED" E320 experiment (see later for a description of the different experiments) are installed in here. The other element hosted in the Interaction region is the aforementioned lithium oven, where the main PWFA experiment takes place. This region also accommodates some diagnostics that do not look at the particles produced during the interaction but rather characterize the beams and the plasma, such as the Electro-Optical Sampling detector for the electron beam or the shadowgraphy plasma diagnostic.

After the interaction region, the beam passes through a new set of magnets referred to as the spectrometer magnets. They consist on three imaging quadrupoles which refocus the beam to the downstream diagnostics, and a spectrometer dipole who disperses vertically the beam particles as a function of their energy. After the spectrometer, particle detectors have been installed in order to detect positrons in small number and low energy electrons, relevant for the Strong-Field QED E320 experiment. These new diagnostics (not existing at FACET) are placed under vacuum, so that the particles propagate freely from the interaction point to the detectors, and moreover they are far from the beam dump to reduce the background signal levels on these detectors.

Finally the beam arrives to the so-called "dump table". The name is due to its proximity to the beam dump, and is where the diagnostics looking at high energy electrons and gamma rays are installed. The dump table diagnostics, except from a high-resolution electron screen, are all in air: a 5 mm Al window separates the high vacuum beamline and the dump-table diagnostics. A schematic overview of the dump table is shown in Fig. 3.3. The electron diagnostics are the Dump Table Optical Transition Radiation (DTOTR) 1 and 2, designed to

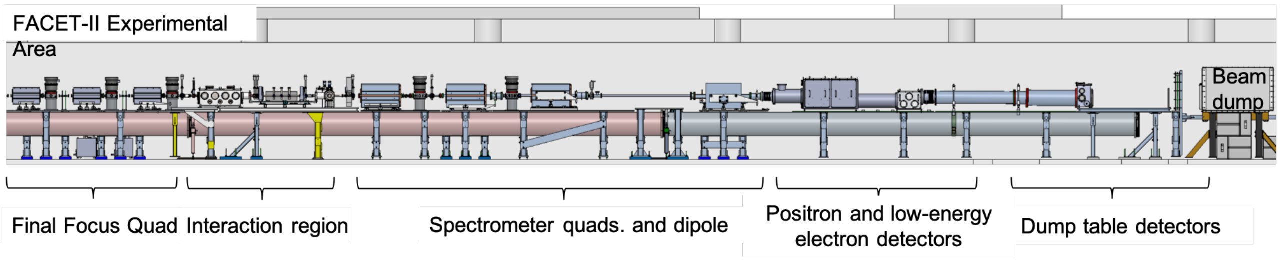

Fig. 3.2: Overview of the FACET-II experimental area.

measure the energy-slice beam size of the particle beam with high resolution, the Large Field-Of-View (LFOV), designed to measure wide particle spectra via a scintillating screen, and the Cherenkov Radiation spectrometer (CHER) [71]. The gamma-ray diagnostics GAMMA1, GAMMA2 and GAMMA3 will be presented in Sec. 3.2.

In terms of experiments, at FACET-II each scientific program has its corresponding Experiment Number. After the completion of the Technical Design Report [72], a peer-review process evaluated the different experimental proposals that different groups and collaborations submitted to the facility. From this process seven experiments were ranked "excellent" and got priority in terms of experimental beam time and hardware installation. Among these experiments, three of them relied at least partially on gamma-ray diagnostics to achieve the experimental goals:

- E300 experiment: *Energy Doubling of Narrow Energy Spread Witness Bunch while Preserving Emittance with a High Pump-to-Witness Energy Transfer Efficiency*. The flagship PWFA experiment at FACET-II has three main experimental goals [68]: studying drive energy depletion to optimise the drive-to-trailing energy transfer efficiency, reducing the energy spread of the accelerated beam and preserving the emittance during the acceleration of the trailing beam. As explained in the previous chapter, for the emittance preservation goal measuring the betatron radiation produced by the beams can be very valuable to assess the matching dynamics, and thus gamma-ray diagnostics will be used to measure betatron radiation in the E300 experiment.

- E305 experiment: *Beam filamentation and bright Gamma-ray Bursts*. This experiment, to whom the second part of this manuscript is devoted, aims at studying the streaming plasma instabilities arising when a relativistic beam propagates in plasma, as well as its potential application to develop an efficient laboratory source of gamma rays. This experiment naturally relies on the gamma diagnostics to measure the capability of producing gamma rays via the instability, but also to retrieve information about the development of the instability itself. More details about this experiment and its relation with the gamma diagnostics are given in Chap. 6.

- E320 experiment: *Probing Strong-field QED at FACET-II*. By colliding the FACET-II electron beam with a high-power laser pulse, this experiment aims at studying the so-called Strong-Field extension of the QED theory (SFQED) relevant under large electromagnetic fields approaching or exceeding the Schwinger limit [73]. The main experimental signature to probe this Strong-Field regime is in the electron-positron pair creation by the high energy photons produced in the electron beam-laser collisions. Nevertheless, for alignment purposes the gamma radiation produced in the collision can provide a good

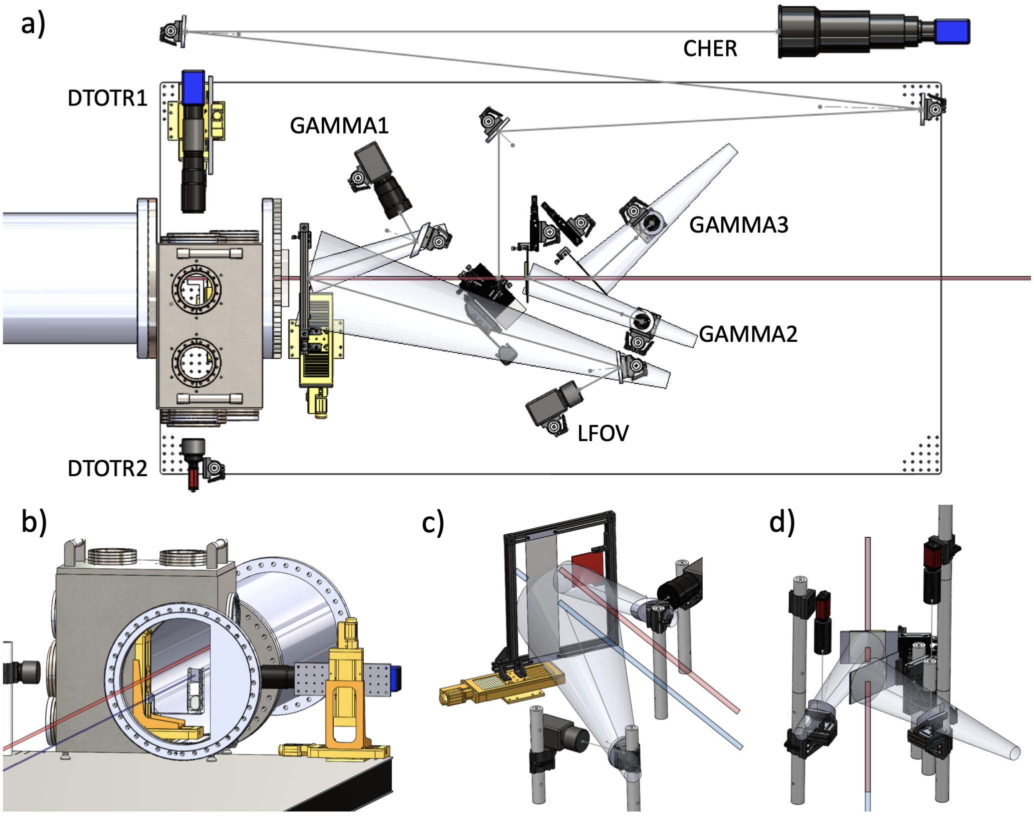

Fig. 3.3: FACET-II dump table. Red line represents the gamma-ray path (LINAC longitudinal axis) and the blue line represents the dispersed electron beam path. The expected field of view of each camera is represented with a transparent gray cone. (a) Top view displaying the main diagnostics with their acronym. b) View of the the under-vacuum particle diagnostics DTOTR1 and DTOTR2 (Al window has been removed to see the scintillating screens). (c) View of the GAMMA1 (camera on the top right) and LFOV (camera on the bottom left). The red square corresponds tto the CsI array and the gray rectangle corresponds to the DRZ-screen (see text for further details). (d) View of GAMMA2 (left camera) and GAMMA3 (right camera). *Credits to D. Storey for the images.*

signature, as well as to measure the real laser strength parameter a_0, as experienced by the colliding electrons.

After this first FACET-II Program Advisory Committee meeting in October 2018, the experiments ranked "excellent" started to work together on the dump-table radiation diagnostics to create a common experimental set-up that would fulfil the scientific needs of all these experiments. Part of this process, together with the first final outcome is presented in the next section.

3.2 Gamma-ray diagnostics at FACET-II

Gamma rays, similarly as X rays, are detected via their interaction with matter. However the low cross sections of the gamma-ray high energy photons with matter make them hard to intercept in a controlled manner. Unlike for visible light, it is not possible with current technologies to disperse a gamma-ray beam as one does for a charged particle beam, which makes the spectral measurement very challenging and results in rough spectral resolutions. Furthermore the typical gamma-ray spectra produced in the beam-plasma or beam-laser interaction are very broad, ranging from hard X rays (> 25 keV) up to the electron energy (10 GeV), i.e. it can span over 6 orders of magnitude.

At FACET-II, the initial design of the gamma-ray detectors come out from a collaboration effort between different experiments to accommodate their needs in terms of desired gamma-ray diagnostics into a common set-up, so that different experiments can run consecutively without the need of an access to the FACET-II tunnel and to remove/reinstall diagnostic frequently. Figure 3.4 shows simulated gamma-ray spectra for different FACET-II experiments as well as the relevant spectral range to which detector would need to be sensitive. Note that the laserwire experiment does not require any type of spectral information and only integrated and angular distribution of the radiation is needed. Furthermore the Trojan Horse injection experiment [74], which aims at measuring the betatron radiation produced by a trailing beam injected optically directly in the plasma (plasma photocathode concept), requires X-ray detectors rather than gamma-ray's and is not considered in the present manuscript. For the remaining experiments E300 (PWFA), E305 (Filamentation) and E320 (SFQED) three main types of gamma-ray measurements are required: total radiated energy, angular distribution and spectral information. A set of three gamma-ray detectors have been designed for this purpose: GAMMA1, GAMMA2 and GAMMA3. The first part of this section is dedicated to GAMMA1 and the second part to GAMMA2 and GAMMA3. Simulation results of the expected performances of each detector are presented, mainly focused on the PWFA experimental conditions.

3.2.1 GAMMA1

The first gamma-ray detector, called GAMMA1, consist on a scintillating material that is imaged via an optical system onto a camera. When the gamma-rays interact with the scintillating material, some of the deposited energy is transformed into visible light, that can then be measured by the chip of a digital camera. The GAMMA1 detector is designed to retrieve information about the integrated radiated energy and its angular distribution. Despite the fact that the scintillator does not respond equally to all gamma-ray energies (see following paragraphs), the different contributions from different energies are added in the total signal and the GAMMA1 detector cannot provide any spectral information by itself.

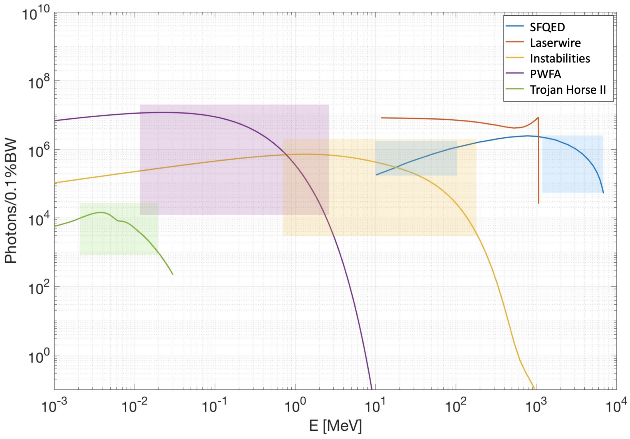

Fig. 3.4: Simulated radiation spectra of several FACET-II experiments. colored boxes depict the relevant part of the spectrum for each experiment.

For a given gamma-ray source, the performance of GAMMA1 can be determined as a function of three main factors: the conversion efficiency of the scintillator (from gammas to visible light), the collection efficiency of the imaging system, and the detection efficiency of scintillation light of the digital camera. In the following, each factor is analyzed separately, and then applied to compute the expected Signal-to-Noise ratio (SNR) of GAMMA1 for the SFQED experimental conditions.

The conversion efficiency measures the amount of gamma-ray energy that is transformed to visible light in the scintillation material. The first important process is the energy deposition of the photons in the scintillator. Complex cross-section calculations are required to compute the fraction of the photon energy that is deposited in a certain material when it propagates through. It is noteworthy that for electron scintillation-based detectors the energy deposition calculations are simpler since after a certain electron energy (≈ 1 MeV) the deposited energy is roughly constant [75], which is not the case for high energy photons. For photon energy deposition, there exists tabulated data for different photon energies and material. However the results presented in this manuscript are based in GEANT4 [76] simulations used to model the energy deposition process. The advantage of GEANT4 is on the one hand that secondary particles and their energy deposition are also simulated, and on the other hand complex detectors with for instance different layers of different materials can be simulated. In this way the GEANT4 simulations presented in this manuscript include, unless otherwise stated, the aluminium window that separates the under-vacuum beamline from the in-air dump table diagnostics, and therefore account for the secondary particles produced in the interaction of the gammas with the Al.

Two different scintillation materials are available for GAMMA1: a GOS-based scintillator, also called DRZ$^{\mathrm{TM}}$ screen, and a pixelised CsI crystal scintillator. The fraction Γ_{dep} of the incident photon energy that is deposited in the scintillator as a function of the incident photon energy $\hbar\omega$, also referred to as the detector spectral response, is computed by the GEANT4 simulations and plotted in Fig. 3.6. In these simulations 10^6 photons are shot at each energy through the Al window and the scintillation screen (including protective layers) placed at the distance of the experimental set-up. The total energy deposited in the GAMMA1 scintillation material is computed (see Fig. 3.5), and then divided by the total incident energy to retrieve Γ_{dep}.

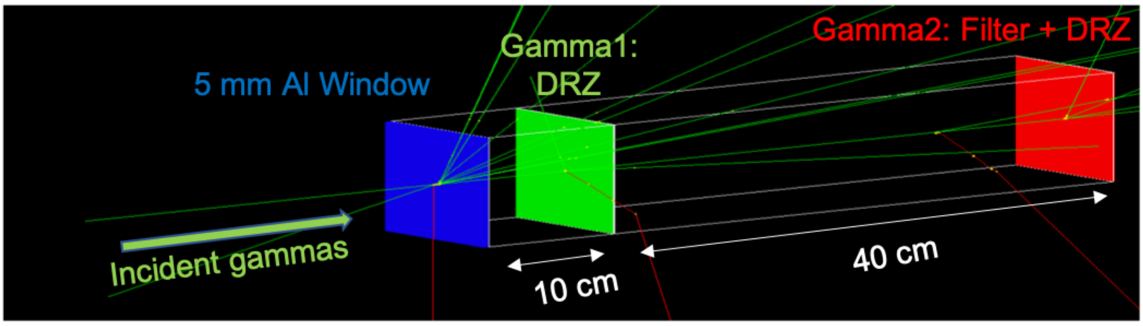

Fig. 3.5: GEANT4 geometry used to compute detector spectral response. Each material is represented by a colored square, and each type of particle is represented by a line: green lines correspond to photons and red lines to leptons.

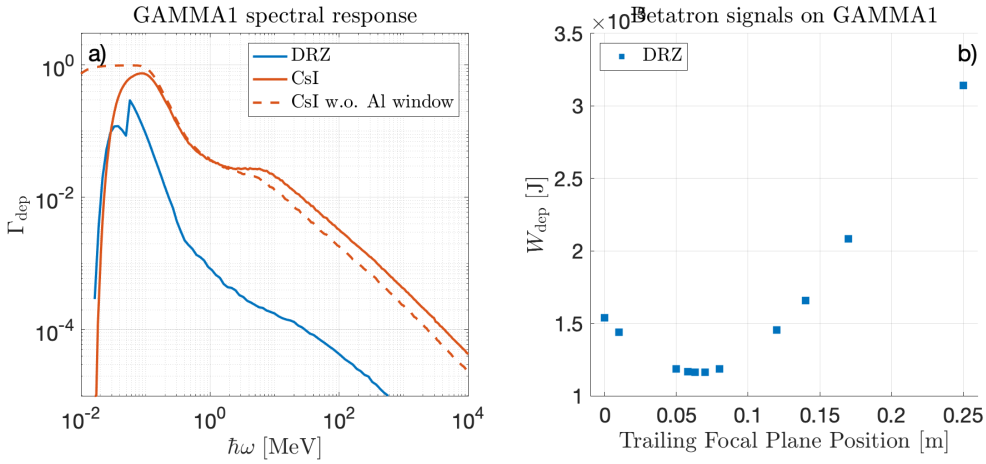

Fig. 3.6: a) Simulated spectral GAMMA1 response (deposited energy fraction as a function of incident photon energy) for the CsI (orange) and DRZ (blue) scintillation materials. The orange dashed line corresponds to the detector response with CsI but without the Aluminium window. b) Deposited energy W_{dep} in the DRZ screen by the E300 trailing beam betatron radiation for different matching conditions (blue dots), see Sec. 2.2.1. The effect of adding a converter right in front of the DRZ scintillator is plotted in orange and yellow dots.

From Fig. 3.6 it is clear that CsI is significantly more sensitive than the DRZ screen. Indeed the utility of the CsI at FACET-II with respect to DRZ is to detect low-level signals. It should be noted that the gamma-ray spectra showed in Fig. 3.4, which would produce enough signal to be detected with the DRZ screen, correspond to the optimal experimental conditions. However, before reaching these optimal conditions a more sensitive detector might be useful to measure and optimise a lower-level signal. It should also be noted that the higher sensitivity of CsI comes at the cost of a poorer spatial resolution due to the pixelised structure. Indeed, whereas the DRZ spatial resolution is mainly limited by the grain size of the GOS crystals ($\lesssim 100\,\mu$m), the CsI scintillator is made out of individual isolated crystals of $0.5 \times 0.5\,\text{mm}^2$ transverse size that scintillate as a whole, limiting the spatial resolution to the size of one of these crystals.

For illustrative purposes, the CsI simulation was also run without the Al window and the corresponding GAMMA1 response is also plotted in Fig. 3.6(a) (orange dashed line). One can observe the effect of the Al window on the detector response. Low energy photons are absorbed by the window and do not reach the scintillation material, and therefore the presence of the Al window prevents the GAMMA1 detector to be sensible to low-energy photons. In contrast, at high energies the window slightly enhances the deposited energy due to secondary particle creation, which starts to be significant from $\approx 1\,\text{MeV}$.

These simulated spectral responses can be applied to the expected gamma-ray spectra (or to the double differential $\frac{\partial W_{\text{rad}}}{\partial\Omega\partial\omega}$) to compute the deposited energy in the scintillator $W_{\text{dep}} = \int d\omega \Gamma_{\text{dep}}(\omega)\frac{\partial W_{\text{rad}}}{\partial\omega}$. It is noteworthy that a higher gamma-ray yield (total radiated energy) does not necessarily means a higher detected signal. For instance an increase in the gamma-ray yield that comes with an energy shift towards higher photon energies would reduce the sensitivity of the detector and therefore might lead to a lower signal. It is therefore important to account for these detector spectral responses when comparing different gamma-ray sources. In Fig. 3.6(b) the deposited energies W_{dep} for the waist position scan of E300 trailing beam presented in Sec. 2.2.1 are plotted using the DRZ spectral response (blue points), confirming that, despite the different gamma spectra produced under different matching conditions, the DRZ screen would produce more signal as the system gets a higher degree of mismatch.

Finally one can also study the effect of adding a converter right in front of the DRZ. Such a converter was installed at FACET where a similar gamma detector was used with a W-converter in front of the scintillating screen to enhance the lower-signal levels of the higher energy gamma-rays produced by the 20 GeV electrons instead of that produced by 10 GeV electrons at FACET-II. The effect on the spectral response of the detector is the same as for the Al window: low-energy photons (< 1 MeV) are absorbed and high-energy photons (> 1 MeV) produce secondary particles that increase the signal. The effect of the convertor then depends on the emitted spectrum. Using the mean photon frequency

$$\omega_{\text{mean}} = \frac{\int_0^\infty d\omega\omega\frac{\partial N_\gamma}{\partial\omega}}{\int_0^\infty d\omega\frac{\partial N_\gamma}{\partial\omega}} \tag{3.1}$$

for the simulated E300 trailing betatron spectra, one obtains $\omega_{\text{mean}} \approx 150$ keV under matched conditions and $\omega_{\text{mean}} \approx 300$ keV for the largest degree of mismatched. These values are below the ≈ 1 MeV threshold, so overall adding a high-Z convertor would decrease the absolute signal. Nevertheless the broadband spectrum of the betatron radiation still provides a significant number of photons above the pair-creation energy threshold for these mean photon energies, and thus lead to a significant increase of the contrast between matched and mismatched signals. As shown in Fig. 3.6(b), a thicker W converter increase the ratio of mismatched/matched signals from ≈ 3 (no converter) to ≈ 8. Therefore if the overall sensitivity of the scintillator is good enough to detect the lowest signals, adding a convertor could be beneficial under this conditions to be more sensible to the high energy part of the spectrum which is significantly affected by the matching dynamics. The underlying idea of this reasoning is the working principle of the GAMMA2 and GAMMA3 detectors, designed to measure spectral information of the incident radiation, as will be explained in Sec. 3.2.2.

With the detector spectral response, the deposited energy W_{dep} in the scintillator can be computed and is then transformed into visible light via the scintillation process. This visible light is often referred as "green photons" due to its central wavelength ($\hbar\omega_{\text{gph}} = 2.25$ eV for CsI). The number of green photons produced in the scintillation material as

$$N_{gph} = \epsilon \cdot \frac{W_{\text{dep}}[\text{eV}]}{\hbar\omega_{\text{gph}}[\text{eV}]} \tag{3.2}$$

where ϵ is called the scintillation conversion efficiency (fraction of the deposited energy transformed into green photons), which is usually tabulated. Note that not all the green photons neccesarely escape the scintillation material due to internal scattering [77] and thus only a fraction ρ_{esc} of the produced green photons escapes the scintillation material. For the CsI crystal, since the $\mathrm{TiO_2}$ coating between the crystals reflects most of the scintillation light produced, we will consider $\rho_{\mathrm{esc}} = 1$. These two factors (conversion efficiency and escaping probability) together make the scintillator calibration, i.e., the number of green photons escaping the scintillation material per deposited MeV. For instance the CsI crystals used for GAMMA1 have a scintillation calibration of 80000 ph/MeV (as given by its manufacturer).

These green photons now need to be imaged onto the chip of a digital camera. To estimate the fraction ρ_{coll} of the emitted photons that is collected by the optics, we need the numerical aperture. The numerical aperture NA (half angle) is given by

$$NA = \frac{m}{2\, f_{\#}} \tag{3.3}$$

where $m = \frac{\mathrm{FOV}}{\mathrm{sensor\,size}}$ is the magnification (FOV stands for field of view) and $f_{\#}$ is the f-number of the lens. In this manuscript the working f-number of the lens is used, which corrects by a factor of $(1 + m)$ the tabulated f-number by accounting for the fact that the focal plane of the objective is not at infinity. Then assuming that the light is isotropically emitted over half a sphere we have

$$\rho_{\mathrm{coll}} = \frac{\pi\, NA^2}{2\pi} \tag{3.4}$$

The number of green photons that after being capture by the objective are detected by the sensor is given by the Quantum Efficiency (QE) of the camera at the green photon wavelength. Each detected photon will deposit a signal in the detector, creating in average ρ_{photoe} photoelectrons and each photoelectron is finally transformed into $N_{\mathrm{count/photoe}}$ counts. All these factors that depend on the detection chip and analog-to-digital converter (ADC) are usually tabulated by the camera manufacturers.

In order to have a good QE, low read-out noise and a large dynamic range, a scientific CMOS camera with a short focal length objective ($f = 35$ mm) is installed to image the GAMMA1 scintillator. Furthermore, in order not to have the camera close to the beam axis, which could damage its chip and electronics, an optical mirror is placed between the objective and the scintillation material as shown in Fig. 3.3(c). With this configuration and the CsI as the scintillating material a signal-to-noise ratio of 10^4 was computed from a simulated E320 (SFQED) gamma-ray radiation. It should be noted though that the noise measurements were not carried out with the experimental conditions, so it is likely that the environmental noise in the tunnel would reduce this SNR value by at least an order of magnitude.

A second GAMMA1 performance study was done using simulated gamma-ray emissions from the E320 electron beam-laser collisions with different laser strength parameter a_0. The gamma-ray divergence should scale linearly with the laser strength parameter a_0, and thus could be used in the E320 experiment to monitor the laser intensity. Similarly to the GAMMA1 performance study of PWFA matching conditions (see Fig. 3.6), the detector response was applied to these simulated gamma-ray radiations and the simulated signal showed a linear correlation between the a_0 and simulated gamma-ray divergence over the laser polarisation axis (see Fig. 3.7).

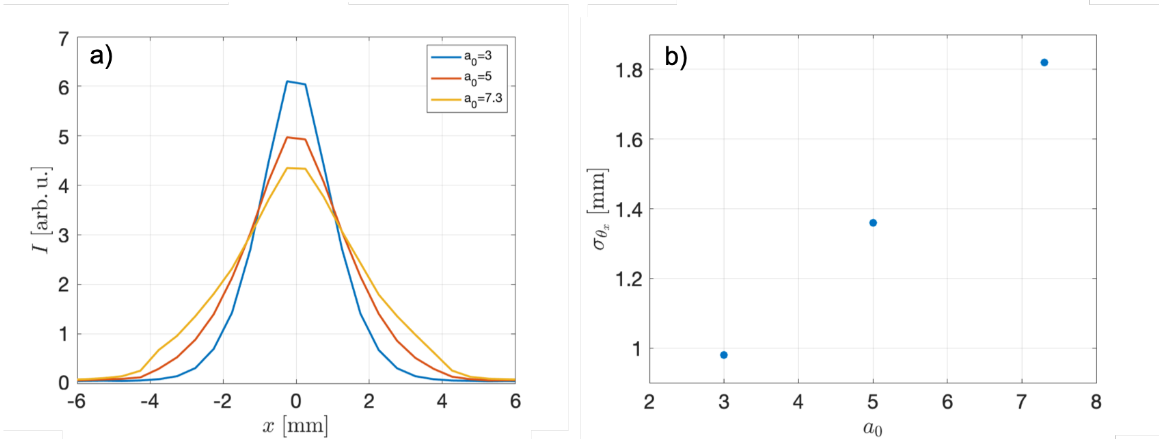

Fig. 3.7: a) Simulated signal, vertically integrated, of the GAMMA1 signal with the pixelised CsI for different simulated beam-laser interactions at different a_0. (b) Horizontal divergence (gaussian fits) of the simulated GAMMA1 signals for different a_0 values.

3.2.2 GAMMA2 and GAMMA3

The GAMMA2 and GAMMA3 detectors were designed to retrieve information on the emitted gamma-ray spectra at FACET-II. The working principle of these detectors is based on the different spectral responses of a scintillator-based photon detector when a converter is placed upstream of the scintillator. Assuming that these spectral responses are known, one can measure the light output from the scintillator with different types of converters and compare their relative signals to extract information about the incident gamma-ray spectrum. For instance, a gamma-ray burst with a significant part of its energy above the $\approx$ 1 MeV pair-creation threshold produces more scintillator signal with higher Z converters, whereas the higher Z converters would lead to less scintillation if most of the gamma-ray energy is below this threshold.

In order to compare the scintillator signal for different converters one can make use of the symmetry of the gamma-ray spatial distribution and use a set of converters symmetrically placed in front of the scintillator. In this way it is possible to measure the scintillator signal behind different converters for a single gamma-ray burst. For the initial FACET-II experimental set-up, a pie or "Camembert" distribution as shown in Fig. 3.8(a) has been installed. This geometry is optimised for cylindrically symmetrical signals, as the betatron radiation distribution shown in the same figure (see later for further details). Two different types of converters have been initially installed: varying thickness Cu and W converters, also called "step filters", and the Au and Ta filter, which correspond to a pair of Ross filters [78]. The latter, a technique based on the K-edge absorption of different materials, can provide valuable information in the X-ray 10 - 100 keV spectral range. However for the expected FACET-II gamma-ray spectra in PWFA experimental conditions only a small fraction of the spectra falls within this range, so the step filters are required to retrieve information on the high energy part of the spectrum.

There is though a geometrical constrain to carry out this type of measurement: secondary particles that enhance the signal after the converter are produced at an angle with respect to the incident gamma direction, and therefore they might either be detected by the scintillator at a different position from where they were produced, or even miss the scintillator and not be detected. Since the angular distribution of secondary particles is strongly directional in the gamma axis, placing the scintillator very close downstream the converter solves this geometrical issue and secondary particles should produce scintillation light at the same position where they were produced, with a small offset contributing to degrading the spatial resolution.

Interestingly, this geometrical aspect can also be used to get information about the incident gamma-ray spectrum: if all the secondary particles and the scattered gammas missed the scintillator, the converter would act as an "absorber" and the scintillator would only measure the transmitted gammas (the gammas that do not interact with the material) through each converter. In this case the converter rather acts as a filter. The same applies for the low-energy gamma rays (or X rays) that do not produce secondary particles, which has been already exploited to diagnose all-optical Compton gamma-ray sources [79]. For high-energy gammas, this transmission measurement could be a complementary measurement of the conversion.

At FACET-II the GAMMA2 scintillator is placed right after the set of filters, so that secondary particles produced are detected at the same position as the incident gamma ray. If the gamma-ray energy is high enough the GAMMA2 detector will be sensitive to the conversion rates, whereas if the gamma-ray energy is well below the secondary particle production threshold the GAMMA2 detector will be sensitive to the transmission rates. In the case where the GAMMA2 detector measures conversion rates, a second scintillator, called GAMMA3, is placed at a certain distance downstream of the set of filters (and the GAMMA2 scintillator) to measure the transmission rates through the filters. As explained before, to be sensitive to the transmission rates secondary particles and scattered gammas should miss the GAMMA3 scintillator, requiring a very long separation between the filters and the scintillator. Instead, one can make use of the fact that after some propagation distance the spatial distribution of secondary particles created by different converters overlap with each other and become very wide, producing an homogenous background on the GAMMA3 scintillator, whereas transmitted gammas still propagate on-axis and produce a non-homogenous signal on the GAMMA3 scintillator that would depend on the transmission rate of each filter. If the signal level of the latter is not significantly below the homogenous background of secondary particles and can be detected, the GAMMA3 detector should be sensitive to the transmission rates through the filters. In this manner GAMMA2 and GAMMA3 provide complementary information about the incident gamma-ray spectrum.

The disposition of the GAMMA2 and GAMMA3 detectors, both with DRZ screens as scintillators, is shown in Fig. 3.3 (d) with a separation distance of ≈ 40 cm. This distance is crucial for the gammas transmission measurement since it needs to be large enough to let the secondary particles contribution to become an homogeneous background. In practice, this distance depends highly on the incident gamma-ray energy: the higher the incident gamma-ray energy the more directional the secondary particle distribution, and therefore a larger distance between the filters and the GAMMA3 scintillator is required.

As for the GAMMA1 detector, GEANT4 simulations were performed to study the GAMMA2 performance in the context of the E300 emittance preservation goal. The GEANT4 simulations provided a simulated spectral response of the GAMMA2 scintillator by sending 10^6 photons per incident photon energy in the GEANT4 geometry shown in Fig. 3.5, corresponding to the FACET-II dump table layout. Note that, as for the GAMMA1 performance study in the context of the PWFA experiment, no angular information is retrieved from the GEANT4 simulation: each GEANT4 simulation included a unique converter (red square in Fig. 3.5) right in front of the GAMMA2 scintillator so that all secondary particles produced at the converter go through the scintillator.

The simulated spectral response of GAMMA2 for each converter/filter is plotted in Fig 3.8(b),

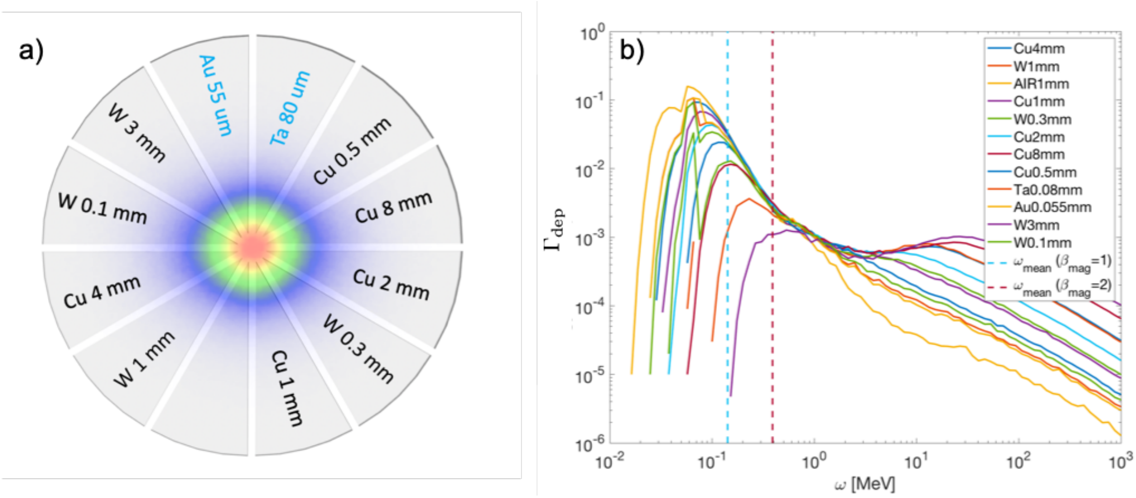

Fig. 3.8: a) Schematic distribution of gamma-ray filters in GAMMA2 detector together with a betatron radiation angular distribution centered on the axis of the set of filter. b) Simulated spectral response of GAMMA2 behind each filter (see text for more details).

together with the ω_{mean} values of two betatron spectra under different matching conditions in the E300 experiment. As in the GAMMA1 performance study, the thickest and highest Z materials absorb the low-energy part of the spectra and enhance the high energy part due to secondary particle creation. The particle trajectories as well as the associated betatron radiation used in this analysis of GAMMA2 performance are different from the one used in the GAMMA1 (see Sec. 3.2.1) and emittance presentation studies (see Sec. 2.2.1). The main difference is the normalized trailing beam emittance considered, $\tilde{\epsilon}_N = 30$ mm mrad, instead of the nominal $\tilde{\epsilon}_N = 3$ mm mrad used before. This "worse" beam parameter would correspond to an initial phase of the FACET-II experiments where the LINAC does not yet operate under fully optimal conditions, or where beam ionisation of the buffer gas of the lithium plasma oven sets a limitation on the peak beam density (see Sec. 2.1).

Furthermore the particle trajectories from which the betatron radiation is computed are not extracted from QuickPIC simulations. Instead, a certain number of macro-particles initialised via the initial Twiss parameter are propagated under a linear focusing force corresponding to the blow-out regime at a plasma density $n_p = 4 \times 10^{16}$ cm^{-3}. These macro-particles are propagated for 20 cm which corresponds to the plateau region of the FACET-II plasma density profile (see Fig. 2.1(a)). As in the QuickPIC framework, changing the initial Twiss parameters in this particle tracking code allows to scan different matching conditions. It should be noted that no acceleration was included in this particle tracking code. The advantage of this method against QuickPIC simulations is that it allows to explore the trailing transverse dynamics for a large number of different initial beam phase-spaces at a greatly reduced computational cost. Nevertheless, the drive evolution, as well as the acceleration and the density ramps, are not included in this study.

From these particle trajectories, one can compute the radiated betatron spectra under different matching conditions and apply to them the spectral detector response of the different filters. To illustrate the expected behaviour of the GAMMA2 detector at the initial phase of FACET-II, the ratio between the mismatched ($\beta_{\text{mag}} = 2$) and matched signals (integrated deposited energy in the GAMMA2 scintillator) after each converter, normalized to the respective

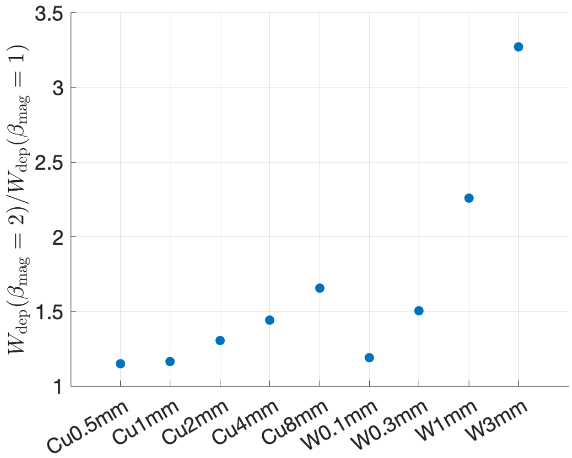

Fig. 3.9: Simulated ratios between the mismatched and matched deposited energies in the scintillator (DRZ screen) after each converter of the GAMMA2 detector. Deposited energies in GAMMA2 are normalized to the deposited energy in GAMMA1 before computing the ratio.

GAMMA1 integrated signals, is shown in Fig. 3.9. The normalisation to GAMMA1 signal allows in principle to remove the overall increase of the radiated energy in the mismatched conditions with respect to the matched conditions.

The W filters, as well as the thick Cu filters, show a significant variation of this signal ratio for different target thicknesses. This variation has the spectral shift between the two signals encoded, and in the next paragraphs a method to retrieve this information is proposed. On the other hand we observe in Fig. 3.9 that the thin Cu filters (0.5 mm and 1 mm) have a similar signal ratios. This can be originated from a compensation of the two opposite responses at low and high photon energies, i.e. the signal enhancement of the Cu 1 mm filter at high energies with respect to the Cu 0.5 mm filter is compensated with the higher absorption of the Cu 1 mm filter at low energies with respect to the Cu 0.5 mm filter.

A more elaborated study can be done by comparing these signals to the signals produced by synchrotron spectra of different critical frequency ω_c, so that a critical frequency can be determined from the simulated GAMMA2 data from the particle trajectories by searching for a "best candidate" ω_c. As before, the deposited energy in the GAMMA2 scintillator is normalized to the deposited energy in the GAMMA1 scintillator, whose spectral response in extracted from the same GEANT4 simulation. The result of this comparision analysis for the two betatron spectra used in Fig. 3.9 ($\beta_{\mathrm{mag}} = 1$ and $\beta_{\mathrm{mag}} = 2$) is shown in Fig. 3.10. In this figure, plots (a), (b), (d) and (e) show the betatron GAMMA2 signals (orange bars) for each converter together with the synchrotron signals (blue bars) and their difference (yellow bars). Plots (a) and (b) correspond to the matched betatron spectrum and plots (d) and (e) correspond to the mismatched ($\beta_{\mathrm{mag}} = 2$) betatron spectrum. These plots show how significant differences (yellow bars) are found between the matched betatron signal and the $\omega_c = 1057$ keV synchrotron signal (Fig. 3.10(b)), the latter producing a much better agreement with the mismatched betatron spectrum (Fig. 3.10(d)). It should be noted that the errors are not only a scale factor or additive constant common to all converters.

Furthermore Fig. 3.10(c) and Fig. 3.10(f) show correspondingly the matched and mismatched betatron spectra (yellow line) together with the synchrotron spectra extracted from

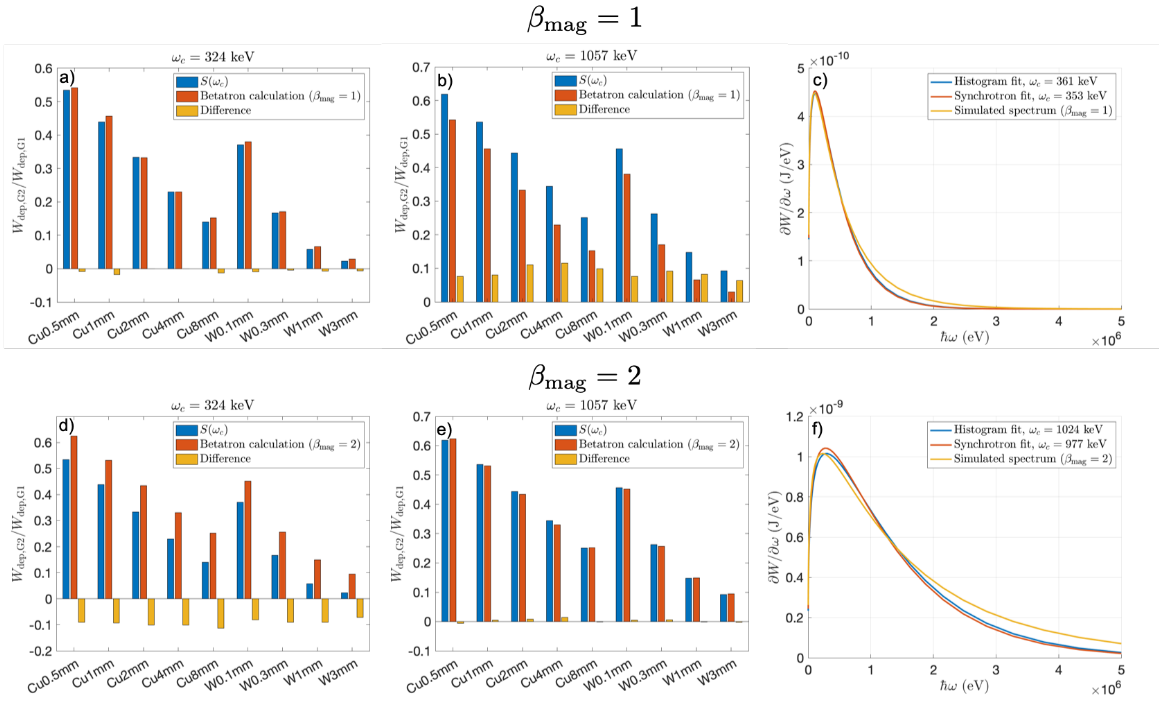

Fig. 3.10: (a), (b), (d) and (e): betatron signals (orange bars) for each GAMMA2 converter together with the synchrotron signals (blue bars) and their difference (yellow bars) normalized to the GAMMA1 signal for different matching conditions of the betatron radiation and different critical frequencies of the synchrotron spectra (see Fig. labels and titles). c) and (f) the matched and mismatched betatron spectra (yellow line) together with the synchrotron spectra extracted from minimising the signal difference by the minimum mean square method (blue lines) and the best-fit synchrotron spectra (orange lines).

"best-candidate" search (blue lines) and the result of a synchrotron fit (orange lines). From these plots one can see how the betatron spectrum slightly differs from a perfect synchrotron spectrum. Indeed, the best-fit synchrotron spectrum (labelled "Synchrotron fit" in the figure) gives different fitted ω_c depending on the fit interval (not shown here), evidencing the difference between the betatron spectral shape and the synchrotron shape. In these plots the fit interval is the whole energy range on display. Despite this difference, the "best-candidate" method (labelled "Histogram fit" in the figure) produces an excellent agreement with the fitted synchrotron spectra, showing the sensitivity capabilities of the method for a known synchrotron-like gamma-ray spectral shape.

To finish this section, a final remark on the spatial distribution that was not simulated in the data presented in this chapter. As already discussed, since GAMMA2 aims at measuring conversion rates from high energy photons in high-Z materials, the scintillator needs to be placed right after the converter. If this is the case, then one should not need to include the spatial distribution of the deposited energy on GEANT4. Yet, due to the spatial distribution of different filters, secondary particles produced at one converter could deposit its energy behind a different filter if they are produced with a large transverse angle. This phenomena, which is strongly reduced as the incident gamma-ray energy gets larger, and that sometimes can be referred to as filter cross-contamination, should be marginal and only happening at the borders of the converters as long as the scintillator is placed right after the converters. This should leave enough uncontaminated space behind each converter to retrieve the right signal for the GAMMA2 detector, with the exception of the case where gamma-ray angular divergence is small and only the very center of the "Camembert" distribution is illuminated, in which case cross-contamination could start to become important.

One of the main difficulties when trying to include the angular distribution of the incident gamma ray is that the correlated angular-spectral distribution of the radiation ($\frac{\partial^2 W}{\partial\Omega\partial\omega}$) needs to be considered. This has been done by hard-coding a Monte-Carlo based algorithm in the GEANT4 framework to reproduce the double differential distributions computed from the particle trajectories. However the statistical weight of each single photon in the GEANT4 simulation is strongly decreased and a much higher number of incidents photons is required to produce a statistically significant signal on the scintillators, specially for the GAMMA3 detector sensitive to the very low transmission rates of the high-Z converters at the studied energies. This makes the GEANT4 simulations almost unaffordable for running them in a personal CPU, and larger computing machines with powerful parallelisation capabilities might be required.

3.3 Gamma Screen commissioning

This last section of the chapter presents experimental results of a first shift of detector commissioning at FACET-II that was carried out in August 2021. This commissioning shift used the first electron beams that were accelerated and transported all the way to the experimental area at the upgraded facility, demonstrating the Key Performance Parameters (KPPs) as defined by the facility [72]. The goals of these user commissioning shifts was to check the working status of several experimental tools, such as the DAQ or the motor controllers, but also to read the first beam-produced signals from the installed detectors. Furthermore, the interaction of the electron beam with the solid targets placed in the E305 target mount (see Fig. 6.1) was measured.

Before the FACET-II LINAC started to accelerate the first beams, the electron and gamma diagnostics were installed in the dump table as part of the diagnostic installation work. The implementation of the cameras and actuators into the SLAC network was done. A picture of the Dump Table after the installation of the electron and gamma detectors is shown in Fig. 3.11. This picture shows the status of the Dump Table during the first commissioning shift, except for the scientific cameras (CMOS) of GAMMA1 and LFOV which were replaced by more economic GigE cameras to avoid damage during the beam commissioning.

In parallel to the installation work, the set of filters for GAMMA2-3 showed in Fig. 3.8 was built and installed. For the building process, large foils of maximum 2 mm thicknesses were acquired, which were then cut in the chosen shape (triangles for the initial experiments). For the thickest filters, several pieces were stuck on each other to achieve the desired thickness. We used regular glue on the external part of the filters to stuck them together and to a 10 μm thick Mylar foil. We checked via GEANT4 simulations the variation of the spectral response of the detectors when adding the 10 μm thick Mylar foil and the differences were found to be negligible. A picture of the filters is shown in Fig. 3.13(a).

This first commissioning shift was the first time that FACET-II delivered beam to users, and the beam parameters as well as beam-control capabilities were not yet at the optimum performances. The mean electron energy was measured at $\approx$ 9 GeV, with an energy spread of $\approx$ 1%. At waist, the beam RMS horizontal and vertical sizes were measured to be $\sigma_x = 46$ μm and $\sigma_y = 23\,\mu$m respectively. The beam charge could not be measured systematically due

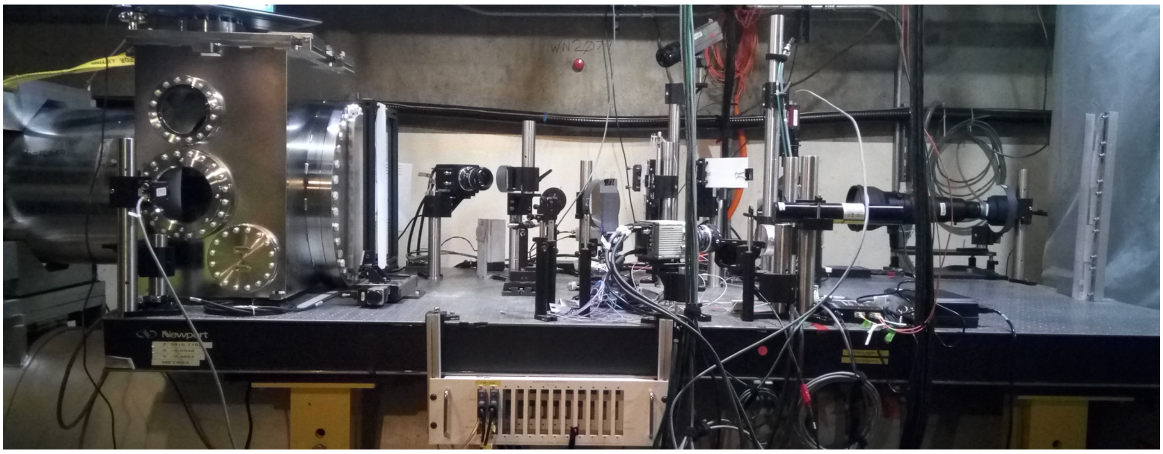

Fig. 3.11: Picture of the Dump Table at FACET-II. Beam (electrons and gammas) arrive from the left side, and the lead block of the right side is the beam dump.

to significant beam losses in the LINAC. The charge detectors near the experimental area measured charge values of ≈ 150 pC, but significant fluctuations of ±50 pC were observed. The RMS bunchlength σ_z was measured using a Transverse Deflecting Cavity (TCAV) giving $\sigma_z \approx 25\,\mu$m. Twiss parameters were not measured at the experimental area.

In order to commission the gamma detectors, the E305 solid targets were inserted in the beam path to produce high energy bremsstrahlung photons. Six different solid targets were installed: aluminium foils of thicknesses 0.1, 0.2, 0.5, 1 and 2 mm, and a tungsten foil of 1 mm thickness. The final focus system was set to achieve the minimum spot size on the closest beam profiler (YAG screen) ≈ 3 m downstream of the solid target location. It should be noted though that the total radiated energy via bremsstrahlung does not depend on beam Twiss parameters and emittance since it is an individual-electron process, and only depends on charge and energy.

An example of bremsstrahlung signal on the GAMMA1 detector with the CsI pixelized crystal is shown in Fig. 3.12(a). This bremsstrahlung signal was produced in the interaction of the electron beam with 1 mm thick aluminium target. Note that the observed asymmetry in the signal originates from the different beam transverse parameters. The central region corresponds to the Al bremsstrahlung signal, whereas the surrounding halo comes from other sources upstream the interaction point, probably related to the significant beam losses in the LINAC. This background halo was measured by removing the foils from the beam path, and is subtracted together with the camera background noise in the upcoming analysis.

A serie of ≈ 100 shots was taken for every solid target. The integrated bremsstrahlung signal, normalized to the beam charge as measured by a toroid element close to the IP, was computed for every shot. The mean value, as well as the standard deviation for each target are plotted in Fig. 3.12(b-c). Fig. 3.12(b) plots the values for the aluminium targets as a function of the target thickness, showing the expected linear behaviour of the GAMMA1 detector for these conditions. Fig. 3.12(c) shows the same data points together with the bremsstrahlung signal produced with the 1 mm thick tungsten target, but as a function of the target thickness normalized by the radiation length X_0 of each target material. This normalisation allows to account for the different atomic numbers of each material. The tungsten signal is plotted in red. In principle the integrated signal should scale linearly with respect to the normalized thickness, since the spectral distribution of bremsstrahlung photons should not depend on the

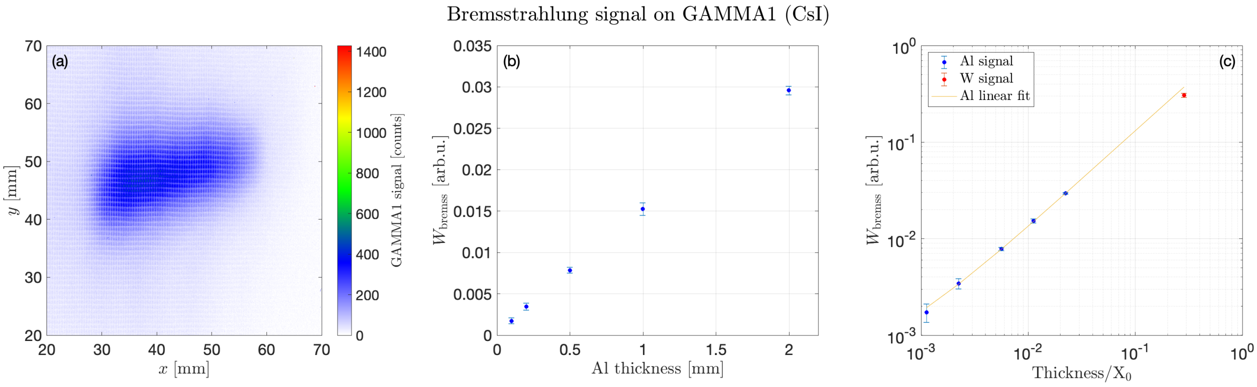

Fig. 3.12: (a) GAMMA1 bremsstrahlung signal produced in the interaction of the electron beam with 1 mm thick aluminium target (b) Mean integrated GAMMA1 signals for different Al thicknesses. (c) Mean integrated GAMMA1 signals as a function of the thicknesses normalized by the radiation length for each solid target, Al targets in blue and W target in red. The result of a linear fit on the Al signal is represented by the yellow line.

target material [56]. The yellow line on Fig. 3.12(c) shows the result of a linear fit on the Al data points and extrapolated to the W case. The slightly lower signal obtained for W could indicate that the bremsstrahlung signal produced by the W filter is starting to saturate the CsI scintillation, but more data points close to this normalized thickness would be required to confirm this hypothesis.

The DRZ screen was also inserted instead of the CsI scintillator in the GAMMA1 detector, but due to the low beam charge and the high bremsstrahlung photon energy only the bremsstrahlung signal produced with the W target was visible. For this target, the integrated signal on DRZ was measured to be a factor of ≈ 10 smaller than for the CsI, which together with the limited dynamic range of the installed camera (12 bits) and the non-negligible noise levels made the DRZ not sensible enough to detect the bremsstrahlung gammas with Al targets.

An example of the GAMMA2 and GAMMA3 measurements, added over ≈ 100 shots, are displayed in Fig. 3.13(b) and (c) respectively. These signals correspond to the 1 mm W solid target. The filter orientation is the same as showed in Fig. 3.13(a). The highest signal on GAMMA2 is clearly obtained for the 3 mm thick W filter conversion, as would be expected from the produced bremsstrahlung radiation whose high energy part of the spectrum can extend up to the beam energy. The GAMMA3 signal seems to be also dominated by the secondary particle signal from the W 3 mm filter, which indicates that for bremsstrahlung photon energies the GAMMA3 separation from the filters is not enough to let secondary particles spread laterally before they reach the GAMMA3 scintillator. Furthermore Fig. 3.13(c) shows that the GAMMA3 signal levels are very close to the noise level of the detector, even for the highest bremsstrahlung signal levels of the W target. These low GAMMA3 signals are a direct consequence of the overall low gamma signal as for GAMMA1 with DRZ, but also of the low sensitivity of DRZ screen (without converter) to the high energy photons, which is an important part of the transmitted photons through the filters.

Unfortunately, the alignment of the filters with respect to the gamma axis could not be consistently checked and the filters were not motorised. The only alignment test that was performed was to turn off the spectrometer dipole to let the electron beam propagate with the gammas, and resulted in the beam hitting the GAMMA2 detector between the W 3 mm

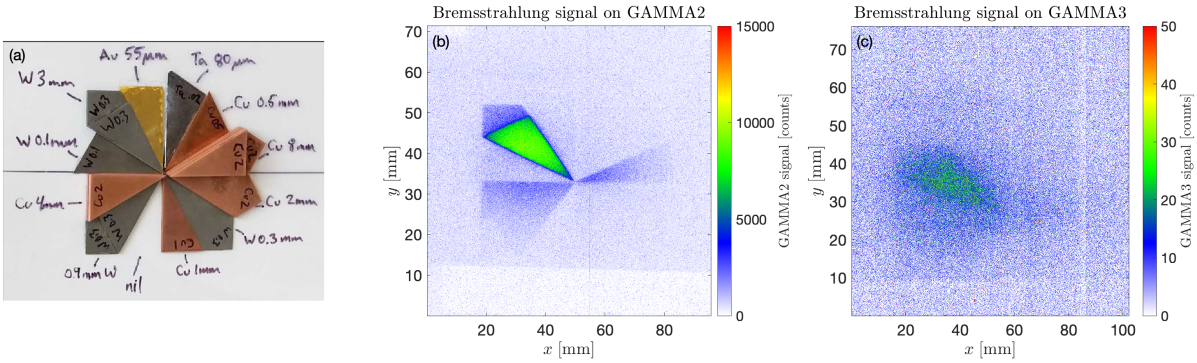

Fig. 3.13: (a) Picture of GAMMA2-3 filters before installation. *Credits to D. Storey for the assembly and the image.* (b-c) Bremsstrahlung signal on GAMMA2 and GAMMA3 added over ≈ 100 shots after background (environmental) subtraction.

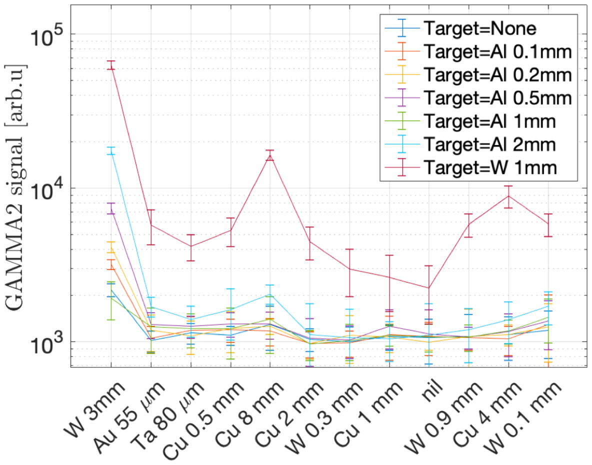

Fig. 3.14: Measured GAMMA2 signals behind each filter for different targets.

and the Au 55 μm filters, indicating that the gamma axis does not coincide with the center of the set of filters. However during this test the spectrometer quadrupoles were on, which could have steered the beam transversely, so no firm conclusion can be drawn concerning the filter alignment.

A preliminary data analysis of the GAMMA2 signals for different targets is displayed in Fig. 3.14. An equally large region behind each filter is selected, over which the signal is integrated after background subtraction. This signal is added over ≈ 100 shots. Overall, it shows the expected trend, i.e. thicker filters produce higher signal. Yet, the W 0.1 mm filter seems to produce more signal than other thicker W filters. Two possible factors can explain this feature: on the one hand the location of this filter, placed between two thick filters (W 3 mm and Cu 4 mm), could lead to cross-contamination signal from the neighbour filters that would enhance the W 0.1 mm signal. On the other hand the aforementioned potential misalignment of the filters, the gamma axis being rather towards the upper left filters on Fig. 3.13, would also enhance the signal of the W 0.1 mm compared to the W 0.3 mm, the latter being placed at the bottom right edge. An equivalent analysis on GAMMA3 is not possible due to the low signal levels as discussed before.

Part II

STREAMING INSTABILITIES IN BEAM-PLASMA INTERACTION

4. INTRODUCTION TO BEAM-PLASMA STREAMING INSTABILITIES

Plasma streaming instabilities arise from the relative motion of the individual plasma constituents, resulting in an exponential amplification of the background electromagnetic fields present in the system. Considering that most of the baryonic matter in the outer universe is believed to exist in an ionised state [80], these instabilities are extremely relevant in several astrophysical scenarios. They are thought to dissipate into heat or radiation the kinetic energy of the relativistic particles produced in some of the most energetic astrophysical events, such as supernovas or neutron star mergers. They are also believed to play a central role in the production of highly energetic particles and radiation in relativistic colissionless shocks [81]. As discussed in Ref. [82], these micro-instabilities can shape the profile of the shock wave, magnetise the shock precursor and promote background particles to be further accelerated by the shock, actively participating in the so-called first order Fermi acceleration. Furthermore, this powerful amplification mechanism is believed to play an important role in solar flares [83], cosmic magnetic field generation [84] and the unknown origin of Gamma Ray Burst (GRB) [85], placing these instabilities at the center of the emerging field of multi-messeneger astrophysics [86].

The astrophysical repercussion of these instabilities has gained interest over the last decades, and it is nowadays one of the main motivations of the field. Nevertheless, these instabilities were initially postulated in the context of laboratory plasmas and their interactions with particles beams. In this context, the main motivation was to use plasmas to transport efficiently high current particles beams, mostly in connection with Inertial Confinement Fusion (ICF), but it was soon realised that the instabilities arising in such a system represent a severe limitation to this process. During my thesis, I have been working on the plasma streaming instabilities excited by a relativistic particle beam when propagating in a plasma, often referred as beam-plasma instabilities. Beam-plasma instabilities can be classified as a subset of the more general set of streaming plasma instabilities, even if the physical mechanism that onset the instability are the same in both cases: the counterflow of charged particle streams. A clear example of the similarities between beam-plasma instabilities and a single-plasma streaming instability is the case of the Current Filamentation Instability and the Weibel Instability. Very often used equivalently, these two instabilities were originally postulated in two different contexts: Current Filamentation Instability was postulated for a beam-plasma system, whereas the Weibel Instability was postulated in a unique plasma with an anisotropy in the velocity distribution function.

This chapter starts with a brief overview of the history of the topic, which will help to clarify the nomenclature herein. Following Ref. [5], the same nomenclature and similar notation will be adopted in this manuscript. Afterwards, some basic theoretical elements and illustrative derivations will be presented. The calculations are first done in detail using the fluid approximation, and then temperature and kinetic effects are briefly discussed. This chapter aims at setting a theoretical base for the results that are presented in the upcoming chapters.

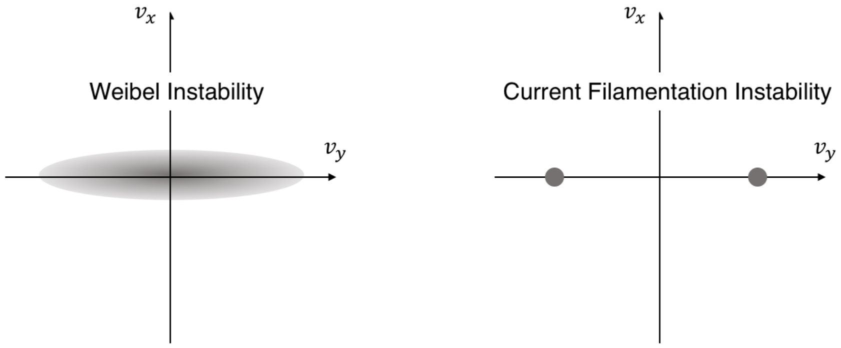

Fig. 4.1: Schematic representation of the original velocity distributions of the Weibel Instability [91] and of the Current Filamentation Instability [90].

4.1 Historical overview

Several years after Langmuir's pioneer observation [87] in 1925 suggesting the existence of oscillations in a beam-plasma system, Pierce [88] demonstrated in 1948 that unstable waves, i.e. with exponentially growing amplitude, can arise during the propagation of a particle beam through a neutral plasma. Shortly afterwards these unstable waves were identified as the Two-Stream Instability (TSI) and a kinetic formalism was developed to model the onset of the instability [89]. These TSI modes were found to be longitudinal (i.e. with a wave vector along the beam direction), and of electrostatic nature. They resulted in beam density longitudinal modulations, or micro-bunching, at the unstable frequency.

The second type of beam-plasma instability was postulated in 1959 by Fried [90]. He discovered that when two charged streams counterflow through each other, electro-magnetic unstable waves can also grow transversely to the flow direction. Since the current profile of each specie is also modulated transversely, breaking the beams into filaments, this instability is usually referred as Current Filamentation Instability (CFI) or just "filamentation" instability. In his article, Fried mentioned the analogy of his discovery with the shortly-before published result of Weibel (WI) [91], which described the mechanism of unstable waves growing in a plasma with a highly anisotropic velocity distribution function, the anisotropy originating from a larger temperature on one spatial axis compared with the others. The so-called Weibel Instability is purely magnetic and also grows with a wave vector perpendicular to the "hot" axis. The analogy that Fried mentioned in his original publication is depicted in Fig. 4.1, highlighting the importance of the tails of the velocity distribution along the hot axis. Moreover, this figure shows how Weibel instability was postulated as a kinetic instability on a unique distribution function, whereas the CFI, not necessarily of kinetic nature, was postulated for a two-component distribution. Interestingly, the maximum growth rate of the WI is the same as the CFI growth rate in the fluid limit (see next section for the exact expression). In this manuscript, focused on beam-plasma instabilities, only distributions with two separated species will be studied: an electron beam with a relativistic velocity and a "cold" isotropic plasma. Therefore the term CFI will refer to the transverse electromagnetic modes arising in such a system.

Initially these two beam-plasma instabilities (TSI and CFI) were studied separately, but it was soon realised (in 1960) that if parallel and transverse unstable modes existed, the unstable spectrum could be two-dimensional [92]. However, most of subsequent theoretical studies of kinetic effects and non-linear evolution were carried out for each instability independently: TSI modes, as well the full 2D unstable spectrum, were often studied using the electrostatic approximation [89, 93], whereas CFI was often studied within the "transverse" approximation, i.e. only describing transverse modes [94]. Probably due to the analytical complexity and the limited computational resources, a fully kinetic electromagnetic 2D formalism was not developed until 2004, which allowed to describe simultaneously the full spectrum of unstable modes in a beam-plasma system [95]. Remarkably, this new formalism allowed to identify a new region of unstable modes with a local maximum in the 2D unstable spectrum [96], named oblique or mixed modes. This off-axis mode (neither purely longitudinal nor transverse) was found to be electrostatic and the associated growth rate to obey different scalings from TSI or CFI scalings with respect to the beam-plasma parameters [96]. This new analysis of the full 2D unstable spectrum revealed that the oblique local maximum is expected to grow faster than TSI and CFI in the ultra-relativistic beam-diluted regime, and therefore would dominate the initial phase of the instability under such a beam-plasma configuration. As will be shown later, the oblique modes share many features with two-stream longitudinal modes, and therefore will be sometimes referred in this manuscript as Oblique Two-Stream Instability (OTSI).

It is worth noticing that beam-plasma instabilities gained a lot of interest with the advent of Inertial Confinement Fusion in the 1990's [97]. In the fast ignition scenario (FIS) [98], a high current electron beam created by a high intensity laser pulse deposits its energy in the nuclear fuel. During the beam transport towards the core of the pre-compressed capsule beam-plasma instabilities will disrupt the beam propagation and therefore deteriorate the control of the energy deposition process. A lot of studies of beam-plasma instabilities in the complex scenario of ICF were carried out with the help of PIC simulations. The extensive development of PIC codes over the last years has enabled the use of these codes as a powerful tool to study beam-plasma instabilities on a kinetic scale. PIC simulations have showed an overall good agreement with the existing theory [5], and have become a robust and often guiding tool to explore the different scenarios where beam-plasma instabilities play an important role.

Experimental studies of beam-plasma instabilities have been, and still remain, a complicated task due to the fast and small scales over which they develop. After Langmuir's observation, later associated to TSI, some experiments were carried out in the early 70's with electron beams propagating in plasma. Transverse beam modulations were observed and diagnosed [99, 100, 101], being associated to filamentation instabilities. These experiments were carried out in the context of beam transport and beam-to-plasma energy transfer. Recently, Allen *et al.* [102] studied beam-plasma instabilities in a modern accelerator facility and were able to observe CFI development for different beam-plasma configurations by looking at the transverse beam profile right after the plasma. They found an overall good agreement with theoretical expectations in terms of number of filaments and its scaling with plasma density. Nevertheless, they remarked that the existing theory does not account for the finite size of electron beams coming from a LINAC in an accelerator facility. They observed that when the beam transverse size was smaller than (or of the order of) the plasma skin depth, the beam density does not show the characteristic filamentary structures expected from CFI.

Accounting for the finite beam dimensions in beam-plasma instabilities was first investigated theoretically for the TSI. The main motivation of these initial studies was to understand the absolute or convective nature of the instability [103] when a finite bunch length was considered. These studies found out that when one considers a beam with a semi-inifinite longitudinal extent (i.e. with a "head" or "front") the TSI has a convective behaviour: the beam front is the source of the initial perturbation which then grows in both a temporal and a spatial manner [104] towards the rear of the beam. Very recently, V.B. Pathack *et al.* [105] investigated the spatiotemporal growth of CFI for an equivalent semi-infinite beam. However they used a different approach based on the work of Ref. [106], such that the initial perturbation can be present all along the beam and not only at the front. Their model, in agreement with PIC simulations, revealed that near the beam front the instability grows in a spatiotemporal manner, whereas at the rear the CFI grows purely temporally as in the infinite beam case. Interestingly, they found out that the spatiotemporal dynamics of CFI, namely the spatial growth, vanish for highly relativistic beams.

4.2 Theory for unbounded beam-plasma systems

In this section, we introduce the fluid formalism to derive the dispersion equation of a relativistic beam-plasma system for each of the three classes of instability (TSI, CFI, OTSI) under the corresponding approximations. Afterwards, we briefly discuss the fully kinetic formalism with some considerations about the kinetic effects. No boundary effect is considered, i.e. all species have an homogeneously infinite spatial extent. To simplify the notation, the units used in these derivations are such that $e = c = \epsilon_0 = m_e = 1$.

4.2.1 Electrostatic fluid approximation: TSI and OTSI modes

We consider a 2D (x, y) unbounded system formed by a relativistic electron beam of density n_b propagating at a velocity $\mathbf{v_b}$ along the x direction and a stationary neutral plasma of density n_p. In this model ions will be considered as a neutralising fixed background, which can be justified by their large masses compared to the electrons. Under the electrostatic approximation, we can write the fluid momentum conservation equation and the continuity equation as

$$(\partial_t + \mathbf{v_i} \cdot \nabla)\, \mathbf{p_i} = \nabla\phi \tag{4.1}$$

$$\partial_t n_i + \nabla \cdot (n_i \mathbf{v_i}) = 0 \tag{4.2}$$

where the index $i = (b, p)$ denotes the corresponding specie and ϕ denotes the electrostatic potential which satisfies Poisson's equation

$$\nabla^2\phi = \sum_i n_i \tag{4.3}$$

Next step is to linearise these equations for each specie. To do so, we will write each variable as $X(\mathbf{x}, t) = X^{(0)} + X^{(1)}(\mathbf{x}, t)$, where $X^{(0)}$ represent the equilibrium quantity and $X^{(1)}$ represents the perturbation such that $X^{(1)} \ll X^{(0)}$. We start with the linearisation of each component of the relativistic linear momentum $\mathbf{p} = \gamma(\mathbf{v})\mathbf{v}$, where $\gamma(\mathbf{v}) = (1 - \mathbf{v}^2)^{-1/2}$. Using the Taylor Expansion (T. E.) around equilibrium, for the longitudinal component p_x we have

$$p_x(\mathbf{v}) = p_x(v_0 + v_x^{(1)}, v_y^{(1)}) \overset{\text{T. E.}}{\approx} p_x(v_0, 0) + v_x^{(1)} \frac{\partial p_x}{\partial v_x}(v_0, 0) + v_y^{(1)} \frac{\partial p_x}{\partial v_y}(v_0, 0) \tag{4.4}$$

The partial derivatives can be computed using the chain rule:

$$\frac{\partial p_x}{\partial v_x} = \frac{\partial\,(\gamma(\mathbf{v}) v_x)}{\partial v_x} = \frac{\gamma(\mathbf{v})}{\partial v_x} v_x + \gamma(\mathbf{v}) = v_x^2 \gamma^3(\mathbf{v}) + \gamma(\mathbf{v})\ , \quad \frac{\partial p_x}{\partial v_y} = v_x v_y \gamma^3(\mathbf{v}) \tag{4.5}$$

which evaluated at equilibrium and inserted in eq. (4.4) give

$$p_x^{(1)}(v_0 + v_x^{(1)}, v_y^{(1)}) = v_x^{(1)} \left(v_0^2\gamma^3(v_0) + \gamma(v_0)\right) + v_y^{(1)} \cdot 0 = v_x^{(1)}\gamma_0^3 \tag{4.6}$$

where $\gamma_0 = \gamma(v_0)$. Similarly, for the transverse component p_y

$$p_y(\mathbf{v}) = p_y(v_0 + v_x^{(1)}, v_y^{(1)}) \overset{\text{T. E.}}{\approx} p_y(v_0, 0) + v_x^{(1)}\frac{\partial p_y}{\partial v_x}(v_0, 0) + v_y^{(1)}\frac{\partial p_y}{\partial v_y}(v_0, 0) \tag{4.7}$$

$$\frac{\partial p_y}{\partial v_x} = \frac{\partial\left(\gamma(\mathbf{v})v_y\right)}{\partial v_x} = \frac{\gamma(\mathbf{v})}{\partial v_x}v_y = v_x v_y\gamma^3(\mathbf{v})\ ,\ \frac{\partial p_y}{\partial v_y} = v_y^2\gamma^3(\mathbf{v}) + \gamma(\mathbf{v}) \tag{4.8}$$

$$\Rightarrow p_y^{(1)}(v_0 + v_x^{(1)}, v_y^{(1)}) = v_x^{(1)} \cdot 0 + v_y^{(1)}\gamma(v_0) = v_y^{(1)}\gamma_0\,. \tag{4.9}$$

Therefore, the linearised momentum conservation equation for beam electrons can be written as

$$(\partial_t + v_{0b}\partial_x)\begin{bmatrix}\gamma_{b0}^3 v_{bx}^{(1)}\\ \gamma_{b0}v_{by}^{(1)}\end{bmatrix} = \begin{bmatrix}\partial_x\phi^{(1)}\\ \partial_y\phi^{(1)}\end{bmatrix} \tag{4.10}$$

The linearised continuity equation for beam electrons

$$\partial_t n_b^{(1)} + \partial_x(n_b v_{bx})^{(1)} + \partial_y(n_b v_{by})^{(1)} = 0\,, \tag{4.11}$$

can be recasted as

$$(\partial_t + v_{b0}\partial_x)\, n_b^{(1)} + n_b^{(0)}\left(\partial_x v_{bx}^{(1)} + \partial_y v_{by}^{(1)}\right) = 0\,. \tag{4.12}$$

If we multiply eq. (4.12) by $(\partial_t + v_{b0}\partial_x)$ and use eq. (4.10) to express $\mathbf{v}_b^{(1)}$ as a function of ϕ we obtain

$$(\partial_t + v_{b0}\partial_x)^2\, n_b^{(1)} = -n_b^{(0)}\left[\gamma_{0b}^{-3}\partial_x^2 + \gamma_{0b}^{-1}\partial_y^2\right]\phi^{(1)} \tag{4.13}$$

For plasma electrons, assuming that they are non-relativistic ($\gamma_{0p} = 1$) and that they are initially at rest ($v_{0p} = 0$), eq. (4.13) gives

$$\partial_t^2 n_p^{(1)} = -n_p^{(0)}\left[\partial_x^2 + \partial_y^2\right]\phi^{(1)} \tag{4.14}$$

The two assumptions above for plasma electrons are valid as long as the beam induced return current can be neglected, which is a good approximation when the beam is neutral (e^+e^- pair beam) or when the beam charge density is much smaller than the plasma density, i.e. the beam to plasma density ratio $\alpha = n_b/n_p$ is small compared to one.

Finally, the linearised Poisson's equations reads

$$\left(\partial_x^2 + \partial_y^2\right)\phi^{(1)} = n_b^{(1)} + n_p^{(1)} \tag{4.15}$$

If we apply $(\partial_t + v_{0b}\partial_x)^2\,\partial_t^2$ to eq. (4.15) and use eq. (4.13) and eq. (4.14) we get

$$(\partial_t - v_{0b}\partial_x)^2\,\partial_t^2\left(\partial_x^2 + \partial_y^2\right)\phi^{(1)} = -n_b^{(0)}\left[\gamma_{0b}^{-3}\partial_x^2 + \gamma_{0b}^{-1}\partial_y^2\right]\partial_t^2\phi^{(1)} - n_p^{(0)}\,(\partial_t + v_{0b}\partial_x)^2\left(\partial_x^2 + \partial_y^2\right)\phi^{(1)} \tag{4.16}$$

which can be recasted as

$$\left[(\partial_t + v_{0b}\partial_x)^2\left(\partial_t^2 + n_p^{(0)}\right)\left(\partial_x^2 + \partial_y^2\right) + n_b^{(0)}\left[\gamma_{0b}^{-3}\partial_x^2 + \gamma_{0b}^{-1}\partial_y^2\right]\partial_t^2\right]\phi^{(1)} = 0 \tag{4.17}$$

From this equation, one can derive the dispersion equation by assuming the perturbation to be of the form $\phi^{(1)} \sim \exp(i\mathbf{k}\cdot\mathbf{r} - i\omega t)$, which is equivalent to to perform the following formal substitutions,

$$\partial_t \to -i\omega \tag{4.18}$$

$$\partial_{x(y)} \to ik_{x(y)} \tag{4.19}$$

In this way one obtains the electrostatic dispersion equation for a relativistic beam-plasma system

$$1 - \frac{n_p^{(0)}}{\omega^2} - \frac{n_b^{(0)}\left[\gamma_{0b}^{-3}k_x^2 + \gamma_{0b}^{-1}k_y^2\right]}{(k_x^2+k_y^2)(\omega - k_x v_{0b})^2} = 0 \tag{4.20}$$

The solutions $\omega(k_x, k_y)$ of eq. (4.20) establish how the electrostatic modes develop in the given beam-plasma system. In an infinite geometry, where both interacting species of plasma and beam electrons are homogenous in space, one can consider the wave vector $\mathbf{k}$ to be real, which means that the modes are uniform modulations in space. The temporal evolution of these modes is then dictated by the imaginary component of the corresponding frequency. For a given $\mathbf{k}$, if $\mathrm{Im}(\omega) < 0$ the mode is dumped, and if $\mathrm{Im}(\omega) > 0$ the mode is amplified and is said to be unstable. Therefore, mathematically speaking, the unstable modes are solutions of the dispersion equation with a frequency whose imaginary part is positive, and the linear growth rate is given by $\Gamma = \mathrm{Im}(\omega)$.

Coming back to the electrostatic dispersion equation (4.20) we recognise the classical plasma dispersion equation $1 - \frac{n_p^{(0)}}{\omega^2} = 0$ together with a term that introduces the contribution of the relativistic beam. As expected, it is in the beam contribution where the asymmetry between the two preferred directions (longitudinal and transverse) arises.

In order to analyze eq. (4.20), we start by looking at the TSI modes by setting $k_y = 0$. Furthermore, we will restrict ourselves to the $\alpha = n_b/n_p \ll 1$ or "diluted-beam" regime. In this regime, the maximum growthrate Γ_{TSI} is found at $k_x \approx k_p$ and can be computed in terms of the beam-plasma parameters as

$$\Gamma_{\mathrm{TSI}} \approx \frac{\sqrt{3}}{2^{4/3}}\frac{\alpha^{1/3}}{\gamma_{0b}}\omega_p \tag{4.21}$$

Several examples of TSI unstable spectra are shown in Fig 4.2 (a), showing how decreasing α or increasing γ_{0b} translates into a narrower spectrum which peaks at $k_x \approx k_p$. Therefore, the linear phase of the TSI instability is dominated by a longitudinal electrostatic mode which creates modulations at the fastest growing (or dominant) wave-vector $\mathbf{k} = k_p\,\hat{\mathbf{e}}_{\mathbf{x}}$. The amplitude of these modulations, common to the plasma and beam density as well as to the electrostatic potential, grows exponentially from noise. Physically it is the coupling of the electrostatic mode with the different species that originates the amplification. The end of the linear phase is considered to occur once the amplitude of the modulation is of the same order of the equilibrium quantities, i.e. when $n^{(1)} \approx n^{(0)}$. Once this condition is reached, the small-perturbation assumption breaks down, the growth slows down and the instability saturates.

The saturation of TSI modes is usually described by electron trapping in the wave, sometimes referred as "phase-space holes creation" [107], which express the fact that most of the particles are trapped near the minima of the electrostatic potential of the growing wave. Since the wave travels close to the beam velocity [89], the trapping acts more efficiently on beam

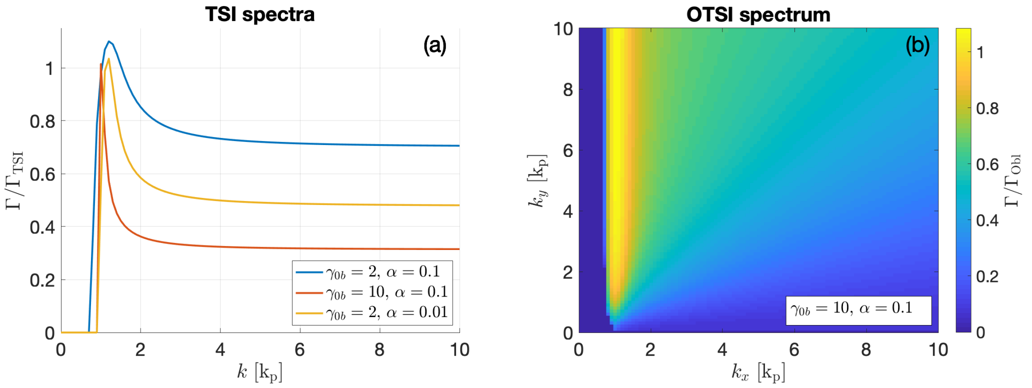

Fig. 4.2: TSI (a) and OTSI (b) unstable spectra computed from eq. (4.20) normalized to the maximum growth rate $\Gamma_{\rm TSI}$ and $\Gamma_{\rm Obl}$ for different beam-plasma configurations.

electrons than on plasma electrons, indicating that beam electron modulations saturate faster and therefore dictate the saturation of the TSI. It is worth mentioning that other non-linear phenomena such as ion motion or multiple-mode effects have an impact on the saturation, but they are out of the scope of the present manuscript.

If we extend the TSI formalism to the 2D plane, i.e. let $k_y \neq 0$ in eq. (4.20), one can derive the 2D unstable spectra of OTSI modes. Figure 4.2 (b) shows the fluid unstable 2D spectrum of a beam-plasma system with $\alpha = 0.1$ and $\gamma_{0b} = 10$. We observe how the maximum is not on the longitudinal axis, but rather along the $k_x \approx k_p$ vertical line. In the diluted-beam regime, the growth rate for a given mode can be computed along $k_x \approx k_p$ as

$$\Gamma_{\rm OTSI} = \frac{\sqrt{3}}{2^{4/3}}\left(\frac{\alpha}{\gamma_{0b}}\frac{k_y^2}{k_p^2+k_y^2}\right)^{1/3}\omega_p\,, \tag{4.22}$$

which shows that indeed the fastest mode in the fluid regime is found at $k_x \approx k_p$ and $k_y \to \infty$. In Fig. 4.2 (b), $\Gamma_{\rm Obl} = \frac{\sqrt{3}}{2^{4/3}}\left(\frac{\alpha}{\gamma_{0b}}\right)^{1/3}\omega_p$ refers to this maximum growth rate. Given the off-axis location of this 2D local maximum, these modes are called "oblique" modes. Nevertheless, they share the same longitudinal component with TSI modes, reason why they are often referred as Oblique Two-Stream Instability.

Oblique modes have both a longitudinal and a transverse component, and so does the beam and plasma density modulations. The fact that the fastest growing mode is at $k_y \to \infty$ turns out to be a consequence of the fluid approximation in the beam-plasma system. As will be discussed a bit later, temperature effects tend to damp high frequency modes, so that one can expect to have a maximum growth rate at a given $k_y < \infty$ as soon as a small transverse temperature is considered for one of the species. Furthermore, the fully kinetic description (discussed in the next section) accounts for Landau damping [108], which is also expected to act so as to suppress high frequency modes. Therefore, in realistic beam-plasma systems, OTSI modes can be interpreted as a proper extremum of the 2D electrostatic unstable spectra.

In terms of saturation, OTSI modes are also believed to saturate mainly due to beam electron trapping. Nevertheless, due to the slower phase velocity of the OTSI modes with respect to TSI modes, simulations have shown that plasma electrons can also be trapped and participate in the saturation mechanism [5]. This last point with respect to the saturation of OTSI modes will also be addressed in the ultra-relativistic regime later in Sec. 5.4.

4.2.2 Transverse electromagnetic fluid approximation: CFI modes

In the last section we have derived the electrostatic dispersion equation describing TSI and OTSI modes, resulting in purely transverse modes that are stable, and thus not growing. In this section we will derive the dispersion equation of the transverse CFI modes by neglecting the electrostatic component and letting the magnetic vector potential $\mathbf{A}$ mediate the beam-plasma interaction.

In the 2D (x, y) slab geometry used before, let us analyze a transverse mode described by the vector potential $\mathbf{A} \propto \exp\left(ik_y y - i\omega t\right)\mathbf{e}_x$ similarly to Ref. [105]. Hence, we can rewrite the linearised beam momentum conservation equation (4.10) as

$$\left(\partial_t + v_{0b}\partial_x\right)\begin{bmatrix}\gamma_{b0}^3 v_{bx}^{(1)} \\ \gamma_{b0} v_{by}^{(1)}\end{bmatrix} = \begin{bmatrix}-\partial_t A_x^{(1)} \\ v_{0b}\partial_y A_x^{(1)}\end{bmatrix} \tag{4.23}$$

From the continuity equation, one can derive the equivalent equations of (4.13) and (4.14) in the transverse approximation as

$$\left(\partial_t + v_{b0}\partial_x\right)^2 n_b^{(1)} = -n_b^{(0)}\left[\gamma_{0b}^{-3}\partial_x\partial_t - v_{b0}\gamma_{0b}^{-1}\partial_y^2\right] A_x^{(1)} \tag{4.24}$$

$$\partial_t^2 n_p^{(1)} = -n_p^{(0)}\left[\partial_x\partial_t\right] A_x^{(1)} \tag{4.25}$$

Instead the linearised Poisson equation, one can use the linearised electromagnetic wave equation

$$(\nabla^2 - \partial_t^2)A_x^{(1)} = j_x^{(1)} = n_p^{(0)} v_{px}^{(1)} + n_b^{(1)} v_{b0} + n_b^{(0)} v_{bx}^{(1)} \tag{4.26}$$

to derive the equivalent equation to eq. (4.17) in the electromagnetic approximation

$$\left[(\partial_t + v_{b0}\partial_x)^2(\partial_x^2 + \partial_y^2 - \partial_t^2 + n_p^{(0)}) + n_b^{(0)}(v_{0b}^2\gamma^{-1}\partial_y^2 + \gamma^{-3}\partial_t^2)\right] A_x^{(1)} = 0 \tag{4.27}$$

Assuming the perturbation to be of the form $A_x^{(1)} \sim \exp(i\mathbf{k}\cdot\mathbf{x} - i\omega t)$, and restricting the modes to $k_x = 0$, one obtains the dispersion equation

$$\omega^4 - \omega^2(k_y^2 + n_p^{(0)}) - n_b^{(0)} v_b^2 \gamma_{0b}^{-1} k_y^2 = 0 \tag{4.28}$$

Solving this bi-quadratic equation for ω in the beam-diluted regime and looking at the imaginary part gives the CFI growth rate

$$\Gamma = v_{b0}\sqrt{\frac{\alpha}{\gamma_{0b}}}\frac{k_y}{\sqrt{k_y^2/n_p^{(0)} + 1}} \tag{4.29}$$

which similarly to the OTSI modes has its maximum at $k_y \to \infty$ and is given in SI units by

$$\Gamma_{\mathrm{CFI}} = \frac{v_{0b}}{c}\sqrt{\frac{\alpha}{\gamma_{0b}}}\omega_p \tag{4.30}$$

CFI modes are therefore electromagnetic modes with a wave vector transverse to the beam velocity, which creates beam and plasma density transverse modulations usually called filaments. Saturation of CFI modes, similarly to TSI and OTSI modes, occurs due to magnetic trapping of beam electrons in the unstable waves [109].

4.2.3 Hierarchy between modes

In the last sections we have identified the three different unstable modes (different w.r.t. the orientation of the wave vector) present in a beam-plasma system, and derived the associated maximum linear growth rate as a function of the beam-plasma parameters. The linear growth rates are important to establish which mode grows the fastest in a given beam-plasma system, and therefore dominates the interaction. In the linear phase, where each mode is independent of the other modes, this is sometimes referred to as a competition between different modes. Comparing the three maximum growth rates Γ_{TSI}, Γ_{Obl} and Γ_{CFI} one immediately observes that oblique modes are faster than TSI modes, and that for high enough γ_{0b} oblique modes grow faster than CFI modes unless $\alpha \gtrapprox 1$. Therefore, in the ultra-relativistic diluted-beam regime, oblique modes dominate the linear phase of the instability and bring the system to the non-linear stage.

4.2.4 Limits of the fluid approach

So far we have considered that the interacting species can be defined at a given position by a unique velocity (fluid or hydrodynamical approach). Nevertheless, in real system different particles of the same specie at a given position can have different velocities. For instance temperature, which measures the velocity spread at a given position (second momentum of the velocity distribution function), was not considered in the presented formalism. To include higher momenta of the distribution function, a kinetic treatment involving Vlasov equation is needed. A fully kinetic and relativistic formalism of beam-plasma instabilities exists and it has been applied to different velocity distribution functions [95]. However, the Vlasov formalism increases significantly the complexity of the analytical derivation, and further restricts the velocity distribution functions that can be tractable to provide analytical solutions.

In this section, we will use an intuitive approach [5] to explain the main effect of beam and plasma temperature in the linear phase of the beam-plasma instabilities, namely the suppression of high frequency modes. We assume a single-mode $\mathbf{k}$ wave interacting at one position with a group of particles propagating initially in phase with the wave. If all particles have the same velocity, after an e-folding time $\Gamma_{\mathbf{k}}^{-1}$ they will still be in phase and therefore the coupling of waves and particles is optimal. If however those particle had an initial velocity spread $\Delta\mathbf{v}_{\mathbf{k}}$ along the wave direction, after an e-folding the particles will have a spatial spread of $\sim \Delta\mathbf{v}_{\mathbf{k}}\Gamma_{\mathbf{k}}^{-1}$. If the spatial spread after one e-folding time is much smaller than the wavelength of the unstable wave, the resonance condition will still be valid, but if its larger or of the order of the wavelength, the wave-particle coupling will be far from the optimum. Hence we can establish the following criterium for the validity of the fluid results:

$$\mathbf{k} \cdot \Delta\mathbf{v}_{\mathbf{k}} \ll \Gamma_{\mathbf{k}} \tag{4.31}$$

This condition explains why the fluid approach used in the derivation of the unstable spectra of OTSI and CFI modes fails to describe the limit $k_y \to \infty$. Furthermore if the main effect of temperature is to decrease the wave-particle coupling efficiency, it can be expected that the growth rate is reduced due to temperature effects compared to the fluid approximation, the latter naturally implying optimal coupling.

Furthermore, this criterium also shows that kinetic effects depend on the relative orientation of the wave-vector and the velocity spread. For relativistic beams, usually the longitudinal velocity spread is smaller than the transverse velocity spread due to relativistic contraction of the velocity distribution. Therefore, in the relativistic regime, kinetic effects have a stronger impact on perpendicular modes than on parallel modes. Together with the smaller CFI growth rate, this tend to suppress more significantly CFI modes than OTSI modes.

5. FINITE BEAM EFFECTS ON BEAM-PLASMA INSTABILITIES

This chapter is devoted to the physical processes arising in a beam-plasma system subject to streaming instabilities when, in contrast with the unbounded beam-plasma system considered in the last chapter, a particle beam of finite spatial extent is considered. The first section of the chapter focuses on the spatiotemporal evolution of the instability, including the recently developed spatiotemporal theory of the dominant oblique modes in the relativistic beam-diluted regime. The second section describes how the beam self-focusing due to plasma wakefields excited by a finite electron beam interplays with the beam-plasma instability. The third section discusses the relevance of the quasi-static approach to model the beam-plasma instability in the relativistic regime. Finally the fourth section presents a new ponderomotive (second-order) saturation mechanism observed in simulations.

5.1 Spatiotemporal evolution of beam-plasma instabilities

In Chap. 4 we have introduced a fluid theory that allows to model the beam-plasma instabilities assuming that both species are homogeneous, i.e. the evolution of the instability is identical at every point in space. If the assumption of spatial homogeneity breaks down, the evolution of the beam-plasma instability will not only have a temporal component but also a spatial component, and different points in space will experience different temporal evolutions. Models accounting for both components of the evolutions are usually referred as spatiotemporal models, and they describe the spatiotemporal development of the instability.

The unbounded geometry used in the previous chapter obviously fails to describe the physics of the region near the boundaries of the system, as well as systems with significant density gradients. A somehow naive reasoning would be to assume that for beam-plasma systems which can be considered locally homogenous over the typical spatial extent of the instability the results of the unbounded geometry hold. For the beam-plasma streaming instabilities, this would typically mean that as long as the species are locally homogenous over a plasma skin depth k_p^{-1}, the system should evolve as in the homogenous case. However, as it will be shown later, one also needs to account for the temporal scale of the instability, and it turns out that under certain circumstances, such as for relativistic particle beams delivered by high energy particle accelerators, the spatial component of the evolution of the instability is significant even for systems that largely satisfy the aforementioned naive criterium of local homogeneity.

In a realistic beam-plasma system subject to streaming instabilities, the specie with the smallest spatial extent, and therefore more likely to introduce a significant spatial unhomogeneity in the system, is the particle beam. As the particle beam propagates through the plasma, plasma electrons flow through the beam and the instability is triggered. However, if we consider a particle beam of finite size such that it is possible to effectively differentiate the front of the beam from the rear, beam electrons sitting at the front always encounter "fresh" plasma, whereas beam electrons sitting at the rear interact with plasma electrons that have already interacted with the front part of the beam. This "memory" effect would intuitively lead to stronger particle-wave coupling at the rear and thus a faster evolution at the rear compared to the front.

The spatiotemporal evolution of beam-plasma instabilities was first studied for TSI modes [104, 103]. These precursory studies were carried out in the context of the Fast Ignition scenario of ICF, and allowed to discuss the absolute vs. convective nature of the instability. Assuming a semi-infinite beam and a point-like initial noise source (see details later), these studies of the TSI confirmed the spatial evolution of the instability and remarked that the overall temporal evolution at a given beam longitudinal position was slower than in the unbounded geometry. Recently, Pathak *et. al.* [105] carried out the first spatiotemporal analysis of CFI modes. Using the same semi-infinite geometry, but assuming a uniformly distributed initial noise source, they found out that the spatial component of the CFI evolution should vanish for ultra-relativistic beams, and therefore CFI modes grow in a purely temporal manner in the ultra-relativistic regime.

During my thesis, I was able to work on the not yet existing spatiotemporal theory of oblique modes, which I develop over the next pages. The developed model, which shares several features with that of TSI modes, also uses the semi-infinite geometry and is applied for the two initial noise sources discussed before. It shows that, in the relativistic regime, the spatiotemporal evolution differs significantly from the purely temporal evolution of the unbounded geometry independently of the considered initial noise source, specially for short ultra-relativistic particle beams such as the ones produced in high energy accelerators. The validity of the model is checked with PIC simulations, showing an overall excellent agreement between theory and simulations.

5.1.1 Spatiotemporal linear model of oblique two-stream instability

Let us resume the electrostatic formalism developed in section 4.2.1, starting from the differential equation (4.17) which leads to the dispersion equation of OTSI modes. It is worth noticing that in order to solve the dispersion equation we restricted ourselves to real wave vectors k, and therefore it results in periodic homogenous modes. If k could also be a complex number sptially growing (or dumped) modes could also be solutions of the resulting dispersion equation. Instead of following this method, the derivation presented here uses the so-called "envelope approximation" where the amplitude of the considered mode is not a constant but depends on the spatial and temporal coordinates.

In order to analyze the spatiotemporal nature of the instability, it is convenient to use co-moving coordinates $(\xi, \tau) = (v_b t - x, t)$ such that $\partial_x = -\partial_\xi$ and $\partial_t = \partial_\tau + v_b \partial_\xi$, x being the longitudinal coordinate (in the co-moving coordinates the beam propagates towards negatives ξ). We consider a semi-infinite beam with the beam front situated at $\xi = 0$ and a sharp beam edge:

$$n_b^{(0)}(\xi) = \begin{cases} 0 & \text{if } \xi < 0 \\ n_b^{(0)} & \text{if } \xi \geq 0 \end{cases} \tag{5.1}$$

The beam is uniform transversely and propagates in a uniform plasma of density $n_p^{(0)}$. We then write the perturbed electrostatic potential (or any perturbed quantity) with a varying amplitude, i.e. $\phi^{(1)} = \delta\phi(\xi, \tau) \exp(-ik_0\xi + ik_y y)$. Hence the derivatives of eq. (4.17) can be rewritten as

$$\partial_x^2\phi^{(1)} = \left(-k_0^2 + \partial_\xi^2 - 2ik_0\partial_\xi\right)\phi^{(1)} \tag{5.2}$$

$$(\partial_t + v_{0b}\partial_x)\phi^{(1)} = \partial_\tau\phi^{(1)} \tag{5.3}$$

$$\partial_t^2\phi^{(1)} = \left[(\partial_\tau + v_{0b}\partial_\xi)^2 - 2ik_0v_{0b}(\partial_\tau + v_{0b}\partial_\xi) - (k_0v_{0b})^2\right]\phi^{(1)} \tag{5.4}$$

From now, we will assume the beam to be relativistic, so that $\gamma_{0b}^{-3} \ll \gamma_{0b}^{-1}$ and we can neglect the longitudinal derivative of the last term of eq. (4.17). By doing so, eq. (4.17) can be written in the co-moving coordinates as

$$\begin{aligned}\left(-k_y^2 - k_0^2 + \partial_\xi^2 - 2ik_0\partial_\xi\right)\partial_\tau^2\left[(\partial_\tau + v_b\partial_\xi)^2 - 2ik_0v_b(\partial_\tau + v_b\partial_\xi) - (k_0v_0)^2 + n_p^{(0)}\right]\\ + \frac{n_b^{(0)}k_y^2}{\gamma_{0b}}\left[(\partial_\tau + v_{0b}\partial_\xi)^2 - 2ik_0v_{0b}(\partial_\tau + v_{0b}\partial_\xi) - (k_0v_{0b})^2\right]\delta\phi(\xi,\tau) = 0\end{aligned} \tag{5.5}$$

Note that this new differential equation applies to the varying amplitude $\delta\phi$, in contrast to eq. (4.17) that applies to the perturbed quantity $\phi^{(1)}$. Taking $k_0 = k_p = \sqrt{n_p^{(0)}}/v_{0b}$ $(= \omega_{0p}/v_{0b}$ in physical units) the first term of eq. 5.5 simplifies, and we get

$$\begin{aligned}\left(-k_y^2 - k_0^2 + \partial_\xi^2 - 2ik_0\partial_\xi\right)\partial_\tau^2(\partial_\tau + v_b\partial_\xi)(\partial_\tau + v_b\partial_\xi - 2ik_0v_b)\\ + \frac{n_b^{(0)}k_y^2}{\gamma_{0b}}\left[(\partial_\tau + v_{0b}\partial_\xi)^2 - 2ik_0v_{0b}(\partial_\tau + v_{0b}\partial_\xi) - (k_0v_{0b})^2\right]\delta\phi(\xi,\tau) = 0\end{aligned} \tag{5.6}$$

Now the so-called slowly varying amplitude (or envelope) approximation is adopted. This approximation assumes that the varying amplitude $\delta\phi(\xi,\tau)$ evolves at a slower rate than the period of the dominant mode, i.e.

$$v_{b0}^{-1}\partial_\tau(\delta\phi) \ll k_p \tag{5.7}$$

$$\partial_\xi(\delta\phi) \ll k_p \tag{5.8}$$

Under this approximation, eq. (5.6) can be written as

$$(-k_p^2 - k_y^2)\partial_\tau^2(\partial_\tau + v_{0b}\partial_\xi)(-2ik_pv_{0b}) - \frac{n_b^{(0)}k_y^2}{\gamma_{0b}}k_p^2v_{0b}^2 = 0 \tag{5.9}$$

Finally, introducing

$$\Gamma_0 = \left(\frac{1}{2\gamma_{0b}}\frac{n_b^{(0)}}{n_p^{(0)}}\frac{k_y^2}{k_p^2 + k_y^2}\right)^{1/3}\omega_{0p} \tag{5.10}$$

we can write the spatiotemporal differential equation for the slowly varying amplitude as

$$\left[\partial_\tau^2(\partial_\tau + v_{0b}\partial_\xi) + i\Gamma_0^3\right]\delta\phi(\xi,\tau) = 0 \tag{5.11}$$

The spatiotemporal coupling is manifested by the $\partial_\tau^2\partial_\xi$ term. Remarkably, this equation has the same form as the spatiotemporal equation of TSI modes [110], the only difference being in the growth rate Γ_0 where the $\gamma_{0b}^{-1/3}$ factor becomes γ_{0b}^{-1} for TSI modes. This similarity originates from the common longitudinal component of oblique and TSI modes, since it is the longitudinal component along the beam direction that will define the spatiotemporal behaviour through the coupling $\partial_\tau^2\partial_\xi$ term.

It is worth noticing that in Ref. [110] Rostomyan derives this equation for TSI modes using a different approach: starting from dispersion equation of TSI modes (eq. (4.20) with $k_y = 0$), which can be recasted as

$$\left(\frac{n_p^{(0)}}{\omega^2} - 1\right)\left(\omega^2 - k_x v_{0b}\right)^2 - \frac{n_b^{(0)}}{\gamma_{0b}^3} = 0 \tag{5.12}$$

one can do the formal substitution $\omega \to \omega_0 + i\partial_t$ and $k \to k_0 - i\partial_x$ where ω_0 and k_0 satisfy satisfy the plasma dispersion equation ($\omega_0 = \sqrt{n_p^{(0)}}$) and the beam charge density wave ($\omega_0 - v_{0b}k_0 = 0$), and then expand in power series near ω_0 and k_0 to find

$$\left(2i\omega_0^{-1}\partial_t - \omega_0^{-2}\partial_t^2\right)\left(\partial_t + v_{0b}\partial_x\right)^2 = \frac{n_b^{(0)}}{\gamma_{0b}^3} \tag{5.13}$$

which under the slowly varying amplitude approximation reads

$$\partial_t(\partial_t + v_{0b}\partial_x)^2 = -i\frac{n_b^{(0)}}{2n_p^{(0)}\gamma_b^3}\omega_0^3 \tag{5.14}$$

which is equivalent to equation (5.11) in the laboratory coordinates (x, t). This method, despite the simplicity of the derivation, fails to identify the physical quantity to which the differential equation applies, hence the interest of the more evolved derivation shown before.

Solving this differential equation involves using advanced mathematical tools, and in this manuscript only the different steps of the derivation are presented. A detailed derivation of the solution can be found in the Supplemental Material of Ref. [111] (also in App. B). For a given set of initial conditions, the solution to eq. (5.11) can be found by means of a double Laplace transform. The main difficulty arises when doing the inverse Laplace transform, which involves contour integrals in the complex plane of singular functions for which the residue cannot be exactly calculated. The solution therefore involves the asymptotic development $\tau \to \infty$ of the integrands in order to apply the steepest descent (or saddle point) method.

Two solutions, each for a different set of initial conditions, are presented and discussed in this manuscript: the impulse response (or Green function), which is associated to a localised initial noise source, and a second solution associated to a uniformly distributed noise source along the beam. Let us start with the impulse solution.

The Green function of eq. (5.11) is found by using the following set of initial conditions:

$$\delta\phi(\tau = 0) = \delta(\xi) \tag{5.15}$$

where $\delta(\cdot)$ is the Dirac function. For this set of initial conditions the following analytical expression can be derived for

$$\delta\phi(\xi,\tau) \simeq \begin{cases} \frac{1}{2\sqrt{3\pi}\Gamma_0 v_{b0}\sqrt{\Gamma_0\xi/v_{0b}}} \exp\left[\frac{3}{2^{5/3}}(\sqrt{3}+i)\Gamma_0\left(\tau - \frac{\xi}{v_{0b}}\right)^{2/3}\left(\frac{\xi}{v_{0b}}\right)^{1/3} - i\frac{\pi}{4}\right] & \text{for } 0 < \xi < v_{0b}\tau \\ 0\,, \quad \text{for } \xi > v_{0b}\tau \end{cases} \tag{5.16}$$

This equation evidences the spatiotemporal character of the solution, and the real part of the exponent, which dictates the growth of the instability, is plotted in Fig. 5.1 in solid lines at different times. These plots evidence the wave packet behaviour of the solution: at the beam front edge $\xi = 0$, as expected, the instability doesn't grow, and the "front" of the instability (the largest ξ at which the instability grows) propagates at the beam velocity. As will be clear later on, the presence of this "front" of the instability can be interpreted as a consequence of the localised initial conditions, since the perturbation needs to propagate from the initial position to the whole spatial extent of the system. Remarkably, the peak of the wave-packet, which propagates at $1/3$ of the beam velocity, has a temporal growth rate equal to the value found for the unbounded geometry (eq. (4.22)). At other unstable longitudinal positions, the temporal evolution is slower than the purely temporal growth rate dictated by the unbounded geometry.

If instead of a localised noise source, we assume the initial noise to be uniform all along the beam, i.e.

$$\delta\phi(\xi = 0, \tau) = \delta\phi(\xi > 0, \tau = 0) = S\,, \tag{5.17}$$

$$\partial_\tau[\delta\phi(\xi, \tau = 0)] = \partial_\tau^2[\delta\phi(\xi, \tau = 0)] = 0\,, \tag{5.18}$$

one can derive the following time asymptotic expression

$$\delta\phi(\xi, \tau) \approx \begin{cases} S_0 \exp\left[\frac{3}{2^{2/3}}\Gamma_0 \left(\tau - \frac{\xi}{v_{0b}}\right)^{2/3} \left(\frac{\xi}{v_{0b}}\right)^{1/3} e^{i\pi/6} - i\frac{\pi}{12}\right]\,, & 0 < \xi < v_{0b}\tau/3 \\ \frac{S}{3} \exp\left(\Gamma_0 \tau e^{i\pi/6}\right)\,, \quad \xi > v_{0b}\tau/3\,, & \end{cases} \tag{5.19}$$

where

$$S_0 = \frac{S}{2^{2/3}\sqrt{3\pi\Gamma_0}} \frac{(\tau - \xi/v_{0b})^{2/3}}{(\xi/v_{0b})^{1/6}(\tau - 3\xi/v_{ob})} \tag{5.20}$$

This solution for the uniform initial noise source (eq. (5.19)) also exhibits the spatiotemporal growth of the instability, and the real part of the leading exponential coincides with that of the Green function for $0 < \xi < v_{0b}\tau/3$, i.e. from front of the beam to the peak of the Green function. For $\xi \gtrsim v_{0b}\tau/3$ the solution for the uniform initial noise source differs from the Green function, exhibiting a purely temporal growth (no spatial dependance) at the maximum growth rate as derived in the unbounded geometry (eq. (4.22)).

Both solutions are depicted in Fig. 5.1, where the leading exponential contribution of both solutions is plotted for an arbitrary set of beam-plasma parameters. Whereas the Green function presents the typical impulse response of a system to a localised perturbation (with a local maximum of the wave packet localised at a given longitudinal position), if the initial noise source is homogeneously distributed along the beam a region where the instability grows purely temporally emerges. In this case there exists a localised transition between the spatiotemporal evolution and the purely temporal evolution. Remarkably, this transition happens at the same position as the peak of the Green function, i.e. $\xi = v_{0b}\tau/3$. Therefore, for a given beam longitudinal position ξ, initially the instability grows purely temporally at the maximum growth rate until the time $\tau = 3\,\xi/v_{0b}$ where the spatiotemporal evolution takes over, slowing its evolution compared to its initial purely temporal evolution.

Physically, the relevance of each solutions depends on the experimental conditions where the beam-plasma interaction takes place. The localised initial noise source should be of most

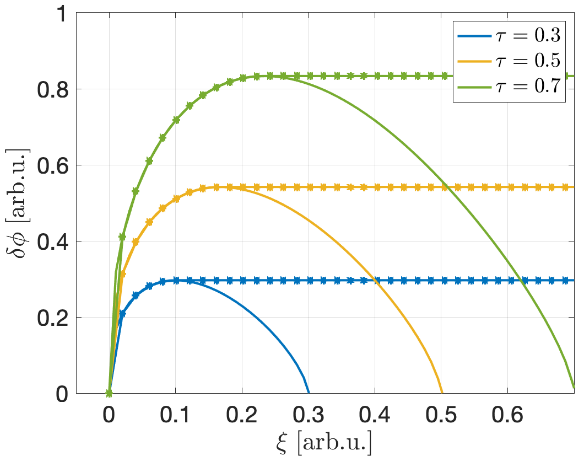

Fig. 5.1: Real exponential part of the solutions of the spatiotemporal differential equation for the slow-varying amplitude of the perturbed potential for the two different initial conditions considered in the text: localised noise source (solid line, eq. (5.16)) and uniform noise source along the beam (line with dots, eq. (5.19)). The beam front is placed at $\xi = 0$ and propagates towards negative ξ.

significance when the relativistic beam crosses a sharp vacuum-plasma boundary, whereas the uniformly distributed noise source should be of most significance when the beam is either created inside the plasma or when the beam enters the plasma through a long plasma density gradient (or ramp). Initially, the spatiotemporal dynamics of the TSI modes were worked out as the impulse response to a localised initial disturbance [104, 103]. To my knowledge, the first time that the uniformly distributed initial disturbance was proposed in a similar context was for the Forward Raman Scattering (RFS) and its spatiotemporal nature [106]. This approach was also used later to analyze the spatiotemporal dynamics of CFI modes [105]. Remarkably, for both RFS and CFI cases this choice of initial perturbation allows to derive an exact analytical solution to the corresponding spatiotemporal differential equation, which is not the case for OTSI since only time-asymptotic analytical expressions can be derived. Nevertheless, the exact analytical solution found for RFS and CFI with the uniformly distributed initial source shows a similar transition from the temporal to the spatiotemporal regime.

It is worth noticing that the transition from the purely temporal evolution to the slower spatiotemporal solution needs to be compared to the characteristic growth of the instability in order to know if most of the growth happens in the temporal or in spatiotemporal regime. For a relativistic beam, at a given longitudinal position ξ this transition happens at $\tau_\xi \approx 3\xi/c$, which is independent of the beam Lorentz factor γ_{0b}, whereas the growth rate $\Gamma_{\mathrm{OTSI}} \propto \gamma_{0b}^{-1/3}$. Therefore, for a large enough γ_{0b} the growth of the instability Γ_{OTSI} will be strongly reduced such that $\tau_\xi \ll \Gamma_{\mathrm{OTSI}}^{-1}$, and thus most of the evolution at this ξ location will be dictated by the spatiotemporal growth. This, as will be evidenced later, is relevant for experiments aiming at studying the ultra-relativistic regime of beam-plasma streaming instabilities, where oblique modes are dominant; the short bunch length of the particle beams delivered in high energy particle accelerator facilities leads the spatiotemporal regime to dominate most of the growth of the instability, which in turns mean that the overall growth rate is strongly reduced compared to the purely temporal evolution as computed with the unbounded geometry.

Finally, one also remarks that in the ultra-relativistic short beam case, where the instability is spatiotemporal, the two solutions found for different initial noise source distributions give the same evolution, since most of the growth will happen for $\xi < c\tau/3$, or in other words, the peak of the wave packet of the Green function will be "behind" the beam from the very beginning of the growth of instability.

5.1.2 PIC simulations of spatiotemporal evolution of beam-plasma instabilities

Particle-in-Cell (PIC) simulations (see App. A) are a powerful tool to study plasma streaming instabilities, allowing to model the kinetic nature of the process. Beam-plasma instabilities have been widely studied in the last decades using PIC simulations, and thanks to the recent development of computational tools such as massive parallel computation these simulations have been used to crosscheck the validity of the linear model and have motivated further investigations of the non-linear regime. In this section PIC simulation results are shown to evidence the spatiotemporal behaviour of OTSI modes for different beam-plasma configurations, showing an overall excellent agreement with the model presented in the previous chapter.

Indeed, it was the results of PIC simulations of a realistic ultra-relativistic beam-plasma system (FACET-II configuration, see Chap 6) which motivated the development of the spatiotemporal model derived in last section. These preliminary simulations, performed prior to the development of the OTSI spatiotemporal model, showed that the growth rate of an ultra-relativistic ($\gamma_{0b} = 2 \times 10^4$) gaussian beam of bunch length $\sigma_x < 10k_p^{-1}$ propagating in a uniform plasma of density $n_p = 10^{20}\,\mathrm{cm}^{-3}$ ($\alpha \approx 0.03$) was smaller than predicted by the theory of unbounded systems. At this time it was not clear that the reason behind was the spatiotemporal dynamics, since oblique modes share its transverse component with CFI modes and the spatiotemporal coupling of the latter is expected to vanish in the ultra-relativistic regime. These simulations also showed spatial dynamics on the instability evolution, but due to the beam gaussian profile they could have been attributed to the beam density gradients.

In order to shed more light on the issue, we performed a scan of 2D simulations where we changed the bunch length σ_x and kept the same $\gamma_{0b} = 2 \times 10^4$ and $\alpha = 0.03$ ($n_p = 10^{20}\,\mathrm{cm}^{-3}$). These beam-plasma parameters (γ_{0b} and α) were chosen to mimic the FACET-II experimental conditions. Transversely, an infinite flat beam profile was used, i.e. periodic boundary conditions (BC) were set along the transverse direction at the edge of the simulation window. Unless otherwise stated, absorbing BC for the fields and particles were used along the longitudinal boundaries of the window. The computational parameters are presented in App A. The results of this scan are depicted in Fig. 5.2.

Figure 5.2(a) displays a snapshot of the beam density modulations during the linear phase of the instability for different bunch lengths. For the bottom snapshot ($k_p\sigma_x = 10,\ c\tau = 3338k_p^{-1}$), the corresponding 2D spectrum of transverse electric field is shown in Fig. 5.2(b), exhibiting the typical spectrum of OTSI modes (see Fig. 4.2). For the infinite case ($k_p\sigma_x = \infty$, periodic BC also in the longitudinal direction) we observe that the beam density modulations have developed uniformly all over the beam profile. By contrast, for the finite bunch length cases, we observe a smaller level of modulation at the front (towards the left in the figure) than at the rear. The temporal evolution of the instability in each simulation is shown in Fig. 5.2(c), where the root-mean-squared (R.M.S.) amplitude of the transverse electric (solid lines) and magnetic (dashed lines) field evaluated around the longitudinal location of the peak beam density ($k_p\xi \in [100 - \sigma_x/2, 100 + \sigma_x/2]$) is plotted as a function of the beam propagation

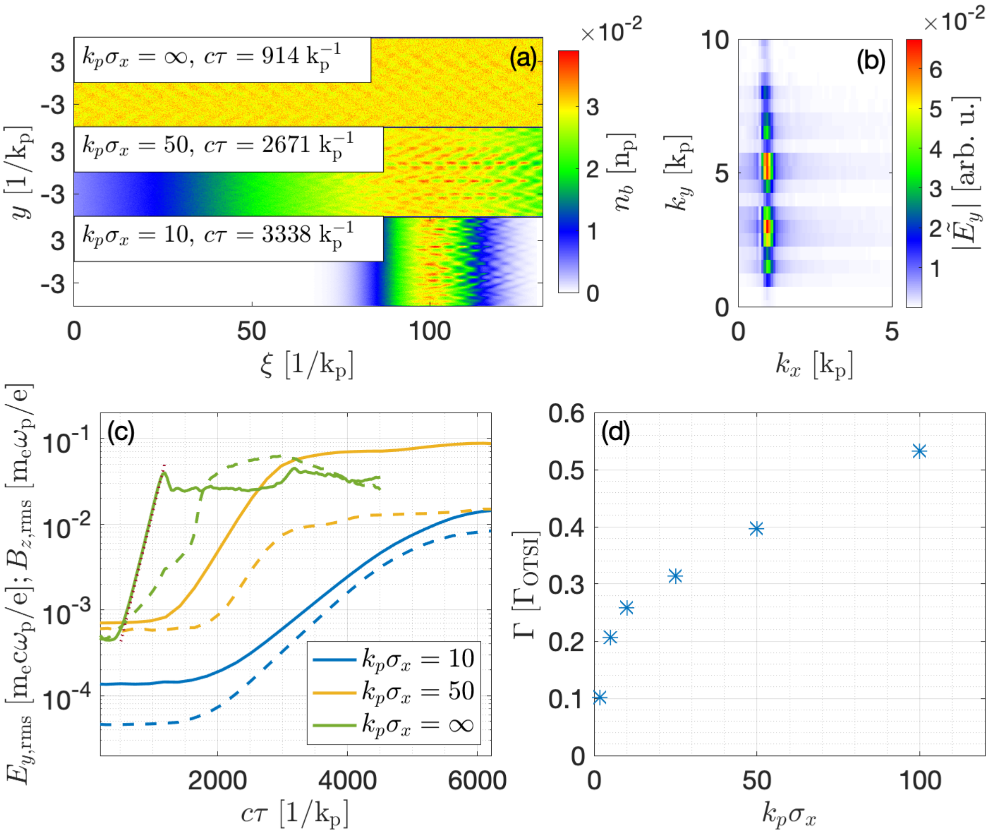

Fig. 5.2: Simulation results of the instability dynamics for ultra-relativistic ($\gamma_{0b} = 2 \times 10^4$), dilute ($\alpha = 0.03$) electron beams of several bunch lengths σ_x. (a) Snapshots of the beam density profile in the comoving coordinates $(\xi, \tau) = (v_b t - x, t)$ for different bunch lengths. (b) 2D Fourier spectrum of the E_y field modulations at $c\tau = 3338 k_p^{-1}$ for $k_p\sigma_x = 10$. (c) Transverse electric field $E_{y,\mathrm{rms}} = \langle E_y^2 \rangle^{1/2}$ (solid line) and magnetic field $B_{z,\mathrm{rms}} = \langle B_z^2 \rangle^{1/2}$ (dashed line), averaged over $\xi \in [\xi_{peak} - \sigma_x/2, \xi_{peak} + \sigma_x/2]$, as a function of the beam propagation distance in the plasma ($c\tau$) and the bunch length. The dotted line shows the theoretical growth of the OTSI, eq. (4.22), in the unbounded geometry. The evaluation of the dominant k_y in eq. (4.22) is carried out using the electrostatic result $\langle E_y^2 \rangle / \langle E_x^2 \rangle \simeq (k_y/k_p)^2$ (see text). (d) Effective growth rate ($\Gamma/\Gamma_{\mathrm{OTSI}}$) for different bunch lengths $k_p\sigma_x$ within the central slice of the beam (see text for details). Figure from Ref. [111].

distance $c\tau$. The evolution of the infinite beam case shows a fairly good agreement with the theoretical growth rate of an unbounded system Γ_{OTSI}, which is represented by the dotted line. The procedure to evaluate the dominant k_y required to estimate Γ_{OTSI} (eq. (4.22)) is discussed at the end of the section. Fig. 5.2(c) further confirms the electrostatic character of the dominant mode over magnetic modes ($E_{\mathrm{r.m.s.}} > B_{\mathrm{r.m.s.}}$). These results evidence the necessity to account for the spatial character of the instability in order to describe the linear growth of the unstable modes when a finite bunch length is considered.

In order to quantify an "effective" growth rate in the simulations with finite bunch length beams, an exponential fit to the evolution of the spectral amplitude of the dominant mode at the position of the peak beam density is performed. Figure 5.2(d) plots the resulting fitted growth rates normalized to Γ_{OTSI} as a function of the normalized bunch length $k_p\sigma_x$. It confirms that the shorter the beam, the slower the instability evolves, and even for beam with a spatial extent much larger than the typical spatial scale of the dominant mode ($k_p\sigma_x \gg 1$), there is a significant slow down compared to what is predicted for an unbounded system.

PIC simulation results shown in Fig. 5.2 motivated the development of the spatiotemporal theory of OTSI that was presented in Sec. 5.1. It should be noted that other studies had already performed and reported results on beam-plasma instabilities using PIC simulations with realistic finite ultra-relativistic beams [112, 113, 114] and in Ref. [115] the authors pointed out the lack of this spatiotemporal description in the scientific literature.

In order to validate the spatiotemporal model of OTSI via PIC simulations, we simulated a semi-infinite beam propagating in and through an uniform plasma of density $n_p = 10^{20}\,\mathrm{cm}^{-3}$. The simulation (moving) window extends from $\xi = -10\,\mu\mathrm{m}$ ($\approx -25k_p^{-1}$) to $\xi = 160\,\mu\mathrm{m}$ ($300k_p^{-1}$), with periodic BC in the transverse direction and absorbing BC in the longitudinal. The beam, propagating towards negative ξ and with the front placed at $\xi = 0$, has a uniform density $n_b = 0.03n_p$ for $\xi \geq 0$. For charged particle beams, the sharp beam edge has the inconvenience of exciting longitudinal plasma waves as the beam propagates through the plasma. These plasma waves can interact with the instability and complicate the analysis, so at a first instance these semi-infinite simulations were performed with a neutral pair e^+e^- beam, often called fireball beams. Yet, at a later time in Sec. 5.1, simulation results with an electron beam are shown and discussed. Note that the model applies for both charged and neutral beams, and that n_b refers to the total particle density.

In the derivation of the solutions of the spatiotemporal model the effect of the initial noise distribution has been extensively discussed. In PIC simulations it is challenging to precisely control the distribution of the initial noise due to the numerical noise inherent to the nature of the algorithm. Furthermore, in the PIC code CALDER the use of a moving window implies that the plasma needs to be initialise outside the initial window, and therefore the beam cannot be created inside the plasma. In order to approach to the uniformly distributed initial noise configuration, and to suppress the effect of the numerical noise created at a sharp entrance of a relativistic beam in the plasma, the beam is propagated ballistically during the entrance. In this way the initial noise (numerical and physical) has time to homogenise throughout the beam before the beam particles are let free to evolve, which will set the time $\tau = 0$.

Under this configuration, PIC simulation results with $\alpha = 0.06$ and $\gamma = 2 \times 10^4$ are shown in Fig. 5.3. The spectral amplitude $|\widetilde{E}_y(k_x, k_y)|$ of the dominant mode $k_y = 3k_p$ is plotted as a function of τ for different ξ-slices in Fig. 5.3(a) and as a function of ξ at different τ in Fig. 5.3(b). In these figures, the dashed lines represent the exponential term of the OTSI spatiotemporal solution (eq. (5.19)). Good agreement is found in the two cases. These two

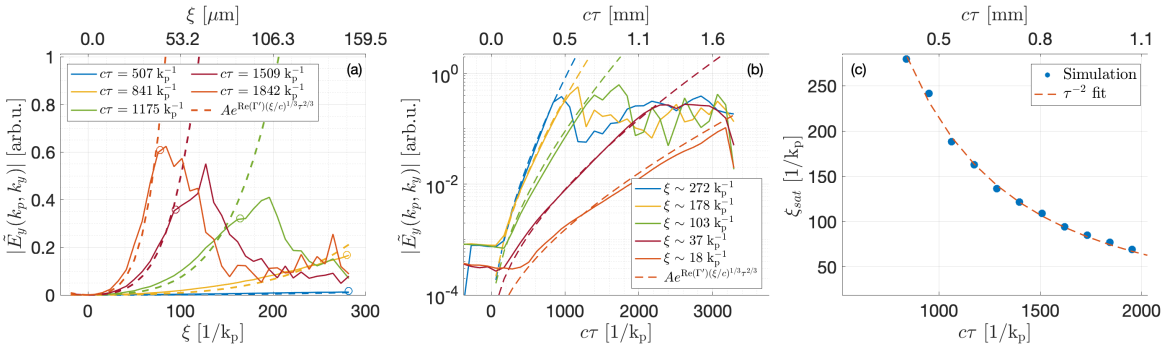

Fig. 5.3: 2D PIC simulations of the OTSI induced by a step-like e^-e^+ pair beam and comparison with linear theory in the spatiotemporal regime for $\gamma_{0b} = 2 \times 10^4$. (a) Spectral amplitude $|\widetilde{E}_y(k_x, k_y)|$ of the dominant oblique mode ($k_x = k_p$, $k_y \simeq 3k_p$) as a function of ξ for different propagation distances $c\tau$. (b): Same quantity but as a function of $c\tau$ for different beam slices ξ. In (a) and (b), the simulation data (solid lines) is fitted to the theoretical law $A\exp[(3/2^{2/3})\Gamma_{\mathrm{OTSI}}(\xi/c)^{1/3}\tau^{2/3}]$ for $\xi \leq \xi_{\mathrm{sat}}$ (dashed lines). (c) Saturation position ξ_{sat} [also shown in (a) as circles] vs. $c\tau$ (filled circles), compared with the theoretical expectation $\xi_{\mathrm{sat}} \propto \tau^{-2}$ (red dashed line). Figures from Ref. [111].

plots (Fig. 5.3(a) and Fig. 5.3(b)) evidence the deviation from the purely temporal exponential evolution.

Assuming that the instability saturates at the same amplitude at different longitudinal positions ξ, one can estimate that, at a given time τ, the smallest saturated longitudinal slice ξ_{sat} should scale as τ^{-2} due to the $\xi^{1/3}\tau^{2/3}$ dependance of the exponential of eq. (5.19). In the simulations, the ξ_{sat} positions are estimated by looking at the ξ-profile of the spectral amplitude at each τ, and are represented in Fig. 5.3(a) as circles. Figure 5.3(c) shows these ξ_{sat} positions as a function of τ, exhibiting the expected τ^{-2} scaling as indicated by the good agreement with the τ^{-2} fit (dashed line).

The validity of the aforementioned assumption about the saturation is not trivial and should not be taken for granted since saturation mechanisms involve non-linear effects which are not addressed here. Still, in Sec. 5.3 some of these mechanisms are discussed, together with its relation with the spatiotemporal dynamics of the instability.

This semi-infinite simulation with $\gamma_{0b} = 2 \times 10^4$ shows an overall excellent agreement with the $\exp(\tau^{2/3}\xi^{1/3})$ spatiotemporal term. Since for this configuration, relevant for FACET-II experiments, $c\Gamma_{\mathrm{OTSI}}^{-1} \approx 131k_p^{-1}$, which is of the same order of magnitude of the longitudinal size of the window, the purely temporal solution that would happen at early times and at the rear is not visible due to the non-negligible noise levels. On the other hand, the large γ_{0b} factor facilitates the direct comparison with the time asymptotic solutions, the instability being slow enough to still grow at $\tau \gg \xi/v_{0b}$.

In order to observe the purely temporal regime at earlier times, a new simulation was performed with the same geometry but $\gamma_{0b} = 20$, i.e. three orders of magnitude smaller. This increases the growth rate of the unbounded geometry by one order of magnitude, allowing to observe the purely temporal growth for propagation distances $c\tau < 3\xi$. This is shown in Fig. 5.4(a), where the spectral amplitude of the dominant mode along the window is plotted at different propagation distances $c\tau$. A uniform growth along $\xi > 100k_p^{-1}$ is retrieved, at approximatively the temporal growth rate Γ_{OTSI} as evidenced by the dashed lines of Fig. 5.4(a),

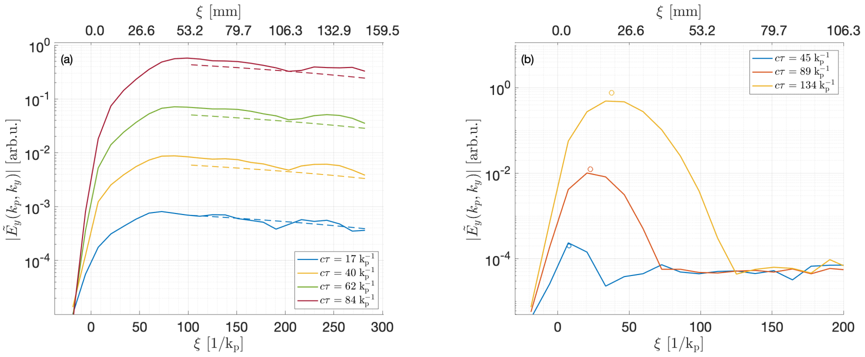

Fig. 5.4: 2D PIC simulations of the OTSI induced by a step-like e^-e^+ pair beam and comparison with linear theory in the spatiotemporal regime for $\gamma_{0b} = 20$. Spectral amplitude $|\widetilde{E}_y(k_x, k_y)|$ of the dominant oblique mode ($k_x = k_p$, $k_y \simeq 3k_p$) as a function of ξ for different propagation distances $c\tau$ with ballistic propagation for beam particles at the beam entrance (a) and without ballistic propagation (b). Dashed lines in (a) plot the theoretical temporal growth of $|\widetilde{E}_y(k_p, 3k_p)|$ at different times $c\tau \geq 17\mathrm{k_p^{-1}}$. Circles in (b) display the temporal growth of the initial (blue) circle propagating at $c/3$. Figure (a) from Ref. [111].

which represent the purely temporal amplification of the initial amplitude level given by blue dashed line (linear fit of the initial $c\tau = 17k_p^{-1}$ spectral amplitude). In this simulation, the dominant mode is found at a slightly lower transverse wave vector $k_y \approx 2.5k_p$. Note that, despite the ballistic entrance of the beam into the plasma, there is still some remaining non-uniformity in the initial noise amplitude along the beam, which starts at $\xi \approx 0$, i.e. at the beam front, raises from the beam front to $\xi \approx 80k_p^{-}1$ and then slightly decreases. Another side effect of the initial noise distribution is the reduced dynamic range that we can observe in the simulation, which as will be shown later is further reduced if we consider a non-neutral beam.

Finally, the same simulation was performed using the semi-infinite beam geometry and $\gamma_{0b} = 20$, but without the ballistic initial propagation of the beam particles and thus fully accounting for the beam entrance in a plasma with a sharp ramp. This is meant to be equivalent the localised initial noise source at the beam front entrance, and therefore an impulse-like response is expected. The results of this simulation are plotted in Fig. 5.4(b), which displays the same quantity as Fig. 5.4(a). Indeed, an impulse Green function response is found, and as expected from theory the peak of the wave packet propagates at roughly $v_{0b}/3$ and its amplitude grows at roughly the temporal growth rate Γ_{OTSI}, as shown by the circles of Fig. 5.4(b). This further confirms our physical interpretation of the two initial conditions considered to solve the spatiotemporal model of the OTSI: the localised initial noise is relevant for configurations where the beam enters a sharp vacuum-plasma boundary, whereas the uniform initial noise distributions applies to beam created or unfrozen in the plasma. The configuration of the beam entering the plasma through a plasma density gradient was not considered in the simulations with this semi-infinite geometry. The reason, as it will become clear in the Sec. 5.2, is that for non-neutral beams the finite transverse size of the beam brings a new phenomena into play, the transverse wakefield excitation, which for some configurations can lead to a severe beam self-focusing before the instability develops and thus quench the instability.

For illustrative purposes, the same simulations with the ballistic beam entrance were performed for an e^- beam and the results are shown in Fig. 5.5. A good agreement between

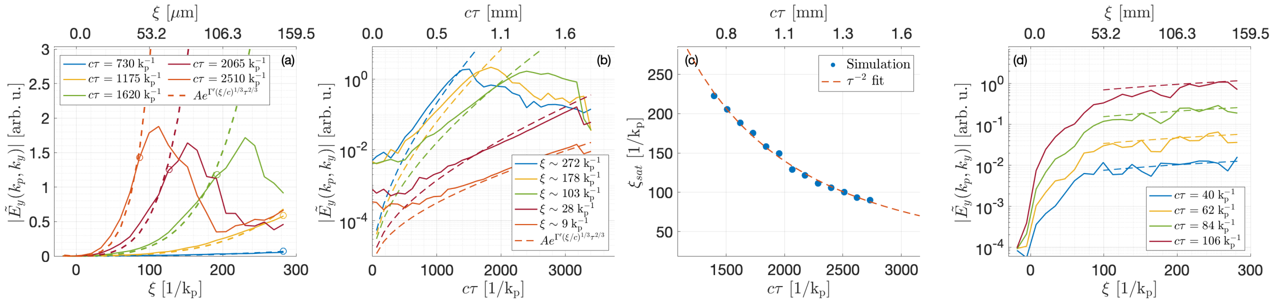

Fig. 5.5: (a,b,c) Same figures as Fig. 5.3 but with an electron beam ($\alpha = 0.03$) instead of a neutral pair beam ($\alpha = 0.06$). (d) Same figure as Fig. 5.4(a) but with an electron beam instead of a neutral pair beam. Figures from the SM of Ref. [111].

simulations and theory can also be observed, but due to the higher initial noise level (approximatively one order of magnitude) the comparison is less accurate than for a neutral beam.

To finish this section, it is worth discussing about effect of temperature and spectra of these PIC simulations and the analysis shown below. First, the evaluation of the dominant mode whose amplitude is plotted in the figures of this section is carried out by using the electrostatic result $k_y = \sqrt{\frac{\int_{\rm OTSI} |\widetilde{E_y}(k_x,k_y)|^2}{\int_{\rm OTSI} |\widetilde{E_x}(k_x,k_y)|^2}}$, where the integrals are carried out over the spectral OTSI domaine $0.5k_p < k_x < 3$ and $0.8k_p < k_y < 8$. This definition of the OTSI domain, even if it is somehow arbitrary, is meant to isolate the OTSI contribution from other unstable modes (TSI, CFI) and from the longitudinal plasma wave. In our simulations this evaluation gives a dominant electrostatic OTSI mode k_y between $2k_p$ and $3k_p$, which is in good agreement with the spectral maximum shown in Fig. 5.2(b) and approximatively validates the $k_y \gg k_p$ assumption made in the derivation of the spatiotemporal model.

Theoretically, the cold fluid model predicts the dominant mode to be at $k_y \to \infty$. This is clearly not retrieved in the simulations, and two reasons can explain this discrepancy. First of all, the space discretisation limits the maximum k-mode that can be simulated. The better the resolution, the higher k-mode can be resolved. Furthermore, our simulation include a high frequency filtering module which dumps the high frequencies present in the simulated currents and the fields (see App. A for details), which further reduces the highest k-vector that can be resolved.

On the other hand, the kinetic description used in PIC simulations brings temperature effects into play. For the plasma species, plasma electrons are initialised with a temperature of 10 eV (maxwellian distribution). For beam particles, the relativistic transverse momentum spread can be expressed as $\Delta p = \gamma\,\Delta\theta$, where $\Delta\theta = \Delta p_y/p_x$ is the angular spread which is set to $\Delta\theta \approx 30\,\mu$rad. Longitudinally, beam particles are initialised with zero longitudinal momentum spread. These values are relevant for the expected FACET-II experimental conditions (see Chap. 6).

To check if these temperatures can significantly affect the fluid results, one can apply the qualitative criterium of eq (4.31). Doing so for the beam electrons one obtains that temperature effects start to be important for wave numbers higher than $k_y = \frac{\Gamma_{\rm obl}}{c\theta} \approx 262k_p^{-1}$ $(2622k_p^{-1})$ for $\gamma_{0b} = 2 \times 10^4$ (20), and therefore temperature effects should not play a significant role in the interaction.

To summarise this discussion, one can conclude that the unstable spectrum obtained in the simulations shown in this section suffers from computational effects at high frequencies, which restricts the valid spectral domain to somehow low frequencies ($|k| \lesssim 5k_p$). Temperature effects are expected to be negligible as long as no significant heating occurs during the linear phase, which is validated by the simulation results. Nevertheless, the quasi-flat spectrum obtained in the fluid approximation for $k_y > 2k_p$ indicates that our simulations with limited spatial resolution are able to capture the fastest temporal scale Γ_{obl} at which the dominant mode would grow.

5.1.3 Extrapolation and implications of the spatiotemporal model to finite bunch length systems

The good agreement with the model found in the simulations for the different beam-plasma configurations reinforces the hypothesis that the spatiotemporal dynamics are responsible for the bunch length dependent growth rate observed in the first set of simulations with gaussian beam longitudinal profiles (see Fig. 5.2). Nevertheless the model assumes a semi-infinite flat beam profile which is far from realistic experimental conditions. The main problem of trying to apply the spatiotemporal model derived in this manuscript to gaussian beams originates from the absence of a proper beam front, i.e. a $\xi = 0$ at which beam electrons only encounter fresh plasma as they propagate.

Rather than trying to generalise our model to an arbitrary beam profile, we use our semi-infinite model and make a correspondence between the ξ value in our model and the value of σ_x for a gaussian longitudinal beam profile, and using the peak beam density for n_b. To find the right correspondence, the simulated temporal evolution of the instability around the peak longitudinal position is compared to the model by fitting the oblique spectral energy $\epsilon = \int_{0.8k_p}^{5k_p} dk_x \int_{0.8k_p}^{8k_p} dk_y |\tilde{E}_y(k_x, k_y)|^2$ to the expected $\propto \exp[\Gamma_{\mathrm{OTSI}}(\frac{\xi_{fit}}{v_{0b}})^{1/3}\tau^{2/3}]$, where ξ_{fit} is the fitting variable and $n_b = n_{b,peak}$ is used to evaluate Γ_{OTSI}. The result of this fit is shown in Fig. 5.6 for two cases, indicating that for a gaussian beam the instability at the density peak position evolves as $\propto \exp[\Gamma_{\mathrm{OTSI}}(\frac{1.3\sigma_x}{v_{0b}})^{1/3}\tau^{2/3}]$. The correspondence $\xi = 1.3\sigma_x$ is actually very close to the integral $\int_{-\infty}^{\xi_{peak}} f(\xi)d\xi \approx 1.25\sigma_x$ for a gaussian distribution $f(\xi)$ centered at ξ_{peak}, of amplitude 1 and standard deviation σ_x. This suggests that the $\Gamma_{\mathrm{OTSI}}\,\xi^{1/3}\tau^{2/3} \propto (n_b\xi)^{1/3}$ dependence in the exponential of the spatiotemporal model for a semi-infinite beam would potentially need to be substituted by $\left(\int_{-\infty}^{\xi} n_b(\xi')d\xi'\right)^{1/3}$ to model an arbitrary beam density profile. This last consideration is still hypothetical, and a spatiotemporal model for an arbitrary longitudinal beam profile would be required. Note that, if confirmed, this would indicate that the aforementioned "effective" growth rate would be determined by the total beam charge rather than by the beam peak density, and therefore the same overall growth rate would be retrieved for different bunch lengths σ_x and if the total charge Q was the same. Remarkably, the latter has been confirmed by PIC simulations not shown in this manuscript.

The spatiotemporal evolution of the OTSI modes with finite bunch length has the important effect of slowing down the growth of the instability. This reduction of the growth can have significant consequences in experiments exploring the ultra-relativistic beam-plasma instabilities and needs to be accounted for in the design of the experiment and interpretation of the experimental data. Furthermore, it is also important to account for this phenomenon when OTSI interplays with other physical processes. For example, Sec. 5.2 is devoted to the interplay between beam self-focusing due to plasma wakefield excitation and the OTSI, putting

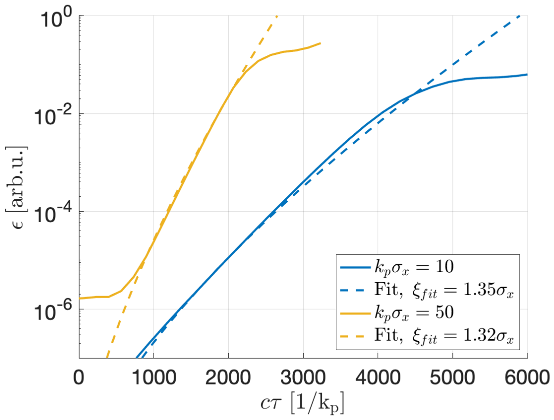

Fig. 5.6: Temporal evolution of the spectral energy of the oblique modes at the longitudinal position of the beam density peak for finite bunch length ($k_p\sigma_x$) simulations (solid lines). Dashed lines correspond to a least-squares fit of the evolution of the spectral densities to the dominant exponential term of the spatiotemporal model $\propto \exp[\Gamma_{\mathrm{OTSI}}(\frac{\xi_{fit}}{v_{0b}})^{1/3}\tau^{2/3}]$ where ξ_{fit} is the fitted variable.

in evidence the relevance of the spatiotemporal evolution. There is yet another interplay which has been studied assuming a purely temporal evolution of the OTSI and that could potentially need to be revisited for the finite bunch length scenario: the interplay (or hierarchy) between CFI and OTSI. In the purely temporal regime, the analysis of this interplay is often carried out by comparing the linear temporal growth rates Γ_{obl} and Γ_{CFI} [116]. As stated in Ref. [112], restricting the analysis to the diluted-beam regime, we have

$$\frac{\Gamma_{\mathrm{obl}}}{\Gamma_{\mathrm{CFI}}} = \frac{\sqrt{3}}{2^{4/3}}\frac{1}{\beta_{0b}}\left(\frac{\gamma_{0b}}{\alpha}\right)^{1/6} \tag{5.21}$$

which leads to the already mentioned conclusion that oblique modes are faster than CFI modes and therefore dominate the linear phase of the instability. Nevertheless, once oblique modes saturate, the slower CFI modes can still develop and dominate the non-linear phase [5, 117].

The comparison of the linear growth rates is not valid if one accounts for the spatiotemporal dynamics, since the growth does not have the form $\exp(\Gamma\tau)$. For this purpose, a more appropriate comparison can be done by taking the time needed for a given beam slice to experience a certain number N_{exp} of exponentiations, which for OTSI is the ultra-relativistic regime reads

$$\tau_{\mathrm{Obl}} = 2\left(\frac{N_{\mathrm{exp}}}{3\Gamma_{\mathrm{OTSI}}}\right)^{3/2}\left(\frac{v_{0b}}{\xi}\right)^{1/2}, \tag{5.22}$$

For CFI, since no spatiotemporal effects are expected in the ultra-relativistic regime [105], $\tau_{\mathrm{CFI}} = N_{\mathrm{exp}}\Gamma_{\mathrm{CFI}}^{-1}$, and therefore

$$\frac{\tau_{\mathrm{Obl}}}{\tau_{\mathrm{CFI}}} \propto \sqrt{\frac{N_{\mathrm{exp}}}{k_p\xi}}, \tag{5.23}$$

Note that, unlike in eq. (5.21), oblique modes dominate when this ratio is smaller than unity. Remarkably, in the ultra-relativistic diluted-beam regime the interplay of these two modes is independent of α and γ_{0b}, and is only dictated by the longitudinal position $k_p\xi$. Doing the substitution $\xi \to 1.3\sigma_x$ based on the previous discussion, this would mean that for short enough beams CFI could dominate over oblique modes in the ultra-relativistic diluted-beam regime. Stating a value of the bunch length for which the transition occurs is out of the scope of the manuscript, since more physics would need to be take into account to accurately predict this transition. Namely, the initial noise level of each mode could be different and a specific number of exponentiations would need to be chosen. In our simulations, we have observed that for short beams $k_p\sigma_x \lesssim 5$ indeed the magnetic and the electric field amplitude is comparable, and they evolve very similarly. Nevertheless, it is not clear to us that our OTSI model nor the CFI model remain valid for these configurations: at $k_p\sigma_x \sim 1$ the plasma does not have time to respond and neutralise the beam charge and current all along the beam.

5.2 Interplay between wakefield excitation and beam-plasma instabilities

Section 5.1 was devoted to the spatiotemporal dynamics of the dominant OTSI in a relativistic beam-plasma system when a finite (or semi-finite) bunch length is considered. In this section we also include the finite transverse size of the beam and discuss its implications for the development of beam-plasma instabilities in realistic systems.

As long the beam can be considered transversely homogenous over the typical transverse scale of the dominant unstable mode, larger scales non-uniformities in the transverse density profile are not expected to modify the linear spatiotemporal evolution of the instability, apart from the fact that at different transverse positions the growth rate $\Gamma \propto n_b(\xi, r)^{1/3}$ takes different values. However, similar to the longitudinal wakefields excited by a non-neutral finite bunch length beam, transverse wakefields are excited when a non-neutral beam of finite transverse size is considered. To study the interplay between wakefields and the instability, only pure e^- beams with bi-gaussian density profiles will be considered.

As discussed in Chap. 1, longitudinal wakefields have a net decelerating effect on the driving electron beam, whereas transverse wakefields have a net focusing effect. The wakefields excited in a beam-plasma system subject to streaming instabilities are typically much weaker than in PWFA configurations since beams with $k_p\sigma_x > 1$ and $k_p\sigma_r > 1$ are required, which sets the beam parameters out of the resonant condition for wakefield excitation (see Sec. 1.2.2). Yet, these wakefields act on the beam as soon as the beam enters the plasma whereas the unstable fields need to be amplified to have a significant impact on the beam dynamics. A competition then occurs between the dynamics induced by the wakefield and the instability. The result of this competition depends on the beam-plasma configuration under which the beam-plasma interaction takes place. Several of these configurations, all in the relativistic regime, are analyzed in this section.

5.2.1 Diluted-beam regime with uniform plasma

The first configuration for which this competition or interplay is studied is a diluted finite beam ($\alpha < 1$) propagating in a uniform plasma. In this regime, the wakefields can be described by the linear theory, and OTSI modes dominate linear phase of the beam-plasma instability. Longitudinally, non-resonant longitudinal wakefields can potentially shape the energy spectrum, but typically they are too weak to cause any significant energy loss. Therefore, other than modifying the initial noise amplitude of the unstable fields, no significant effect from the longitudinal wakefields is expected on the evolution of the instability.

In contrast to longitudinal wakefields, transverse wakefields and the associated self-focusing dynamics can have a significant effect in this regime for low angular spread (or emittance) beams. The self-focusing dynamics can be described as follows: initial transverse wakefields immediately impart a focusing dynamic on the beam; the focusing effect leads to an increase of the peak beam density, which in its turn leads to the excitation of stronger wakefields; these stronger wakefields impart a more severe focusing on the beam, establishing a positive feedback loop until emittance prevents further focusing. In this way the interplay between the self-focusing dynamics and the instability can have two major effects on the development of the instability. On the one hand, the self-focusing creates a correlated transverse momentum spread which can have an effect on the orientation of the dominant unstable mode (see Fig. 5.7(k)). On the other hand, the increase of n_b due to self-focusing increases α and reduces $k_p\sigma_r$, favouring the transition from excitation of linear wakefields to non-linear wakefields in which ultimately plasma electrons are fully expelled out by the electron beam and don't flow through the beam, quenching the beam-plasma instability (see Fig. 5.7(d)).

The interplay between self-focusing dynamics and the instability is depicted in Fig. 5.7. In this figure, results from PIC simulations of three beam-plasma configurations are displayed. The beam propagates ballistically during the entrance. The three beam-plasma configurations, which are chosen to be relevant for FACET-II experiments, correspond to the same electron beam parameters propagating in uniform plasma of three different densities $n_p = 1$, 2.5 and $5 \times 10^{19}\,\mathrm{cm}^{-3}$. Beam parameters are 10 GeV ($\gamma_b = 2 \times 10^4$), $\sigma_x = 5\ \mu\mathrm{m}$, $\epsilon_n = 3\,\mathrm{mm\,mrad}$, and a beam peak density $n_b \simeq 1.5 \times 10^{18}\,\mathrm{cm}^{-3}$ (i.e., $\alpha \simeq 0.15$, 0.06 and 0.03), corresponding in 3D to a total charge of $Q \approx 2\,\mathrm{nC}$. For each configuration, the same simulation is also performed for a transversely uniform and infinite beam (i.e. periodic BC are used in the transverse direction) to suppress the transverse wakefield excitation and self-focusing dynamics.

For each configuration, four snapshots at different propagation distances are displayed to show the evolution of the beam. The corresponding transverse phase-spaces (y, p_y) of the beam slice indicated by the blue dashed line on the beam profiles are displayed as an inset plot. At $n_p = 10^{19}\,\mathrm{cm}^{-3}$, it is clear that the self-focusing dynamics dominate the interaction for the finite beam case, quenching the instability that indeed develops in the equivalent transversely infinite beam simulation. At $n_p = 2.5 \times 10^{19}\,\mathrm{cm}^{-3}$ the self-focusing effect is slower, mainly visible in the transverse phase-space (see inset plot of Fig. 5.7(j)). At this density the linear phase of instability is not quenched as at $n_p = 10^{19}\,\mathrm{cm}^{-3}$, but yet a slight difference in the orientation of the beam modulations is observed between the finite case (Fig. 5.7(k)) and the transversely infinite case (Fig. 5.7(o)). The effect of transverse wakefields is more visible when comparing the non-linear stage of the finite beam case (Fig. 5.7(l)) with the transversely infinite beam case (Fig. 5.7(p)), where a strong central filament is only present in the finite case due to the cumulated self-focusing effect. Finally, at $n_p = 5 \times 10^{19}\,\mathrm{cm}^{-3}$, no significant self-focusing effect is observed and the instability dynamics are revealed equivalent in both the finite and transversely infinite beam simulation.

Quantitatively, this interplay can be examined by comparing the characteristic time scales of each phenomenon. The time scale of the dominant OTSI mode, accounting for the spatiotemporal dynamics, is given by τ_{OTSI} as derived in eq. (5.22) evaluated at $\xi = 1.3\sigma_x$ (based on the last discussion of the Sec. 5.1.3) and for $N_{\mathrm{exp}} = 5$. This number of exponentiations is equivalent to the dynamic range of the unstable fields observed in our simulations. For the self-focusing dynamics, the time scale of the process can be evaluated by the inverse betatron frequency ω_β^{-1} (see Sec. 1.3.2), where the transverse wakefield is evaluated numerically using

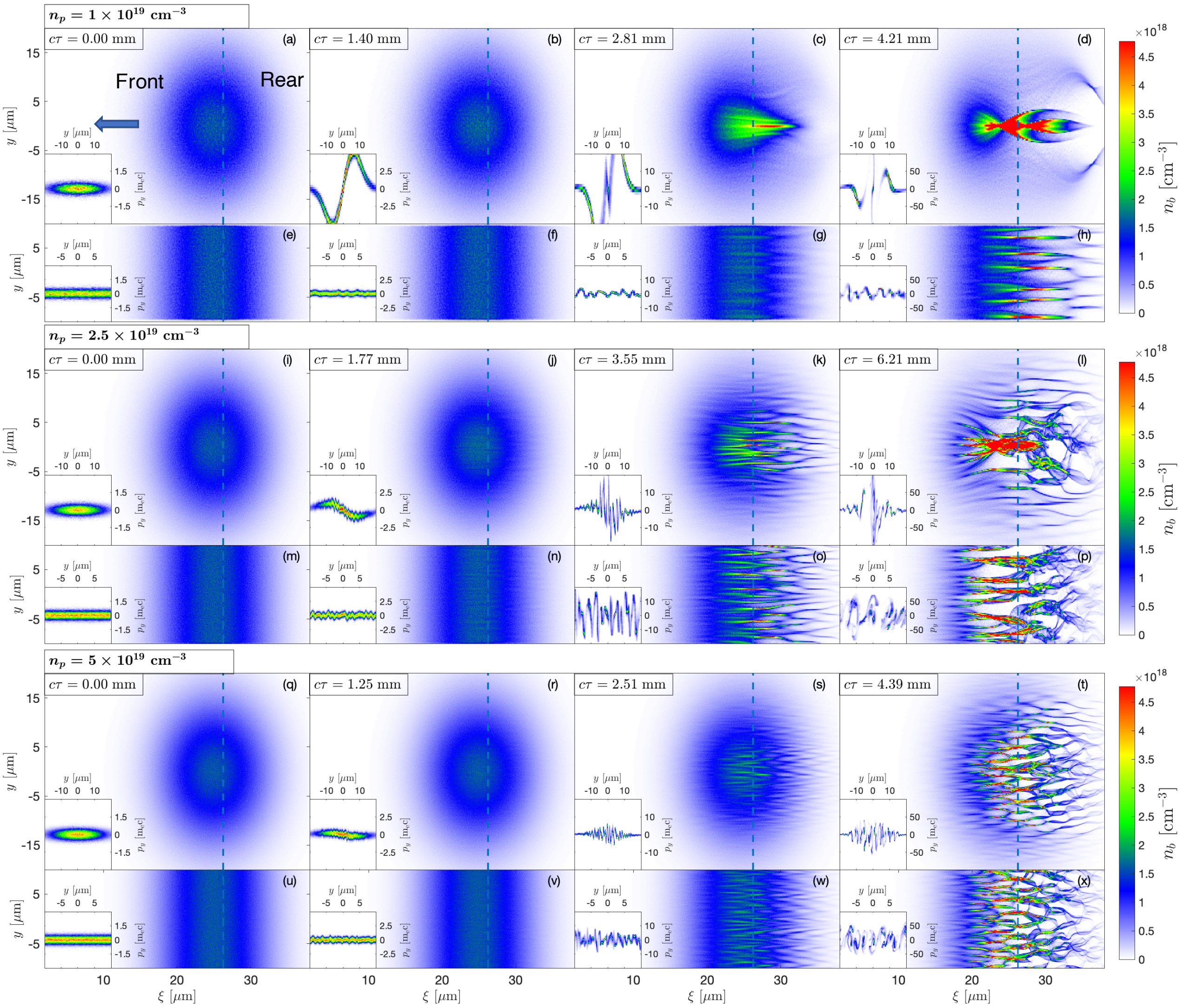

Fig. 5.7: Simulated electron beam density maps at different propagation distances in a uniform plasma of density $n_p = 10^19\ \mathrm{cm}^{-3}$ [(a)-(h)], $2.5 \times 10^{19}\ \mathrm{cm}^{-3}$ [(i)-(p)], and $5 \times 10^{19}\ \mathrm{cm}^{-3}$ [(q)-(x)]. The transverse beam profile is taken to be either finite with $\sigma_r = 10\ \mu$m RMS width [(a)-(d), (i)-(l), and (q)-(t)] or infinite, i.e., with transverse periodic boundary conditions [(e)-(h), (m)-(p), and (i)-(x)]. In all cases, the beam has a 10 GeV energy ($\gamma_b = 2 \times 10^4$), a Gaussian longitudinal profile with $\sigma_x = 5\ \mu$m RMS length, a transverse normalized emittance $\epsilon_n = 3$ mm mrad, and a peak density $n_b \simeq 1.5 \times 10^{18}\ \mathrm{cm}^{-3}$ [i.e., $\alpha \simeq 0.15$ for (a)-(f),$\alpha \simeq 0.06$ for (g)-(l), and $\alpha \simeq 0.03$ for (m)-(r)], which would correspond to a total beam charge of 2 nC in 3D. The insets show the transverse beam phase space along the slices indicated by the dashed blue lines.

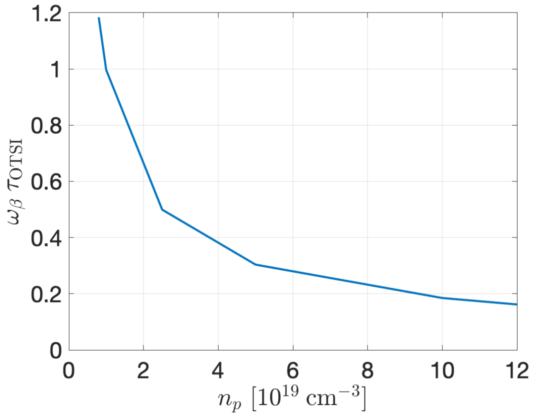

Fig. 5.8: Ratio of the characteristic time scales of the OTSI ($\tau_{\rm OTSI}$) and beam self-focusing (ω_β^{-1}) in the ultra-relativistic beam limit. Beam parameters are the same as in Fig. 5.7 Figure from the SM of Ref. [111].

eq. (1.15) and eq. (1.16) at the beam central slice.

For the beam-plasma parameters shown in Fig. 5.7, the ratio between these two timescales is plotted in Fig. 5.8, showing that for a given set of beam parameters the plasma density n_p dictates if the interaction is dominated by wakefield dynamics or instability dynamics. Furthermore, this ratio also predicts the transition to happen around $n_p \approx 10^{19}$ cm^{-3}, so that at $n_p \leq 10^{19}$ cm^{-3} the instability is quenched by the self-focusing effect. This value is in good agreement with the simulation results showed in Fig. 5.7.

Indeed, increasing the plasma density reveals to be the most efficient way to favour the instability with respect to the self-focusing, since it decreases $\tau_{\rm OTSI}$ and increases ω_β^{-1}. Both phenomena have the same scaling with respect to γ_{0b}, so the interplay is independent of the beam energy. Varying the beam density leads to equal first-order[1] variations for both time scales, ($\tau_{\rm OTSI} \propto 1/\sqrt{n_b}$ and $\omega_\beta^{-1} \propto 1/\sqrt{n_b}$). Accounting for second order contributions both timescales follow similar trends when changing n_b. Accounting for the full ω_β^{-1} scaling, one finds that in order to favour the instability over the wakefield dynamics one needs to decrease the beam density, which experimentally can be done by either decreasing the total charge or increasing the beam dimensions.

For experimental purposes it is useful to consider a fixed beam charge and vary the beam dimensions. We have discussed that in this case the growth of the instability at the beam density peak is presumably independent of the bunch length σ_x. The transverse wakefield amplitude seen by the bunch depends on the bunch length: for beams with bunch length $k_p\sigma_x > 1$, the shortest the beam the higher the peak beam density, and therefore the stronger the wakefields. Therefore moving away from this value tends to favour the instability over the self-focusing dynamics. The same applies for beams with $k_p\sigma_x \lesssim 1$, i.e. shorter beams drive stronger wakefields, but the largest wakefield amplitude will at some point not be seen by the beam since it will be "behind" the beam. Furthermore for a given charge going to very short beams might not be compatible, as discussed before, with the excitation of OTSI modes since one might enter the $\alpha > 1$ regime. It should also be noted that in this regime a different analysis needs to be carried out for the wakefield dynamics. Overall, this indicates that going above

---

[1] Ignoring the $k_p\sigma_r$ dependance inside the modified Bessel functions in eq. (1.15) and eq. (1.16)

$k_p\sigma_x > 1$ is a better choice to favour OTSI versus the self-focusing effect in the diluted-beam regime. The case $k_p\sigma_x \lesssim 1$ might be interesting if the strong wakefields are indeed not seen by the beam, potentially allowing to reach the $\alpha \lesssim 1$ regime for a given charge. Yet, since the current models of charged beam-plasma instabilities are not expected to hold in this regime (see last paragraph of Sec. 5.1.3). Concerning the beam transverse size σ_r, it mainly affects both time scales via $n_b \propto \sigma_r^{-2}$, and therefore an equivalent scaling applies to both timescales.

Finally, one could also consider to increase the beam emittance (or transverse momentum spread) to decrease the self-focusing effect. Though, an increase of beam emittance (or beam transverse temperature) would also be detrimental for the instability. Comparing the scaling of both phenomena is out of the scope if this manuscript, since thermal effects have not been taken into account so far. Nevertheless, intuitively we would require a very large increase of the beam emittances so as to oppose to the self-focusing effect associated to plasma wakefields. Typically, the emittance should be increased to have a beta function of the order of the scale of the self-focusing dynamics, that is mm scale, which is not achievable by an accelerator facility such as FACET-II.

5.2.2 Beam-diluted regime with plasma density gradient at the plasma boundaries

Plasma density gradients (or ramps) at the boundaries of a plasma target have already been discussed in this manuscript in the context of PWFA and beam matching in Sec. 1.3.2, showing that the beam transverse dynamics in plasma gradients associated to the excited wakefields is a complex topic that is usually assessed via simulations. In this section only ramps that are relevant for FACET-II experimental conditions will be analyzed. As it will be explained in Chap. 6, the gas density plasmas produced at FACET-II are expected to have ramps with gradient lengths in the 0.5 - 2 mm range. To illustrate the effect of the ramps, only linear density gradients will be considered here.

The effect of the ramps is depicted in Fig. 5.9. In this figure, PIC simulation results show the effect of adding a linear ramp of different length on the $n_p = 5 \times 10^{19}$ cm^{-3} beam-plasma configuration of Fig. 5.7 (bottom raw). For this beam-plasma configuration, linear wakefields turned out to have a negligible effect on the instability dynamics when a uniform plasma was considered. In these simulations beam particles are not frozen at the entrance, and the propagation distance $c\tau = 0$ is defined as the beginning of the uniform plasma region. Figure 5.9(a) shows the correlation $\langle y p_y \rangle$ of the beam transverse phase, and Fig. 5.9(b) shows the phase-advance $\phi = \int \omega_\beta(\tau) d\tau$ computed from the simulated transverse wakefield. The $\langle y p_y \rangle$ correlation reflects the focusing inertia imparted by the transverse wakefields on the beam, whereas the phase-advance represents the focusing phase of the beam: being initially zero, a phase-advance of $\phi = \frac{\pi}{2}$ corresponds to a fully focused beam. It is clear from the simulated evolution of both quantities (Fig. 5.9(a-b)) that the longer the length of the gradient the stronger the self-focusing effect is.

In the transverse phase-space correlation one observes two different evolutions in the ramp: initially there is a fast evolution which slows down as the beam gets closer to the uniform plasma region. This suggests that the main self-focusing effect occurs at the beginning of the ramp, i.e. when $n_b \gtrsim n_p$ and non-linear wakefields are excited. Shortening the overall length of the gradient decreases the part where $n_b \gtrsim n_p$, and therefore less severe focusing is obtained.

Figure 5.9(c-j) show snapshots of the beam density profile at two propagation distances. Together with the inset plots, where the ξ-integrated transverse phase-space is displayed, they

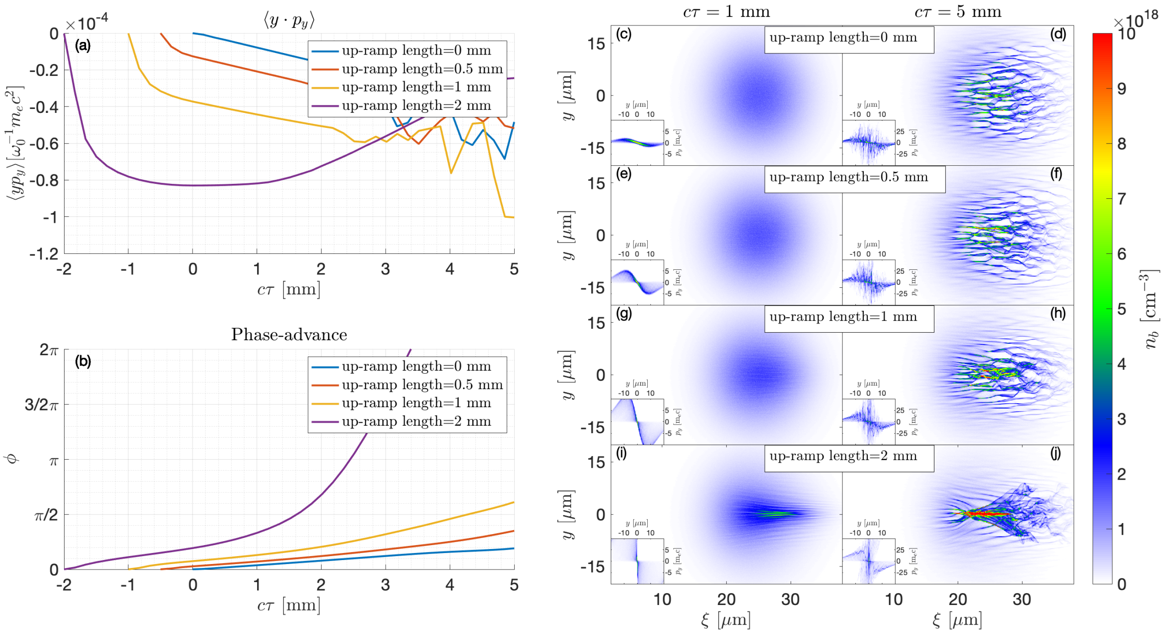

Fig. 5.9: Simulated transverse phase-space correlation $\langle yp_y \rangle$ (a) and phase-advance $\phi = \int \omega_\beta(\tau) d\tau$ as a function of propagation distance for different length scales of linear ramp. (c-j) Corresponding beam profiles and transverse phase-spaces at $ct = 1$ mm (left column) and $ct = 5$ mm (right column). In all plots, $c\tau = 0$ corresponds to the end of the up-ramp.

evidence the increasing self-focusing experienced by the electron beam as the linear density gradient gets longer. For this beam-plasma configuration a linear gradient length of ~ 2 mm at the plasma entrance severely quenches the instability.

Deriving a model to describe the self-focusing dynamics in a plasma ramp for the beam-plasma systems under consideration is not a trivial task, the main complexity being the fact that the model should account for both the initial non-linear excitation of wakefields and the later linear excitation. This kind of models have already been derived for purely non-linear wakefield excitations [51, 52], which benefits from the linear focusing force present in the ion cavity. Though, they could only be analytically solved for a reduced number of density profiles.

Linear density gradients are typically far from being realistic, but they provide a good qualitative understanding of the role of ramps at the entrance of the plasma target. One could argue that in any realistic plasma density gradient there will always be a main region where the gradient is strong and can be approximatively described by a linear ramp. This intuitive reasoning does not hold in many cases, and this is due to the strong focusing of non-linear wakefields at low plasma densities: if a sharp density gradient is preceded by a long almost uniform low-density region, the main focusing effect will happen in the long low-density region. Therefore a proper control of the focusing in the plasma not only requires to control the main gradient length but also the preceding low-density region, which in experiments can be challenging to measure.

5.3 Quasi-static approach to ultra-relativistic beam-plasma instabilities

This section of the chapter presents preliminary results on applying the quasi-static formalism to model beam-plasma instabilities. The quasi-static approximation consists in assuming that there are two different time-scales that dictate the evolution of the system: a short time-scale and a long time-scale. This approach allows to describe the short time-scale processes neglecting long term evolutions. In a relativistic beam-plasma interaction, due to the different γ factor of each specie, the quasi-static approximations usually comes down to assuming that the evolution of plasma electrons happens at much shorter timescales than beam electrons.

In Sec. 1 this approach is used to model the wakefield excited by a relativistic electron beam by neglecting the ∂_τ derivatives in the plasma equation of motion, given that $\partial_\xi \gg \partial_\tau$ (note that $\xi = v_{0b}t - x$, so neglecting ∂_τ does not mean that the temporal evolution of the system is zero). It should be noted that this approximation has already been applied for other spatiotemporal analysis of plasma instabilities [106, 105].

On the other hand, the derivation of plasma wakefields of Sec. 1.2 only resolves the short-scale ξ evolution of the plasma and of the fields, but not the "long-scale" τ evolution of the beam. This approach is not valid to model the linear growth of a beam-plasma instability since it is the coupled motion of both species (plasma and beam electrons) which enables the exponential growth of the instability. Nevertheless, this approach, i.e. looking at the linear plasma response and associated electromagnetic fields for a given density perturbation, could still be used to retrieve interesting characteristics of the evolution of the system. Results from preliminary investigations in this direction are not presented in this manuscript, but under certain conditions they have provided accurate predictions of the field amplitude at saturation when compared to PIC simulations.

5.3.1 Linear phase of OTSI under the quasi-static approximation

The quasi-static approximation applies to plasma electrons, for which the ∂_τ derivatives are neglected. In the co-moving variables ξ, τ the equation of motion and continuity of plasma electrons are written as

$$(\partial_\tau + v_{0b}\partial_\xi)\begin{bmatrix} v_{px}^{(1)} \\ v_{py}^{(1)} \end{bmatrix} = \begin{bmatrix} -\partial_\xi \phi^{(1)} \\ \partial_y \phi^{(1)} \end{bmatrix} \tag{5.24}$$

$$(\partial_\tau + v_{b0}\partial_\xi)\, n_p^{(1)} + n_p^{(0)} \left(-\partial_\xi v_{px}^{(1)} + \partial_y v_{py}^{(1)}\right) = 0\,. \tag{5.25}$$

Neglecting ∂_τ and putting together both equations leads to

$$v_{0b}^2 \partial_\xi^2 n_p^{(1)} = -n_p^{(0)} \left[\partial_\xi^2 + \partial_y^2\right] \phi^{(1)} \tag{5.26}$$

which is the quasi-static version of eq. (4.14). The rest of the derivation is equivalent to what has been done in the Chap. 4. Using the beam equation (4.13) and Poisson equation one finds

$$\left[(\partial_\xi^2 + \partial_y^2)\partial_\tau^2(v_{0b}^2\partial_\xi^2 + n_p^{(0)}) + n_b^{(0)}\left(\frac{\partial_\xi^2}{\gamma_{0b}^3} + \frac{\partial_y^2}{\gamma_{0b}}\right) v_{0b}^2 \partial_\xi^2\right] \phi^{(1)} = 0 \tag{5.27}$$

Writing $\phi^{(1)} = \delta\phi(\xi,\tau)\exp(-ik_0\xi + ik_y y)$ and using the slowly-varying amplitude approximation (eq. (5.8)) one finds

$$[v_{0b}\partial_\tau^2\partial_\xi + i\Gamma_0^3]\delta\phi(\xi,\tau) = 0 \tag{5.28}$$

As in [106, 105], one finds that the quasi-static approximation is equivalent to neglecting the purely temporal derivative (∂_τ^3 for OTSI) of the "full" differential equation (5.11). The following expression is a time asymptotic solution for eq. (5.28)

$$\delta\phi(\tau,\xi) \propto \exp\left(\frac{2^{2/3}}{3}e^{i\pi/6}\Gamma_0\tau^{2/3}\xi^{1/3}\right) \tag{5.29}$$

We observe the same spatiotemporal leading exponential term as without the quasi-static approximation. This analytical result shows that the quasi-static description of the system can be fully relevant to describe the spatiotemporal regime of OTSI.

5.4 Ponderomotive saturation of ultra-relativistic beam-plasma instabilities

This last section of Chap. 5 focuses on the non-linear phase of the OTSI, mainly trying to identify the saturation mechanisms in the ultra-relativistic scenario. A beam-plasma instability is expected to saturate as electrons get trapped in the unstable wave. When all the electrons of one specie are trapped, the mode can no longer couple to the density modulations and therefore the growth is quenched. For the longitudinal TSI, the phase velocity of the most unstable mode is very close to the beam velocity, and therefore beam electrons get trapped first. For CFI, the phase velocity of the unstable modes is zero, so both beam and plasma electrons get trap at the same rate. For the mixed OTSI modes, the electrostatic approximation results in non-zero phase velocities but slower than for the longitudinal two-stream modes. Using the fluid electrostatic theory in the unbounded geometry gives a phase velocity $v_\phi \approx 0.33c$ for FACET-II-like parameters, very similar to what has been reported in Ref. [118] for mid-relativistic beams. In this publication, they also reported that due to the lower phase-space velocity they observed in their simulations a significant trapping of both beam and plasma electrons at saturation. In our simulations of the ultra-relativistic spatiotemporal beam-plasma instability, we have also observed this strong plasma modulations (trapping) at saturation, at a similar modulation level as beam electrons. In this section we propose a non-linear mechanism that can contribute to the strong plasma modulations observed in some of our simulations. This mechanism, based on the second-order ponderomotive effect, arises due to the superposition of two unstable modes with the same wave vector but of opposite transverse direction.

The ponderomotive force driven by an oscillating electric field E experienced by a particle of mass m and charge e can be written as

$$\mathbf{F}_{\text{pond}} = -\frac{e^2}{4m\omega^2}\nabla(E^2) \tag{5.30}$$

where ω denotes the frequency of the oscillating field. On the other hand, the superposition of two OTSI modes with opposite transverse wave vectors, which is schematically shown in Fig. 5.10, results in a transversely stationary quincunx-shape pattern responsible for the ponderomotive effect. Mathematically, we have that $E_y \sim \sin(k_px + k_yy - \omega_pt) + \sin(k_px - k_yy - \omega_pt+\theta) \sim 2\sin(k_p - \omega_pt+\theta/2)\cos(k_yy-\theta/2)$, whose squared transverse gradient is non-zero and thus originates a ponderomotive force. Since $\partial_y < E_y^2 >_t \sim \sin(2k_yy-\theta)$, the ponderomotive

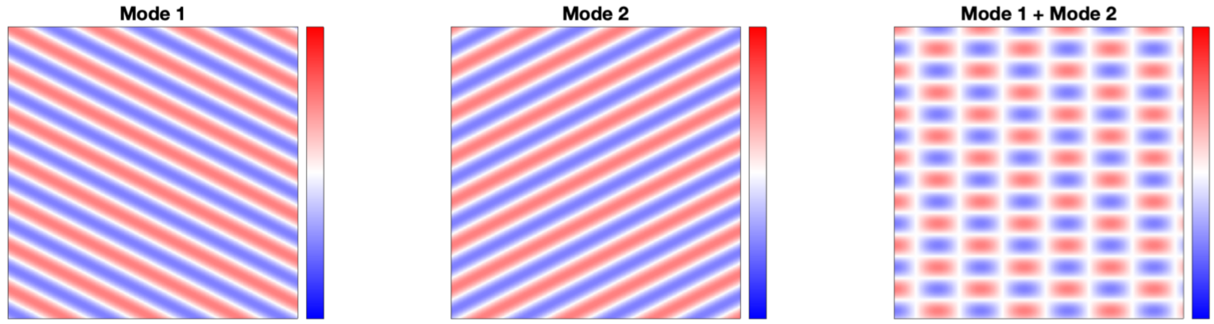

Fig. 5.10: Schematics of two oblique modes and its superposition.

effect gives rise to transverse modulations at twice the frequency of the dominant linear OTSI mode with zero transverse phase velocity.

This force is a second order effect since it involves the square of the perturbed field, and therefore cannot be captured in linear models. However, once the linear modes have developed enough so that the quincunx structure is built up, the ponderomotive force will impart transverse modulations on the plasma density that will become important when approaching the nonlinear phase, and can become the dominant contribution for the creation of phase-space holes in the nonlinear saturation phase.

The presence of the ponderomotive effect is observed in the PIC simulations that were performed to validate the linear model of OTSI, both in the infinite and in the semi-infinite geometries. As depicted in Fig. 5.11, which shows PIC simulation results in the semi-infinite geometry and $\alpha = 0.03$, $\gamma_{0b} = 2 \times 10^4$, at a distance of $\xi \approx 110$ μm behind the beam front, the initial beam and plasma density modulations are imparted by the dominant OTSI modes, but then the second order transverse ponderomotive effect takes over and dominates the plasma density modulations.

In order to assess if the ponderomotive effect is the main process driving the saturation of OTSI modes, we compare the evolution of each contribution (by computing the spectral energy of the beam and plasma modulations) with the evolution of the dominant OTSI mode. The definition of the spectral domain of each phenomena (OTSI and ponderomotive) used for the computation of spectral energies is based on the obtained spectra (Fig. 5.11(f)) and is $k_x \in (0.8k_p, 2k_p)$, $k_y \in (0.8k_p, 8k_p)$ for OTSI and $k_x \in (0, 0.8k_p)$, $k_y > 5k_p$ for the ponderomotive effect. It has been checked that small variations of these boundaries, which are indeed somewhat arbitrary, do not modify significantly the final results.

The results of this analysis are displayed in Fig. 5.12. The contribution of each specie is depicted for three beam-plasma configurations: $\alpha = 0.03$ and $\gamma_{0b} \approx 2 \times 10^4$ (a), $\alpha = 0.003$ and $\gamma_{0b} \approx 2 \times 10^4$ (b), and $\alpha = 0.03$ and $\gamma_{0b} \approx 20$ (c). These simulations are carried out in the semi-infinite geometry with the beam frozen at the entrance in the plasma, and the quantities are evaluated at the rear of the window ($\xi \approx 200k_p^{-1}$), in the region that is displayed in Fig. 5.11. Note that in order to compare the contribution from each different specie the densities are normalized to their initial (unperturbed) values. In all cases we observe the onset of the ponderomotive contribution later than the OTSI but roughly twice faster, as expected from the squared dependence of the ponderomotive force. Moreover, the evolution of the transverse electric field E_y in the OTSI mode (solid blue line) follows very closely the evolution

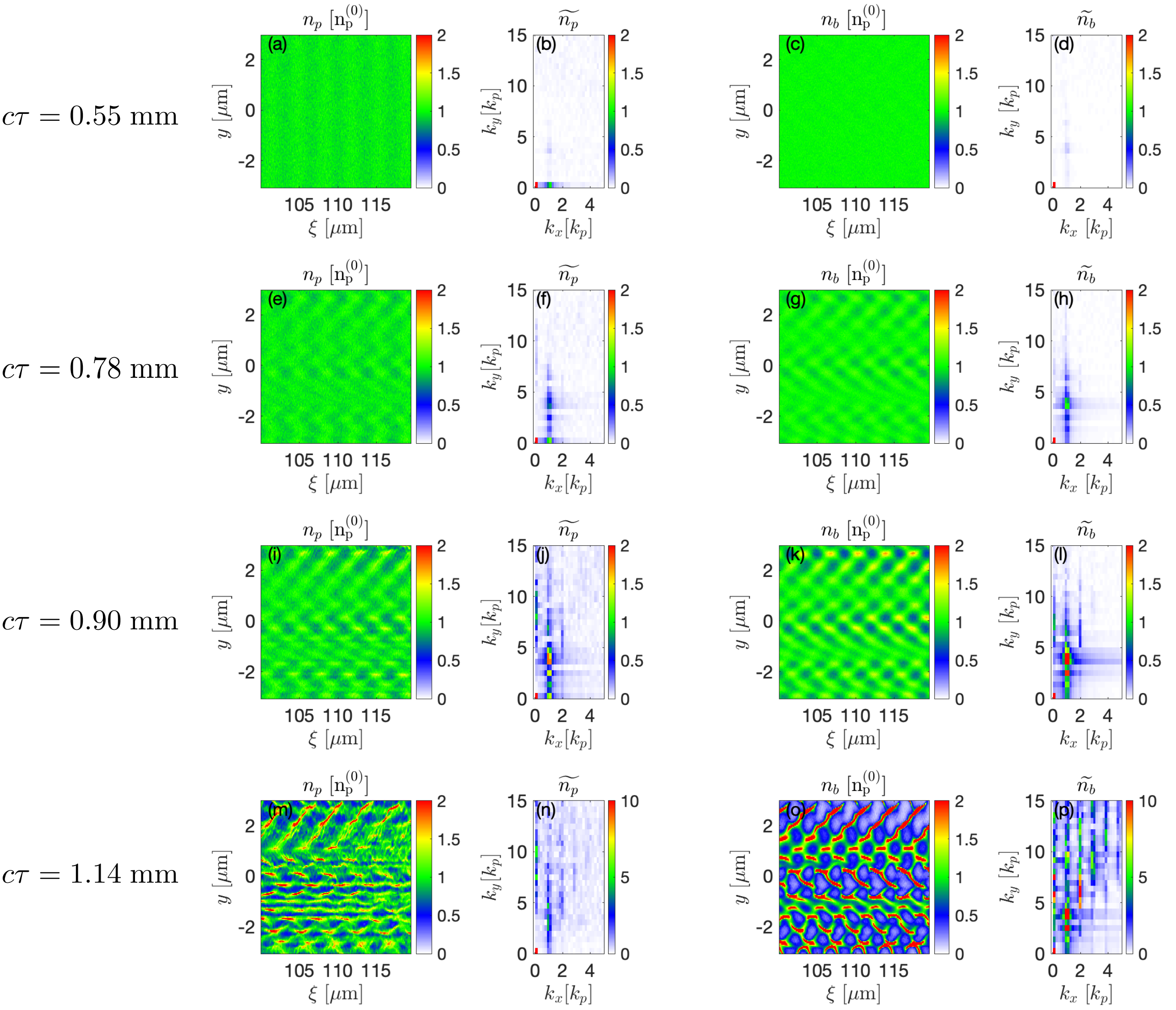

Fig. 5.11: Simulated plasma (a,e,i,m) and beam (c,g,k,o) density distributions normalized to its initial value, together with the corresponding 2D Fourier spectra (b,f,j,n) for the plasma and (d,h,l,p) for the beam. Each raw correspond to a different propagation distances. These distributions are obtained from a PIC simulation with the semi-infinite geometry, but only a smaller window at ≈ 110 μm behind the beam front is plotted. Other beam plasma parameters are $\alpha = 0.03$ ($n_p = 10^{20}$ cm^{-3}) and $\gamma_{0b} = 2 \times 10^4$.

of the oblique plasma modulation in all cases. Yet, this does not mean that the plasma dictates the saturation. Figure 5.12(d) shows the evolution of the maximum electric field E_y amplitude for each case. We now analyze each case separately.

The first case $\alpha = 0.03$ and $\gamma_{0b} \approx 2 \times 10^4$ (a) is the same simulation showed in Fig. 5.11. As stated before, we observe in this case that the ponderomotive contribution of plasma modulations takes over the plasma density oblique contribution. Moreover, after saturation of the E_y OTSI mode, the oblique beam density modulations still grow but a slower rate and not coupled to the OTSI mode. This indicates that the ponderomotive effect acting on plasma electrons prevents the plasma oblique modulation to grow further and therefore stops the growth of the instability.

We can also compute the electrostatic field driven by a transverse plasma modulation of $\Delta n_p = n_p^{(0)} = 10^{20}$ cm^{-3} with a transverse wave vector k_y, we obtain

$$E_{y,\max} \approx \frac{E_0}{\sqrt{1 + \left(\frac{k_y}{k_p}\right)^2}} \tag{5.31}$$

where E_0 is the wave-breaking field. Remarkably, inserting the ponderomotive wave vector $k_y = 6k_p$, i.e. twice that of the dominant OTSI, we obtain $E_{y,\max} \approx 0.16E_0$, which is very close to the value observed in the simulation at saturation (Fig. 5.12(d)). For the same beam-plasma parameters but in the unbounded geometry (not shown here), a similar evolution occurs near saturation and the same amplitude is found at saturation.

The second case corresponds to a more diluted beam ($\alpha = 0.003$) but still ultra-relativistic ($\gamma_{0b} \approx 2 \times 10^4$). Looking at the evolution of each contribution (Fig. 5.12(b)), it seems clear that the beam density modulations are the first to saturate, with the oblique contribution dominating over the ponderomotive. The saturation of the beam density modulations lead to a slow down of the growth of all the other contributions and of the dominant OTSI mode. Yet, there is some remaining growth in the plasma density modulations and in the field, which drives the dominant OTSI mode to grow further after the saturation of beam density modulations. This could be due to the spatiotemporal character of the OTSI: since we are evaluating the fields and the densities at the rear of the beam, after the saturation of beam density modulations at the rear the instability is still developing at the front, and therefore plasma modulations at the rear can be amplified by the bunch train formation at the front, leading to a further growth of the modulations. Two arguments tend to support this interpretation: first, a fully periodic simulation (i.e. with unbounded geometry) with the same beam-plasma parameters shows significantly different dynamics at saturation, with the ponderomotive contribution of plasma electrons clearly dominating the evolution at saturation and with an amplitude at saturation of approximatively one order of magnitude lower than in the semi-infinite geometry. It should be noted though that significant ion motion is observed in this simulation, which makes more complicated the comparison. The second argument is based on the spatiotemporal analysis of the saturation in the semi-inifinite geometry, which shows higher saturation amplitudes at the rear (around a factor of 2) than at the front, which would indicate that there is a coherence effect allowing to build up stronger plasma oscillations at the rear than at the front. Yet, these simulations, which are a clear proof of different saturation dynamics under different geometries (infinite vs semi-infinite), deserve further scrutiny to elucidate the mechanisms involved in the saturation of the OTSI.

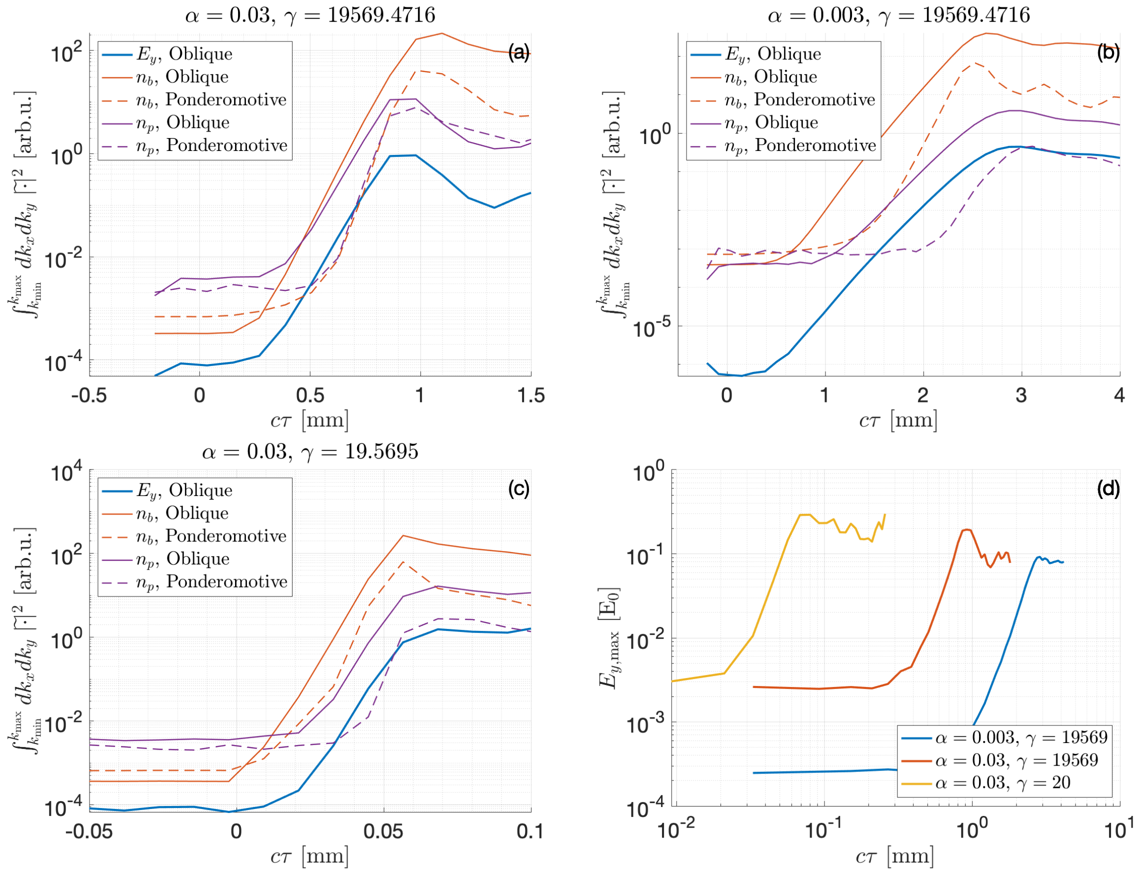

Fig. 5.12: Plasma density spectral energies contributions in the oblique domain (blue) and in the ponderomotive (orange) domain. Exponential fits for each case within the exponential growth are plotted in dashed lines.

Finally, the third case corresponds to the less diluted ($\alpha = 0.03$) and mildly relativistic ($\gamma_{0b} \approx 20$) beam. As expected, both species react very similarly and couple equally to the dominant OTSI mode. Both species probably contribute equally to the saturation, and due to the fast growth the ponderomotive contribution does not have time to significantly modulate the densities of the species. Very similar behaviour is found in the corresponding simulation with the unbounded geometry.

To summarise this last section of the chapter, we have identified a new second-order mechanism that can contribute to the saturation of OTSI modes in the ultra-relativistic limit: a ponderomotive effect arising from the superposition of two modes with opposite transverse wave vector. This mechanism contribute to the strong plasma density modulations (phase-space holes) observed in simulations, but differ from the simple particle trapping in the unstable wave. Through PIC simulations, we have shown the presence of these mechanisms for some beam-plasma configurations and we have tried to identify regimes where they dominate at saturation. Importantly, the presence of these non-linear processes needs to be confirmed in 3D simulations.

6. E305 EXPERIMENT AT FACET-II

This chapter is devoted to the design and implementation of a multi-year experimental program, the E305 experiment, aiming at probing the ultra-relativistic regime of beam-plasma instabilities using particles beams delivered by a high energy particle accelerator. This project was conceived at the very beginning of my PhD as an international collaboration lead by my group at LOA, and became a big part of my research activities during these years. The strategy was to use the new accelerator facility FACET-II at SLAC National Accelerator Laboratory, which at that time had just finalise the design studies, notably with the goal of exploring the feasibility of using the instability as a novel chain of gamma ray production, as was shortly before suggested by *Benedetti et al.* [119]. Moreover, as explained in Chap. 4, these beam-plasma instabilities have strong implications in astrophysics, and the ultra-relativistic regime remains largely unexplored experimentally.

The FACET-II facility is interesting to perform this experiment because it was designed to produce high peak current particle beams, which is expected to maximise the gamma-ray yield produced during the beam-plasma instability. Furthermore, at FACET the beam-plasma interaction had already been extensively studied in the context of PWFA, so they had an important expertise with the implementation of plasma targets in an accelerator environment. The E305 collaboration, named after the acronym used for the experiment, was created and brought together experts in theory, simulations and experiments in the field of beam-plasma interaction.

The project was divided in two main parts, corresponding to the two different plasma sources installed in the experimental area: E305-gas, which would study the onset of the beam-plasma instability in an optically ionised plasma produced with the help of a gas jet, and E305-solid, which would study the instability in a solid target (foil) ionised by the beam itself and/or carrying free electrons (conductors). Apart from having different plasma targets, this division also concerns the type of physics involved for each interaction: in a gaseous density plasma ($n_p \lesssim 10^{20}\,\mathrm{cm}^{-3}$), collisions are not expected to play a major role and at FACET-II the $\alpha \approx 1$ regime could presumably be explored (see Sec. 6.3). On the other hand, in a solid density plasma ($n_p \approx 10^{23}\,\mathrm{cm}^{-3}$), collisions could potentially play a significant role and only the $\alpha \ll 1$ regime can be studied at FACET-II.

I have mainly worked in the context of E305-gas, i.e. collisionless beam-plasma instabilities in the $\alpha \lesssim 1$ regime. Before discussing my contributions to the E305-gas project, which are presented in the upcoming sections, I would like to comment some qualitative features that make E305-solid different to E305-gas and that have enabled the discovery of interesting processes based on the relativistic beam-solid plasma interaction. First of all, the role of collisions has never been studied in the ultra-relativistic regime of beam-plasma instabilities, and most of the work has been done for CFI modes in the context of ICF [120, 121]. As expected, they show that the role of collisions for a given beam-plasma configuration depends on the beam and plasma temperature. When we tried to perform PIC simulations to know how relevant collisions are for the FACET-II configurations, we immediately realised that the initial "cold" temperature of plasma electrons in the solid made the collisional module of our PIC code unreliable, since it was not designed to this end. Hence the E305-solid experiment can potentially be a first test for new or adpated collisional modules used in PIC simulations for low plasma temperatures. As a first approximation to the effect of collisions on the beam-plasma instability, we performed several simulations under these conditions where we artificially modify the collisional frequency in the code. In these simulations we observed interesting phenomena, namely an interesting spatio-temporal interplay of CFI and OTSI modes which depends on the collisional frequency and which is still under study. Furthermore, these simulations showed a very strong transverse force at the sharp entrance of the electron beam in the solid. After close inspection, this force turned out to originate from the beam self-field reflection on the surface of the solid, similarly to the Transition Radiation process. Thanks to the focusing effect of this force on the electron beam, this process can be used to tightly focus an electron beam and reach several orders of magnitude larger peak beam densities, enabling the creation of relativistic beams with peak densities comparable to solid densities [122].

All this physics is out of reach at gas plasma densities: collisions are negligible at these densities and due to the density gradients at the boundaries (gas expanding in vacuum) the self-fields of the beam are not effectively reflected. Yet, at the available gas-density plasma, the $\alpha \approx 1$ regime could potentially be explored, a regime where the gamma-ray production via the beam-plasma instability is expected to reach the highest efficiency. In this chapter the first section starts with an overview of the E305 experimental set-up and the base-line beam parameters for the E305 experiment. The second chapter shows simulation results where we scan beam and plasma parameters and estimate how the main experimental observables depend on the different configurations.

6.1 E305-gas experimental set-up

The implementation of a plasma target in the beamline of a particle accelerator is often a complicated task due to the ultra high vacuum requirements for the accelerator to operate. In most beam-plasma interaction experiments there are windows that separate the accelerator beamline from the interaction point. These windows need to be thin in order not to significantly distort the beam propagation, and they can set important limitations to the beam peak current that can go through. An alternative solution is to use differential pumping to pump out all the gas released in the IP and avoid contamination of the beamline. This solution will be implemented at FACET-II, allowing the beam to interact with the plasma target directly from the beamline.

In terms of the plasma target, the choice was to use a gas jet and a laser pulse to ionise the released gas. This choice has several advantages: gas compounds can be changed without access to the accelerator hall, and it allows to easily modify the plasma density from shot to shot. One of the main drawbacks is that it relies on a laser system to ionise the gas, which is not the case for a capillary discharge plasma target. The plasma sources based on gas targets are very often used in laser facilities in the context of LWFA. In beam-driven PWFA experiments, long plasma targets are generally required, whereas gas jets are usually limited to millimeter scales, and therefore plasma cells (or ovens) are preferably used. Furthermore, plasma densities ranging from $10^{17}\,\mathrm{cm}^{-3}$ to $10^{20}\,\mathrm{cm}^{-3}$ can be obtained using gas jets, which is a very convenient range for the typical peak beam densities of $n_b \sim 10^{18}\,\mathrm{cm}^{-3}$ expected at FACET-II [4]. Finally,

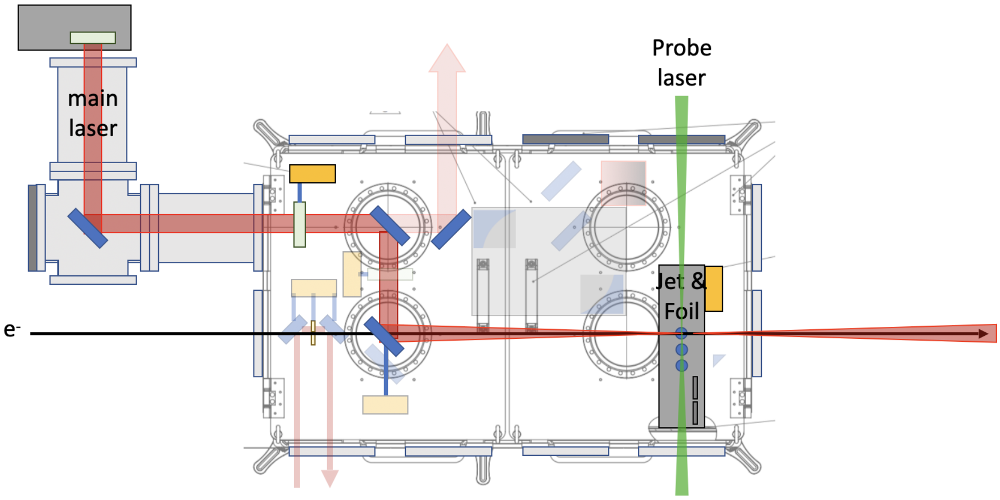

Fig. 6.1: Schematic overview of the E305 experimental experimental set-up. The electron beam goes from left to right, main laser comes from the top left, and probe laser from the bottom right. Blue rectangles are mirrors and light green rectangle is a focusing optic.

gas jets produced plasmas are suitable for optical probing of the interaction, which as will be explained later could provide valuable information about the development of the beam-plasma instability.

A schematic overview of the set-up around the Interaction Point (IP) is displayed in Fig. 6.1. The vacuum chamber containing the IP is shared with other experiments, but components not relevant to E305 are dimmed in color. The gas jet mount was designed to support three different gas jets, which gives us a broader range of plasma geometries, for instance different plasma length and/or density profiles. In order to choose the right optics and gas jets, different types of simulations have been carried out. Fluid simulations provide a gas density profile for a given gas jet, and then optical ionisation studies allow to choose the right focusing optic to fully ionise homogeneously the gas.

These simulations provided also information about the ramps, density and length of the designed plasma target. For most of the considered gas jets, the density ramps at the boundaries of the plasma target a length of around 1 mm. A maximum achievable plasma density of $n_p \approx 10^{20}\,\mathrm{cm}^{-3}$ was found, and for a gas jet with 5 mm exit diameter, simulations resulted in a 4 mm long plateau of uniform density.

For the single bunch configuration, the nominal beam parameters of the FACET-II facility are listed in Tab. 6.1 together with an optimised set of beam parameters for E305-gas. The beam parameter optimisation for E305-gas is driven by the need of the largest peak beam density but keeping a relatively large transverse size in order to satisfy the $k_p\sigma_r \gg 1$ condition required for the instability. For plasma densities of $n_p \approx 10^{20}\,\mathrm{cm}^{-3}$ we have $\lambda_p \approx 3.34\,\mu\mathrm{m}$ and therefore $\sigma_r = 10\,\mu\mathrm{m}$ is a good compromise. With this constrained transverse beam size, increasing peak beam density can only be achieved by longitudinal compression, i.e. increasing the current. For E305-solid the $k_p\sigma_r \gg 1$ condition does not constrain the transverse size of the beam due to the small plasma wavelength associated to solid plasma densities, thus allowing to further compress the beam transversely and effectively reaching higher peak beam densities.

Parameter	Baseline Design	E305 Design	Unit
Energy	10	10	GeV
Beam Charge	2	2	nC
RMS Bunch Length	1.8	2.4	μm
RMS Beam Size	18	10	μm
Normalized transverse emittance	3	3	mm mrad
Energy Spread	1.4	1.4	%

Tab. 6.1: FACET-II design beam parameters [72] and E305-gas beam parameters.

One of the most challenging parts of the E305 experiment are the diagnostics. To my knowledge, all the existing experiments that have measured relativistic beam-plasma instabilities rely on either temporally or spatially integrated signals. For instance, in the most recent experiment on beam-plasma instabilities using an accelerator facility [102], the main diagnostic was a beam profile monitor at the end of the plasma to observe the beam modulations after the passage through the plasma, which provided a longitudinally integrated 2D map of the beam transverse filaments. Having a plasma cell of fixed length, the only temporal information on the growth of the instability that they reported was correlated with a change of the plasma density. The difficulty arises due to the small and fast kinetic scales over which the beam-plasma instabilities typically develop, which together with the experimental constraints imposed by the accelerator facility make very challenging to resolve the instability both temporally and spatially.

For the E305-gas experiment, the extreme beam parameters and the high plasma densities also make a challenging task resolving the beam micro-structures after the propagation in the plasma with a beam profile monitor. Therefore a different diagnostic apparatus has been designed, which mainly relies on three different types of measurements: beam energy spectrum and divergence, gamma rays and optical probe. As for the E300 experiment, my work has been devoted mostly to the gamma-ray diagnostics and the type of information that one can retrieve about the instability, but I have also tried to correlate this information with the beam divergence and energy spectrum. These two diagnostics only provide temporally and spatially integrated information about the instability, but as explained in the Sec. 6.2 they can still provide valuable guidance for the experimental realisation. The transverse optical probe, which is still under development, is expected to provide the best temporal and spatial resolution, and will in principle provide for the first time detailed measurements of the evolution of the beam-plasma instability.

In terms of hardware, the gamma-ray diagnostics of E305 are the same as for E300, and are explained in Chap. 3. The beam divergence information is retrieved with beam profile monitors (OTR screens) placed several meters downstream of the interaction point. The optical probe has 1 mJ, 1 cm diameter and 30 fs (FWHM) pulse duration. It comes from the Ti:Sapphire laser system of FACET-II, which delivers a laser pulse that is split into a main pulse and several probe pulses, including the one used for E305. This E305 pulse will be used to probe the plasma modulations, and by implementing a 10× magnification microscope objective a few centimeters away from the plasma, a micrometer-scale spatial resolution is expected, similar to what was done in [36].

6.2 PIC simulations under FACET-II experimental conditions

Based on the plasma parameters obtained with the aforementioned simulations (fluid and optical ionisation) and the electron beam parameters optimised for the E305-gas experiment (second column of Tab. 6.1), PIC simulations were performed to assess the type of instability that could be studied at FACET-II with the designed gaseous plasma targets. These simulations, mainly carried out in 2D geometry, but also in 3D, included a finite bi-gaussian beam and a longitudinally finite plasma of density $n_p \leq 10^{20}\,\mathrm{cm}^{-3}$. The plasma density plateau was 4 mm long and linear density gradients of 1 mm at the entrance and at the exit of the plasma target were included in the simulation. It was precisely these first simulations that motivated the theoretical and simulation study of finite beam effects on beam-plasma instabilities developed in Chap. 5. These simulations further confirmed, both in 2D and 3D, that under these FACET-II experimental conditions the beam-plasma instability is onset and can reach saturation during the propagation of the electron beam through the plasma.

In order to assess the dynamic range of the instability that can be studied at FACET-II, we performed PIC simulation scans where we changed the initial beam-plasma configuration in a way that can be reproduced in experiments. We scan two different parameters: beam transverse size and plasma density. For the scan of beam transverse size σ_r, we keep the total charge of the beam ($Q = 2\,\mathrm{nC}$), the normalized beam emittance ($\epsilon_n = 3\,\mathrm{mm\,mrad}$) and plasma flat-top density ($n_p = 10^{20}\,\mathrm{cm}^{-3}$) constant, so that the variations in σ_r are equivalent to different beam focusing settings in the final focus system. The plasma density scan can be experimentally realised by changing the backing pressure of the gas jet.

From these simulation scans we can try to extract observables as measured in the experiments. For the beam diagnostics, we can just retrieve information about the beam by looking at the beam phase-space distributions at the end of the simulation. The angular spread can be retrieved from the transverse phase-space, and the energy spectrum from the longitudinal phase-space. For the gamma diagnostics, two different methods have been employed to compute the radiation produced by the electron beam during the interaction. As explained in Chap. 2, the first method consists in extracting the beam trajectories from CALDER and use them to compute the emitted radiation, which allows to compute the spectral and angular distribution of the radiation. The second method is to use an internal radiation module in CALDER, which can also provide spectral and angular information but at the cost of slowing down significantly the PIC simulation. In these scans we activated the radiation module of CALDER to be able to account for beam energy losses due to high energy photon emission, which turned out not to be a significant process, but without the spectral nor the spatial distributions. Only the total radiated energy was computed with the radiation module. It is worth mentioning that a good agreement was found between the total radiated energy as a function of the propagation distance when computed by the PIC module and by the trajectory post-processing.

The results of the beam transverse size scan for a fixed beam charge, bunch length and plasma plasma density are depicted in Fig. 6.2. The scanned beam transverse sizes go from $5\,\mu$m ($\approx 11k_p^{-1}$) to $30\,\mu$m ($\approx 55k_p^{-1}$), and α varies between 0.092 and 0.003. The four "observable" quantities plotted are the beam divergence, the beam energy loss, the gamma-ray divergence and the total radiated gamma-ray energy, all evaluated at the end of the simulation. They are plotted in logarithm scale to evidence its exponential behaviour.

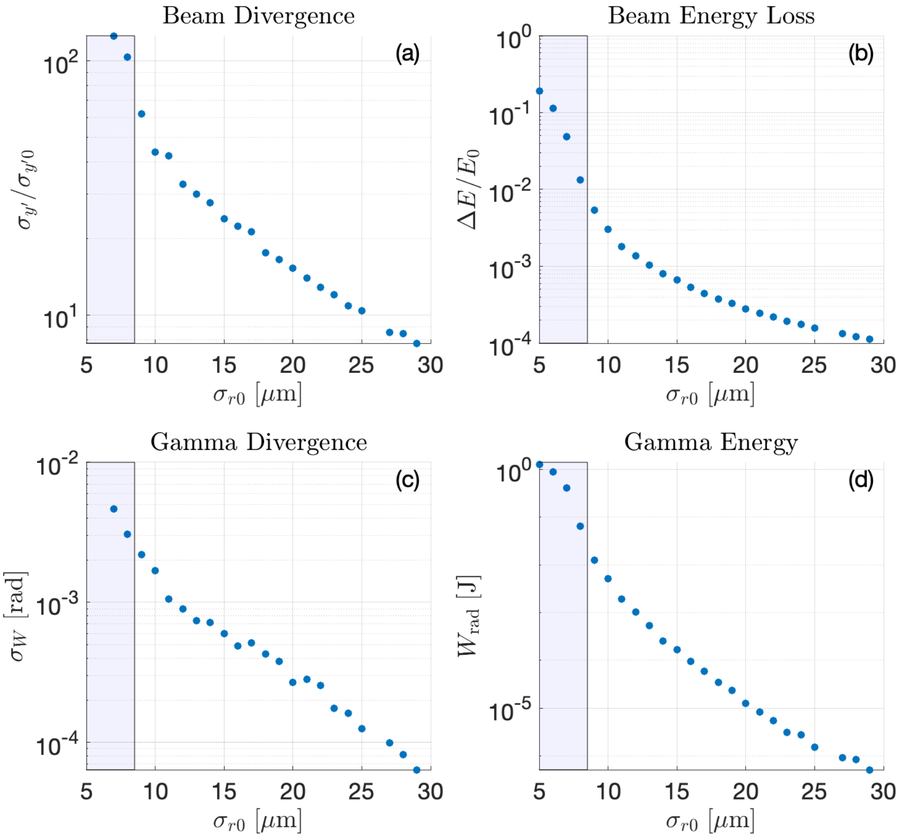

Fig. 6.2: Results of a simulation scan over initial electron beam size σ_{r0} under E305-gas experimental conditions. Four quantities are plotted from each simulations: beam divergence (a), beam energy loss (b), spatial divergence of the radiation produced in the interaction (c) and total radiated energy (d). All values are taken at the end of the simulation. See text for a detailed explanation of the computation of each quantity. Blue shaded areas indicate the beam configurations for which the beam-plasma instability is quenched and evolves towards a plasma blow-out. All simulations have a bi-gaussian beam profile with a total charge of 2 nC, bunch length of $\sigma_z = 2.4\,\mu$m, and beam emittance of $\tilde{\epsilon}_n = 3\,$mm mrad. The plasma longitudinal profile is given by a 1 mm long up-ramp and down-ramp, and a 4 mm long flat-top of density $n_p = 10^{20}\,\mathrm{cm}^{-3}$.

The divergence values, both for the beam and for the gamma-ray, are computed by means of a gaussian fit on angular distributions instead of computing the R.M.S. values. The main reason behind this choice is to reduce the large weight assigned by the R.M.S. calculation to the particles (or gammas) with large angles, and therefore give more importance to the main central part of the signal. The beam energy loss is computed from the mean energy of the beam particles. The longitudinally integrated beam spectrum, not discussed here but which can also be measured at FACET-II, did not show in these simulations any significant feature that could hint the instability due to the high initial energy of the beam. Both the beam energy loss and divergence are normalized by its initial value. Note that the initial divergence is not the same for each simulation, it is the normalized emittance that is kept the same. The total radiated energy is integrated over all photon energies and angles.

The smallest beam size simulations show that the instability is quenched due to beam self-focusing and non-linear plasma wave excitation (see Sec. 5.2). In Fig. 6.2 the beam-plasma configurations for which the self-focusing dynamics dominate over the instability are represented by the blue shaded areas. The transition between self-focusing and instability happens around $\sigma_{r0} = 10\,\mu\text{m}$ ($\approx 19k_p^{-1}$), value for which the instability dominates and reaches saturation before the beam leaves the plasma target. This sets the higher limit for the beam-to-plasma density ratio that can be experimentally study at FACET-II at $\alpha_{\max} \approx 0.03$, at the considered beam charge, bunch length and plasma density. On the other extreme, for $\sigma_{r0} = 30\,\mu\text{m}$ only the beginning of the linear phase of the instability evolution is observed in the simulation before the beam exits the plasma. The exponential behaviour of all quantities as a function of the beam size is a consequence of the different peak beam densities of each configuration. The growth rate being proportional to $n_b^{1/3}$ and $\tau_{\text{OTSI}} \propto n_b^{-1/2}$ (see eq. (5.22)), larger beam sizes have smaller peak beam densities (total beam charge is kept constant) and therefore lead to slower growths. Since the plasma parameters are the same for each configuration, a smaller growth rate results in a smaller signal since the unstable mode reaches lower amplitudes. Furthermore, we observe a change in the overall exponential trend when self-focusing effect starts to be significant, i.e. for small beam sizes.

In the following we will try to decipher the transition between the two regimes (instability and blow-out) by studying each observable quantity separately. Identifying this transition in the experiments will be of key importance to rule out the beam wakefield dynamics from the measurements.

In terms of beam divergence, a much larger beam divergence increase is observed in the blow-out regime than when the instability dominates. Yet, a similar trend is observed in both regimes with respect to the beam size, indicating that the beam divergence diagnostic provide limited information about the regime where the interaction takes place, but could help confirm where the transition occurs. It is noteworthy though that even for the configurations where the instability only reaches amplitudes far from saturation we still observe a factor of ~ 10 increase in the beam divergence.

The beam energy loss also shows much greater values in the blow-out regime than due to the instability. Furthermore a typical very broad spectrum is present in the blow-out regime, which is not present for the instability. This can be a clear signature that indicates that the beam-plasma interaction is dominated by plasma blow-out and not by the instability, even if one needs to be careful to exclude possible similarities with non-linear features of the beam-plasma instability, though they haven't been observed in this simulation scan. Finally, note that the initial beam energy spread is $\sim 1\%$, so very likely the beam energy spectrum will not provide any valuable information about the evolution of the instability, but a substantial increase of this initial energy spread will indicate that the beam plasma interaction in dominated by the blow-out regime.

For the radiation observables, the gamma-ray divergence, as expected, has many similarities with the beam divergence and does not necessarily provide any new input on the transition between self-focusing and instability. The total radiated energy, similarly to the beam energy loss, shows a large dynamic range over the scanned beam sizes, but with the advantage that there is no "initial" radiation and therefore a gamma diagnostic with a good dynamic range can be very useful to diagnose different instability evolutions (and this justifies the implementation of a CsI crystal together with DRZ to be sensible to low levels radiation, see Chap. 3). Yet, the trends are not substantially different in both regimes, so by itself the gamma diagnostic might not be enough to assess the blow-out versus instability competition, unless it has been cross-calibrated with another diagnostic.

Overall, although the results of this simulation scan showed that these integrated observables are sensible to different experimental configurations and could therefore provide information about the evolution of the instability onset under different conditions, they cannot give a direct measurement that unambigously distinguish these two regimes.

A second simulation scan was performed changing only the plasma density at the plateau, keeping the ramps length and the beam parameters constant. Since the beam size scan was already at the maximum plasma density available at FACET-II, only lower plasma densities were simulated down to $n_p = 10^{18}\,\mathrm{cm}^{-3}$. As explained in Chap. 5, decreasing the plasma density favours the self-focusing dynamics over the instability, and therefore a larger beam (and the corresponding lower n_b) is required for the instability to dominate. The plasma density scan was done for two beam configurations of Fig. 6.2: $\sigma_r = 12\,\mu\mathrm{m}$ ($\approx 22k_p^{-1}$, $n_b = 2.3\times10^{18}\,\mathrm{cm}^{-3}$) and $\sigma_r = 5\,\mu\mathrm{m}$ ($\approx 9k_p^{-1}$, $n_b = 1.3\times10^{19}\,\mathrm{cm}^{-3}$). We only present here the total radiated energy; the other observables did not provide interesting trends to identify the dominant beam dynamics. As before, blue shaded areas correspond to beam-plasma configurations where the blow-out dominated over the instability.

The results are displayed on Fig. 6.3. In both beam configurations, the blow-out regime dominates for plasma densities $n_p \lesssim 2\times10^{19}\,\mathrm{cm}^{-3}$. As expected, in this regime the higher the plasma density the more radiation is produced by the beam. For higher plasma densities the simulations with $\sigma_r = 12\,\mu\mathrm{m}$ showed that the instability dominates over the self-focusing dynamics, and a very quick and remarkable drop of the total gamma yield is observed. For the more compressed beam with $\sigma_r = 5\,\mu\mathrm{m}$, blow-out still dominates for $n_p > 2\times10^{19}\,\mathrm{cm}^{-3}$ all the way to $n_p = 10^{20}\,\mathrm{cm}^{-3}$, and the drop in the gamma yield is not observed.

This analysis therefore shows that in order to experimentally know if for a given beam-plasma configuration the interaction is dominated by wakefield dynamics or by the instability, one possibility is to vary the plasma density: if a sudden drop in the gamma total yield is observed around $n_{p,\,\mathrm{drop}}$, it means that we are in the wakefield-dominated regime for plasma densities below $n_{p,\,\mathrm{drop}}$, and the instability can be studied for densities above $n_{p,\,\mathrm{drop}}$. It should be noted that we are assuming that when we change the plateau plasma density (backing pressure of the gas jet) the density gradients at the entrance are not modified. Furthermore, if the beam size is too small, it may not be possible to observe the drop within the experimentally available range of plasma densities (see Fig. 6.3).

To summarise this section, we have performed PIC simulations trying to mimic the experimental E305 conditions of FACET-II. It should be noted that this "simulated experiment" is

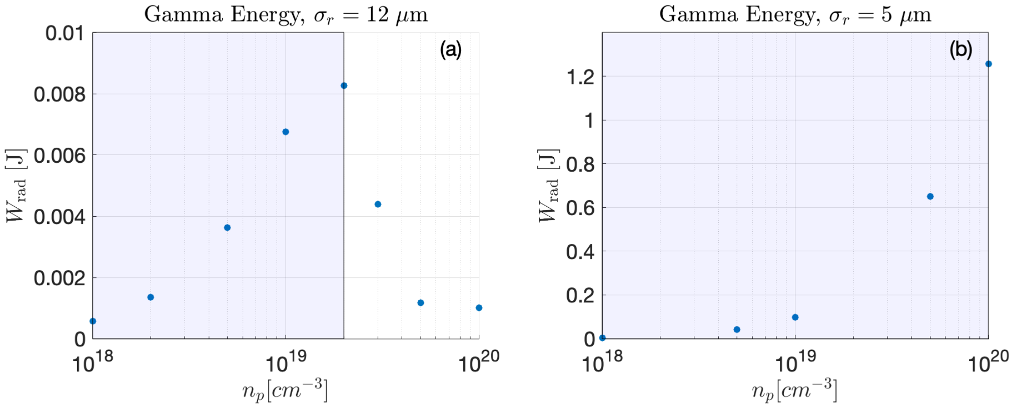

Fig. 6.3: Simulated total radiated energy by the electron beam for different plasma density n_p under E305-gas experimental conditions. Two of the beam configuration of Fig. 6.2 are simulated: beam size of $\sigma_r = 12\,\mu$m (a) and beam size of $\sigma_r = 5\,\mu$m (b). Blue shaded areas indicate the beam configurations fo which the beam-plasma instability is quenched and evolves towards a plasma blow-out.

still not yet fully realistic: it assumes gaussian beams, a transversely uniform plasma, linear plasma ramps, and the simulated observables are free of any experimental noise. Yet, these simulation scans provide a precious overview of the type of physics that can be studied during the E305 experiment, and can be used as guidance for the design of new detectors and also for the realisation of the experiment.

To finish this chapter, I would like to comment on the gamma-ray yields observed in our simulation. In Fig. 6.2 and Fig. 6.3 the gamma-ray yield is plotted in Joules. The total beam energy of the 2 nC 10 GeV FACET-II beam is approximatively 20 J. Therefore the conversion efficiencies from beam energy to gamma-rays in the instability-dominated regime are smaller than 1%. Higher values are obtained in the blow-out regime up to $\approx 5\%$ in these simulations. The main limitation of going higher in conversion efficiency via the instability comes from the competition with the blow-out, since it quenches the instability when $\alpha \to 1$. This evidences the importance of including realistic finite beam size when performing simulations of beam-plasma instabilities with an ultra-relativistic electron beam.

6.3 Beam-plasma systems with $\alpha \approx 1$

To finish this section, we would like to address the following question that naturally raises from the analysis presented in this chapter: can a finite electron beam-plasma system with $n_b \approx n_p$, in which the electron beam immediately drives non-linear wakefields, be subject to beam-plasma streaming instabilities? Unfortunately, to my knowledge there is no analytical model to describe non-linear transverse wakefields in the $k_p\sigma_r \gg 1$ limit required for the instability. For beams with $k_p\sigma_r < 1$ and $k_p\sigma_x \approx 1$, as long as the normalized charge per unit length is large ($\Lambda = \frac{n_b}{n_p}(k_p\sigma_r)^2 \gg 1$) plasma electrons do not flow through the electron beam, and therefore no streaming beam-plasma instability can develop [20]. If $k_p\sigma_x \ll 1$ it is not Λ but the normalized charge $\tilde{Q} = \frac{N}{n_p\sigma_r^2\sigma_x}$, N being the total number of beam particles, that is relevant, but again this has only been validated via simulations for $k_p\sigma_r < 1$ [22].

The physics behind all these non-linear models is related to the fact that when the relativistic beam is dense enough the plasma electrons are expelled mainly radially. One can however suspect that this might break down at some transverse beam size $k_p\sigma_r > 1$ for which a non-negligible fraction of plasma electrons penetrate several skin-depths in the beam before being expelled radially. In this sense, probably short beams with $k_p\sigma_x \ll 1$ represent the best scenario to reach unstable beam-plasma systems with $\alpha \approx 1$, but the models of the instability presented in this chapter are not valid in this regime. It should be noted that the interest of the $\alpha \approx 1$ regime comes from the fact that this regime is thought to be the best for achieving the largest electromagnetic fields during the interaction, and therefore the largest gamma-ray conversion efficiency.

This discussion, based on hand-waving arguments, originates from considering the finite size of an electron beam in an unstable beam-plasma system. This allows to identify significant limitations of the parameter space that can be studied in an experimental system, but also to define strategies to overcome these limitations. Clearly, the most straight-forward solution to reach the $\alpha \approx 1$ regime is to use neutral e^+e^- beams, which do not excite wakefields. However the production of relativistic pair beams remains nowadays an important challenge.

Part III

PROBING LASER-SOLID INTERACTIONS WITH LWFA-ELECTRON BEAMS

7. EXPERIMENT IN SALLE JAUNE AT LOA

This final chapter presents results of an experimental campaign aiming at probing the onset and development of plasma streaming instabilities in the interaction of an ultra-high intensity laser pulse and a solid target via an LWFA electron beam. This experiment took place during the month of October 2020 in the Salle Jaune laser facility of the Laboratoire d'Optique Appliquée (LOA), and was initially conceived as a follow-up campaign of the first set of experimental measurements of the laser-solid interaction that were carried out in the same facility [123]. During my PhD I took an active part in this experiment: installation, running the experiment and getting experimental data, and finally data analysis. The main outcomes and conclusions are presented in this chapter.

The first section puts into context the experimental campaign and briefly presents the main motivations. The second section describes two relevant physical mechanisms that can be explored with the presented experimental set-up when a high intensity laser pulse hits a solid target: the onset of plasma streaming instabilities in the bulk of the target and the Target Normal Sheath Acceleration (TNSA) electromagnetic fields developing along the solid surface. Finally the third section presents the experimental observations and discusses their connection with the aforementioned physical mechanisms.

7.1 Motivation and context

The experimental campaign of October 2020 at LOA aiming at studying the onset of streaming instabilities originates from the Hybrid LWFA-PWFA experimental program developed at LOA in collaboration with other universities. This Hybrid program, which has been briefly discussed at the end of Section 1.1, aims at developing a beam-driven PBA using a drive electron beam that is produced in a laser-driven PBA stage, referred to as the LWFA electron beam. This project, which has produced significant results [34, 36, 123], makes use of a solid foil to reflect the LWFA laser pulse before it propagates into the second PWFA plasma target. In this way only the LWFA electron beam, that propagates through the solid foil, reaches the PWFA plasma stage and can excite a beam-driven plasma wave. A typical hybrid LWFA-PWFA set-up with a solid foil is displayed in Fig. 7.1(a).

The role of the foil in the LWFA-PWFA staging is crucial: unless the laser intensity is drastically reduced from the LWFA to the PWFA stage, the presence of the laser pulse in the latter could significantly disrupt the beam-driven plasma-wave excitation. A possible alternatives to the foil is increasing the LWFA-PWFA inter-stages distance, which reduces the laser intensity on the PWFA stage. This technique has been successfully implemented in other laser facilities, but at the cost of deteriorating the coupling of the LWFA electron beam into the PWFA stage (amount of useful charge to excite a beam-driven wakefield) due to the large LWFA electron beam size at the PWFA entrance. A more elaborated solution would be to use beam optics (quadrupoles) to transport and focus the electron beam, but the chromaticity of these beam

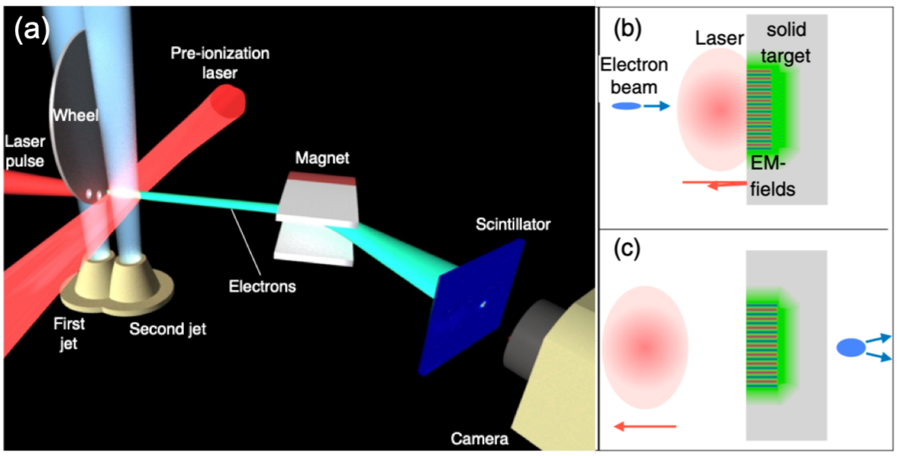

Fig. 7.1: (a) Schematic representation of an experimental set-up of hybrid LWFA-PWFA staging. *Credits to A. Doche.* (b) and (c) Schematic representation of the physical process through which the LWFA electron beam probes the CFI onset by the laser-solid interaction. Figures (b) and (c) are from Ref. [123].

optics made them hard to use with the broad-spectrum electron beams from LWFA. Nevertheless, the choice of foil is not free of drawbacks: even if it effectively reflects all the laser pulse energy, the electron beam naturally suffers from multiple scattering when propagating through the solid foil, which further increases the electron beam divergence. The multiple scattering effect on the beam can be reduced by using very thin low-Z materials. It should be noted that at the ultra-high laser intensities of the LWFA laser pulse ($I_L > 10^{18}$ W cm^{-2}) the foil acts as a plasma mirror [124], i.e. the laser ionises the foil and cannot propagate in the over-dense plasma. Therefore any material solid at room temperature can be used for this purpose.

Before 2018, several experimental campaigns at LOA tried to get an experimental signature of a PWFA driven by an LWFA electron beam. However, a significant divergence increase of the LWFA electron beam was observed due to the foil, which lead to a decrease of the peak electron beam density at the entrance of the PWFA stage, degrading the beam-driven plasma wave excitation. Remarkably, this divergence increase turned out not to obey the scalings of multiple scattering, namely in terms of foil thickness. Numerical simulations (PIC) were then performed to simulate the laser-beam-foil interaction with similar physical parameters as in the experiment. These simulations revealed a new process to be responsible of the divergence increase of the relativistic electron beam: the Current Filamentation Instability onset by the so-called "hot" plasma electrons (the plasma electrons located near the surface and accelerated by the laser, and thus being responsible for most of the laser energy absoption) when propagating into the bulk of the plasma (see Fig. 7.1(b) and (c)).

The kinetic nature of the CFI, already introduced in the Chapter 4, results under these conditions in unstable fields that can grow significantly before the arrival of the electron beam. Therefore when the electron beam enters the foil it experiences the unstable fields in the bulk, leading to an important increase of electron beam divergence. This process is illustrated in Fig. 7.2, which shows 3D PIC simulation results of the beam density profile prior (Fig. 7.2(a)) and after (Fig. 7.2(c)) the interaction. Furthermore, the beam angular divergence after the interaction (Fig. 7.2(d)), the spatial distribution of the CFI fields in the foil (Fig. 7.2(b)) and the temporal evolution of the longitudinally integrated CFI fields (Fig. 7.2(e)) are also

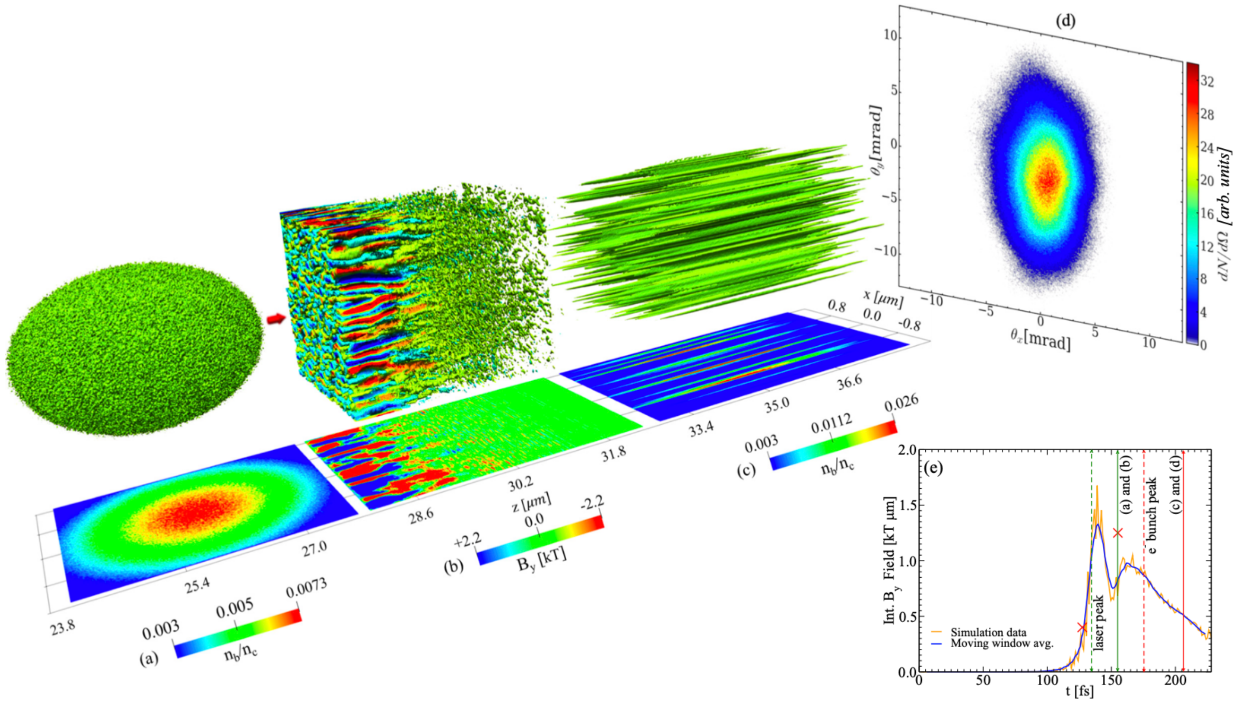

Fig. 7.2: PIC simulation results of electron beam probing CFI onset in a laser-solid interaction. (a) Initial electron beam density. (b) CFI magnetic field developing in the target after the interaction with the LWFA laser pulse. (c) Electron beam density after propagation in the target where the CFI fields have developed. (d) Longitudinally integrated angular distribution of the electron beam after the propagation through the foil. (e) Integrated magnetic field evolution in the foil. Figure from Ref. [123].

displayed.

The onset of CFI fields and the resulting electron divergence increase deteriorates the LWFA-PWFA staging, and requires to increase the LWFA-foil separation distance so that the laser peak intensity is reduced at the foil position, suppressing the development of CFI [123]. However this solution also leads to a smaller peak beam density at the entrance of PWFA which needs to move consequently downstream as much as the foil. Yet, the agreement between experimental and simulation data confirmed that CFI fields are the main responsible for the observed divergence increase and not multiple-scattering, since the latter should be independent of the LWFA-foil separation, and that therefore the LWFA electron beam can be used to probe the volumetrically integrated CFI fields in such an experimental platform.

It should be noted that the onset of CFI in laser-solid interactions had already been experimentally explored but rather in the context of proton/ion Target Normal Sheath Acceleration (TNSA, see next section). This leads to significant differences with respect to the presented LWFA set up, namely that in the TNSA context longer laser pulses (ps instead of fs) are preferably used. Not only this reduces the temporal resolution under which the instability can be studied, but also leads to more significant density gradients at the front and rear side of the target in which the CFI mainly develops (rather than in the bulk). In this type of laser platforms, the onset of CFI in a laser-solid interaction has been measured by using the features of the accelerated protons itself [125] or by using a second foil to produce a proton beam, which then probes the CFI onset by a different laser-foil interaction [126]. Furthermore optical probing of the CFI via polarimetry measurements has also been used to explore the unstable fields on the surface [127].

The described hybrid LWFA-PWFA set-up shown in Fig. 7.1 allows to measure the onset of CFI by a laser-solid interaction but it cannot provide temporal information of the evolution of the instability. Indeed the delay between the laser pulse driving the CFI and the electron beam is fixed by the LWFA stage. The laser pulse driving the non-linear plasma wave (ion cavity) and the electron beam being injected at the rear of the ion cavity, the typical separation distance between the LWFA laser pulse and the electron beam is $\approx \lambda_p$. Changing this value requires to change the LWFA plasma density, which would further modify the laser intensity at the exit of the LWFA plasma as well as the electron beam parameters. The only parametric study of CFI that the hybrid set-up allows is the aforementioned LWFA-foil distance which is equivalent to varying the laser-peak intensity at the foil.

In order to be able to do more parametric scans of the CFI onset in a laser-solid interaction, namely laser-electron beam delay scans to probe the temporal evolution of the CFI, a new experimental campaign with a new experimental layout was designed. Three major upgrades were done to the experimental set-up: the first and more important modification is to use two different laser pulses, one for the onset of the CFI (the "pump laser") and another one for the LWFA stage (the "LWFA laser"). This was carried out by shooting the CFI laser pulse on the "rear" side of the solid target, i.e. in the opposite direction to the LWFA laser pulse. In this way the onset of CFI and the generation of the probe electron beam are completely decoupled, similarly to the well-known pump-probe technique. It is important though to ensure that the LWFA laser, which will still hit the foil on the front side, does not create a sufficiently important population of hot electrons to also drive the CFI. This was done by reducing the LWFA laser energy (which furthermore allows to increase the pump laser pulse energy) and by having a large separation distance (≈ 3 mm) from the LWFA stage to the foil. The second major upgrade was to combine the electron beam probing of the CFI with an optical probe as in Ref. [128] to try to have a second measurement that could be correlated to the electron beam probe measurement. Finally the set up allowed to change the polarisation of both the LWFA and pump laser pulses, from linear (P and S) to circular.

The experimental layout and the results of this experiment will be shown in Section 7.3. Beforehand, Section 7.2 briefly discusses the physical processes arising in a laser-solid interaction as well as the state-of-the-art experimental campaigns that have been performed to study these processes. Namely, the generation of TNSA magnetic fields is discussed, which is relevant to understand the experimental results of the following section.

7.2 Streaming instabilities and TNSA in laser-solid interactions

The interaction of a high intensity relativistic laser pulse ($a_0 = \frac{eE}{m_e c\omega} > 1$ where E is the laser peak electric field and ω the laser frequency) with an overdense plasma ($n_p > \frac{m\epsilon_0\omega^2}{e^2}$) is characterized by the reflection of the laser pulse and the absorption of part of the laser energy by the plasma electrons sitting at the vacuum-plasma boundary (which will be considered a sharp boundary in the following). These plasma electrons are "heated" by the laser pulse, i.e. their average temperature is greater than that of the bulk [129]. The heating mechanisms of this process are various and of several natures (wave-particle couplings and collective plasma effects), and a proper discussion and identification of the relevant heating mechanisms in our experimental system is out of the scope of this manuscript.

Due to momentum conservation, the heated electrons have an average velocity towards the bulk of the plasma, which for high enough laser intensities can be relativistic. The charged current driven by hot electrons induces a return current in the bulk of the plasma driven by the "cold" electrons. The latter being more numerous ($\alpha < 1$), the return current is not relativistic. Under these conditions, the bulk of the plasma is prompt to streaming instabilities. Given that the hot electrons are rather mid-relativistic (for the experimental conditions presented in this chapter $\gamma \sim 2$ is expected), the transverse magnetic unstable modes of CFI are expected to dominate. To clarify the nomenclature used in this chapter, since the anisotropy of the velocity distribution function of plasma electrons does not arise from a two-temperature distribution but rather from a two-species distribution (hot and cold electrons), the dominant instability will be referred as CFI and not Weibel Instability (see Chap. 4). It should be noted though that the results derived in Chap. 4 using the fluid approximation do not apply to the onset of CFI in a laser-plasma interaction, since the shape of the electron momentum distribution is far from a double-peak distribution.

The CFI onset in a laser-solid interaction leads to the growth of electromagnetic fields which develop from the front surface towards the core of the solid target, where the hot and cold electrons flow through each other. There are though other important mechanisms that arise in a laser-solid interaction that also generate strong electromagnetic fields at the surfaces, where the currents driven by the hot electrons cannot be effectively screened. One of these process, that is believed to be relevant for the experimental results presented in the next section, is the generation of TNSA magnetic fields.

The TNSA fields generated in a laser-solid interaction typically refer to the longitudinal electric field that is responsible for ion/proton acceleration [130]. Nevertheless it is also known that a strong azimuthal magnetic field is also generated at the solid surface surrounding the accelerating structure [131] (see Fig. 7.3). Several physical mechanisms are thought to be responsible for the generation of these azimuthal magnetic fields, which develop in both the front and the rear surface of the soild but with opposite azimuthal direction. A recent study of these mechanisms and the corresponding temporal evolution can be found in Ref. [132]. In this reference, special attention is paid to the comparison between the TNSA magnetic fields produced at the front and those produced at the rear when a picosecond laser pulse is focused onto a thin solid foil. It is shown that for the considered parameters the magnetic fields at the rear surface initially grow at a similar rate as those at the front, but they are quickly dumped and the magneto-hydrodynamical plasma expansion at the front surface leads to larger amplitude magnetic fields at the front than at the rear.

These TNSA magnetic fields have already been measured in several experiments using an optical probe [133], a TNSA proton beam [134] or a LWFA electron beam [135]. For the experimental set-up presented in this chapter, the latter case is the most relevant. In this experiment, a LWFA electron beam is first diffused using a first solid foil (which is also used to reflect back the LWFA laser pulse) and then is used to probe the interaction of a tightly focused Ti:Sa ($\sim$ 30 fs) laser pulse with a second solid foil. From the LWFA stage to the laser-solid interaction point, the scattered LWFA electron beam is much wider than the laser spot-size in the interaction point. In this way they observe a radially evolving structure in the probe electron beam profile, only present at the center at short delays and expanding towards larger radius at longer delays. The expansion velocity of this feature was measured to be $\approx c$.

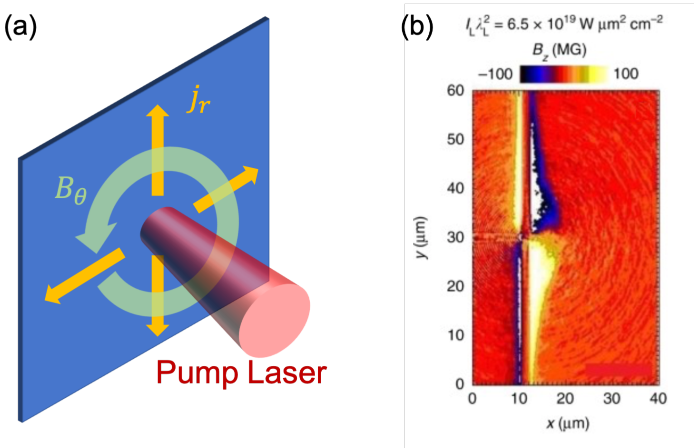

Fig. 7.3: (a) Schematic representation of laser-solid interaction and the generated TNSA magnetic fields on one of the surfaces. (b) Simulated TNSA spatial distribution on both surfaces of a thin Al foil when radiated by a 400 fs laser pulse with $I_L\lambda_L^2 = 6.5 \times 10^{19}$ $\mathrm{Wcm^{-2}\mu m^2}$. Figure (b) from Ref. [131].

The observed feature on the central part of the probe electron beam was in most cases an area depleted of electrons. This feature was associated to the surface TNSA magnetic fields excited by the pump laser whose spatial extent expands from the interaction point at roughly the speed of light as corroborated by PIC simulations. It is worth noticing that in this article the authors claim that, in agreement with their simulations, the dominant TNSA fields are those excited at the front surface where the laser pulse hits the target. Those fields should act as a focusing structure for the central part of the probe electron beam. However, no focusing structure was observed for high contrast shots. For short delays this is explained due to an over-focusing of the central electrons. At longer delays, for which the over-focusing should not occur, a sinusoidal magnetic perturbation is added in the central part of their simulations to reproduce the observed depleted central area, which reproduces the effect from the filamentation of the hot electrons.

7.3 Salle Jaune experimental set-up

The October 2020 experiment aiming at probing the onset and evolution of CFI in a laser-solid interaction was carried out in the Salle Jaune facility at LOA. This laser facility is equipped with a Ti:Sa laser system able to provide up to ≈ 4.5 J (before compression) in three laser beams at a central wavelength of 800 nm. Using the Chirped Pulse Amplification technique [13], each pulse can be compressed down to ≈ 30 fs. Most of the available energy is divided in two pulses (referred here as P1 and P2), whereas the third pulse (P3) is typically of much lower energy and used for optical probing.

The experimental layout of the experiment is shown in Fig. 7.4. In this figure the three laser pulses enter the experimental chamber from the bottom right part. The most energetic pulse (2.7 J before compression) is the pump laser, which is represented in red. A first mirror sends this laser beam towards a wave plate and then to the focusing optic which is a spherical mirror of 80 cm focal length. This spherical mirror, which for the experimental data that is shown in this manuscript was placed at ≈ 8° w.r.t. the target normal direction, focuses the laser

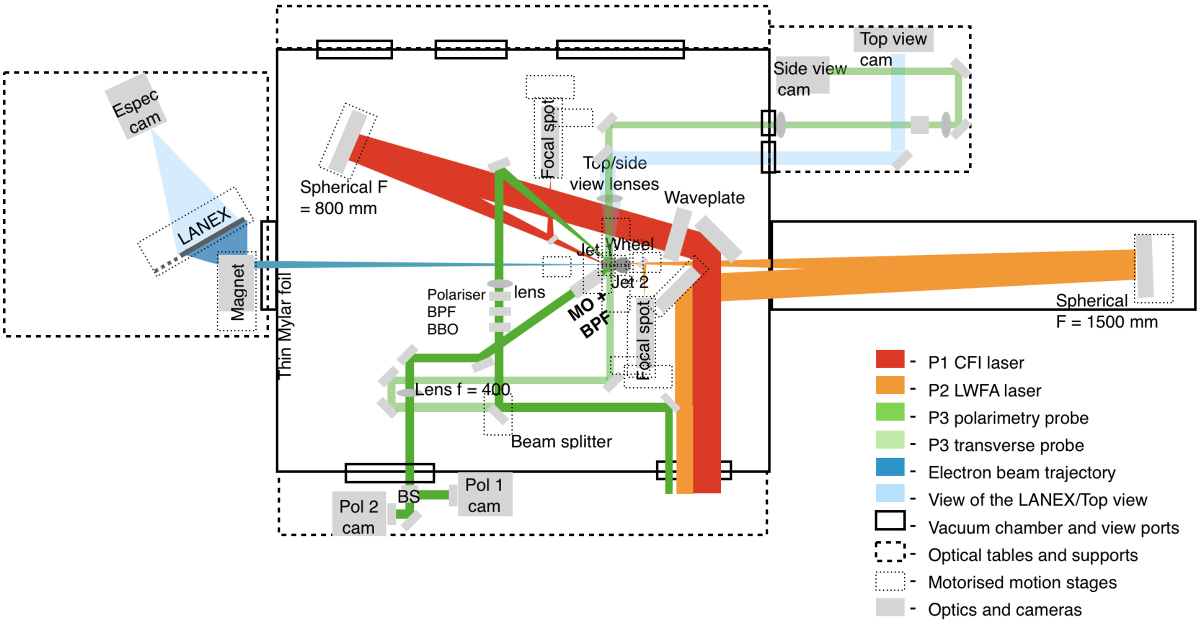

Fig. 7.4: Experimental layout of the CFI experiment of October 2020 in Salle Jaune. Note that the CFI spherical mirror is placed at 25° w.r.t. the target normal direction instead of the $\approx 8°$ that was used during the experiment. *Credits to O. Kononenko.*

into the solid target surface. This geometry and the choice of focusing optic (spherical mirror) lead to an astigmatic focus, which was corrected with a deformable mirror placed upstream. Accounting for $\approx 55\%$ transmission during the pulse compression and transport and the $\approx 30\%$ of the energy going to halo surrounding the main laser focal spot, together with the measured 10 μm spot size and 30 fs pulse length FWHM, a normalized vector potential of $a_0 \approx 3.5$ is obtained for the laser on target. Unless otherwise stated, P-polarised light was used for the pump laser.

The second laser pulse, the LWFA laser, is displayed in orange in Fig. 7.4. Similarly to the pump laser, a flat mirror sends the LWFA laser pulse to a focusing optic, which in this case is a spherical mirror with 1.5 m focal length that focuses the LWFA laser to the gas jet. The angle of incidence being small, much less astigmatic correction was needed compared to the pump laser pulse. Following the same procedure as before, the laser normalized vector potential at the entrance of the gas jet can be estimated for the LWFA laser, resulting in $a_0 \approx 1.4$. Using a Helium-Nitrogen 99%-1% mixture in the gas jet, electrons were injected via ionisation injection and accelerated up to relativistic energies, typically reaching 100-200 MeV energy range

The LWFA electron beam properties were measured with two electrons diagnostic placed outside the vacuum chamber: the divergence screen (not shown in Fig. 7.4) and the electron spectrometer. The choice of placing the electron diagnostic outside the chamber was partially due to the counterpropagating geometry between the pump and LWFA laser pulses, which restricted the available space for the electron spectrometer. The LWFA electron beam went then through a 200 μm Mylar window (referred as exit window) before reaching the electron diagnostics. The divergence screen consisted on a Lanex screen intercepting the electron beam at 45° with respect to the beam direction that was imaged by a camera also under a 45° angle. Placed a few centimeters downstream the exit window, the divergence screen measured the transverse electron beam profile, showing typically ≈ 3.5 mrad FWHM divergences for the accelerated electron beam.

The electron beam spectrometer consisted in a dipole magnet to disperse the electron beam energies horizontally and a Lanex screen that intercepts the dispersed electron beam and that is imaged by a camera. In this way the spectrometer provides spectral information along the horizontal dispersed direction and angular information along the vertical direction, as well as the correlation between these two quantities. Energies up to 200 MeV with a rather continuum spectrum, as expected from ionisation injection with Salle Jaune parameters, were measured, with an energy-slice FWHM vertical divergence of ≈ 2 mrad, which is as expected smaller than the energy-integrated divergence measured with the divergence screen.

The third laser pulse, with a mJ-level energy, is displayed in green in Fig. 7.4. After a first mirror the laser beam is divided into two paths: one for transverse optical probing of the interaction (called side view) and the other one for polarimetry measurements. The side-view diagnostic consists on a delay stage, used to precisely control the arrival time at the interaction point of the probe, and an imaging system. The polarimetry diagnostic consisted on three main elements: a BBO crystal [136] that produces second harmonic light, a Band Pass Filter (BPF) that filters out the remaining 800 nm light after the BBO, and a lens that focuses the polarimetry beam down to the CFI interaction point under a 35° angle. The polarimetry beam was then reflected from the solid and captured by a high resolution imaging system that sends the reflected light to two cameras and that also includes several BPFs to reduce the 800 nm light produced by the pump at the interaction point. Each of the two polarimetry cameras had a polariser in front of it to measure the rotation of polarisation induced by the surface fields at the interaction point on the second harmonic probe.

Figure 7.4 also shows several other diagnostics that provide complementary information to optimise the set-up. The pump and LWFA lasers had each their corresponding focus diagnostic, and a top-view diagnostic imaged the LWFA gas jet to provide information about the LWFA laser alignment onto the gas jet. Figure 7.4 also shows a second gas jet placed downstream of the LWFA gas jet, very similar to the hybrid LWFA-PWFA set-up illustrated in Fig 7.1. This second gas jet, that was placed at the same longitudinal position as the solid target, was used together with the side-view diagnostic to temporally synchronise the pump and LWFA laser pulses at the position of the solid foil. By imaging with the ≈ 30 fs side-view probe the position of the ionisation front of each laser pulse when propagating in the gas released by this second gas jet, a sub-picosecond temporal synchronisation between the LWFA and pump laser pulses was achieved. This was used to establish the zero-delay conditions, showing an overall good agreement with the expected no-signal measurements performed later at negative delays, i.e. when the probe electron beam reaches the solid target before the pump laser.

A more challenging task was the spatial overlap between the pump laser and the probe electron beam at the interaction point. As stated before, the pump laser had a $\approx 10 \times 10\,\mu\mathrm{m}^2$ FWHM spot size at waist, whereas the electron beam FWHM transverse size can be estimated from its divergence (≈ 3.5 mrad) and the LWFA gas-solid distance (≈ 3 mm) resulting in $\approx 9 \times 9\,\mu\mathrm{m}^2$ beam FWHM transverse size at the foil. The side-view images of the plasma trace allowed to get a first rough overlap in the vertical direction, but given the typical width of the plasma trace ($> 50\,\mu$m) another diagnostic was needed to achieve the required resolution.

The best imaging resolution of the interaction point was achieved via the imaging system of the polarimetry diagnostic. Thanks to a Mitutoyo ×10 objective placed at a ≈ 3 cm distance from the interaction point, a sub-micron pixel size resolution ($\approx 0.5\,\mu$m/pixel) was achieved.

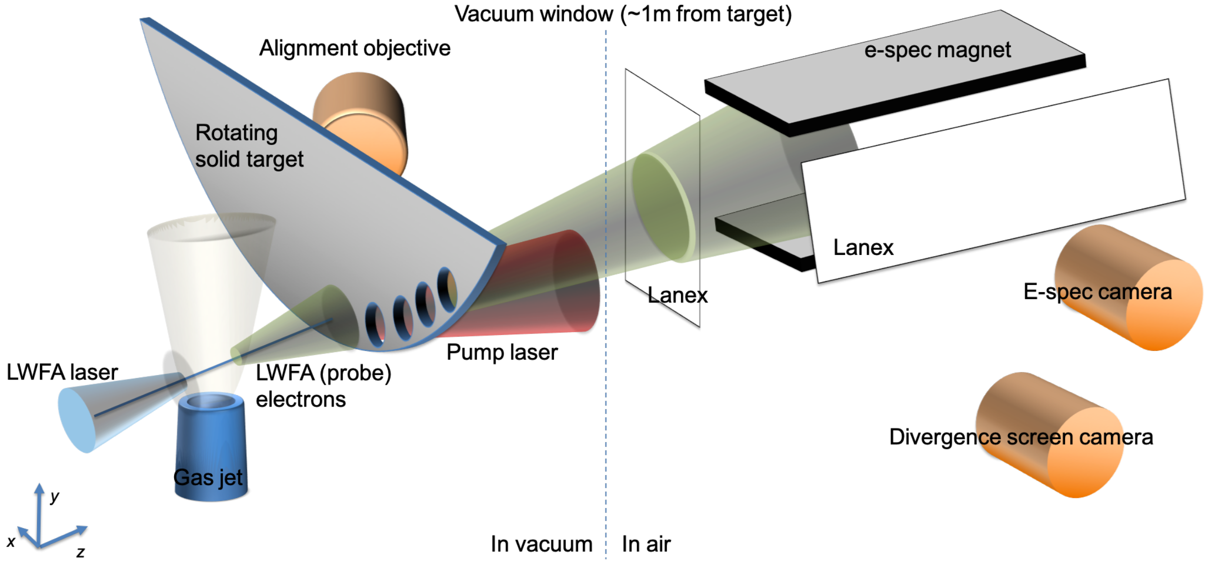

Fig. 7.5: Schematic representation of the interaction point and diagnostics in perspective.

This imaging system captured the scattered light of the attenuated pump laser on the target. The size of the scattered light feature was measured to be around 20 μm on both dimensions. When the solid target was transparent (30 μm thick Mylar), the scattered light from the attenuated LWFA laser hitting the opposite face of the solid target could also be captured by the imaging system, equally producing $20 \times 20\,\mu\text{m}^2$ features which could then be overlapped in both transverse dimensions with the pump laser scattered light feature. For opaque materials, such as Aluminium, a slightly attenuated LWFA laser pulse was sent to the target to drill a small hole on the target that could then be imaged by the objective and overlapped to the scattered pump laser light.

It is noteworthy that these procedures allow to spatially overlap and temporally synchronise the pump and the LWFA laser pulses, but not the electron beam. Generally, the electron beam is assumed to be behind (at a $\sim \lambda_p$ distance) and collinear with the LWFA laser pulse after the propagation in the plasma. Therefore the spatial overlap of the pump laser and the probe electron beam, as well as the temporal synchronisation (up to λ_p/c), can be achieved using the LWFA laser pulse to mimic the electron beam propagation. Nevertheless, deviations from the collinearity assumptions have been observed previously in experiments [137, 138]. Since our electron diagnostics were placed outside the vacuum chamber, the laser-electron beam collinearity could not be measured. Other experiments in the same Salle Jaune facility were able to quantify this phenomena, and resulted in mrad-scale deviations between the LWFA laser pulse and the electron beam, and this this effect can play a role in contributing to the offset between electron probe and pump laser.

Once the whole set-up was built and tested with full power laser pulses, one of the first things that was realised was that a too high parasitic signal of second harmonic light was detected on the polarimetry diagnostic, originating from the pump laser hitting the target, and that was much larger than the second harmonic probe signal itself. This result automatically prevented us to use the polarimetry to probe the interaction point in our experimental set-up. Possible solutions for future experiments could be to change the probe angle of incidence with respect to the pump laser or go to higher harmonics in the probe. Instead, the high resolution

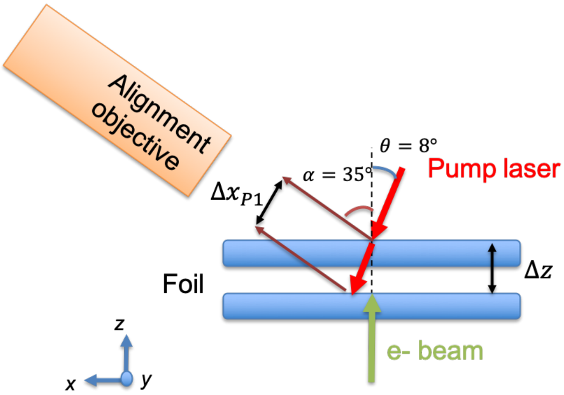

Fig. 7.6: Schematic representation of the horizontal drift Δx_{P1} of pump laser as observed with the alignment objective due to the longitudinal displacement Δz of the solid foil.

imaging system of the polarimetry diagnostic, together with several ND filters to attenuate the signal, turned out to be very useful to monitor online the pointing of the pump laser on the target on a shot-to-shot basis.

To help with the visualisation of the interaction point and the main components of the experiment, a schematic representation is displayed in Fig. 7.5. The different elements are labelled in the figure itself. Note that the high resolution objective of the polarimetry set-up is labelled as "Alignment objective" since as explained before it was mainly used in practice to monitor the pump laser pointing on the target. Furthermore in the bottom-left corner of Fig. 7.5 the direction of the three spatial axis is defined: z is the longitudinal coordinate, positive in the electron beam direction, y is the vertical coordinate, positive in the direction of the gas flow released by the gas jet, and x is the horizontal coordinate.

Let us now briefly discuss the implementation of the solid target. Since after each shot the solid target is damaged, the foil needs to be motorised to shift the part of the foil that is at the focus of the pump beam. For this purpose a rotating wheel was used (see Fig. 7.5). The central part of this wheel is made out of stainless steel to make the structure stiff, and in the outer-most part, where the interaction occurs, only the thin foils extend out. After each shot, the wheel was rotated around its axis and therefore fresh foil was placed at the pump laser focus position. However it was soon realised by using the alignment objective that there were significant drifts in the pointing of the pump laser on the foil from shot to shot, mainly in the horizontal direction. It was found out that this drift originated from a longitudinal displacement of the foil when the wheel was rotated, together with the fact that the pump laser was not at normal incidence (see Fig. 7.6).

These wheel longitudinal displacement, which was undesired but unavoidable due to the lack of stiffness of the thin foils that were used, lead not only to a misalignment between the pump laser and the probe electron beam but also to a different temporal delay between the arrival of both beams. Fortunately the alignment objective allowed us to monitor online in a shot-to-shot basis this drift, which could then be taken into account in the analysis. Furthermore, given that the longitudinal displacement of the foil does not lead to any horizontal drift in the probe electron beam at the foil (since it propagates under normal incidence), if the spatial overlap is achieved for one shot (by the aforementioned overlap procedure) it was possible to change the pointing of the pump spherical mirror (tip-tilt motorised) on a shot-to-shot basis

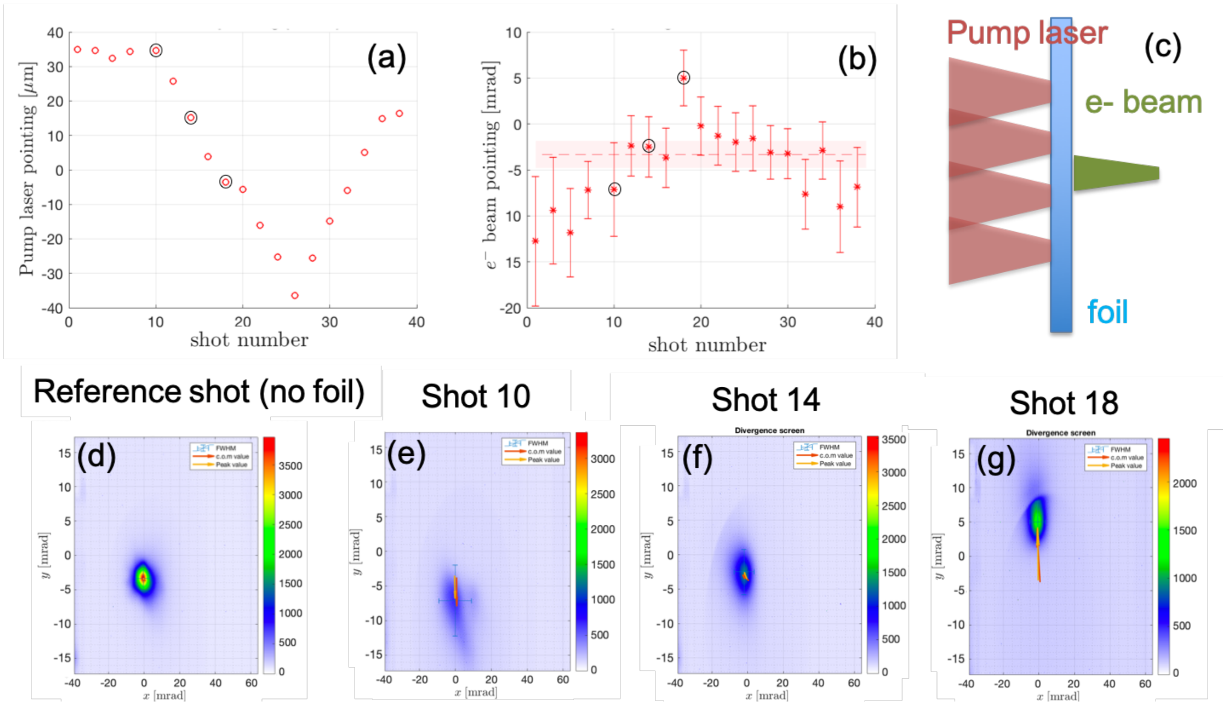

Fig. 7.7: (a) Vertical pointing of pump laser on the foil as measured by the alignment objective for a set of shots. (b) Corresponding vertical pointing of the electron beam on the divergence screen. (c) Schematics of the experimental conditions for the vertical kick scan: each pump laser (red) represents one shot. (d-g) Divergence screen images of the electron beam profile for a selection of shots. For this data set, the installed solid foil was 60 μm thick Aluminium, the LWFA to foil distance was 3 mm and the energy on target of each laser was 0.9 J (LWFA) and 1.5 J (pump).

to compensate for the horizontal drift of the foil and therefore keep approximatively the same pump-probe alignment for several shots. In this way we managed to minimise an important source of pump-probe misalignment inherent to our set-up. In the future, a tape foil with very precise positioning is considered to overcome this issue.

7.4 Experimental results

The first remarkable feature that was observed on the probe electron beam with the CFI pump laser on was significant transverse deviations of the electron beam pointing (i.e. centroid position on the divergence screen). These transverse deviations, also referred as "kicks", were clearly visible on the divergence screen (Fig. 7.7 (d-g)), as well as on the electron spectrometer, where a vertical kick translates to a correlation between energy and vertical position (see Fig. 7.8).

The first hypothesis we considered to explain this observation was the effect of the TNSA magnetic fields on the probe electron beam due to a pump-probe misalignment. Similarly to the experimental results of Ref. [135] discussed in section 7.2, the probe electron beam experiences the TNSA magnetic fields which act as a magnetic lens. In our experimental set-up, the electron beam is much smaller than the radial extent of the magnetic lens, which together with the pump-probe misalignment would lead to the observed transverse kicks. To validate this

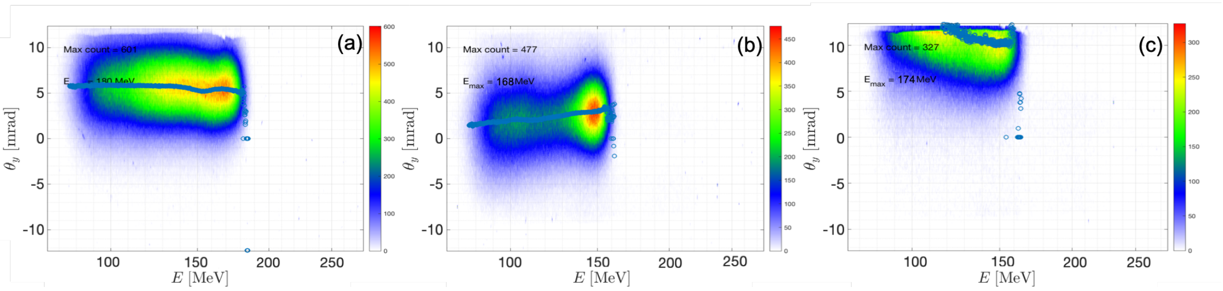

Fig. 7.8: Examples of electron spectra: (a) Reference spectrum, with solid foil in but no pump. (b) Pump laser on, pump laser vertical pointing at $\approx 60\,\mu$m. (b) Pump laser on, pump laser vertical pointing at $\approx -40\,\mu$m. Pump laser pointings were measured with the alignment objectiive.

hypothesis we changed the pump-probe vertical offset (see Fig. 7.7 (c)) so as to scan vertically the magnetic structure with the probe electron beam. As expected from a lens-like structure, the vertical kick direction changed from upwards to downwards after a certain offset. One of these vertical offset scans is shown in Fig. 7.7, where the vertical pointing of the pump laser is plotted for each shot as measured by the alignment objective in Fig. 7.7 (a) and the corresponding electron beam centroid position on the divergence screen are plotted in Fig. 7.7 (b). Examples of divergence screen images of a reference shot (no pump), upwards, center and downwards kicks of this scan are shown in Fig. 7.7(d-f) respectively. In these selected divergence screen images, the blue error bars represent the FWHM size of the beam profile and the orange and yellow arrows indicate the kick direction and magnitude with respect to the reference value (i.e. without pump laser). In order to check the sensitivity of this measurement to the definition of the beam centroid position, the center of mass (c.o.m.) calculation (orange arrows) is compared to the position of the signal peak value (yellow arrows), not showing a significant difference that could affect the ulterior analysis. This analysis were done with a 60-μm-thick Aluminium target.

As mentioned before, the vertical kicks were also observed in the electron spectrometer via the correlation between energy and vertical position. Two examples of "kicked" electron spectra are shown in Fig. 7.8. Fig. 7.8 (a) corresponds to a downwards kick (towards negative y) and Fig. 7.8 (b) corresponds to an upwards kick. Due to the limited aperture of the spectrometer dipole and the relatively long distance from the interaction point to the entrance of the dipole spectrometer, strongly kicked particles could not be detected in the spectrometer. Yet, assuming that the energy slice-divergence has a gaussian distribution, a gaussian fit was performed to the visible part of the energy-slice signal to retrieve the center of the gaussian and therefore the energy-slice vertical centroid position, plotted in blue dots in Fig. 7.8. The main advantage of the energy-kick correlation, quantified via the the slope $\frac{\partial \theta_y}{\partial E}$, is that it is not sensitive to the pointing jitter of the LWFA electron beam (in contrast to the kick measurement on the divergence screen).

Assuming that every energy slice of the probe electron beam sees the same average magnetic field one can estimate the longitudinally integrated average magnetic field from the correlation between energy and vertical centroid position. The angular kick experienced by a relativistic electron beam of energy $E \approx \gamma mc^2$ propagating under a uniform magnetic field B for a distance

δz can be expressed as $\theta = \frac{e\,c\,B\delta z}{E}$. Therefore the energy-slice centroid position $\theta_y(E)$ satisfies

$$\left|\frac{\theta_y(E_2) - \theta_y(E_1)}{E_2 - E_1}\right| = \frac{e\,c\,B\delta z}{E_2 E_1} \tag{7.1}$$

This equation shows that it is possible to retrieve the longitudinally integrated magnetic field $B\delta z$ experienced by the electron beam from the measured "kicked" spectra. In order to carry out this analysis, the electron energy range over which the energy-slice pointing was measured needed to be selected on a shot-by-shot basis due to energy fluctuations and the limited angular acceptance of the spectrometer. Following this method, azimuthal magnetic fields of several kT μm were retrieved, compatible with previous simulations performed in the aforementioned experimental set-up [135].

Using these integrated magnetic values for different vertical pump-probe offsets, an effective focal length of the magnetic structure could also be estimated, similar to what was done in Ref. [139]. Even if the magnetic-lens structure created in the surface of the solid is very likely non-linear unlike for a real lens, the focal length estimation can be used to evaluate what kind of electron beam profiles one should measure for a given energy at a given distance. Focal distances of $\sim$ 10 mm for $\sim$ 150 MeV were retrieved. However, a posterior analysis showed that depending on the experimental conditions focusing or defocusing effects were measured. Unfortunately there is not enough experimental data taken in a consistent manner to study this subject (focusing or defocusing focal length) from the vertical pump-probe offset scan to draw relevant conclusions. Yet, the results from the delay scans presented in the following paragraph might hint a possible explanation for this observation.

A second type of scan was done to study the kick feature: pump-probe temporal delay scans. For this purpose, the offset between the electron beam and the pump laser was kept constant by checking the pump pointing via the alignment objective and correcting for the longitudinal drift of the foil on a shot-to-shot basis. Results of this scan for the 60 μm thick Al foil are shown in Fig. 7.9. In this figure the average pointing of the electron beam on the divergence screen (Fig. 7.9(a)) and the averaged slope of the electron beam spectrum ($\frac{\partial \theta_y}{\partial E}$) (Fig. 7.9(b)) are plotted as a function of the pump-probe delay. The reference values without pump laser and without the solid target are plotted as a shadowed blue and red area respectively, which are centered at the mean value and whose width correspond the standard error. Figures 7.9(c-g) show examples of divergence screen images at different delays. Remarkably the vertical kick feature is present over several picoseconds, up to at least 40 ps which was the largest delay achievable with the experimental set-up. Note that for TNSA magnetic fields excited by longer laser pulses, simulations have also shown long-lived TNSA magnetic fields at the surface where the laser pulse hits the solid foil [132].

At short delays both the divergence screen and spectrometer measurements seemed to indicate a transition between upwards and downwards kicks. A zoom version at these short delays, together with the individual shot measurements (without the averaging) is plotted in Fig. 7.10. Note that in this figure, and in Fig. 7.9, the zero-delay does not necessarily correspond to the physical zero-delay situation due to possible experimental errors in the synchronisation measurement. Yet, for both plots in Fig. 7.9, the measurements at $\Delta t < -1$ ps are compatible with the reference values, indicating that indeed the electron probe arrives before the pump laser to the interaction point. At short delays, the results showed in Fig. 7.9 indicate that the direction of the vertical kicks is opposite (at least in average) to the consistently measured kick direction at long delays ($\Delta t > 0.5$ ps), the transition happening on a temporal scale of $\sim$ 1 ps.

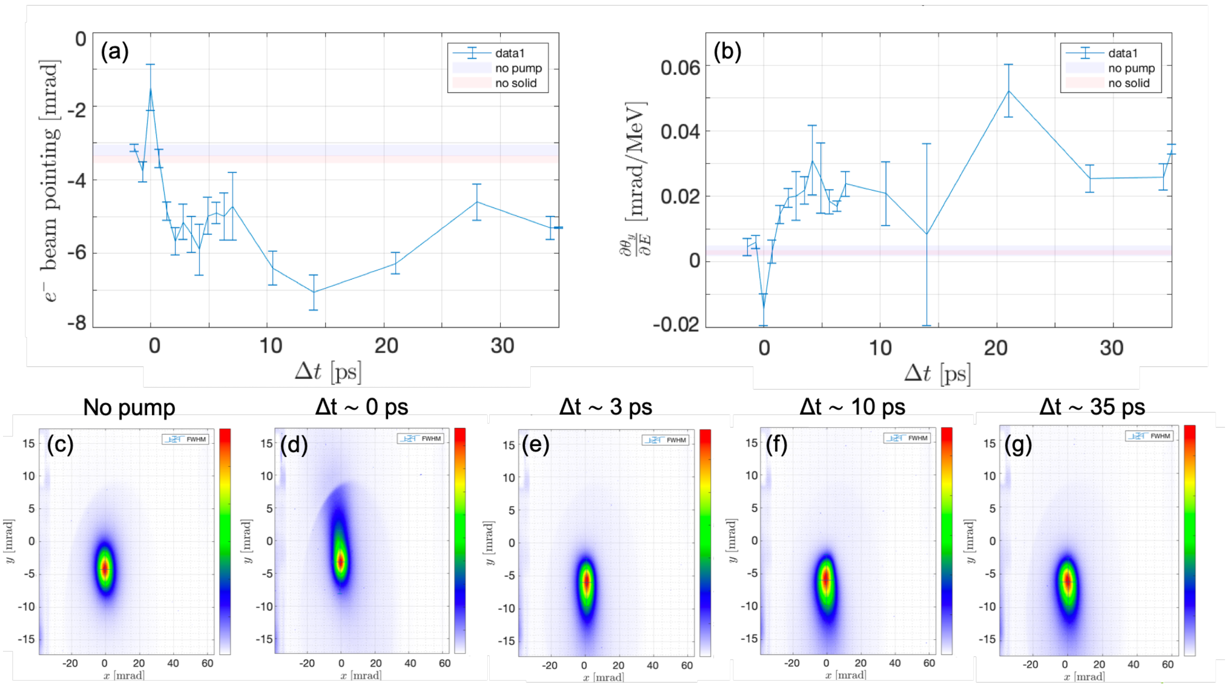

Fig. 7.9: Temporal scan at a fixed pump-probe offset. (a) Vertical pointing of the electron beam on the divergence screen. (b) Reconstructed slope from the probe electron energy spectra. In (a) and (b) vertical errors bars represent standard error of the mean (c-g) Divergence screen images of selected shots at different delays. See text for more details.

Remarkably, other data sets taken with the same experimental conditions also show this ~ 1 ps transition.

Assuming that the TNSA magnetic fields are responsible for the kicks, this transition of the kick direction at short delays could be explained by the two azimuthal magnetic structure on each side of the foil with different polarity and the evolution of their relative strength. This hypothesis would need further verifications to be confirmed, such as comparing different thicknesses, using a different foil or comparing different radial offsets. Also PIC simulations are underway to assess this phenomenon.

So far we have only discussed the kick feature on the electron probe. Indeed, for the Aluminium 60 μm thick foils this was the only significant feature that was measured by the diagnostics. For Mylar 13 μm, some shots taken at short delays and right after the alignment procedure showed a stronger effect on the electron beam, leading to the absence of any beam-like feature observed by the probe diagnostics, which instead measured a strongly disorded beam profile (see Fig. 7.11). To differentiate this type of shots from the transverse kicks we will refer to them as the "blow-up" feature, since the probe beam is blown-up at the interaction point. For these first observations of blown-up beams with Mylar 30 μm, we were not able to consistently reproduce these feature to take a useful data set. The main reason was that the Mylar 13 μm foils required to use a metallic support with individual holes where the Mylar was placed, one hole per shot, but our control of the rotation stage was not able to accurately shift from one hole to the next one. This lead to significant amount of shots being centered on the metallic structure rather than on the Mylar foil, which triggered the decision to only shoot on Aluminium foils.

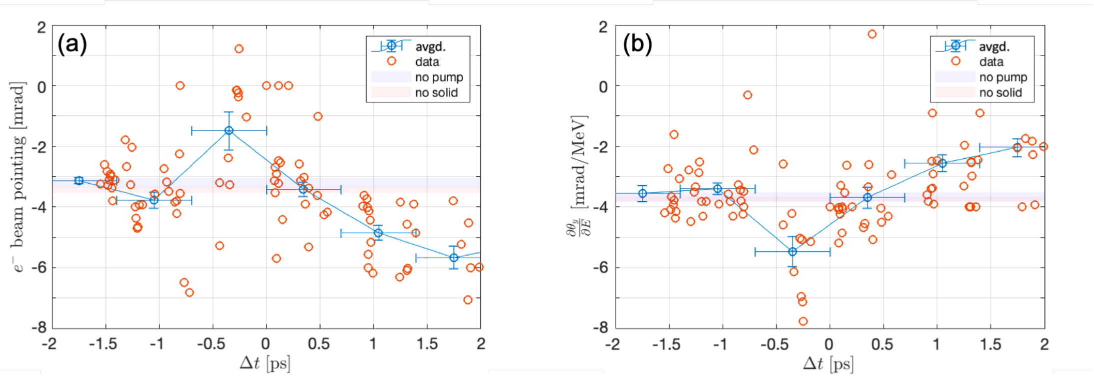

Fig. 7.10: Zoom on temporal scan at a fixed pump-probe offset. (a) Vertical pointing of the electron beam on the divergence screen and (b) reconstructed slope from the probe electron energy spectra. Orange circles are individual shot measurements, blue circles are averaged values. Vertical errors bars represent standard error of the mean, and horizontal error bars represent the interval over which the averaging is carried out. See text for more details.

The blow-up feature was also observed when an Aluminium 15 μm thick foil was used, and we were able to consistently reproduced the feature by keeping the same pump laser pointing on the foil. Indeed, when the system was misaligned, i.e. when the pump laser pointing drifted due to the longitudinal displacement of the foil, the blow-up feature disappeared and instead the transverse kick feature was observed. This clearly hinted that the blow-up feature corresponds to the position where the pump-probe spatial overlap was achieved. Examples of divergence screen images with the blown-up beam profile are shown in Fig. 7.11(b-e).

Despite the clear interest of these blow-up beams, which need to be driven by much more intense electromagnetic fields than those leading to the kick feature, they have the problem that one cannot retrieve typical beam features such as divergence or pointing from the probe measurements. Furthermore a large amount of the beam charge was lost and not detected, due to their large angular defections and the large distances between the interaction point and our detectors. Therefore quantifying the effect of the pump on the blown-up probe remains a challenging task with the current experimental set-up. As a first approach, the divergence screen images were analyzed in terms of the number of pixels that had a certain level of signal relative to the maximum detected signal in the same image. To do so, only the signal in the central region of the screen is considered, i.e. only those electrons that escaped the vacuum chamber through the exit window and not through the chamber walls.

For each divergence screen image, the percentage of central pixels with a level of signal between 0-20%, 20-40%, 40-60%, 60-80% and 80-100% of the maximum signal were computed. Comparing these values for the blow-up shots, kick shots and reference shots, it was found out that the 20-40% interval provided the strongest difference between the blow-up feature and the rest. Therefore this value was used as a scalar to quantify the presence or absence of the blow-up feature.

By compensating online the small misalignments due to the longitudinal motion of the wheel, we were able to scan the temporal evolution of the blow-up feature. The results of this pump-probe delay scan are plotted on Fig. 7.11(a), indicating that ~ 1 ps after the laser-solid interaction the blow-up feature disappears. The measured temporal evolution, together with the fact that it only happens when the pump-probe spatial overlap is presumably achieved,

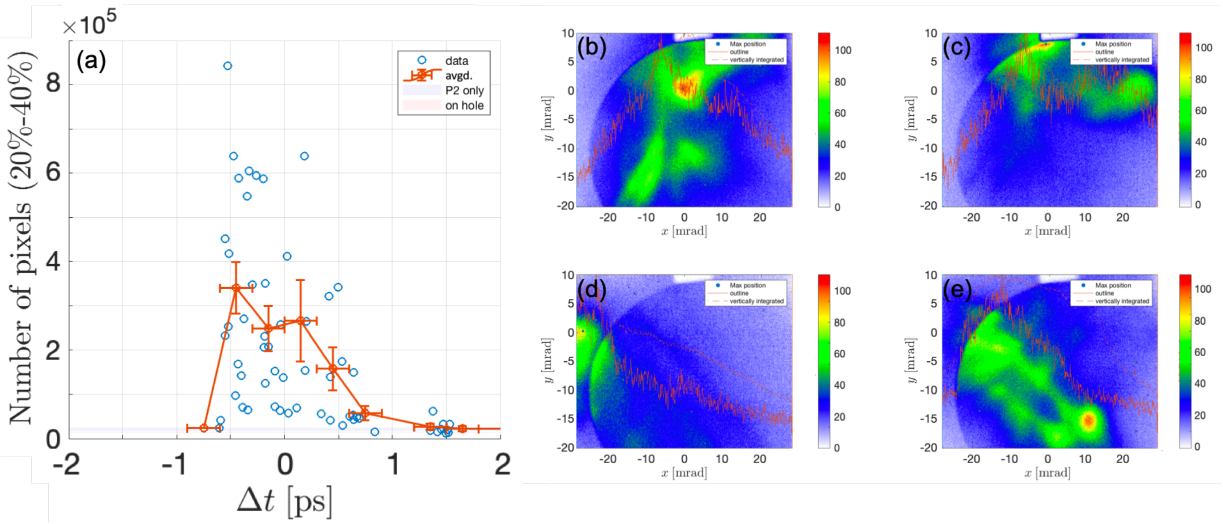

Fig. 7.11: (a) Number of pixels with a signal level between 20% and 40% of the maximum pixel signal on the divergence screen as a function of the pump-probe delay. (b-e) Examples of beam divergence screen images of "blown-up" probes.

suggests that this feature could correspond to the CFI unstable fields driven by the CFI pump at the central part of the interaction. Nevertheless it remains unclear to us at the moment why this feature was not observed with the Aluminium 60 μm foil. The Al 60 μm data was taken on a different day that the Al 15 μm, and between the two days the laser experimental conditions were different.

To summarise the main experimental results presented in this chapter, two features have been observed on the electron beam when probing the pump laser-solid interaction:

- The transverse kicks, observed in the divergence screen and in the electron spectrometer. For a given pump-probe offset the kick feature were present on the probe in the same direction at long pump-probe delays ($\Delta t \gtrsim 40$ ps). At short delays though ($\Delta t \lesssim 1$ ps) the kick feature changed direction (upwards at short delays and downwards at long delays). The kick feature, for which the useful data sets were taken with a 60 μm solid foil, could be explained by the TNSA magnetic field driven by the pump laser-solid interaction over radial scales larger than the laser spot-size. In this case, integrated magnetic fields of several kTμms were estimated, and a transition at around $\Delta t \sim 1$ ps from the rear-to-front dominated interaction was inferred.

- The blown-up beams, for which the probe propagation is so disrupted that many of the probe electrons miss the detectors, which complicated their quantitative analysis. Useful data sets with this feature were only taken with 15 μm thick Aluminium, but it was also observed with 13 μm thick Mylar. This blow-up feature is only observed at short pump-probe delays $\Delta t \lesssim 1$ ps and, when observed, small pump-probe misalignments tracked via the alignment objective lead to its disappearance (and only the kick feature remains). The hypothetical origin of this feature would be the CFI driven by the pump laser on the solid target.

Apart from these two types of observation, the polarisation of the pump laser was changed from P to S, but no significant change was observed neither for the transverse probe kicks nor for the beam blow-ups. This could be due to the small angle of incidence of the pump laser (8°), but unfortunately we did not have time to modify the set-up to increase this angle.

PIC simulations could shed light on the physical processes that could originate under these experimental conditions and gave raise to the experimental observations. In order to properly simulate the physics of the laser-solid interaction, not only the femtosecond high peak intensity part of the laser needs to be considered but also the nanosecond scale pre-pulse. This pre-pulse can be intense enough to create a pre-plasma in the front of the target which will impact the main laser energy deposition process and therefore the posterior dynamics in the bulk of the solid target. Furthermore the computational cost of these simulation is non negligible since ideally one would like to simulate a large window that transversely extends up to several times the pump laser spot-size and longitudinally the foil thickness. All this over at least a picosecond time scale. These simulations are still underway.

In conclusion, this experimental campaign tested an upgraded version of the previously used laser-based platform to study the onset of CFI in laser-solid interactions [123]. This new set-up allowed to retrieve temporal information of the evolution of the electromagnetic fields arising in the interaction, at the cost of the loss of the inherent spatial overlap. The pump-probe spatial overlap was identified as an important limitation to the robustness of the experimental data due to the longitudinal drift of the solid target from shot to shot, which lead to an involuntary drift of the pump laser pointing on the foil. Nevertheless this drift was monitored online with a high resolution objective which allowed to correct for it on a shot-to-shot basis. Compared to the previous set-up, two new probe features were observed: transverse kicks, present over 10's of picoseconds when the pump-probe spatial overlap was not achieved, and a severe beam disruption or beam blow-up present only in the first picosecond after the laser-solid interaction and presumably when the pump-probe spatial overlap is achieved.

Several lessons were learned for future experiments, but clearly the most important aspect that jeopardises the achievement of the experimental goals is the pump-probe spatial overlap. The main source of misalignment in the presented set-up came from the foil mount, but even if this was solved there would still be an inherent jitter in the laser system that would ideally need to be monitored. In terms of lay-out, the first important modification is to replace the wheel mount by another mechanisms that allow to change the foil material at the interaction point without shifting its longitudinal position. A new set-up with a tape instead of a wheel, is currently being commissioned, showing a significant improvement in the positioning and reproducibility of its motion. Secondly, larger angular acceptance is required for the probe diagnostics, which could be achieved by placing them significantly closer to the interaction point. Finally a higher harmonic could be used for the polarimetry diagnostic to reduce the light produced by the pump laser at the probe wavelength, as well as a larger angle between reflected pump laser and the optical axis of the polarimetry objective.

CONCLUSION

Results obtained during the PhD

In this manuscript I have presented the main scientific contributions of my work during the three years of my PhD. This work has been mainly focused in two different aspects of the interaction of a relativistic particle beam with plasmas: the beam-driven plasma wakefield excitation and its application to accelerate charged particles, and the beam-plasma streaming instabilities. Both processes were studied in the context of the FACET-II facility, where each process will have a devoted experimental program using the delivered high energy (10 GeV) particle beam and different plasma sources. For both experiments, the X-ray/gamma radiation diagnostics will be of key importance to achieve the experimental goals. An ensemble of radiation diagnostics has been designed, installed and commissioned at FACET-II, and its performance has been successfully simulated in the context of both experiments. Finally, an experimental campaign was carried out at LOA to measure the onset and evolution of the electromagnetic field structures arising in an ultra-short laser-solid interaction.

In the context of beam-driven plasma wakefield acceleration, a new experimental technique has been proposed to measure the matching conditions of an electron beam propagating in a plasma ion cavity [46]. This technique relies on the emitted betatron radiation to assess the transverse beam dynamics, and via PIC simulations it has been shown how this diagnostic can be used to retrieve information about the beam matching conditions with FACET-II parameters. Furthermore this diagnostic can further provide an insight into the beam centroid oscillations and the associated development of the hosing instability. GEANT4 simulations were also performed to account for the photon detector response to the different signals, showing the capability of FACET-II detectors to measure the required radiation features to assess the relevant beam dynamics. This study bears important implications to achieve one of the next milestones in the field of PWFA: the trailing beam emittance preservation.

In the context of beam-plasma instabilities, the effects of the system boundaries on the oblique instability, dominant in the relativistic diluted regime, have been examined [111]. A new spatiotemporal model has been developed, allowing to model the instability when a longitudinally finite beam is considered. A significant slow-down of the instability is found with respect to the theory of unbounded systems in the ultra-relativistic regime ($\gamma \gg 1$). Accounting for the spatiotemporal evolution is crucial for experiments studying the interaction of a high energy particle beam with plasmas, such as the beam filamentation experiment at FACET-II. Furthermore, including the finite extent of the electron beam brings the transverse wakefield excitation and the associated self-focusing effect into play. The interplay between the instability and the self-focusing process is studied, revealing that the self-focusing effect can quench the instability for a non-negligible set of electron beam-plasma parameters. Finally a preliminary analysis of the quasi-static approximation applied within the formalism of beam-plasma instabilities has been discussed, and an original non-linear saturation mechanism observed in simulations has been presented.

Concerning the experimental campaign at LOA aiming at probing the laser-solid interaction with a LWFA electron beam, a new experimental layout enabling to measure the temporal evolution of the electromagnetic fields was successfully implemented. Two probe features were observed depending on the relative spatial alignment between the pump laser and the probe electron beam. The temporal evolution of both features was measured, showing different features at short delays ($\lesssim 1$ ps) and at long delays (from 1 ps to at least 40 ps). At short delays, a good pump-probe spatial alignment lead to strong probe disruption, with a significant part of the probe electron beam being deflected out of the acceptance of the diagnostics. At the same short delays, a pump-probe misalignment lead to a steering of the probe electron beam. For a fixed misalignment offset, the direction of this steering changed sign at pump-probe delay of ~ 1 ps. This last observation could be reconstructed thanks to the undesired longitudinal motion of the solid target. At large delays ($\gtrsim 1$ ps) the severe probe disruption, measured with the pump-probe spatial alignment at short delays, was no longer observed. However the steering feature remained up to a delay of ~ 40 ps (the maximum achievable delay with the experimental set up). Presumably, these results indicate that the misaligned shots were sensitive to the TNSA magnetic field, with a transition between the rear-face dominated to front-face dominated regimes at ~ 1 ps, and that the aligned shots correspond to the onset of CFI in the target whose unstable fields severely disrupt the probe propagation before their relaxation ~ 1 ps after the laser-solid interaction.

Short-term perspectives

A personal view of the short-term perspectives to continue with the presented lines of research are proposed in the following paragraphs. With the FACET-II facility delivering the first beams to users as early as beginning of 2022, the experimental campaigns will provide a natural test of the validity of the theoretical/simulation work presented in this manuscript. If confirmed, these results will likely have a major impact in the realisation of the experiments.

For the E300 PWFA experiment, the betatron radiation diagnostic will need a significant experimental effort and dedicated beam time to test step-by-step the working principles and identify possible limitations. First of all, a single bunch configuration could be tested and the integrated betatron signal should be compared to the direct emittance measurements, for instance using the proposed method of shifting its waist position. Moreover, some of the beam parameters could be scanned to reproduce their correlation with the betatron radiation angular distribution observed in simulations. A potential limitation of using the single bunch configuration, i.e. the drive-only betatron radiation, is the broad energy spectrum of the beam after propagating in the plasma, with different particle energies having significantly different dynamics in the plasma. As a second step, the retrieval process of the trailing betatron radiation from the integrated drive and trailing radiation should be worked out under experimental conditions. If all these preliminary steps worked, then the final correlation plot emittance vs integrated energy could be produced. As explained in the manuscript, accurate and assumption-free beam emittance measurement at the nominal FACET-II parameters would be needed, which might require multi-shot methods and therefore stable and reproducible acceleration. If these simulations results are validated in the experiment, the betatron diagnostics would significantly contribute to the experimental demonstration of the trailing emittance preservation by directly assessing the beam matching dynamics in the plasma, providing a powerful diagnostic to minimise the emittance growth.

In terms of the gamma diagnostics, the absolute calibration of the GAMMA1 diagnostic could provide useful information for different experiments. For this, an accurate characterisation of the gamma source is required: a bremsstrahlung source with a properly characterised electron beam and solid target can be used for this purpose. For the GAMMA2 and GAMMA3 diagnostics, a procedure to align the filters to the gamma-ray axis is required. As a first tentative, the filters will be motorised in the vertical direction with a stepper motor so that the the GAMMA2 signal can be measured without filters and then the filters can be centered to the measured signal. Finally, in order to increase the GAMMA3 sensitivity to the transmitted high energy gammas, a converter could be installed in front of the GAMMA3 scintillator.

In the context of the PWFA experiments at FACET-II, these gamma diagnostics aim to retrieve information on the electron beam dynamics. Yet, the process of inferring all the beam Twiss parameters from the gamma-ray parameters is a multidimensional problem with many inter-correlations that have not been discussed in this manuscript, and requires to make simplifying assumptions to decrease the number of degrees of freedom of the system. A different approach to this problem is to use bayesian inference or machine learning techniques to do optimisation studies, in which one or two beam parameters are optimised and for which the gamma-ray signal can be used as an input to the optimisation process. Such approach is currently gaining popularity in the fields of LWFA [140] and in conventional acceleration [141], and using AI techniques to retrieve beam dynamics information from betatron radiation in PWFA would be, if successful, an excellent evidence showing the power of AI techniques in experimental physics.

For the beam-plasma instability experiment at FACET-II, the main experimental challenges will come from being able to consistently measure the signatures of the instability from the measured signals. In this sense the shadowgraphy diagnostics will provide precious information for the gas density plasma target: by measuring the high frequency signal of the probe for different propagation distances in the plasma, this diagnostic will be the most sensitive to the instability signatures. Furthermore the optimisation and characterisation of a gamma-ray source based on the beam-plasma interaction could be explored, with the most-likely scenario of non-linear plasma wakefields at high density plasmas as the best candidate, reaching or exceeding $\sim 10\%$ conversion efficiencies from the beam energy to the radiation according to our simulations.

In terms of the theoretical modelling of the instability, several fronts could be further investigated. The quasi-static approximation together with the finite size of the electron beam could be used to model the system from the perspective of the plasma response to a given quasi-static perturbation. This approach could be useful to model finite beam-plasma systems for which the beam length is of the order of the plasma skin depth, for which the existing theories (temporal or spatiotemporal) are not valid. The use of quasi-static PIC codes could shed some light on this modelling. Moreover this theory could be use to describe some aspects of the non-linear evolution of the system, such as the field amplitude at saturation.

Finally a new experimental campaign at LOA is planned to correct for the identified limitations of the designed layout. The main device to upgrade is the solid target mount, which has already been designed and implemented in another experiment and that will allow to collect the data in a more consistent and robust manner. Secondly, the acceptance of the probe diagnostic need to be widen to capture the severely disrupted probe electron beams observed during the last campaign. Finally, the polarimetry diagnostic needs to be modified to reduce the parasitic light originated by the pump laser on the target at the probe wavelength. This could be done by going to higher probe frequencies (third harmonic instead of second harmonic) and increasing the angle between polarimetry and pump lasers. With these upgrades a more accurate temporal evolution of the observed features could be retrieved, and this for a wider variety of materials and target thicknesses. The results from these experiments could help to refine and validate the existing models of these high-power laser interaction with solid targets, relevant for the TNSA scheme of ion acceleration as well as for the physics of the CFI.

Outlook and long-term perspectives

The different mechanisms involved in the interaction of a relativistic particle beam or a high power laser pulse with plasmas are of fundamental importance to understand some of the most energetic electromagnetic events in the Universe. In laboratories, these interactions allow to convey energy into the plasma, exciting collective electromagnetic phenomena that can potentially be harnessed for industrial or societal applications. The fast and microscopic spatiotemporal scales over which these interactions take place in laboratories make very challenging its experimental characterisation and control with currently available technologies, but understanding the underlying mechanisms is crucial to build new technologies based on these processes. Furthermore at much larger scales these physical mechanisms are thought to play a fundamental role in several astrophysical scenarios, whose modelling could be refined by the results of these experiments.

The plasma-based accelerator technology is nowadays very close to pass the first "proof-of-concept" stage. Indeed, electron acceleration with acceleration gradients much larger than those provided by conventional accelerators are regularly obtained in high-power laser facilities around the globe, as well as in PWFA experiments at large-scale accelerator facilities. Laser plasma-based accelerators are starting to become a tool to perform experiments in other fields [30, 123], which otherwise would need to be hosted by one of the conventional accelerator facilities. Furthermore several limitations to the laser wakefield acceleration concept are overcome with the use of original techniques [32], making of this quickly evolving field a promising technology that can widen the access to particle accelerator in the years to come.

A large part of the required improvement in laser wakefield acceleration comes from the existing femtosecond laser technology rather than from the plasma process itself, namely in terms of wall-plug efficiency and stability. A new and promising approach to the stability limitation is the use bayesian inference or machine learning. However the wall-plug efficiency of the laser wakefield accelerators does not have nowadays a clear solution and will require extensive R&D in the next decades, setting a very important limitation for high energy particle acceleration. Due to the better stability and wall-plug efficiency, the beam-driven concept represents the most promising scenario for this purpose. If the emittance preservation goal is achieved in a beam-driven plasma wakefield acceleration, together with the already demonstrated high transfer efficiency and low energy spread of the accelerated beam, this technology should be ready to perform as an energy-booster of a conventional accelerator. Nevertheless, there would remain some issues before relying solely on this technology to build a particle collider, such as the repetition rate, staging, hosing instabilities, ion motion or even the more essential positron acceleration, not addressed in this manuscript.

Concerning the plasma streaming instabilities, having accurate models for these processes is going to be critical for several scenarios involving the interaction of a relativistic stream of particles with plasmas. To capture all the relevant physics under realistic conditions, models beyond the unbounded collisionless approximations are required. Laboratory experiments will help to explore some of these additional physics, such as the influence of collisions. The beam-plasma instabilities in solid plasma targets are expected to be affected by collisions, but at plasma temperatures where existing models have never been tested. Another phenomenon for which existing models might fail at the solid plasma densities is the ionisation, where processes as the Ionisation Potential Depression [142] might play an important role and for which these experiments might provide a precious insight.

These experiments on extreme interactions at accelerator facilities are complementary to the experiments performed in laser facilities, in which a laser pulse is the element that supplies the energy to the plasma. The main difference of using a laser pulse instead of an electron beam is that the laser pulse do not propagate through overdense plasmas, and therefore can deposit efficiently a large amount of its energy in a very small region of the target. However the light-matter interaction under these extreme conditions is not fully understood and the existing models can only be tested indirectly via the byproducts of the interaction. This field is quickly evolving and original solutions to better characterise the experimental conditions of the laser-matter interaction are being implemented. A remarkable example is the use of plasma mirrors to clean the laser pre-pulse, which shows how the accurate understanding of one aspect of the laser-solid interaction can later be used as a tool to further explore this interaction at a different scale.

Another important field that is gaining popularity in the recent years, substantially thanks to the design and construction of these experimental facilities where extreme beam or laser-plasma interactions can be explored, is the Strong-Field regime of QED. The results presented in this manuscript have important implications and can be extended to this topic and the associated production of bright gamma-ray bursts. Besides the contributions presented in this manuscript to the E320 SFQED experiment at FACET-II, the studies of this manuscript have lead to new (or revisited) experimental concepts involving the beam-plasma interaction with strong connections with the field of SFQED. For example the work of Ref. [122], in which the beam-solid interaction is used to self-focus the electron beam and reach peak beam densities of the order of the solid plasma density, would allow to reach electromagnetic field amplitudes close to the Schwinger limit in a beam-plasma interaction at FACET-II (E332 experiment). Furthermore, a new experimental proposal has recently appeared to go beyond the Schwinger limit and reach the non-pertubative regime of QED using HEP beam collisions [143]. In the intersection of both works, we are currently studying the potential use of a solid density plasma to replace one of the beams in the collision of the aforementioned concept. The plasma acting as a mirror for the beam self-fields, the beam could collide with its own self-fields, ultimately simplifying the proposed concept (one beam instead of two) and offering more flexibility in terms of its experimental realisation. This example shows how the physics studied in my PhD of beam-plasma interaction under extreme conditions can be extended to the research on SFQED.

Appendices

Appendix A

PARTICLE IN CELL FRAMEWORK

This appendix briefly describes the principles of the Particle-In-Cell (PIC) algorithm following Ref. [144]. It also provides information about its implementation in the simulations whose results are presented throughout the manuscript. In plasma physics, the PIC method gained popularity in the early 1960s, enabling the modelling of plasmas with a large number of degrees of freedom [145], and is nowadays the leading tool to explore numerically several plasma processes such as plasma-based acceleration [146].

The electromagnetic PIC method consists on modelling a system by tracking its individual macro-particles (simulated particles that represent several particles of the real system) in a continuous phase space, and computing the associated electromagnetic fields on a discrete grid. In this way the trajectories of charged particles can be tracked under the self-consistently computed electromagnetic fields. Mathematically, this is carried out by a finite-difference on-grid discretisation of the particle's equations of motion and of Maxwell's equations.

Figure A.1 illustrates the main processes of the electromagnetic PIC method. On the left figure, a schematic representation of the PIC method in 2D is displayed. Individual Macro-Particles are represented by the red (positively charged) and blue (negatively charged) circles. Their position and velocity, represented by the arrow, evolve in continuous space. From their distributions, the charge and current can be computed on the discretised grid of a given cell size $\Delta x \times \Delta y$. From these values, the electromagnetic fields on the grid can be derived using the discretised Maxwell's equations, which can then be extrapolated to the individual positions of the Macro-Particles. Note that the temporal evolution of the system, required to solve Maxwell's equation, is also discretised with a characteristic time-step Δt. Finally the equation of motion allows to advance (or push) the Macro-Particles using the extrapolated electromagnetic force at their position. Once the Macro-Particles have been pushed the process can restart, closing the loop that is schematically displayed by the yellow squares in the right image of Fig. A.1.

Additional steps can be inserted in the PIC loop, represented by the blue squares in the right image of Fig. A.1. For instance, the emission of EM radiation by relativistic particles can be computed internally in the PIC code right after the particle pushing, which is exploited in Sec. 6.2 to extract the radiation emitted by the beam during the development of beam-plasma instabilities. Numerical filtering can also be applied to the currents and fields to dump high frequency modes that are numerically unstable due to the space-time discretisation [147], which is mentioned at the end of Sec. 5.1.2 to discuss the numerical resolution of the simulations.

The PIC algorithm is a powerful tool to study the evolution of a complex plasma system which often cannot be modelled from basic equations, such as the multi-dimensional excitation of a non-linear plasma wave. However the PIC method can be very demanding in terms of computational power, especially when several spatiotemporal scales are involved in the simu-

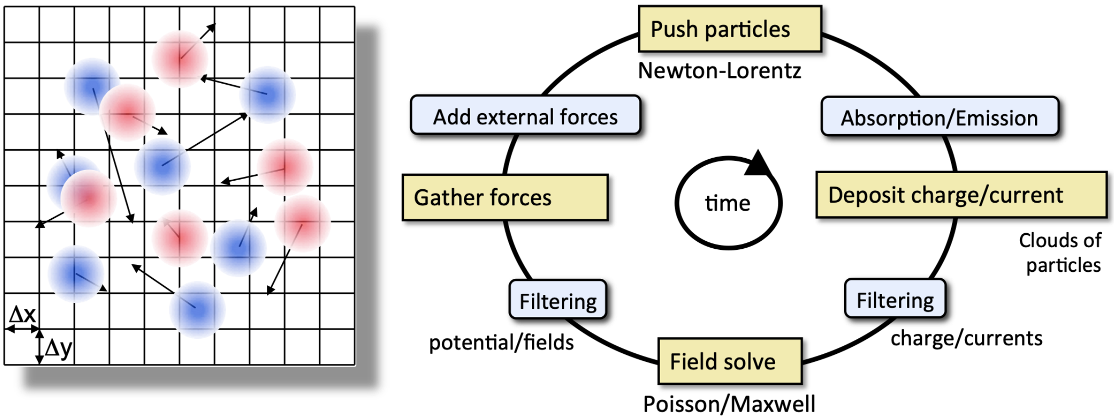

Fig. A.1: Left: schematic representation of a two-dimensional PIC cell together with the Macro-Particles represented by red and blue circles and their velocities, represented by the arrows. Right: schematic representation of a PIC loop. The main steps of the loop are displayed in the yellow squares, and additional steps are displayed are displayed in blue squares. Figure from Ref. [144].

lated process, the spatiotemporal scales of the simulated process typically setting the limits of the numerical resolution. This has motivated the development of massively parallel PIC codes, being usually run in super-computers.

The space-time discretisation of PIC simulations leads to the appearance of numerical processes of non-physical nature, which can dominate the evolution of the simulated system if the numerical parameters are not properly set. Apart from the cell size and time-step, each step of the PIC loop has its corresponding numerical process which needs to be set accordingly to each other to control the numerical effects. A introductory overview of the different numerical processes relevant in PIC simulations of the interaction of a relativistic electron beam or laser pulse with plasmas can be found in Ref. [144].

The ensemble of numerical parameters and algorithms used in a PIC simulation are often called a numerical scheme. Depending on the properties of the system that is simulated, different numerical schemes can be used. For the CALDER [148] simulations performed in Part II, i.e. of relativistic beam-plasma instabilities, an important numerical effect is the so-called Numerical Cherenkov Instability [149]. This process arises from the coupling of poorly-resolved electromagnetic modes with spurious beam modes. In CALDER a numerical scheme has been implemented based on Ref. [150] to suppress the growth of this numerical phenomenon.

In these simulations, the space time discretisation is given by cell size $(\Delta x, \Delta y) = (0.042, 0.084)k_p^{-1}$ (x being the longitudinal coordinate) and the time step $\Delta t = 0.041\omega_p^{-1}$. All charged particles (beam electrons, plasma electrons and plasma ions) are simulated using 100 Macro-Particles per cell. For the grid depositions, third order interpolations are used. To suppress the Numerical Cherenkov Instability, a compensated bilinear filter is applied twice per time step to the currents and once every five time steps to the fields. Convergence studies were carried out in terms of cell size and number of Macro-Particles to find these appropriate numerical parameters.

These PIC simulations were run in the supercomputer TGCC Joliot Curie of CEA [151]. As an illustrative example of the computation cost of these simulations, the cost of the 2D simulation used in Fig. 5.3 was $\approx 50,000$ CPU hours for mm-scale beam propagation distances.

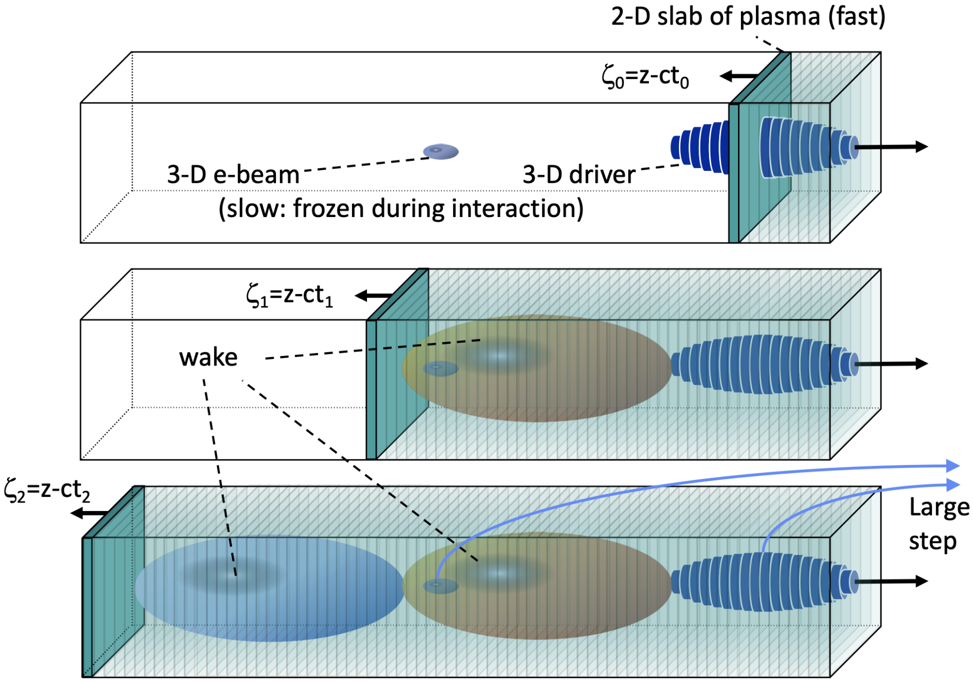

Fig. A.2: Schematic representation of the quasi-static method. Figure from Ref. [144].

An equivalent simulation in 3D (i.e. including the second transverse direction), even with somewhat relaxed numerical parameters, typically has a computational cost of $\approx 5 \times 10^6$ CPU hours.

For the m-scale simulations performed in Part I of this manuscript, a simplified PIC numerical scheme based on the quasi-static approximation was used [49]. This approximation, explained in Sec. 1.2.2, allows to decouple the evolution of plasma electrons from the evolution of beam particles. For the plasma pusher, the temporal (t) and longitudinal (z) evolutions are dictated by the comoving variable $\xi = z - ct$, c being the speed of light and supposed to be close to the drive velocity. Therefore the 3D EM field solve and the particle push can be substituted by a sequence of 2D solves and particle pushes. A schematic representation of the quasi-static PIC scheme is shown in Fig. A.2.

This approximation allows to reduce significantly the simulation cost and to simulate the relativistic beam dynamics that happen over very long timescales compared to the plasma timescales. For instance in the simulations of Sec. 2.2.1, the beam particles were pushed over a time step of $150\,\omega_p^{-1}$. The spatial resolution of these simulations was $(\Delta x, \Delta y, , \Delta z) = (0.022, 0.022, 0.022)\,k_p^{-1}$. These simulations were run on the Hoffman2 Cluster of the Institute for Digital Research and Education of UCLA [152]. The typical computational cost of each simulation was ≈ 320 CPU hours.

Appendix B

PUBLICATIONS

arXiv:submit/3803956 [physics.plasm-ph] 22 Jun 2021

Spatiotemporal dynamics of ultrarelativistic beam-plasma instabilities

P. San Miguel Claveria,[1, *] X. Davoine,[2, 3] J. R. Peterson,[4, 5] M. Gilljohann,[1] I. Andriyash,[1] R. Ariniello,[6]
H. Ekerfelt,[4] C. Emma,[4] J. Faure,[2, 3] S. Gessner,[4] M. Hogan,[4] C. Joshi,[7] C. H. Keitel,[8] A. Knetsch,[1] O. Kononenko,[1]
M. Litos,[6] Y. Mankovska,[1] K. Marsh,[7] A. Matheron,[1] Z. Nie,[7] B. O'Shea,[4] D. Storey,[4] N. Vafaei-Najafabadi,[9]
Y. Wu,[7] X. Xu,[4] J. Yan,[9] C. Zhang,[7] M. Tamburini,[8] F. Fiuza,[4] L. Gremillet,[2, 3, †] and S. Corde[1, ‡]

[1] *LOA, ENSTA Paris, CNRS, Ecole Polytechnique,*
Institut Polytechnique de Paris, 91762 Palaiseau, France
[2] *CEA, DAM, DIF, 91297 Arpajon, France*
[3] *Université Paris-Saclay, CEA, LMCE, 91680 Bruyères-le-Châtel, France*
[4] *SLAC National Accelerator Laboratory, Menlo Park, CA 94025, USA*
[5] *Stanford University, Physics Department, Stanford, CA 94305, USA*
[6] *University of Colorado Boulder, Department of Physics,*
Center for Integrated Plasma Studies, Boulder, Colorado 80309, USA
[7] *University of California Los Angeles, Los Angeles, CA 90095, USA*
[8] *Max-Planck-Institut für Kernphysik, Saupfercheckweg 1, D-69117 Heidelberg, Germany*
[9] *Stony Brook University, Stony Brook, NY 11794, USA*

(Dated: June 22, 2021)

An electron or electron-positron beam streaming through a plasma is notoriously prone to micro-instabilities. For a dilute ultrarelativistic infinite beam, the dominant instability is a mixed mode between longitudinal two-stream and transverse filamentation modes, with a phase velocity oblique to the beam velocity. A spatiotemporal theory describing the linear growth of this oblique mixed instability is proposed, which predicts that spatiotemporal effects generally prevail for finite-length beams, leading to a significantly slower instability evolution than in the usually assumed purely temporal regime. These results are accurately supported by particle-in-cell (PIC) simulations. Furthermore, we show that the self-focusing dynamics caused by the plasma wakefields driven by finite-width beams can compete with the oblique instability. Analyzed through PIC simulations, the interplay of these two processes in realistic systems bears important implications for upcoming accelerator experiments on ultrarelativistic beam-plasma interactions.

A large number of astrophysical and laboratory systems involve the collective interaction between beams of relativistic charged particles and plasmas. In many cases, this interaction is governed by plasma micro-instabilities which lead to electrostatic and electromagnetic fluctuations growing at kinetic scales, and mediating most of the energy and momentum transfers between the beam and plasma particles [1, 2].

In astrophysics, these instabilities are thought to dissipate into heat or radiation the kinetic energy of relativistic outflows from various powerful sources (e.g. pulsar wind nebulae, neutron star mergers, active galactic nuclei). Notably, as a result of their nonlinear evolution [3], they can spawn relativistic collisionless shock waves [4] which, in turn, are believed to generate the most energetic particles and radiations in the Universe [5], including the electromagnetic counterpart of gravitational wave sources [6]. Beam-plasma instabilities therefore lie at the heart of the fast-emerging field of multi-messenger astrophysics [7]. Another topic of active current research is their possibly crucial role in shaping the GeV photon emission from blazars, the microphysics of which remaining little understood [8].

Beyond their fundamental and astrophysical significance, these instabilities have a prominent place in experimental concepts utilizing relativistic beam-plasma interactions, such as staging of laser (LWFA) and plasma wakefield acceleration (PWFA) [9], or laser-driven ion acceleration [10, 11], against which they act detrimentally. Lately, it has also been proposed to harness them as a novel channel of γ-ray radiation [12]. Now, progress in particle accelerators make it possible to envision probing these plasma processes in the laboratory [13]. In particular, extreme beam parameters, with Lorentz factors $\gamma_b > 10^4$ and densities $n_b = 10^{18} - 10^{20}\,\mathrm{cm}^{-3}$ will soon be available at the new Facility for Advanced Accelerator Tests II (FACET-II) [14]. This will open unprecedented opportunities to investigate, under various plasma conditions and in a very controlled way, the effects of micro-instabilities on the beam propagation in the ultrarelativistic regime.

The micro-instabilities arising in a relativistic beam-plasma system are usually classified into three types: the longitudinal two-stream instability (TSI), the transverse current filamentation instability (CFI) and the mixed mode, or oblique two-stream instability (OTSI) [2, 15]. While several modes can develop simultaneously from thermal noise or beam-induced perturbations, a specific instability class generally dominates the early beam-plasma interaction. A fully kinetic theory exists which describes the linear phase of the instability for unbounded (i.e., infinite) beam-plasma systems, allowing the dominant mode to be predicted for a given set of beam-plasma parameters [2, 16]. A key finding is the dominance of the mixed mode over CFI and TSI in the case of ultrarelativistic ($\gamma_b \gg 1$) and dilute ($\alpha \equiv n_b/n_p \ll 1$, where n_p is the electron plasma density) beams. This leads to density and field modulations with a longitudinal wavenumber $k_x \simeq c/\omega_p \equiv k_p$ and a transverse wavenumber $k_\perp \gtrsim k_p$, growing at a maximum rate

$$\Gamma_{\text{OTSI}} = \frac{\sqrt{3}}{2^{4/3}} \left(\frac{1}{\gamma_b} \frac{n_b}{n_p} \frac{k_\perp^2}{k_p^2 + k_\perp^2} \right)^{1/3} \omega_p \, . \qquad (1)$$

where ω_p is the background plasma frequency, and n_b is the sum of the number densities $n_{b\pm}$ of the beam electrons and positrons. Still, this temporal theory cannot be directly applied to the finite-size beams or plasma boundaries involved in realistic settings, such as future high-energy accelerator experiments. The first attempts to account for inhomogeneity effects on linear beam-plasma instabilities concerned the TSI [17, 18], revealing its pulse-shaped profile in case of localized initial disturbances. Recently, a model of the CFI excited by a longitudinally semi-infinite beam was proposed [19], showing that for moderate Lorentz factors ($\gamma_b \leq 10$), spatiotemporal effects are present at the beam head. Interestingly, this model predicts spatiotemporal effects to vanish in the ultrarelativistic limit.

For oblique modes, thought to dominate for $\gamma_b \gg 1$ and $\alpha \ll 1$, no spatiotemporal theory exists [20]. Yet, from the above previous works and related studies of laser-plasma [21, 22] or beam-plasma [23, 24] instabilities, one may expect finite beam dimensions –or, more generally, boundaries in the beam-plasma system– to strongly impact the dynamics of the oblique modes.

In this Letter we address two phenomena arising when a relativistic beam of finite spatial extent is considered in a beam-plasma system subject to streaming instabilities. First, we develop a spatiotemporal theory for the evolution of the OTSI, highlighting its spatiotemporal nature and resulting slower dynamics when a finite beam length is considered. Second, we show that the interplay of beam-plasma instabilities and the wakefield that is excited by a beam of finite length and width conveys constraints on the system parameters for the instabilities to dominate the interaction. These results are particularly relevant to future accelerator experiments aiming to explore ultrarelativistic beam-plasma instabilities and their radiative by-products [12].

We start by presenting the results of 2D PIC CALDER [25] simulations of an ultrarelativistic ($\gamma_b = 2 \times 10^4$), low-density ($\alpha = 0.03$) electron beam interacting with a uniform electron-proton plasma. The mesh size was set to $(\Delta x, \Delta y) = (0.042, 0.084)k_p^{-1}$, the time step was $\Delta t = 0.041\omega_p^{-1}$, and 100 macroparticles per cell were used for each species (beam electrons, plasma electrons and ions). The beam profile was taken to be Gaussian in the longitudinal (x) direction with a RMS length of σ_x, and uniform in the transverse (y) direction. Unless otherwise mentioned, the boundary conditions were absorbing along x and periodic along y, for both the fields and particles.

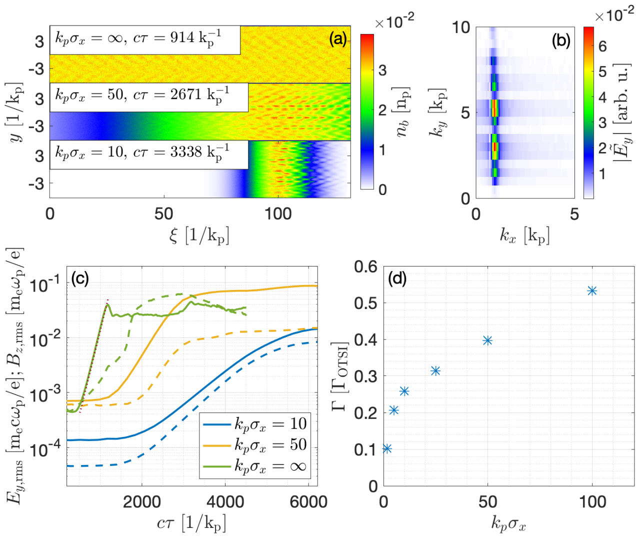

FIG. 1. Simulated instability dynamics for ultrarelativistic ($\gamma_b = 2 \times 10^4$), dilute ($\alpha = 0.03$) electron beams of various normalized lengths ($k_p\sigma_x$). (a) Snapshots of the beam density profile in the comoving coordinates $(\xi, \tau) = (v_b t - x, t)$ for different beam lengths. (b) 2D Fourier spectrum of the E_y field fluctuations at $c\tau = 3338k_p^{-1}$ for $k_p\sigma_x = 10$. (c) Transverse electric field $E_{y,\text{rms}} = \langle E_y^2 \rangle^{1/2}$ (solid line) and magnetic field $B_{z,\text{rms}} = \langle B_z^2 \rangle^{1/2}$ (dashed line) averaged over $\xi \in [\xi_{peak} - \sigma_x/2, \xi_{peak} + \sigma_x/2]$ as a function of the beam propagation distance in the plasma ($c\tau$) and the beam length. The dotted line plots the theoretical growth of the OTSI, Eq. (1), in the infinite beam case. The evaluation of the dominant $k_\perp$ in Eq. (1) is carried out using the electrostatic result $\langle E_y^2 \rangle / \langle E_x^2 \rangle \simeq (k_\perp/k_p)^2$. (d) Effective growth rate ($\Gamma/\Gamma_{\text{OTSI}}$) vs. $k_p\sigma_x$ within the central slice of the beam (see text for details).

Figure 1(a) illustrates the chevron-shaped pattern imprinted on the beam density profile by the OTSI in the cases of finite and infinite (i.e. with periodic boundary conditions along x) beam lengths. Galilean beam-frame coordinates $(\xi, \tau) = (v_b t - x, t)$ are used here, and the beam density maximum is located at $\xi \simeq 100k_p^{-1}$ for $k_p\sigma_x \in (10, 50)$. While the density modulations are uniform in the infinite beam case, they exhibit a clear spatial growth for finite σ_x. Figure 1(b) shows the 2D Fourier spectrum of the transverse E_y fluctuations within a slice around the beam maximum, for $k_p\sigma_x = 10$ [i.e. corresponding to the bottom plot of Fig. 1(a)] and $c\tau = 3338k_p^{-1}$. A narrow continuum of modes located at $k_x \simeq k_p$ and $k_\perp \gtrsim k_p$ are excited, a characteristic feature of the OTSI [2].

The evolution of the RMS amplitude of the transverse E_y and B_z fields during the beam propagation in the

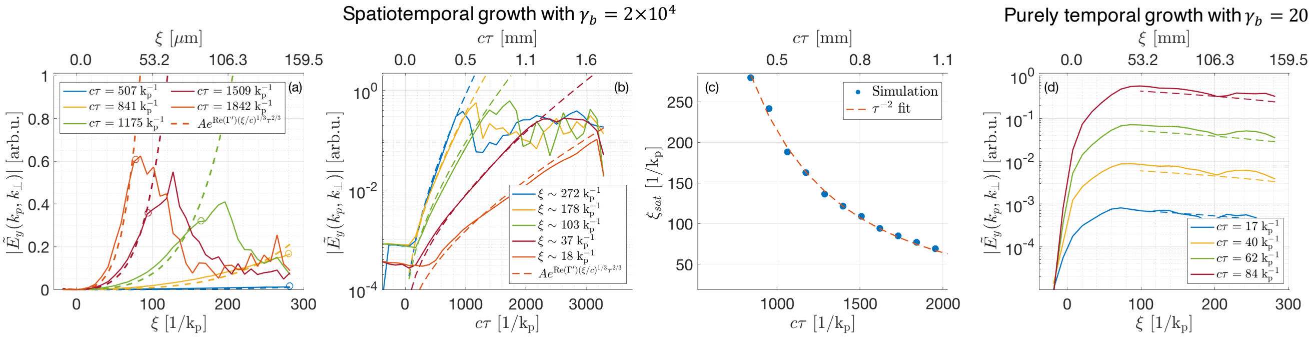

FIG. 2. 2D PIC simulations of the OTSI induced by a step-like e^-e^+ pair beam and comparison with linear theory in the spatiotemporal regime for $\gamma_b = 2 \times 10^4$ (a-c) and the temporal regime for $\gamma_b = 20$ (d). (a) and (d): Spectral amplitude $|\widetilde{E}_y(k_x, k_\perp)|$ of the dominant oblique mode ($k_x = k_p$, $k_\perp \simeq 3k_p$) as a function of ξ for different propagation distances $c\tau$. (b): Same quantity but as a function of $c\tau$ for different beam slices ξ. In (a) and (b), the simulation data (solid lines) is fitted to the theoretical law $A \exp[(3/2^{2/3})\Gamma_\text{OTSI}(\xi/c)^{1/3}\tau^{2/3}]$ for $\xi \leq \xi_\text{sat}$ (dashed lines). (c) Saturation position ξ_sat [also shown in (a) as circles] vs. $c\tau$ (filled circles), compared with the theoretical expectation $\xi_\text{sat} \propto \tau^{-2}$ (red dashed line). Dashed lines in (d) plot the theoretical temporal growth of $|\widetilde{E}_y(k_p, 3k_p)|$ at different times $c\tau \geq 17\text{k}_\text{p}^{-1}$.

plasma is presented in Fig. 1(c). In all cases considered, E_y prevails over B_z, as is expected for the OTSI [26]. For an infinite beam, good agreement is found with the temporal growth rate given by Eq. (1). By contrast, we observe a slowdown in the E_y field growth as the beam length is decreased from $k_p\sigma_x = 50$ to $k_p\sigma_x = 10$. To get a spatially resolved estimate of the effective OTSI growth rate in the finite-σ_x simulations, we have fitted to an exponential the temporal evolution of the E_y energy contained in the "oblique" spectral range $0.8 \leq k_x/k_p \leq 5$ and $0.8 \leq k_\perp/k_p \leq 10$, and normalized the resulting growth rate, Γ, to Γ_OTSI. In doing so, we have evaluated $k_\perp$ from the ratio of the E_y and E_x spectral energies integrated in the above k-range. Figure 1(d) displays the results of this procedure as a function of $k_p\sigma_x$. It is clearly seen that, even for $k_p\sigma_x \gg 1$, the effective growth rate is substantially smaller than is predicted for an unbounded system.

To understand the simulation results, we have developed a spatiotemporal model describing the growth of linear electrostatic oblique modes in a relativistic beam-plasma system. We consider a longitudinally semi-infinite, transversely infinite beam (composed of electrons or electron-positron pairs) propagating at velocity v_b in a uniform plasma, with the beam front located at $x = 0$ at $t = 0$. Using the comoving coordinates defined above, we write the plasma density perturbation as $\delta n_p(\tau, \xi)e^{-ik_p\xi + ik_\perp y}$, where $\delta n_p(\tau, \xi)$ represents the slowly varying envelope ($v_{b0}^{-1}\partial_\tau, \partial_\xi \ll k_p$) of the perturbation. Coupling the linearized cold-fluid equations for the beam and plasma electrons with Poisson's equation, one can derive the approximate equation satisfied by δn_p (see Supplemental Material [27]):

$$\left(\partial_\tau^3 + v_b\partial_\tau^2\partial_\xi + \frac{8i}{3^{3/2}}\Gamma_\text{OTSI}^3\right)\delta n_p = 0\,. \tag{2}$$

Following Refs. [19, 21], we assume an initial noise source throughout the beam, i.e., $\delta n_p(\tau = 0, \xi) = \delta n_p(\tau, \xi = 0) = S$, and $\partial_\tau \delta n_p(\tau = 0, \xi) = \partial_\tau^2 \delta n_p(\tau = 0, \xi) = 0$, where S is some amplitude parameter. Such conditions mainly apply to a situation where the beam is created within the plasma or penetrates a plasma with a long density ramp. Equation (2) can then be solved in the $\tau \to \infty$ limit using a double Laplace transform and a saddle-point expansion [27]. When $\xi \ll v_b\tau$, one obtains

$$\delta n_p(\tau, \xi) \simeq \frac{S}{\sqrt{6\pi}}\left(\frac{3\sqrt{3}v_b}{16\Gamma_\text{OTSI}^3\,\xi\tau^2}\right)^{1/6} \times \exp\left[\frac{\sqrt{3}}{2^{2/3}}(\sqrt{3}+i)\Gamma_\text{OTSI}\left(\frac{\xi}{v_b}\right)^{1/3}\tau^{2/3} - i\frac{\pi}{12}\right]\,, \tag{3}$$

This solution, similar to the asymptotic impulse solution of the TSI [18], demonstrates the spatiotemporal character of the oblique instability. Different longitudinal ξ-slices of the beam experience different temporal evolutions, the fastest growth being present at the rear of the beam, as might be intuitively surmised. The same leading exponential term is found for an initial noise source localized at the beam front, as expected when the beam enters a sharp vacuum-plasma boundary [27].

Further away from the beam front, i.e., for $\xi \geq v_b\tau$, the solution asymptotically evolves as

$$\delta n_p(\tau, \xi) \simeq \frac{S}{3}\exp\left[\left(1 + \frac{i}{\sqrt{3}}\right)\Gamma_\text{OTSI}\,\tau\right]\,, \tag{4}$$

which exhibits a purely temporal growth at the rate given by Eq. (1). In fact, the same exponential behavior sets in for $\xi \gtrsim v_b\tau/3$ but with a smaller prefactor [27]. In the comoving coordinates, the region of purely temporal growth recedes from the front to the rear of the beam at a velocity of $\sim v_b/3$. Therefore, at a location ξ behind the beam front, the instability initially grows in a purely temporal manner at a rate $\Gamma_{\rm OTSI}$, up to $\tau \simeq 3\xi v_b^{-1}$, after which spatiotemporal effects turn prominent and result in a slower growth. The same reasoning applied to a finite beam length σ_x implies that for $\sigma_x \ll v_b\Gamma_{\rm OTSI}^{-1}$, the instability is essentially of spatiotemporal nature. The latter condition holds in particular for the short ultrarelativistic bunches produced in particle accelerators.

To support this analysis, we carried out 2D PIC simulations with a step-like beam profile. A neutral electron-positron (e^-e^+) pair beam was employed in order to avoid plasma wakefield excitation and minimize initial noise, and thus enable accurate comparison with the model (yet similar results were obtained with an electron beam [27]). To reproduce even more closely the model assumptions, the beam entering the plasma was propagated ballistically till being completely immersed, and then (at $t = 0$) let to evolve freely. We used beam-plasma parameters relevant to FACET-II: $\gamma_b = 2 \times 10^4$, $\alpha = (n_{b-} + n_{b+})/n_p = 0.06$ ($n_{b\pm}$ is the equal density of the beam electrons and positrons), and $n_p = 10^{20}\,\mathrm{cm}^{-3}$. The simulation (moving) window covered the longitudinal range $-10 \le \xi \le \xi_{\max} = 150\,\mu$m (i.e. $-19 \le k_p\xi \le 282$), the beam front being placed at $\xi = 0$. For these parameters, one finds $\xi_{\max} < v_b\Gamma_{\rm OTSI}^{-1}$, hence the instability should evolve in a spatiotemporal manner.

Figure 2(a) displays (in solid curves) the spectral amplitude $|\widetilde{E}_y(k_x, k_\perp)|$ of the dominant oblique mode (at $k_x = k_p$ and $k_\perp \simeq 3k_p$) along the beam at different propagation distances $c\tau$, and in Fig. 2(b) the same quantity is plotted as a function of $c\tau$ for different positions ξ. Both figures show very good agreement with the predicted spatiotemporal evolution $\propto \exp[(3/2^{2/3})\Gamma_{\rm OTSI}(\xi/c)^{1/3}\tau^{2/3}]$ of the instability (dashed lines).

For large enough propagation distances ($c\tau \gtrsim 1000k_p^{-1}$), the simulation curves in Fig. 2(a) peak at some position ξ, beyond which they rapidly decay. This behavior is due to the nonlinear saturation of the OTSI [8, 28]. The saturation mechanisms involved in the ultrarelativistic regime will be studied in a separate paper, yet one can exploit here their observed weak spatial dependence to further validate the theory. Indeed, assuming that the instability ceases when a certain field level is reached, the saturation position, $\xi_{\rm sat}$, should vary with τ as $\xi_{\rm sat} \propto \tau^{-2}$. This prediction matches well with the simulation results of Fig. 2(c), which plots $\xi_{\rm sat}$ vs. τ.

Finally, to confirm the existence of a purely temporal regime, we repeated the same simulation but with a lower beam Lorentz factor ($\gamma_b = 20$), so that $\xi_{\max} > v_b\Gamma_{\rm OTSI}^{-1}$. Figure 2(d) shows that the instability then grows at a rate that is essentially independent of the beam slice $\xi > 50\,\mu$m. This nicely agrees with Eq. (4), as shown by the dashed lines representing the predicted amplification of the initial (recorded at $c\tau = 14k_p^{-1}$) ξ-dependent fluctuations.

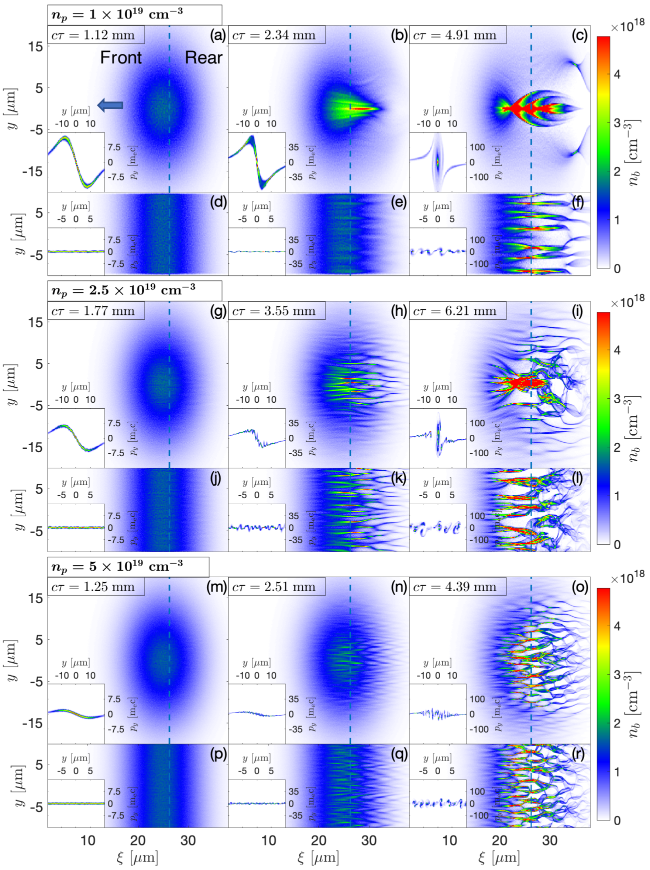

FIG. 3. Simulated electron beam density maps at different propagation distances in a uniform plasma of density $n_p = 1 \times 10^{19}\,\mathrm{cm}^{-3}$ [(a)-(f)], $2.5 \times 10^{19}\,\mathrm{cm}^{-3}$ [(g)-(l)], and $5 \times 10^{19}\,\mathrm{cm}^{-3}$ [(m)-(r)]. The transverse beam profile is taken to be either finite with $\sigma_r = 10\,\mu$m RMS width [(a)-(c), (g)-(i), and (m)-(o)] or infinite, i.e., with transverse periodic boundary conditions [(d)-(f), (j)-(l), and (p)-(r)]. In all cases, the beam has a 10 GeV energy ($\gamma_b = 2 \times 10^4$), a Gaussian longitudinal profile with $\sigma_x = 5\,\mu$m RMS length, a transverse normalized emittance $\epsilon_n = 3$ mm mrad, and a peak density $n_b \simeq 1.5 \times 10^{18}\mathrm{cm}^{-3}$ [i.e., $\alpha \simeq 0.15$ for (a)-(f),$\alpha \simeq 0.06$ for (g)-(l), and $\alpha \simeq 0.03$ for (m)-(r)], which would correspond to a total beam charge of 2 nC in 3D. The insets show the transverse beam phase space along the slices indicated by the dashed blue lines.

Another important finite-size effect is the excitation of plasma wakefields by nonneutral beams with relatively small transverse width (σ_r). These fields act back on the beam to pinch it, which reinforces them and causes the beam to self-focus as it further propagates through the plasma [29]. The time scale of beam self-focusing can be estimated by the inverse betatron frequency $\omega_\beta^{-1} = \sqrt{\gamma_b m_e/\partial_r W_\perp}$, where $W_\perp$ is the amplitude of the transverse wakefield [30]. If this time scale is smaller than the effective growth time of the dominant oblique instability [i.e. lengthened by spatiotemporal effects, see Fig. 1(d)], the beam can shrink into a narrow and dense filament expelling the plasma electrons away from it, hence quenching the instability. For a beam with fixed charge and length, changing its transverse width affects both processes similarly, and so barely modifies their interplay. By contrast, raising the plasma density tends to favor the instability over the beam self-focusing.

We ran additional 2D PIC simulations to examine the interplay of the beam self-focusing and beam-plasma instability depending on the plasma density. We considered a FACET-II-like electron beam ($10\,\mathrm{GeV}$, $2\,\mathrm{nC}$, $\sigma_x = 5\,\mu\mathrm{m}$, $\sigma_r = 10\,\mu\mathrm{m}$, peak density $n_b \simeq 1.5 \times 10^{18}\,\mathrm{cm}^{-3}$, normalized emittance $\epsilon_n = 3\,\mathrm{mm\,mrad}$) injected through a uniform plasma of different densities. Each simulation was repeated with a transversely infinite (periodic) beam to suppress the effects of plasma wakefields and beam self-focusing. Comparing ω_β^{-1} to the time scale of the spatiotemporal OTSI with the above parameters, one finds that beam self-focusing should dominate for $n_p \lesssim 10^{19}\,\mathrm{cm}^{-3}$ (see Supplemental Material [27]). This prediction is confirmed by the simulation results depicted in Fig. 3. At $n_p = 10^{19}\,\mathrm{cm}^{-3}$ [Figs. 3(a)-(c)], the transverse wakefield starts focusing the finite-width beam [see its rotation in the transverse phase space in the inset of Fig. 3(a)] before the OTSI can impart significant modulations on the beam profile. This leads the whole beam to collapse into a narrow filament [Figs. 3(b)-(c)], hence inhibiting the OTSI in stark contrast with the equivalent infinite-beam simulation [Figs. 3(d)-(f)]. At $n_p = 2.5 \times 10^{19}\,\mathrm{cm}^{-3}$ [Figs. 3(g)-(i)], the self-focusing dynamics is slower, and so the competition between the two processes is more balanced. Still, although the OTSI-driven modulations have time to grow, a compressed filament eventually forms at the beam center [Fig. 3(i)], which is absent for an infinite beam width [Fig. 3(l)]. Finally, when further increasing the plasma density to $n_p = 5 \times 10^{19}\,\mathrm{cm}^{-3}$ [Figs. 3(m)-(r)], the system dynamics is clearly governed by the OTSI, and, as expected, no significant difference arises when changing from a finite to an infinite beam width.

In conclusion, we have conducted the first spatiotemporal analysis of the oblique two-stream instability triggered by finite-size particle beams. For ultrarelativistic, short-duration bunches, such as delivered by state-of-the-art particle accelerators, we have shown analytically that, in terms of the comoving coordinates (τ, ξ), the instability mainly evolves as a function of $(\xi/v_b)^{1/3}\tau^{2/3}$. It develops from the head to the tail of the beam, and, within a fixed beam slice, more slowly than in unbounded geometry. Close agreement has been found between the theory and PIC simulations in several beam-plasma setups. Furthermore, when realistic finite-width electron beams are considered, self-focusing induced by plasma wakefields may hinder the instability growth, and thus dominate the beam dynamics. Neutral pair beams, though, can circumvent the limitation placed by wakefields, and facilitate laboratory investigations of ultrarelativistic streaming instabilities. These results are critical to guide and interpret future experiments on high-energy beam-plasma interactions and their envisioned applications, such as the development of instability-based light sources.

This work was performed in the framework of the E-305 Collaboration. E-305 is a SLAC experiment which aims at the study of astrophysically relevant beam-plasma instabilities and at the generation of bright gamma rays. The work at CEA and LOA was supported by the ANR (UnRIP project, Grant No. ANR-20-CE30-0030). The work at LOA was also supported by the European Research Council (ERC) under the European Union's Horizon 2020 research and innovation programme (M-PAC project, Grant Agreement No. 715807). We acknowledge GENCI-TGCC for granting us access to the supercomputer IRENE under Grants No. 2019-A0060510786, 2020-A0080510786 and 2021-A0100510786 to run PIC simulations. J. R. Peterson was supported by DOE NNSA LRGF fellowship under grant DE-NA0003960. The work at SLAC was supported by U.S. DOE FES Grant No. FWP100331. UCLA was supported by U.S. Department of Energy Grant No. DE-SC001006 and NSF Grant No. 1734315.

---

[*] pablo.san-miguel-claveria@polytechnique.edu
[†] laurent.gremillet@cea.fr
[‡] sebastien.corde@polytechnique.edu

[1] R. N. Sudan, in *Handbook of Plasma Physics*, Vol. 2, edited by M. N. Rosenbluth and R. Z. Sagdeev (North-Holland Physics Publishing, Amsterdam, 1984) Chap. 6.3, pp. 337–382.

[2] A. Bret, L. Gremillet, and M. E. Dieckmann, Phys. Plasmas **17**, 120501 (2010).

[3] A. Bret, A. Stockem, F. Fiuza, C. Ruyer, L. Gremillet, R. Narayan, and L. O. Silva, Phys. Plasmas **20**, 042102 (2013).

[4] A. Spitkovsky, Astrophys. J. Lett. **682**, L5 (2008); M. Lemoine, L. Gremillet, G. Pelletier, and A. Vanthieghem, Phys. Rev. Lett. **123**, 035101 (2019).

[5] R. Blandford and D. Eichler, Phys. Rep. **154**, 1 (1987); A. M. Bykov and R. A. Treumann, Astron. Astrophys. Rev. **19**, 42 (2011).

[6] B. P. Abbott et al., Astrophys. J. Lett. **848**, L12 (2017).

[7] P. Mészáros, D. B. Fox, C. Hanna, and K. Murase, Nat. Rev. Phys. **1**, 585 (2019).

[8] A. E. Broderick, P. Chang, and C. Pfrommer, Astrophys. J. **752**, 22 (2012); L. Sironi and D. Giannios, Astrophys. J. **787**, 49 (2014); P. Chang, A. E. Broderick, C. Pfrommer, E. Puchwein, A. Lamberts, M. Shalaby, and G. Vasil, Astrophys. J. **833**, 118 (2016).

[9] G. Raj, O. Kononenko, M. F. Gilljohann, A. Doche, X. Davoine, C. Caizergues, Y.-Y. Chang, J. P. Couperus Cabadağ, A. Debus, H. Ding, M. Förster, J.-P. Goddet, T. Heinemann, T. Kluge, T. Kurz, R. Pausch, P. Rousseau, P. San Miguel Claveria, S. Schöbel, A. Siciak, K. Steiniger, A. Tafzi, S. Yu, B. Hidding, A. Martinez de la Ossa, A. Irman, S. Karsch, A. Döpp,

U. Schramm, L. Gremillet, and S. Corde, Phys. Rev. Res. **2**, 023123 (2020).

[10] J. Fuchs, T. E. Cowan, P. Audebert, H. Ruhl, L. Gremillet, A. Kemp, M. Allen, A. Blazevic, J.-C. Gauthier, M. Geissel, M. Hegelich, S. Karsch, P. Parks, M. Roth, Y. Sentoku, R. Stephens, and E. M. Campbell, Phys. Rev. Lett. **91**, 255002 (2003).

[11] S. Göde, C. Rödel, K. Zeil, R. Mishra, M. Gauthier, F.-E. Brack, T. Kluge, M. J. MacDonald, J. Metzkes, L. Obst, M. Rehwald, C. Ruyer, H.-P. Schlenvoigt, W. Schumaker, P. Sommer, T. E. Cowan, U. Schramm, S. Glenzer, and F. Fiuza, Phys. Rev. Lett. **118**, 194801 (2017).

[12] A. Benedetti, M. Tamburini, and C. H. Keitel, Nat. Photon. **12**, 319 (2018).

[13] B. Allen, V. Yakimenko, M. Babzien, M. Fedurin, K. Kusche, and P. Muggli, Phys. Rev. Lett. **109**, 185007 (2012).

[14] V. Yakimenko, L. Alsberg, E. Bong, G. Bouchard, C. Clarke, C. Emma, S. Green, C. Hast, M. J. Hogan, J. Seabury, N. Lipkowitz, B. O'Shea, D. Storey, G. White, and G. Yocky, Phys. Rev. Accel. Beams **22**, 101301 (2019).

[15] M. Lemoine and G. Pelletier, MNRAS **402**, 321 (2010).

[16] A. Bret, L. Gremillet, D. Bénisti, and E. Lefebvre, Phys. Rev. Lett. **100**, 205008 (2008).

[17] A. Bers, in *Handbook of Plasma Physics*, edited by M. N. Rosenbluth and R. Z. Sagdeev (North-Holland Physics Publishing, Amsterdam, 1983) Chap. 3.2, pp. 451–517.

[18] M. E. Jones, D. S. Lemons, and M. A. Mostrom, Phys. Fluids **26**, 2784 (1983).

[19] V. B. Pathak, T. Grismayer, A. Stockem, R. A. Fonseca, and L. O. Silva, New J. Phys. **17**, 043049 (2015).

[20] S. F. Shukla, N. Martins, J. Muggli, P. Vieira, and L. O. Silva, New J. Phys. **22**, 013030 (2020).

[21] C. D. Decker, W. B. Mori, T. Katsouleas, and D. E. Hinkel, Phys. Plasmas **3**, 1360 (1996).

[22] C. J. McKinstrie and E. J. Turano, Phys. Plasmas **3**, 4683 (1996).

[23] C. Huang, W. Lu, M. Zhou, C. E. Clayton, C. Joshi, W. B. Mori, P. Muggli, S. Deng, E. Oz, T. Katsouleas, M. J. Hogan, I. Blumenfeld, F. J. Decker, R. Ischebeck, R. H. Iverson, N. A. Kirby, and D. Walz, Phys. Rev. Lett. **99**, 255001 (2007).

[24] N. Kumar, A. Pukhov, and K. Lotov, Phys. Rev. Lett. **104**, 255003 (2010).

[25] E. Lefebvre, N. Cochet, S. Fritzler, V. Malka, M.-M. Aléonard, J.-F. Chemin, S. Darbon, L. Disdier, J. Faure, A. Fedotoff, O. Landoas, G. Malka, V. Méot, P. Morel, M. Rabec LeGloahec, A. Rouyer, C. Rubbelynck, V. Tikhonchuk, R. Wrobel, P. Audebert, and C. Rousseaux, Nucl. Fusion **43**, 629 (2003).

[26] A. Bret, L. Gremillet, and D. Bénisti, Phys. Rev. E **81**, 036402 (2010).

[27] See Supplemental Material at, `http://link.aps.org/supplemental/doi`, for the detailed derivation of the spatiotemporal instability model, its comparison to electron-beam-plasma simulations and a criterion for the dominance of the instability over the beam self-focusing.

[28] L. E. Thode, Phys. Fluids **19**, 305 (1976).

[29] S. Corde, E. Adli, J. M. Allen, W. An, C. I. Clarke, B. Clausse, C. E. Clayton, J. P. Delahaye, J. Frederico, S. Gessner, S. Z. Green, M. J. Hogan, C. Joshi, M. Litos, W. Lu, K. A. Marsh, W. B. Mori, N. Vafaei-Najafabadi, D. Walz, and V. Yakimenko, Nat. Commun. **7**, 11898 (2016).

[30] R. Keinigs and M. E. Jones, Phys. Fluids **30**, 252 (1987).

Supplemental Material for
"Spatiotemporal dynamics of ultrarelativistic beam-plasma instabilities"

P. San Miguel Claveria,[1,*] X. Davoine,[2,3] J. R. Peterson,[4,5] M. Gilljohann,[1] I. Andriyash,[1] R. Ariniello,[6]
H. Ekerfelt,[4] C. Emma,[4] J. Faure,[2,3] S. Gessner,[4] M. Hogan,[4] C. Joshi,[7] C. H. Keitel,[8] A. Knetsch,[1] O. Kononenko,[1]
M. Litos,[6] Y. Mankovska,[1] K. Marsh,[7] A. Matheron,[1] Z. Nie,[7] B. O'Shea,[4] D. Storey,[4] N. Vafaei-Najafabadi,[9]
Y. Wu,[7] X. Xu,[4] J. Yan,[9] C. Zhang,[7] M. Tamburini,[8] F. Fiuza,[4] L. Gremillet,[2,3,†] and S. Corde[1,‡]

[1] *LOA, ENSTA Paris, CNRS, Ecole Polytechnique,*
Institut Polytechnique de Paris, 91762 Palaiseau, France
[2] *CEA, DAM, DIF, 91297 Arpajon, France*
[3] *Université Paris-Saclay, CEA, LMCE, 91680 Bruyères-le-Châtel, France*
[4] *SLAC National Accelerator Laboratory, Menlo Park, CA 94025, USA*
[5] *Stanford University, Physics Department, Stanford, CA 94305, USA*
[6] *University of Colorado Boulder, Department of Physics,*
Center for Integrated Plasma Studies, Boulder, Colorado 80309, USA
[7] *University of California Los Angeles, Los Angeles, CA 90095, USA*
[8] *Max-Planck-Institut für Kernphysik, Saupfercheckweg 1, D-69117 Heidelberg, Germany*
[9] *Stony Brook University, Stony Brook, NY 11794, USA*

(Dated: June 22, 2021)

S1. SPATIOTEMPORAL LINEAR THEORY OF THE OBLIQUE TWO-STREAM INSTABILITY

A. Derivation of the master equation

Let us consider a transversely uniform, relativistic electron beam moving through an unmagnetized electron-ion plasma. We seek to derive the equation governing the spatiotemporal perturbative evolution of the oblique two-stream instability (OTSI) as triggered by disturbances at the leading edge of the beam and within its body. According to previous studies [1, 2], the OTSI is mainly of electrostatic nature, so that the problem can be analytically addressed by combining the fluid conservation equations for the beam and plasma electrons and Poisson's equation. The ions will be assumed immobile throughout.

In the following, the subscripts $_b$ and $_p$ will refer to the beam and plasma electrons, respectively. For population $\alpha = (b, p)$, n_α is the number density, γ_α the Lorentz factor, and $\mathbf{v}_\alpha$ the velocity. Moreover, ϕ will represent the electrostatic field potential. All plasma and field quantities will be linearized as $X(\mathbf{r}, t) = X_0 + X^{(1)}(\mathbf{r}, t) = X_0 + \delta X(x, t) \exp[i(\mathbf{k} \cdot \mathbf{r} - \omega t)]$, where X_0 and $X^{(1)}$ denote unperturbed and perturbed quantities, and δX represents the spatiotemporal envelope of the perturbation, characterized by its real wavenumber $\mathbf{k}$. The (longitudinal) x-axis is defined as the beam propagation direction. Only the case of an ultrarelavistic ($\gamma_{b0} \gg 1$), dilute ($n_{b0}/n_{p0} \ll 1$) beam will be treated and thermal effects will be neglected. Our analysis will be restricted to a 2D (x, y) geometry, so that $\mathbf{k} = (k_x, k_\perp)$ and $\mathbf{v}_\alpha = (v_{\alpha x}, v_{\alpha y})$. We will use units such that $e = m_e = c = \epsilon_0 = 1$.

From the above assumptions, the momentum and continuity equations for the beam electrons can be written as

$$(\partial_t + v_{b0}\partial_x) \begin{pmatrix} \gamma_{b0}^3 v_{bx}^{(1)} \\ \gamma_{b0} v_{by}^{(1)} \end{pmatrix} = \begin{pmatrix} \partial_x \phi^{(1)} \\ ik_\perp \phi^{(1)} \end{pmatrix} , \tag{S1}$$

$$\partial_t n_b^{(1)} + \partial_x (n_b v_{bx})^{(1)} + ik_\perp (n_b v_{by})^{(1)} = 0 \, . \tag{S2}$$

Combining both equations leads to

$$(\partial_t + v_{b0}\partial_x)^2 \, n_b^{(1)} = n_{b0} \left(\gamma_{b0}^{-1} k_\perp^2 - \gamma_{b0}^{-3} \partial_x^2 \right) \phi^{(1)} \, . \tag{S3}$$

The plasma electrons are taken to be initially at rest ($v_{p0} = 0$). Since $n_{b0}/n_{p0} \ll 1$ is further assumed, their dynamics can be treated nonrelativistically. As a result, they fulfill an equation similar to Eq. (S3) except for the

---

[*] pablo.san-miguel-claveria@polytechnique.edu
[†] laurent.gremillet@cea.fr
[‡] sebastien.corde@polytechnique.edu

changes $v_{b0} \to 0$ and $\gamma_{b0} \to 1$:

$$\partial_t^2 n_p^{(1)} = n_{p0} \left(k_\perp^2 - \partial_x^2\right) \phi^{(1)} \,. \tag{S4}$$

We now plug Eq. (S4) into Poisson's equation

$$\left(\partial_x^2 - k_\perp^2\right) \phi^{(1)} = n_p^{(1)} + n_b^{(1)} \,, \tag{S5}$$

to obtain

$$\left(\partial_t^2 + n_{p0}\right) n_p^{(1)} + n_{p0} n_b^{(1)} = 0 \,. \tag{S6}$$

Applying the $(\partial_x^2 - k_\perp^2)$ operator to Eq. (S3) and using Eq. (S4), we find

$$\left(\partial_x^2 - k_\perp^2\right) \left(\partial_t + v_{b0}\partial_x\right)^2 n_b^{(1)} = \frac{n_{b0}}{n_{p0}} \left(\gamma_{b0}^{-3}\partial_x^2 - \gamma_{b0}^{-1} k_\perp^2\right) \partial_t^2 n_p^{(1)} \,. \tag{S7}$$

Substituting this relation in Eq. (S6) gives the general equation verified by $n_p^{(1)}$:

$$\left[\left(\partial_x^2 - k_\perp^2\right) \left(\partial_t + v_{b0}\partial_x\right)^2 \left(\partial_t^2 + n_{p0}\right) + n_{b0} \left(\gamma_{b0}^{-3}\partial_x^2 - \gamma_{b0}^{-1} k_\perp^2\right) \partial_t^2\right] n_p^{(1)} = 0 \,. \tag{S8}$$

When discarding spatiotemporal effects, i.e., by taking $\partial_x = ik_x$ and $\partial_t = -i\omega$ (ω is the complex growth rate), the above equation reduces to the standard, electrostatic cold-fluid dispersion of the OTSI [1]:

$$1 - \frac{n_{p0}}{\omega^2} - \frac{n_{b0}\left(\gamma_{b0}^{-3} k_x^2 - \gamma_{b0}^{-1} k_\perp^2\right)}{\left(k_x^2 + k_\perp^2\right)\left(\omega - k_x v_{b0}\right)^2} = 0 \,. \tag{S9}$$

To describe the spatiotemporal evolution of the perturbation, it is convenient to make a Galilean transformation to the beam-frame coordinates $(\xi, \tau) \equiv (v_b t - x, t)$, and write $n_p^{(1)} = \delta n_p(\tau, \xi) \exp(-ik_p\xi + ik_\perp y)$. Equation (S8) can therefore be recast as

$$\begin{aligned} &\left(2ik_0\partial_\xi + k_p^2 + k_\perp^2\right) \partial_\tau^2 \left[\left(\partial_\tau + v_{b0}\partial_\xi\right)^2 - 2ik_p v_{b0}\left(\partial_\tau + v_{b0}\partial_\xi\right) + n_{p0} - \left(k_p v_{b0}\right)^2\right] \delta n_p \\ &+ \frac{n_{b0}k_\perp^2}{\gamma_{b0}} \left(\partial_\tau + v_b\partial_\xi - ik_0 v_{b0}\right)^2 \delta n_p = 0 \,. \end{aligned} \tag{S10}$$

We assume γ_{b0} to be large enough that $\gamma_{b0}^{-3}\partial_x^2$ can be neglected relative to $\gamma_{b0}^{-1}k_\perp^2$ in the second term of Eq. (S8).

We now choose $k_p = \sqrt{n_{p0}}/v_{b0}$ ($\equiv \omega_{p0}/v_{b0}$ in physical units, where ω_{p0} is the background plasma frequency) and adopt the slow-varying-amplitude approximation: $v_{b0}^{-1}\partial_\tau, \partial_\xi \ll k_p \sim \sqrt{n_{p0}}$. The above equation can then be approximated as

$$\left(k_p^2 + k_\perp^2\right) \partial_\tau^2 \left(\partial_\tau + v_{b0}\partial_\xi\right) \delta n_p - ik_\perp^2 \frac{n_{b0}\sqrt{n_{p0}}}{2\gamma_{b0}} \delta n_p = 0 \,. \tag{S11}$$

Finally, introducing

$$\Gamma_0 = \left(\frac{1}{2\gamma_{b0}} \frac{n_{b0}}{n_{p0}} \frac{k_\perp^2}{k_p^2 + k_\perp^2}\right)^{1/3} \omega_{p0} \,, \tag{S12}$$

we recover Eq. (2) of the main text:

$$\left[\partial_\tau^2 \left(\partial_\tau + v_{b0}\partial_\xi\right) + i\Gamma_0^3\right] \delta n_p = 0 \,. \tag{S13}$$

Note that this equation could also have been obtained by applying the method of [3] to the OTSI dispersion relation (S9). While quite straightforward, this method does not allow us to identify the physical quantity exactly governed by the resulting equation, hence the interest of our detailed derivation. It should also be pointed out that Eq. (S13) holds as well for an ultrarelativistic pair beam, in which case n_{b0} in Eq. (S12) should be understood as the sum of the unperturbed number densities of the beam electrons and positrons.

B. Analysis of the spatiotemporal behavior of the OTSI

An important observation is that Eq. (S13) is formally identical to Eq. (6) of [3] (assuming vanishing dissipation and group velocity of the unstable wave packet), which describes the longitudinal ($k_\perp = 0$) two-stream instability (TSI). In the following, we will solve Eq. (S13) for two sets of initial and boundary conditions. The first configuration is characterized by a Dirac function source at $\tau = \xi = 0$, and will give the Green's function response of the system, recovering the well-known spatiotemporal impulse behavior of the TSI [3–5]. As an alternative setup, we will consider disturbances both throughout the beam ($\xi \geq 0$) at $\tau = 0$ and at the beam front ($\xi = 0$) at $\tau \geq 0$. Similar conditions were used in [6] in the case of Raman forward scattering of short laser pulses, and, more recently, to investigate the spatiotemporal properties of the current filamentation instability (CFI) [7]. We will show that the solution to Eq. (S13) then exhibits both spatiotemporal and purely temporal behaviors.

Following [6], we consider the double Laplace transform of δn_p, defined by

$$\delta n_p(\alpha,\beta) = \int_0^\infty d\tau \int_0^\infty d\xi\, \delta n_p(\tau,\xi) e^{-i\alpha\tau - i\beta\xi} \,. \tag{S14}$$

To obtain the Green's function of the system, we put $\delta(\tau)\delta(\xi)$ in the r.h.s of Eq. (S13), and apply the above transformation:

$$i\left(\alpha^3 + \alpha^2\beta v_{b0} + \Gamma_0^3\right)\delta n_p(\alpha,\beta) = -1 \,. \tag{S15}$$

Inverting the Laplace transforms gives

$$\delta n_p(\tau,\xi) = \frac{i}{4\pi^2 v_{b0}} \int_{C_\alpha} d\alpha\, e^{i\alpha\tau} \int_{C_\beta} d\beta \frac{e^{i\beta\xi}}{\alpha^2\left(\beta + \frac{\alpha^3+\Gamma_0^3}{\alpha^2 v_{b0}}\right)} \,. \tag{S16}$$

with the Bromwich contours, C_α and C_β, extending from, respectively, $\Re\,\alpha = -\infty$ to $\Re\,\alpha = +\infty$ and $\Re\,\beta = -\infty$ to $\Re\,\beta = +\infty$, and lying below the integrand singularities. The integral over β can be readily evaluated using the residue theorem for the pole at $\beta = -\frac{(\alpha^3+\Gamma_0^3)}{\alpha^2 v_{b0}}$:

$$\int_{C_\beta} d\beta \frac{e^{i\beta\xi}}{\beta + \frac{\alpha^3+\Gamma_0^3}{\alpha^2 v_{b0}}} = 2\pi i e^{-i\frac{(\alpha^3+\Gamma_0^3)}{\alpha^2 v_{b0}}\xi} H(\xi) \,. \tag{S17}$$

The Heaviside function $H(\xi)$ expresses the fact that when $\xi < 0$, one can close the C_α contour with a semicircle of infinite radius in the half-plane $\Im(\alpha) < 0$, along which the exponential vanishes. Since no singularity is enclosed, the integral also vanishes.

Equation (S16) then becomes

$$\delta n_p(\tau,\xi) = -\frac{1}{2\pi v_{b0}} \int_{C_\alpha} \frac{d\alpha}{\alpha^2}\, e^{i\alpha\tau - i\frac{(\alpha^3+\Gamma_0^3)}{\alpha^2 v_{b0}}\xi} H(\xi) \,. \tag{S18}$$

This integral vanishes for $\tau < \xi/v_{b0}$. When $\tau > \xi/v_{b0}$, the residue of the essential singularity at $\alpha = 0$ cannot be exactly calculated. To get an asymptotic approximation when $\tau \to \infty$, we use the saddle-point method [8]. To this purpose, we introduce the dimensionless parameter $\theta = \xi/v_{b0}\tau$, and write the above expression as

$$\delta n_p(\tau,\xi) = -\frac{1}{2\pi v_{b0}} \int_{C_\alpha} d\alpha g(\alpha) e^{\tau h(\alpha,\theta)} \,, \tag{S19}$$

where

$$\begin{aligned} h(\alpha,\theta) &= i\left[(1-\theta)\alpha - \frac{\Gamma_0^3\theta}{\alpha^2}\right] \,, \\ g(\alpha) &= \frac{1}{\alpha^2} \,, \end{aligned} \tag{S20}$$

The saddle points of $h(\alpha,\theta)$ are located at $\alpha_{\mathrm{sp}0}(\theta) = \Gamma_0\left(\frac{2\theta}{1-\theta}\right)^{1/3} e^{i\pi}$ and $\alpha_{\mathrm{sp}\pm}(\theta) = \Gamma_0\left(\frac{2\theta}{1-\theta}\right)^{1/3} e^{\pm i\pi/3}$, where $h(\alpha_{\mathrm{sp}0}(\theta),\theta) = 3\Gamma_0\left(\frac{1-\theta}{2}\right)^{1/3} e^{-i\pi/2}$, $h(\alpha_{\mathrm{sp}+}(\theta),\theta) = 3\Gamma_0\left(\frac{1-\theta}{2}\right)^{1/3} e^{i5\pi/6}$ and $h(\alpha_{\mathrm{sp}-}(\theta),\theta) = 3\Gamma_0\left(\frac{1-\theta}{2}\right)^{1/3} e^{i\pi/6}$. The dominant saddle point is $\alpha_{\mathrm{sp}-}(\theta)$ since $\Re\, h(\alpha_{\mathrm{sp}-}(\theta),\theta) > \Re\, h(\alpha_{\mathrm{sp}0}(\theta),\theta), \Re\, h(\alpha_{\mathrm{sp}+}(\theta),\theta)$ for $0 < \theta < 1$, and the initial contour C_α can be continuously deformed to an Olver-type path with respect to $\alpha_{\mathrm{sp}-}$, C_{sdp}, along which $\Re\, h(\alpha,\theta) < \Re\, h(\alpha_{\mathrm{sp}-},\theta)$. Furthermore, this path goes from $(\Re\,\alpha, \Im\,\alpha) = (-\infty,+\infty)$ to $(\Re\,\alpha, \Im\,\alpha) = (+\infty,+\infty)$ and follows the path of steepest descent in the vicinity of $\alpha_{\mathrm{sp}-}$. Since C_α is deformable to C_{sdp} without crossing $\alpha = 0$ for $0 < \theta < 1$, there is no residue contribution of the pole singularity [8]. The resulting integral can therefore be approximated as [8]

$$\int_{C_{\mathrm{sdp}}} d\alpha\, g(\alpha) e^{i\tau h(\alpha,\theta)} \simeq g(\alpha_{\mathrm{sp}-})\sqrt{\frac{2\pi}{\tau|h''(\alpha_{\mathrm{sp}-},\theta)|}}\, e^{\tau h(\alpha_{\mathrm{sp}-},\theta)+i\psi_{\mathrm{sdp}}}\,, \tag{S21}$$

where $h''(\alpha,\theta) \equiv \partial_\alpha^2 h(\alpha,\theta)$ and

$$\psi_{\mathrm{sdp}} = \frac{\pi}{2} - \frac{\arg\left[h''(\alpha_{\mathrm{sp}-},\theta)\right]}{2} \tag{S22}$$

is the slope angle of the steepest-descent path through $\alpha_{\mathrm{sp}-}(\theta)$ [8]. Using $g(\alpha_{\mathrm{sp}-}(\theta)) = \left(\frac{1-\theta}{2\theta}\right)^{2/3} \frac{e^{2i\pi/3}}{\Gamma_0}$ and substituting the above expressions for $h(\alpha_{\mathrm{sp}-}(\theta),\theta)$ and $h''(\alpha_{\mathrm{sp}-}(\theta),\theta)$, we find $\psi_{\mathrm{sdp}} = \pi/12$ and

$$\begin{aligned}\delta n_p &\simeq -\frac{1}{2\sqrt{3\pi}\Gamma_0 v_{b0}\sqrt{\Gamma_0\tau\theta}} \exp\left[3\Gamma_0\tau\left(\frac{1-\theta}{2}\right)^{2/3}\theta^{1/3}e^{i\pi/6} + i\frac{3\pi}{4}\right] \\ &\simeq \frac{1}{2\sqrt{3\pi}\Gamma_0 v_{b0}\sqrt{\Gamma_0\xi/v_{b0}}} \exp\left[\frac{3}{2^{5/3}}(\sqrt{3}+i)\Gamma_0\left(\tau-\frac{\xi}{v_{b0}}\right)^{2/3}\left(\frac{\xi}{v_{b0}}\right)^{1/3} - i\frac{\pi}{4}\right]\,,\end{aligned} \tag{S23}$$

for $0 < \xi/v_{b0}\tau < 1$, and $\delta n_p = 0$ otherwise. This solution coincides with that previously obtained for the TSI [3–5], albeit with a different expression for Γ_0. It describes a wave packet growing approximately as

$$\delta n_p \propto \exp\left[\frac{3^{3/2}}{2^{5/3}}\Gamma_0\left(\tau-\frac{\xi}{v_{b0}}\right)^{2/3}\left(\frac{\xi}{v_{b0}}\right)^{1/3}\right] = \exp\left[\frac{3^{3/2}}{2^{5/3}}\Gamma_0\left(\frac{x}{v_{b0}}\right)^{2/3}\left(t-\frac{x}{v_{b0}}\right)^{1/3}\right] \tag{S24}$$

while propagating through the plasma. The peak of the wave packet is located at $\xi = v_{b0}\tau/3$ (i.e. $\theta = 1/3$), and so moves at a speed of $2v_{b0}/3$ in the laboratory. Its amplitude grows with time at a rate

$$\frac{\sqrt{3}}{2}\Gamma_0 = \frac{\sqrt{3}}{2^{4/3}}\left(\frac{1}{\gamma_{b0}}\frac{n_{b0}}{n_{p0}}\frac{k_\perp^2}{k_p^2+k_\perp^2}\right)^{1/3}\omega_{p0}\,, \tag{S25}$$

that is, the well-known temporal growth rate of the cold-fluid OTSI in the $\gamma_{b0} \gg 1$ limit [2, 9], as given by Eq. (1) of the main text.

The above impulsive solution should be of most significance when the relativistic beam crosses a sharp vacuum-plasma boundary. The initial disturbance is then localized at $\xi = 0$ given the absence of plasma at $\xi > 0$. This solution, however, is likely inappropriate if the uniform plasma region where the instability mainly develops is preceded by a long increasing density ramp, or if the beam is directly created within the plasma. Such situations can be modeled by the following initial and boundary conditions [6, 7]:

$$\delta n_p(\tau=0,\xi) = \delta n_p(\tau,\xi=0) = S\,, \tag{S26}$$

$$\partial_\tau \delta n_p(\tau=0,\xi) = \partial_\tau^2\delta(n_p\tau=0,\xi) = 0\,, \tag{S27}$$

where S is some initial fluctuation amplitude. The double Laplace transformation of Eq. (S13) then yields

$$\left(\alpha^3+\alpha^2\beta v_{b0}+\Gamma_0^3\right)\delta n_p(\alpha,\beta) = -i\frac{\alpha}{\beta}(\beta v_{b0}+\alpha)S\,, \tag{S28}$$

use being made of $\delta n_p(\tau=0,\beta) = -iS/\beta$, $\delta n_p(\alpha,\xi=0) = -iS/\alpha$, and $\partial_\tau \delta n_p(\tau=0,\beta) = \partial_\tau^2\delta n_p(\tau=0,\beta) = 0$. It follows that

$$\delta n_p(\alpha,\beta) = -\frac{(\alpha+\beta v_{b0})S}{v_{b0}\alpha\beta\left(\beta+\frac{\alpha^3+\Gamma_0^3}{\alpha^2 v_{b0}}\right)}\,, \tag{S29}$$

and hence

$$\delta n_p(\tau,\xi) = -\frac{S}{4\pi^2 v_{b0}} \int_{C_\alpha} d\alpha\, e^{i\alpha\tau} \int_{C_\beta} d\beta\, \frac{(\alpha+\beta v_{b0})\, e^{i\beta\xi}}{\alpha\beta\left(\beta + \frac{\alpha^3+\Gamma_0^3}{\alpha^2 v_{b0}}\right)}\,, \tag{S30}$$

where C_α and C_β denote again the Bromwich contours. We recast this double integral as

$$\delta n_p(\tau,\xi) = -\frac{S}{2\pi}\int_{C_\alpha} d\alpha\, I(\alpha,\xi) e^{i\alpha\tau}\,, \tag{S31}$$

where

$$I(\alpha,\xi) = \frac{1}{2\pi v_{b0}}\int_{C_\beta} d\beta\, \frac{(\alpha+\beta v_{b0})\, e^{i\beta\xi}}{\alpha\beta\left(\beta+\frac{\alpha^3+\Gamma_0^3}{\alpha^2 v_{b0}}\right)}\,. \tag{S32}$$

Applying the residue theorem to the pole singularities at $\beta = 0$ and $\beta = -\frac{(\alpha^3+\Gamma_0^3)}{\alpha^2 v_{b0}}$ gives

$$I(\alpha,\xi) = i\left[\frac{\alpha^2}{\alpha^3+\Gamma_0^3} + \frac{\Gamma_0^3}{\alpha(\alpha^3+\Gamma_0^3)} e^{-i\frac{(\alpha^3+\Gamma_0^3)}{\alpha^2 v_{b0}}\xi}\right] H(\xi)\,. \tag{S33}$$

Plugging Eq. (S33) into Eq. (S31) yields

$$\delta n_p(\tau,\xi) = -i\frac{S}{2\pi}\int_{C_\alpha} d\alpha\, e^{i\alpha\tau}\left[\frac{\alpha^2}{\alpha^3+\Gamma_0^3} + \frac{\Gamma_0^3}{\alpha(\alpha^3+\Gamma_0^3)} e^{-i\frac{(\alpha^3+\Gamma_0^3)}{\alpha^2 v_{b0}}\xi}\right] H(\xi)\,, \tag{S34}$$

which can be expressed in the form

$$\delta n_p(\tau,\xi) = S\left[J_1(\tau,\xi) + J_2(\tau,\xi)\right] H(\xi)\,, \tag{S35}$$

where

$$J_1(\tau) = -\frac{i}{2\pi}\int_{C_\alpha} d\alpha\, \frac{\alpha^2 e^{i\alpha\tau}}{\alpha^3+\Gamma_0^3}\,, \tag{S36}$$

$$J_2(\tau,\xi) = -\frac{i\Gamma_0^3}{2\pi}\int_{C_\alpha} d\alpha\, \frac{e^{i\alpha\tau - i\frac{(\alpha^3+\Gamma_0^3)}{\alpha^2 v_{b0}}\xi}}{\alpha(\alpha^3+\Gamma_0^3)}\,. \tag{S37}$$

Let us first address J_1. For the same reason as above, $J_1(\tau<0) = 0$, as expected from causality. Its integrand, $G_1(\alpha)$, has simple poles at $\alpha_{\mathrm{p}0} = -\Gamma_0$ and $\alpha_{\mathrm{p}\pm} = \Gamma_0 e^{\pm i\pi/3}$, and their residues are

$$\operatorname{Res}\left[G_1(\alpha); \alpha_{\mathrm{p}0}\right] = \frac{1}{3} e^{-i\Gamma_0\tau}\,, \tag{S38}$$

$$\operatorname{Res}\left[G_1(\alpha); \alpha_{\mathrm{p}\pm}\right] = \frac{1}{3} e^{\frac{i}{2}(1\pm i\sqrt{3})\Gamma_0\tau}\,. \tag{S39}$$

Summing the residues leads to

$$J_1(\tau) = \frac{1}{3}\left[e^{-i\Gamma_0\tau} + 2\cosh\left(\frac{\sqrt{3}}{2}\Gamma_0\tau\right) e^{i\frac{\Gamma_0}{2}\tau}\right] H(\tau)\,. \tag{S40}$$

Similarly to Eq. (S19), the integral J_2 cannot be exactly evaluated, and so instead we approximate it in the $\tau\to\infty$ limit. We therefore rewrite J_2 as

$$J_2(\tau,\xi) = -\frac{i\Gamma_0^3}{2\pi}\int_{C_\alpha} d\alpha\, g(\alpha) e^{\tau h(\alpha,\theta)}\,, \tag{S41}$$

where $h(\alpha,\theta)$ is defined by Eq. (S20) and

$$g(\alpha) = \frac{1}{\alpha(\alpha+\Gamma_0^3)}\,. \tag{S42}$$

The function $g(\alpha)$ possesses four simple pole singularities at $\alpha = 0$, $\alpha_{\mathrm{p}0}$ and $\alpha_{\mathrm{p}\pm}$ (as defined above). We note that the saddle points of $h(\alpha, \theta)$ fulfill $\arg[\alpha_{\mathrm{sp}0}(\theta)] = \arg[\alpha_{\mathrm{p}0}]$ and $\arg[\alpha_{\mathrm{sp}\pm}(\theta)] = \arg[\alpha_{\mathrm{p}\pm}]$. Moreover, $\alpha_{\mathrm{sp}0}(\theta) \to \alpha_{\mathrm{p}0}$ and $\alpha_{\mathrm{sp}\pm}(\theta) \to \alpha_{\mathrm{p}\pm}$ when $\theta \to 1/3$.

The asymptotic expansion of the integral (S41) is more involved than that of (S19), owing to the interaction between the dominant saddle point $\alpha_{\mathrm{sp}-}(\theta)$ of $h(\alpha, \theta)$ and the pole singularity at $\alpha_{\mathrm{p}-} = \Gamma_0 e^{-i\pi/3}$ when the parameter θ varies over $(0, 1)$. Specifically, for $\theta \le 1/3$, the path of steepest descent through $\alpha_{\mathrm{sp}-}(\theta)$ passes above $\alpha_{\mathrm{p}-}$ so that the residue contribution of the latter should be taken into account. For $\theta > 1/3$, by contrast, the path of steepest descent through $\alpha_{\mathrm{sp}-}(\theta)$ passes below $\alpha_{\mathrm{p}-}$, so that there is no residue contribution. As a result,

$$\int_{C_\alpha} d\alpha\, g(\alpha) e^{\tau h(\alpha,\theta)} = \int_{C_{\mathrm{sdp}}} d\alpha\, g(\alpha) e^{\tau h(\alpha,\theta)} + \begin{cases} i2\pi \,\mathrm{Res}\,[g(\alpha); \alpha_{\mathrm{p}-}]\, e^{\tau h(\alpha_p,\theta)} & \theta < 1/3 \\ i\pi \,\mathrm{Res}\,[g(\alpha); \alpha_{\mathrm{p}-}]\, e^{\tau h(\alpha_p,\theta)} & \theta = 1/3 \\ 0 & \theta > 1/3\,, \end{cases} \tag{S43}$$

where C_{sdp} is an Olver-type path with respect to $\alpha_{\mathrm{sp}-}$, as defined above [8].

Another difficulty arises when the saddle point $\alpha_{\mathrm{sp}-}(\theta)$ approaches the pole at $\alpha_{\mathrm{p}-}$, so that $|h(\alpha_{\mathrm{sp}-}(\theta), \theta) - h(\alpha_{\mathrm{p}-}, \theta)|\tau$ may not be necessarily large. Introducing

$$\Delta(\theta) = [h(\alpha_{\mathrm{sp}-}(\theta), \theta) - h(\alpha_{\mathrm{p}-}, \theta)]^{1/2}\,, \tag{S44}$$

a uniform asymptotic approximation of the saddle-point integral is then given by [8]

$$\int_{C_{\mathrm{sdp}}} d\alpha\, g(\alpha) e^{\tau h(\alpha,\theta)} \simeq e^{\tau h(\alpha_{\mathrm{sp}-},\theta)} \Bigg\{ \pm i \mathrm{Res}\,[g(\alpha); \alpha_{\mathrm{p}-}]\; \mathrm{erfc}\left[\mp\sqrt{\tau}\Delta(\theta)\right] e^{\tau[h(\alpha_{\mathrm{sp}-},\theta) - h(\alpha_{\mathrm{p}-},\theta)]} + \sqrt{\frac{\pi}{\tau}} \left[g(\alpha_{\mathrm{sp}-}) \sqrt{\frac{2}{|h''(\alpha_{\mathrm{sp}-},\theta)|}} e^{i\psi_{\mathrm{sdp}}} + \frac{\mathrm{Res}\,[g(\alpha); \alpha_{\mathrm{p}-}]}{\Delta(\theta)} \right] \Bigg\}\,, \tag{S45}$$

when $\Im\Delta(\theta) \gtrless 0$, and by

$$\int_{C_{\mathrm{sdp}}} d\alpha\, g(\alpha) e^{\tau h(\alpha,\theta)} \simeq \sqrt{\frac{2\pi}{\tau |h''(\alpha_{\mathrm{sp}-},\theta)|}} e^{\tau h(\alpha_{\mathrm{sp}-},\theta) + i\psi_{\mathrm{sdp}}} \left[g(\alpha_{\mathrm{sp}-}) - \frac{\mathrm{Res}\,[g(\alpha); \alpha_{\mathrm{p}-}]}{\alpha_{\mathrm{sp}-} - \alpha_{\mathrm{p}-}} - \mathrm{Res}\,[g(\alpha); \alpha_{\mathrm{p}-}]\, \frac{h^{(3)}(\alpha_{\mathrm{sp}-})}{6h''(\alpha_{\mathrm{sp}-})} \right] \tag{S46}$$

when $\Delta(\theta) = 0$.

The function $\mathrm{erfc}(z) = (2/\sqrt{\pi}) \int_z^\infty du\, e^{-u^2}$ is the complementary error function. In Eq. (S44), the argument of $\Delta(\theta)$ is defined so that

$$\lim_{\alpha_{\mathrm{p}-} \to \alpha_{\mathrm{sp}-}} \arg[\Delta(\theta)] = \arg(\alpha_{\mathrm{p}-} - \alpha_{\mathrm{sp}-}) - \psi_{\mathrm{sdp}} + 2\pi n\,,$$

the integer n being chosen so that $\arg[\Delta(\theta)]$ lies within $(-\pi, \pi)$. Here, we have $\psi_{\mathrm{sdp}} = \pi/12$ and $\arg(\alpha_{\mathrm{p}-} - \alpha_{\mathrm{sp}-}) = -\pi/3$ (resp. $2\pi/3$) for $\theta < 1/3$ (resp. $> 1/3$). Hence, $\arg[\Delta(\theta)] = -5\pi/12$ (resp. $7\pi/12$) for $\theta < 1/3$ (resp. $> 1/3$).

Combining Eqs. (S35), (S43) and (S45), and using the expressions

$$\begin{aligned} &\mathrm{Res}\,[g(\alpha); \alpha_{\mathrm{p}-}] = -\frac{1}{3\Gamma_0^3}\,, \\ &h(\alpha_{\mathrm{p}-}, \theta) = \Gamma_0 e^{i\pi/6}\,, \\ &|\Delta(\theta)| = \left[\Gamma_0 \left(1 - 3(\frac{1-\theta}{2})^{2/3} \theta^{1/3}\right)\right]^{1/2}\,, \\ &h^{(3)}(\alpha_{\mathrm{sp}-}, \theta = 1/3) = \frac{8e^{i\pi/6}}{\Gamma_0^2}\,, \\ &\lim_{\alpha \to \alpha_{\mathrm{p}-}} \left\{ g(\alpha) - \frac{\mathrm{Res}\,[g(\alpha); \alpha_{\mathrm{sp}-}]}{\alpha - \alpha_{\mathrm{p}-}} \right\} = \frac{2e^{i\frac{\pi}{3}}}{3\Gamma_0^4}\,, \end{aligned}$$

one can obtain the following approximate solution for $\tau \to \infty$:

$$\delta n_p(\tau, \xi) \simeq \frac{S}{6} e^{3\Gamma_0 \tau (\frac{1-\theta}{2})^{2/3} \theta^{1/3} e^{i\pi/6} - i\pi/12} \Bigg\{ \frac{1}{\sqrt{\pi \Gamma_0 \tau}} \left[2^{1/3}\sqrt{3} \frac{(1-\theta)^{2/3}}{\theta^{1/6}(1-3\theta)} - \frac{1}{\left[1 - 3(\frac{1-\theta}{2})^{2/3}\theta^{1/3}\right]^{1/2}} \right]$$

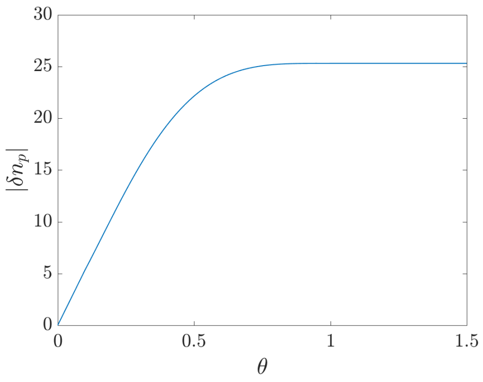

FIG. S1. Asymptotic profile of the OTSI as a function of $\theta = \xi/v_{b0}\tau$ for the initial conditions (S27).

$$\left. + \operatorname{erfc}\left[\sqrt{\tau}|\Delta(\theta)|e^{i\frac{\pi}{12}}\right] e^{\Gamma_0\tau[1-3(\frac{1-\theta}{2})^{2/3}\theta^{1/3}]e^{i\pi/6}+i\pi/12} \right\}, \quad 0<\theta<1/3\,, \tag{S47}$$

$$\delta n_p(\tau,\xi) \simeq \frac{S}{6}\left(1+\frac{4}{3\sqrt{\pi\Gamma_0\tau}}\right)e^{\Gamma_0\tau e^{i\pi/6}}, \quad \theta = 1/3\,. \tag{S48}$$

$$\delta n_p(\tau,\xi) \simeq \frac{S}{6}e^{3\Gamma_0\tau(\frac{1-\theta}{2})^{2/3}\theta^{1/3}e^{i\pi/6}-i\pi/12}\left\{\frac{1}{\sqrt{\pi\Gamma_0\tau}}\left[2^{1/3}\sqrt{3}\frac{(1-\theta)^{2/3}}{\theta^{1/6}(1-3\theta)}+\frac{1}{\left[1-3(\frac{1-\theta}{2})^{2/3}\theta^{1/3}\right]^{1/2}}\right]\right.$$
$$\left. + \operatorname{erfc}\left[\sqrt{\tau}|\Delta(\theta)|e^{i\frac{\pi}{12}}\right] e^{\Gamma_0\tau[1-3(\frac{1-\theta}{2})^{2/3}\theta^{1/3}]e^{i\pi/6}+i\pi/12} \right\} + \frac{S}{3}e^{\Gamma_0\tau e^{i\pi/6}}, \quad 1/3<\theta<1\,, \tag{S49}$$

$$\delta n_p(\tau,\xi) \simeq \frac{S}{3}e^{\Gamma_0\tau e^{i\pi/6}}, \quad \theta > 1\,. \tag{S50}$$

Figure S1 illustrates the shape of the above solution as a function of θ for fixed $\Gamma_0\tau = 5$. We observe a clear transition from a space-time behavior for $\theta \lesssim 1$ to a purely temporal growth for $\theta \gtrsim 1$. This can be understood as follows. When the saddle point and the pole are remote enough from each other such that $\sqrt{\tau}|\Delta(\theta)| \gg 1$, i.e., $\sqrt{\tau}\left[1-3(\frac{1-\theta}{2})^{2/3}\theta^{1/3}\right]^{1/2} \gg 1$, one has $\operatorname{erfc}\left[\sqrt{\tau}|\Delta(\theta)|e^{i\frac{\pi}{12}}\right] \simeq \frac{e^{-\tau|\Delta(\theta)|^2e^{i\pi/6}-i\pi/12}}{\sqrt{\pi\tau}|\Delta(\theta)|}$, and so the erfc term in the r.h.s of Eqs. (S47) and (S50) cancels out the second term between brackets. One then obtains the limiting expressions

$$\delta n_p(\tau,\xi) \simeq \frac{S}{2^{2/3}\sqrt{3\pi\Gamma_0\tau}}\frac{(1-\theta)^{2/3}}{\theta^{1/6}(1-3\theta)}\exp\left[3\Gamma_0\tau\left(\frac{1-\theta}{2}\right)^{2/3}\theta^{1/3}e^{i\pi/6}-i\frac{\pi}{12}\right], \quad 0<\theta<1/3\,, \tag{S51}$$

$$\delta n_p(\tau,\xi) \simeq \frac{S}{3}\exp\left[\Gamma_0\tau e^{i\pi/6}\right], \quad \theta > 1/3\,, \tag{S52}$$

when $\sqrt{\tau}|\Delta(\theta)| \gg 1$. Equation (3) in the main text follows from further assuming $\theta \ll 1$ in Eq. (S51). One can see that, as expected, the instability shares the same spatiotemporal evolution as the Green's function for $\xi \ll v_{b0}\tau$, while it grows in a purely temporal manner for $\xi \gtrsim v_{b0}\tau/3$. A similar mix of spatiotemporal and temporal growth regimes was found for the CFI under the same set of initial and boundary conditions [7].

S2. EVOLUTION OF THE OBLIQUE INSTABILITY IN ELECTRON-BEAM-PLASMA SIMULATIONS

In the main text, we benchmark the spatiotemporal theory of the OTSI against 2D PIC simulations in which a semi-infinite, relativistic electron-positron pair beam propagates in a uniform plasma (see Fig. 2 of the main text). The reason behind using a pair beam rather than an electron beam is to suppress plasma wakefields and other sources of noise induced by a nonneutral charged particle beam, which hamper the observation of the OTSI evolution over a large dynamic range.

Despite this complication, however, it remains possible to capture the spatiotemporal behavior of the instability in an electron beam-plasma simulation as is shown in Fig. S2. Except for the pair beam being replaced with an electron beam of halved relative density ($n_b/n_p = 0.03$ vs. 0.06 for the pair beam), the simulation parameters are identical to those of Fig. 2 in the main text. Although the initial plasma disturbances are stronger and vary appreciably with the longitudinal coordinate ξ, one still clearly observes the spatiotemporal character of the linear phase of the instability in the ultrarelativistic regime [$\gamma_b = 2 \times 10^4$, see Fig. S2(a)-(c)], with reasonable agreement with the cold-fluid model. Similarly, the expected transition to a purely temporal growth at increasing distance from the beam edge can be observed at more moderate Lorentz factors, as illustrated by Fig. S2(d) for $\gamma_b = 20$. Note that in the latter simulation, the dominant OTSI mode has a lower transverse wavenumber ($k_\perp \simeq 1.3 k_p$) than that ($k_\perp \simeq 3k_p$) found in all the other simulations, a difference that is taken into account in computing the theoretical curves (dashed lines) of Fig. S2(d).

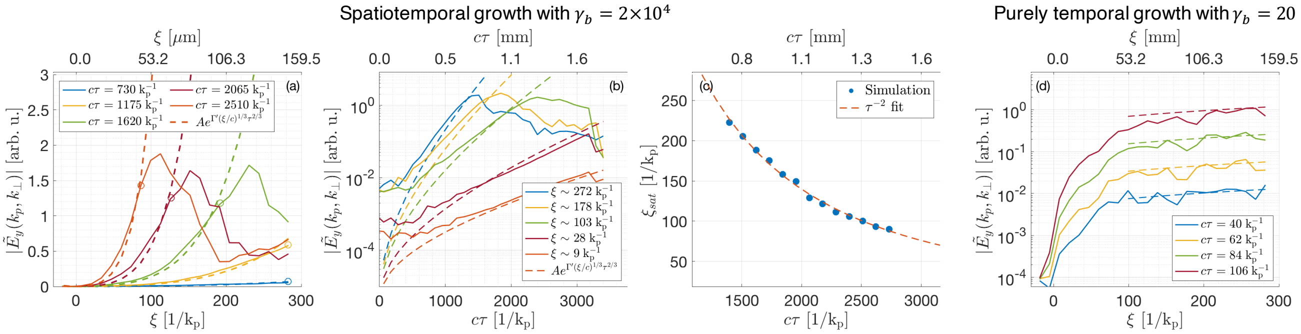

FIG. S2. Same figures as Fig. 2 of the main text but with an electron beam instead of a neutral pair beam.

S3. COMPETITION BETWEEN THE SPATIOTEMPORAL OBLIQUE INSTABILITY AND BEAM SELF-FOCUSING

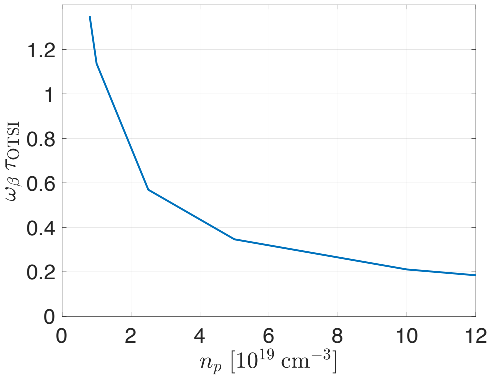

FIG. S3. Ratio of the characteristic time scales of the OTSI (τ_{OTSI}) and beam self-focusing (ω_β^{-1}) in the ultrarelativistic beam limit. The beam parameters are those associated with Fig. 3 of the main text.

In the main text, we show that the plasma wakefields driven by finite-size electron beams cause the resulting beam self-focusing to compete with the OTSI. The interplay of these two processes can be gauged by comparing their respective characteristic time scales. The time scale for beam self-focusing is estimated to be the inverse betatron frequency $\omega_\beta^{-1} = \sqrt{\gamma_b m_e/\partial_r W_\perp}$, where $W_\perp$ is the focusing force associated with the plasma wakefield in the linear regime. In the ultrarelativistic beam limit ($\gamma_b \gg 1$), $W_\perp$ is given by [10]:

$$W_\perp(\xi, r) = 4\pi k_p \int_0^\infty dr' r' I_1(k_p r_<) K_1(k_p r_>) \int_{-\infty}^{\xi} d\xi' \partial_{r'} n_b(\xi', r') \sin(k_p(\xi - \xi')) \,, \tag{S53}$$

where I_1 and K_1 are modified Bessel functions, and $r_<$ (resp. $r_>$) denotes the minimum (resp. maximum) of r and

r'. The radial derivative of $W_\perp$ can be numerically computed (at the beam center and $r = 0$) for a Gaussian beam with RMS length σ_x and width σ_r.

Since the electron beam being considered is short enough that $\Gamma_{\mathrm{OTSI}}\sigma_x/c \ll 1$ [Γ_{OTSI} is the maximum growth rate given by Eq. (1) of the main text], the OTSI develops in a spatiotemporal manner. Consequently, its effective growth time, τ_{OTSI}, can be estimated from the leading exponential term of Eq. (3) in the main text. Taking τ_{OTSI} to be the time needed for a given beam slice, located at ξ, to experience a certain number N_{exp} of e-foldings, one obtains

$$\tau_{\mathrm{OTSI}} = 2\left(\frac{N_{\mathrm{exp}}}{3\Gamma_{\mathrm{OTSI}}}\right)^{3/2}\left(\frac{v_b}{\xi}\right)^{1/2}, \tag{S54}$$

To get an approximate value for the Gaussian beam considered in Fig. 3 of the main text, we take $\xi = \sigma_x$, $n_b = \max n_b$, $k_\perp = 2k_p$ and $N_{\mathrm{exp}} = 5$ (consistent with the observed dynamic range of the growing field amplitude).

Figure S3 plots $\omega_\beta\,\tau_{\mathrm{OTSI}}$ as a function of the background plasma density for the beam parameters of Fig. 3 in the main text. One can see that $\omega_\beta\,\tau_{\mathrm{OTSI}} > 1$, meaning that beam self-focusing prevails over the OTSI, for $n_p \lesssim 10^{19}\,\mathrm{cm}^{-3}$, in good agreement with the simulation results (see main text).

---

[1] L. E. Thode, "Energy lost by a relativistic electron beam due to two-stream instability," Phys. Fluids **19**, 305–315 (1976).

[2] A. Bret, L. Gremillet, and D. Bénisti, "Exact relativistic kinetic theory of the full unstable spectrum of an electron-beam-plasma system with Maxwell-Jüttner distribution functions," Phys. Rev. E **81**, 036402 (2010).

[3] E. V. Rostomian, "Space-time evolution of beam-plasma instabilities," Phys. Plasmas **7**, 1595–1600 (2000).

[4] A. Bers, "Space-Time Evolution of Plasma Instabilities - Absolute and Convective," in *Handbook of Plasma Physics*, edited by M. N. Rosenbluth and R. Z. Sagdeev (North-Holland Physics Publishing, Amsterdam, 1983) Chap. 3.2, pp. 451–517.

[5] Michael E. Jones, Don S. Lemons, and Michael A. Mostrom, "Space-time evolution of the beam-plasma instability," Phys. Fluids **26**, 2784–2786 (1983).

[6] C. D. Decker, W. B. Mori, T. Katsouleas, and D. E. Hinkel, "Spatial temporal theory of Raman forward scattering," Phys. Plasmas **3**, 1360–1372 (1996).

[7] V. B. Pathak, T. Grismayer, A. Stockem, R. A. Fonseca, and L. O. Silva, "Spatial-temporal evolution of the current filamentation instability," New J. Phys. **17**, 043049 (2015).

[8] K. E. Oughstun, *Electromagnetic and Optical Pulse Propagation. Volume 2: Temporal Pulse Dynamics in Dispersive Attenuative Media* (Springer International Publishing, 2009).

[9] R. L. Ferch and R. N. Sudan, "Linear two-stream instability of warm relativistic electron beams," Plasma Phys. **17**, 905–915 (1975).

[10] R. Keinigs and M. E. Jones, "Two-dimensional dynamics of the plasma wakefield accelerator," Phys. Fluids **30**, 252–263 (1987).

PHILOSOPHICAL TRANSACTIONS A

rsta.royalsocietypublishing.org

Research

Article submitted to journal

Subject Areas:
Plasma-based particle accelerators

Keywords:
plasma, accelerators, particle beams, radiation, gamma-rays

Author for correspondence:
Sebastien Corde
e-mail:
sebastien.corde@polytechnique.edu

THE ROYAL SOCIETY
PUBLISHING

Betatron radiation and emittance growth in Plasma Wakefield Accelerators

P. San Miguel Claveria[1], E. Adli[2], L. D. Amorim[3], W. An[4], C. E. Clayton[4], S. Corde[1], S. Gessner[5], M. J. Hogan[6], C. Joshi[4], O. Kononenko[1], M. Litos[7], W. Lu[8], K. A. Marsh[4], W. B. Mori[4], B. OâĂŹShea[6], G. Raj[1], D. Storey[6], N. Vafaei-Najafabadi[3], G. White[6], Xinlu Xu[4,6] and V. Yakimenko[6]

[1]LOA, ENSTA ParisTech, CNRS, Ecole Polytechnique, Université Paris-Saclay, 91762 Palaiseau, France
[2]University of Oslo, NO-0316, Oslo, Norway
[3]Stonybrook University, Stony Brook, NY 11794, USA
[4]University of California Los Angeles, Los Angeles, CA 90095, USA
[5]CERN, Geneva, Switzerland
[6]SLAC National Accelerator Laboratory, Menlo Park, California 94025, USA
[7]University of Colorado Boulder, Boulder, Colorado 80309, USA
[8]Tsinghua University, Beijing 10084, China

Beam-driven plasma wakefield acceleration (PWFA) has demonstrated significant progress during past two decades of research. The new Facility for Advanced Accelerator Experimental Tests (FACET) II, currently under construction, will provide 10 GeV electron beams with unprecedented parameters for the next generation of PWFA experiments. In the context of the FACET II facility, we present simulation results on expected betatron radiation and its potential application to diagnose emittance preservation and hosing instability in the upcoming PWFA experiments.

© The Authors. Published by the Royal Society under the terms of the Creative Commons Attribution License http://creativecommons.org/licenses/by/4.0/, which permits unrestricted use, provided the original author and source are credited.

1. Introduction

Plasma wakefield acceleration (PWFA) is a method for accelerating charged particles using large electric fields sustained by plasma waves (up to 100's of GV/m for the accelerating longitudinal field) [1]. In this scheme, a relativistic electron bunch (called *"drive"* bunch) is sent through the plasma, exciting perturbations in the plasma density that forms a plasma wave. A second electron bunch (or *"trailing"* bunch) can then be injected at the accelerating phase of this plasma wave, receiving a substantial gain in energy.

When the drive bunch density is significantly greater than the plasma density, all free plasma electrons are expelled out from the beam propagation axis, creating a positively charged ion cavity behind. This regime is called the *"bubble"* or *"blow-out"* regime [2–4], and it is considered as one of the most suitable regimes for electron acceleration. This nonlinear regime allows acceleration of electrons using large accelerating gradients (typically an order of magnitude larger than in the linear regime, where the density perturbation behind the drive bunch does not reach 100 %), and has an ideal field structure for preserving the quality of an electron beam during its acceleration [5] and for reaching high energy transfer efficiencies from the drive to the trailing beam [6]. But to reach this blow-out regime, the drive beam needs to have extreme parameters: very high bunch density and beam size and bunch length of the order or smaller than the plasma wavelength. FACET is one of the only facilities in the world to provide an electron beam of this kind, where in 2016 a 9 GeV energy gain in a beam-driven plasma wakefield accelerator was experimentally demonstrated [7].

Such large accelerating fields make this technique a promising alternative to conventional accelerators based on radio-frequency (RF) cavities, whose maximum acceleration gradient can be several orders of magnitude below the typical accelerating gradients of PWFA. However, in terms of beam quality, the PWFA scheme has not yet reached the same performance as conventional acceleration technique. Beam quality preservation is one of the most important issues to overcome for most of the PWFA applications, such as the PWFA-based Linear Collider. This new milestone of PWFA will be explored at the future FACET II facility [8], which is expected to produce unprecedented electron beams, in particular in terms of beam current, spot size and beta function at focus, bunch length, and emittance.

Several processes might deteriorate the quality of an electron beam during acceleration. In this article we will focus on the emittance growth caused by a mismatched propagation of the beam in the plasma and by the presence of the hosing instability. These processes are expected to be the most relevant for beam quality degradation in actual state of PWFA experiments. Furthermore, they are both difficult to measure experimentally *in-situ* with a non-destructive method. As shown in this article, a possible non-destructive diagnostic for these processes would be the use of the betatron radiation emitted by the beam electrons in the ion cavity.

2. Betatron Radiation at FACET II – Simulation Results

The betatron radiation in PWFA accelerators is emitted by the drive and trailing electron bunches due to the transverse forces present in the ion cavity acting upon the electrons. These forces are proportional to the transverse displacement of the electrons with respect to the propagation axis and result in oscillating trajectories, called betatron oscillations. The spatial period of the electron oscillation is called the betatron wavelength given by $\lambda_\beta = \sqrt{2\gamma}\lambda_p$ in the blow-out regime, where λ_p is the plasma wavelength and γ the Lorentz factor of the electron. For conditions relevant to FACET II, the radiation emitted by an electron following this type of trajectory is very similar to the radiation produced in high-K wigglers, i.e., very collimated in the forward direction ($\theta \simeq K/\gamma \ll 1$) and with a synchrotron-like photon energy spectrum [9]. This is the so-called betatron radiation [9–11].

When the beam is said to be “matched”, its spot size remains constant during its propagation in the plasma. The Twiss parameters of the bunch need to be tuned in order to obtain a matched

	Drive Beam	Trailing Beam
$\hat{\alpha}_{x,y}$	4.2, 1.6	0, 0
$\hat{\beta}_{x,y}$ [m]	0.7, 0.7	0.05, 0.05
Q [nC]	1.6	0.5
σ_z [μm]	6.4	2.8
E [GeV]	10	10
$\epsilon_{N_{x,y}}$ [mm·mrad]	3.4, 3.0	3.2, 3.2
Δz [μm]	150	
$\Delta W_{x,y}$ [cm]	16, 31	

Table 1. Relevant beam parameters at the location of the x and y trailing waist used in the simulations: $\hat{\alpha}$ and $\hat{\beta}$ are the Twiss parameters, Q is the beam charge, σ_z is the RMS bunch length, E is the energy, $\epsilon_{N_{x,y}}$ is the normalised emittance, Δz is the longitudinal separation distance between the bunches and $\Delta W_{x,y}$ is the distance between locations of the drive waist and the trailing waist (ΔW_x for x waist, ΔW_y for y waist).

propagation, and in the blow-out regime, the matched Twiss parameters read $\beta_{\text{matched}} = \lambda_\beta/2\pi$ and $\alpha_{\text{matched}} = 0$ [12,13]. When matching conditions are not met, individual oscillations of the electrons give rise to beam envelope oscillations: the spot size (or RMS radius) of the beam will oscillate while propagating in the plasma [13,14].

FACET II will deliver electron bunches with optimal parameters, such as high current,Âăsmall spot size and beta function at focus, small bunch length and low emittance, for the next generation of PWFA experiments. In the two bunch configuration, the drive bunch will excite a plasma wave in the pre-ionised lithium vapour target, and the trailing bunch will propagate behind the drive bunch, experiencing the accelerating and focusing fields of the plasma wave. The plasma density profile used in the simulations corresponds to the expected vapour density profile of the lithium oven [15,16] that will be used as the plasma target in the experiment. The coordinate system used in our simulations is such that z is the longitudinal coordinate corresponding to the propagation direction of the electron bunch, x and y are the transverse coordinates forming a right-handed cartesian coordinate system. Taking $z = 0$ as the beginning of the simulation, the simulated plasma density profile consists of a semi-gaussian up-ramp with maximum at $z = 20$ cm, a plateau region ($n_0 = 4 \cdot 10^{16}$ cm^{-3}) from $z = 20$ cm to $z = 40$ cm, followed by a semi-gaussian down-ramp from $z = 40$ cm to $z = 60$ cm. Parameters of the drive and trailing electron bunches used in the simulations are showed in Table 1 and the plasma density profile is plotted in Fig. 1(a).

In order to explore potential use of the betatron radiation in PWFA accelerators to assess beam quality deterioration, we simulated using the QuickPIC code [17,18] the expected FACET II electron bunches passing through the aforementioned plasma target, and then output the trajectories of the electrons to numerically compute emitted radiation using the Lienard-Wiechert fields [19]. Since the electrons are highly relativistic and the strength parameter K of the betatron oscillations [9] is large compared to 1, we used the synchrotron approximation to describe the angular and spectral distribution of the betatron radiation. Figure 1(b) shows the photon energy spectrum and Figs. 1(c) and 1(d) show the angular distributions of the betatron radiation emitted by both bunches when the focal plane of the trailing bunch is set at $z = 6.3$ cm, shown as a red dashed line in Fig. 1(a). These plots show typical values of divergence ($\sim$ mrad), total radiated energy ($\sim$ mJ) and gamma-ray spectrum for the FACET II beam parameters.

The difference between the angular distribution of the radiation emitted by the drive bunch and the trailing bunch is related to beam parameters of each bunch. As mentioned above, if the matching conditions are not met beam envelope oscillations are present during the propagation of

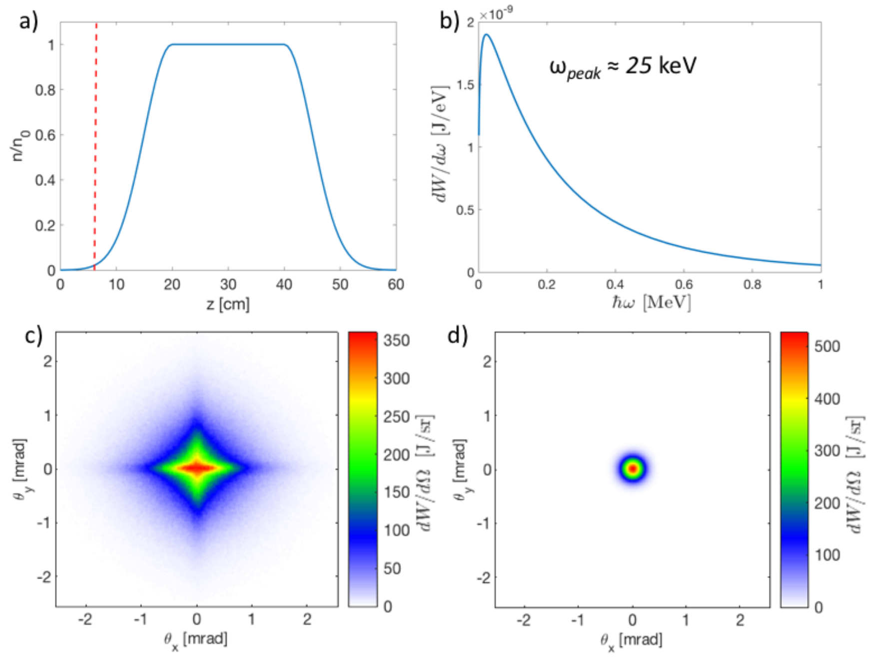

Figure 1. a) Plasma density profile used for QuickPIC simulations ($n_0 = 4 \cdot 10^{16}$ cm^{-3}). Red-dashed line shows the position of the focal plane of the trailing bunch for the matched conditions. b) Photon energy spectrum of the radiation emitted by the two bunches. c) Radiation angular distribution of the drive bunch (J/sr). d) Radiation angular distribution of the trailing bunch (J/sr).

the bunch in the ion cavity. These envelope oscillations are described by the following differential equation

$$\sigma_i'' + k_\beta^2 \sigma_i - \frac{\epsilon_i^2}{\sigma_i^3} = 0$$

where the derivatives are with respect to the longitudinal coordinate z, σ is the spot size, $k_\beta = 2\pi/\lambda_\beta = k_p/\sqrt{2\gamma}$ with k_p the wavenumber associated to the plasma frequency, ϵ is the geometrical emittance and i represent the transverse coordinate x or y. When a beam is azimuthally symmetric both spot sizes σ_x and σ_y oscillate in phase, so that the electron beam preserves its azimuthal symmetry during propagation. This is the case for the FACET II trailing beam and leads to an azimuthal symmetry in the radiation angular distribution. If the beam parameters are not symmetric in the transverse directions, as for the FACET II drive beam, the transverse spot sizes evolve differently, leading in some cases to not-in-phase envelope oscillations, so that the transverse profile of the bunch oscillates between a horizontal and a vertical ellipse. These not-in-phase envelope oscillations, as shown in Fig. 2, affect the radiation angular distribution. This figure shows asymmetric betatron radiation angular distribution emitted in 6 consecutive timesteps separated by 3.1 ps, in which we can observe the transition from a horizontal ellipse (Fig. 2(c)) to a vertical ellipse (Fig. 2(e)).

3. Betatron Diagnostics – Simulation Results

Beam quality preservation in PWFA is one of the most important aspects to be experimentally proven in future PWFA research. Here we present the simulation results that demonstrates ability to use betatron radiation to detect mismatched propagation and beam centroid oscillation which lead to emittance growth and hosing instability.

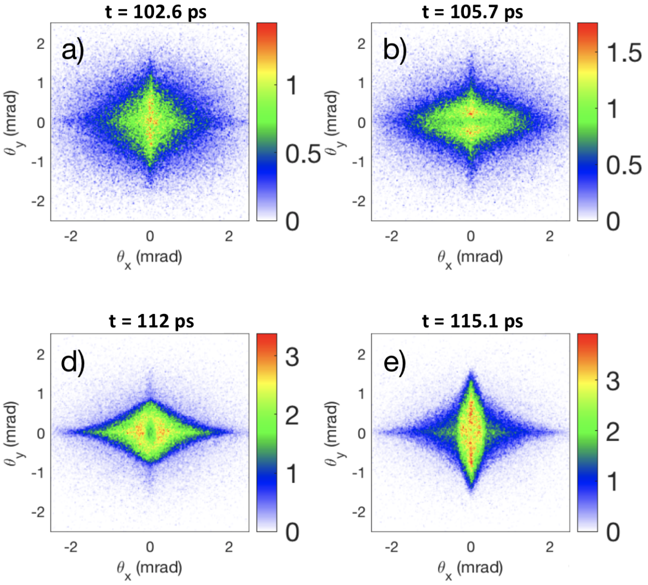

Figure 2. Betatron radiation angular distributions in J/sr emitted by the drive bunch at 6 consecutive timesteps. The timesteps represented here are $t = 102.6, 105.7, 108.8, 112, 115.1$ and 118.2 ps, corresponding to the beginning of the plateau region ($z = 20$ cm). In this simulation the trailing focal plane position is at $z_{\text{trailing}} = 12$ cm, the x drive focal plane position is at $z_{\text{drive},x} = z_{\text{trailing}} + \varDelta W_x = 28$ cm and the y drive focal plane position is at $z_{\text{drive},y} = z_{\text{trailing}} + \varDelta W_y = 43$ cm.

(a) Mismatched propagation and emittance growth

For many applications of the PWFA technique, especially for the Plasma-based Linear Collider, normalised transverse emittance must be kept constant during the acceleration process. Emittance growth in current PWFA accelerators is caused mainly by mismatched propagation in the plasma and chromatic effects due to the finite energy spread: trace-space ellipses of electrons with different energies rotate at a different rate in the trace space (x, x') (or equivalently in the phase space (x, p_x), with $x' = p_x/p_z$), leading to an increase of the emittance (see Fig. 3(a)) [12].

When the ellipses for each energy are circular[1] instead of elliptical, even if individual particles would still describe circular orbits in trace space, the overall distribution remains the same as the beam propagates in the plasma. This beam matching leads to a constant spot size and allows mitigation of the emittance growth.

The matched beta function $\beta_{\text{matched}} = \lambda_\beta/2\pi$ for a trailing beam inside an ion cavity can be determined for a given plasma density, since the betatron wavelength λ_β depends on plasma density. In experiments plasma density is not uniform, and usually the electron beam goes through an up-ramp and down-ramp, which complicates prediction of matching conditions for a given plasma profile. It is then important for experiments to know when the beam is matched in the plasma, and betatron diagnostic can be a powerful tool to do this.

We run several simulations for the expected FACET II beam and plasma parameters for different focal plane positions of the trailing bunch inside the plasma. The drive bunch focal plane was also shifted consistently, so that different simulations correspond to different tunings of the final focusing magnets. In all these simulations we measured the emittance growth and correlated results with simulated betatron radiation. The results are shown in Fig. 4(a): we observe that the trailing beam is matched in the flat-top region when its focal plane is at $z = 6.3$ cm (red dashed line

---

[1] Circular in the (x, x') trace space where x is plotted in normalised units, so that $x^2 + x'^2 = \text{constant}$.

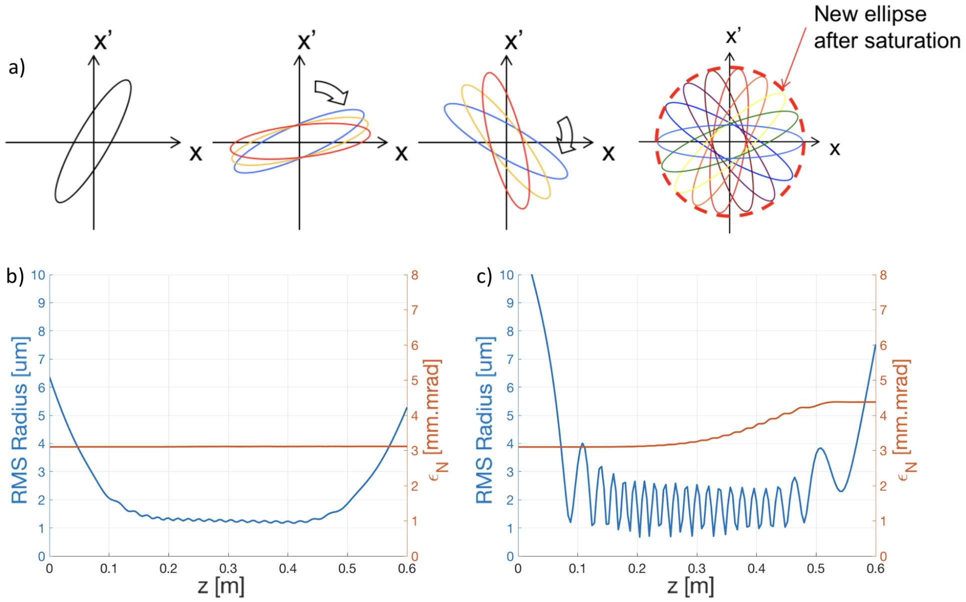

Figure 3. a) Trace-space ellipse evolution for different energies (colours), red dashed circle illustrates geometrical emittance saturation. b) and c) RMS radius (in blue) and mean normalised emittance ($\sqrt{\epsilon_{Nx} \cdot \epsilon_{Ny}}$, in orange) for matched (b) and mismatched (c) cases.

in Fig. 1(a)). When we either increase or decrease this distance, the trailing beam is not matched and this is translated into beam envelope oscillations and – as a consequence – an increase of the emittance growth.ÂăIn these simulations, the trailing bunch has zero energy spread initially, but acquires a finite energy spread as it is accelerated in the plasma, which in turns lead to emittance growth depending on its matching to the plasma. The total betatron radiation emitted by the trailing bunch also has a minimum at 6.3 cm and it increases when we move apart from this focal position. This can be understood as follows: if the beam is not matched, individual electrons oscillate with a higher amplitude than in the matched case, so electrons radiate more energy. Thus this correlation shows that the betatron radiation emitted by an electron bunch in an ion cavity can be used to retrieve information about beam matching and the evolution of its emittance.

Experimentally it is difficult to measure the radiation emitted by the trailing bunch separately from the radiation of the drive bunch. Therefore, since the matching conditions for the drive bunch are not the same as for the trailing bunch, the subtraction of the drive bunch radiated energy is required (see Fig. 4(b)). This could be done by measuring first the betatron radiation of a single-bunch configuration (drive only), and then subtracting the "drive-only" radiation from the total radiation emitted by the two bunches (drive + trailing). Such measurements of the betatron radiation can be used to tune the experiment for trailing beam matching and emittance preservation.

(b) Beam centroid oscillation and hosing instability

Hosing is a transverse instability that has been predicted theoretically to occur in the blow-out regime of PWFA [20,21] and studied experimentally [22]. This instability arises when longitudinally-dependent transverse force acts upon the beam. Such a situation can occur when an electron beam is offset in a uniform ion column, which results in centroid oscillations with a growing amplitude. This instability yields to a large increase of the emittance and, if the

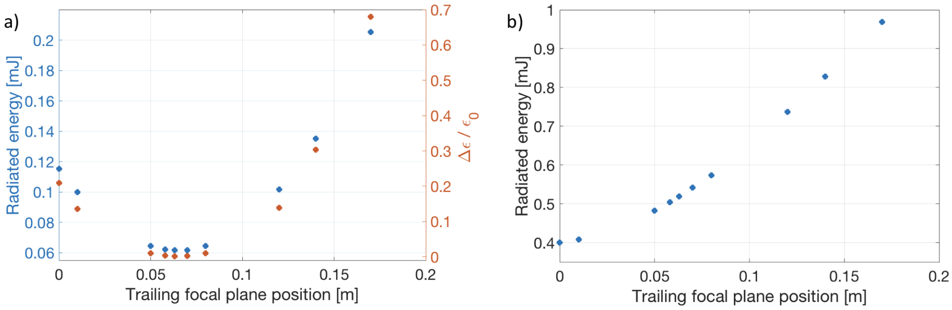

Figure 4. a) Total radiated energy (blue) and relative emittance growth (orange) from the trailing bunch as a function of the focal plane position of the trailing bunch. b) Total radiated energy from the trailing and drive bunches.

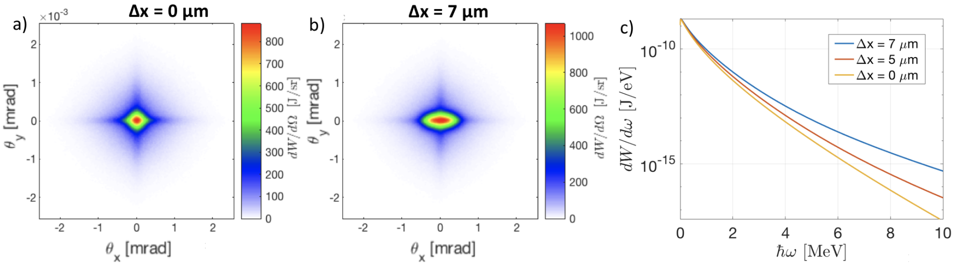

Figure 5. a) Angular distribution (J/sr) of the betatron radiation emitted by both beams when no offset in the trailing was induced. b) Angular distribution (J/sr) of the betatron radiation emitted by both beams when a 7 μm offset is introduced along the x axis for the trailing bunch. c) Energy spectrum of the betatron radiation emitted by both bunches for three different offset values.

instability grows enough, it might even cause the loss of portions of the bunch. Therefore study and mitigation of this instability are very important for PWFA experiments.

Our simulations show that betatron radiation could be exploited to also assess hosing instability. To simulate the hosing instability we introduced at the beginning of the simulations a small transverse offset in the trailing bunch. Figure 5 shows the effect of this offset on the angular distribution and energy spectrum of the betatron radiation. In Fig. 5(a) we present the angular distribution of the betatron radiation emitted by both beams when no offset is introduced. Similar distribution is presented in Fig. 5(b) when an offset of 7 μm in the x direction is introduced. We observe an increase of the radiated energy when an offset in the trailing beam is induced, and an increase in the divergence of the angular distribution in the direction where this offset was induced. Figure 5(c) shows the energy spectrum of the betatron radiation for three different values of the initial offset. A small difference at the tail of the distribution, at high photon energies, can be observed. In a similar way as for the emittance preservation, beam centroid oscillations leads to a larger oscillation amplitude of individual electrons, so that the total radiated energy also increases. These results demonstrate the possibility to use betatron radiation to fully characterise (in terms of direction and magnitude) an offset in the trailing beam which may seed hosing instability.

4. Conclusion and overlook

We presented simulation results of the expected betatron radiation properties for the future PWFA experiments at FACET II and the potential application of betatron radiation to investigate several processes occurring in Plasma Wakefield Acceleration. For FACET II electron beam and plasma target (lithium oven) parameters, the betatron radiated energy is expected to be of the order of the millijoule, with a milliradian divergence and a photon energy spectrum ranging from a few kiloelectronvolts up to the megaelectronvolt.

In our study we demonstrated that the betatron radiation can be used to assess information about dynamics of the trailing electron beam propagating in a plasma wave, in particular regarding its matched or mismatched propagation and the beam centroid oscillations, which can lead to emittance growth and hosing. Thus, we conclude that betatron radiation is a powerful diagnostic to experimentally assess and mitigate emittance growth and hosing instability, which are of key importance for the next generation of PWFA experiments.

Data Accessibility. The data that support the findings of this study are available from the corresponding author upon request.

Competing Interests. The authors declare that they have no competing interests.

Funding. Work at LOA was supported by the European Research Council (M-PAC project, Contract No. 715807). Simulations were performed on the UCLA Hoffman2 cluster through NSF OCI-1036224. Work at UCLA was supported by DOE Contracts No. DE-SC0010064, No. DE-SC0008491, No. DE-SC0008316 and NSF Contracts No. PHY-1415386, No. PHY-1734315, No. ACI-1339893, No. PHY-0960344. Work at SLAC was supported by DOE Contract No. DE-AC02-76SF00515.

References

1. P. Chen et al., *Acceleration of Electrons by the Interaction of a Bunched Electron Beam with a Plasma.* Phys. Rev. Lett. 54, 693, 1985.
2. W. Lu et al., *Nonlinear Theory for Relativistic Plasma Wakefields in the Blowout Regime.* Phys. Rev. Lett. 96.165002, 2006.
3. J. B. Rosenzweig, B. Breizman, T. Katsouleas, and J. J. Su, *Acceleration and focusing of electrons in two-dimensional nonlinear plasma wake fields.* Phys. Rev. A 44, R6189(R), 1991.
4. A. Pukhov and J. Meyer-Ter-Vehn, *Laser wake field acceleration:the highly non-linear broken-wave regime.* Appl. Phys. B 74, 335-361, 2002.
5. C. E. Clayton et al., *Self-mapping the longitudinal field structure of a nonlinear plasma accelerator cavity*. Nat. Commun. 7, 12483, 2016.
6. M. Litos et al., *High-efficiency acceleration of an electron beam in a plasma wakefield accelerator*. Nature 515, 92, 2014.
7. M. Litos et al., *9 GeV energy gain in a beam-driven plasma wakefield accelerator.* Plasma Physics and Controlled Fusion, 0741-3335-58-3-034017, 2016.
8. C. Joshi et al., *Plasma wakefield acceleration experiments at FACET II.* Plasma Phys. Control. Fusion 60, 034001, 2018.
9. S. Corde et al., *Femtosecond x rays from laser-plasma accelerators.* Rev. Mod. Phys. 85, 1, 2013.
10. S. Wang et al., *X-Ray Emission from Betatron Motion in a Plasma Wiggler*. Phys. Rev. Lett. 88, 135004, 2002.
11. A. Rousse et al., *Production of a keV X-Ray Beam from Synchrotron Radiation in Relativistic Laser-Plasma Interaction*. Phys. Rev. Lett 93, 135005, 2004.
12. T. Mehrling et al., *Transverse emittance growth in staged laser-wakefield acceleration*. Phys. Rev. Accel. Beams 15, 111303, 2012.
13. K. A. Marsh et al., *Beam matching to a plasma wake field accelerator using a ramped density profile at the plasma boundary*. Proceedings of the 2005 Particle Accelerator Conference (IEEE, Knoxville, USA), pp. 2702-2704, 2005.
14. C. E. Clayton et al., *Transverse envelope dynamics of a 28.5-GeV electron beam in a long plasma.* Phys. Rev. Lett. 88, 154801, 2002.
15. P. Muggli et al., *Photo-ionized lithium source for plasma accelerator applications*. IEEE T rans. Plasma Sci. 27, 791-799, 1999.

16. S. Z. Green et al., *Laser ionized preformed plasma at FACET*. Plasma Phys. Contr. Fusion 56, 084011, 2014.
17. C. Huang et al., *QUICKPIC: A highly efficient particle-in-cell code for modeling wakefield acceleration in plasmas*. J. Comput. Phys. 217, 658, 2006.
18. W. An et al., *An improved iteration loop for the three dimensional quasi-static particle-in-cell algorithm: QuickPIC*. J. Comput. Phys. 250, 165-177, 2013.
19. J. D. Jackson, *Classical Electrodynamics*. (Wiley, New York, 2001).
20. C. Huang et al., *Hosing Instability in the Blow-Out Regime for Plasma-Wakefield Acceleration.*. Phys. Rev. Lett. 99, 255001, 2007.
21. T. J. Mehrling et al. *Mitigation of the Hose Instability in Plasma-Wakefield Accelerators.*. Phys. Rev. Lett. 118, 174801, 2017.
22. E. Adli et al., *Transverse Oscillations in Plasma Wakefield Experiments at FACET*. Nucl. Instrum. Methods Phys. Rev. A 829, 94, 2016.

Extremely Dense Gamma-Ray Pulses in Electron Beam-Multifoil Collisions

Archana Sampath,[1] Xavier Davoine,[2,3] Sébastien Corde,[4] Laurent Gremillet,[2,3] Max Gilljohann,[4] Maitreyi Sangal,[1]
Christoph H. Keitel,[1] Robert Ariniello,[5] John Cary,[5] Henrik Ekerfelt,[6] Claudio Emma,[6] Frederico Fiuza,[6] Hiroki Fujii,[7]
Mark Hogan,[6] Chan Joshi,[7] Alexander Knetsch,[4] Olena Kononenko,[4] Valentina Lee,[5] Mike Litos,[5] Kenneth Marsh,[7]
Zan Nie,[7] Brendan O'Shea,[6] J. Ryan Peterson,[6,8] Pablo San Miguel Claveria,[4] Doug Storey,[6] Yipeng Wu,[7] Xinlu Xu,[6]
Chaojie Zhang,[7] and Matteo Tamburini[1,*]

[1]*Max-Planck-Institut für Kernphysik, Saupfercheckweg 1, D-69117 Heidelberg, Germany*
[2]*CEA, DAM, DIF, 91297 Arpajon, France*
[3]*Université Paris-Saclay, CEA, LMCE, 91680 Bruyères-le-Châtel, France*
[4]*LOA, ENSTA Paris, CNRS, Ecole Polytechnique, Institut Polytechnique de Paris, 91762 Palaiseau, France*
[5]*University of Colorado Boulder, Department of Physics, Center for Integrated Plasma Studies,*
Boulder, Colorado 80309, USA
[6]*SLAC National Accelerator Laboratory, Menlo Park, California 94025, USA*
[7]*University of California Los Angeles, Los Angeles, California 90095, USA*
[8]*Stanford University, Physics Department, Stanford, California 94305, USA*

(Received 25 September 2020; revised 18 December 2020; accepted 8 January 2021; published 12 February 2021)

Sources of high-energy photons have important applications in almost all areas of research. However, the photon flux and intensity of existing sources is strongly limited for photon energies above a few hundred keV. Here we show that a high-current ultrarelativistic electron beam interacting with multiple submicrometer-thick conducting foils can undergo strong self-focusing accompanied by efficient emission of gamma-ray synchrotron photons. Physically, self-focusing and high-energy photon emission originate from the beam interaction with the near-field transition radiation accompanying the beam-foil collision. This near field radiation is of amplitude comparable with the beam self-field, and can be strong enough that a single emitted photon can carry away a significant fraction of the emitting electron energy. After beam collision with multiple foils, femtosecond collimated electron and photon beams with number density exceeding that of a solid are obtained. The relative simplicity, unique properties, and high efficiency of this gamma-ray source open up new opportunities for both applied and fundamental research including laserless investigations of strong-field QED processes with a single electron beam.

DOI: 10.1103/PhysRevLett.126.064801

The generation of high-energy, dense, and collimated photon beams is of great interest both to fundamental and applied research. Indeed, such beams enable new avenues for research in strong-field QED, relativistic plasma astrophysics, and high-energy physics [1–4]. In particular, solid-density photon beams allow matterless photon-photon physics studies, where traditional schemes are limited in luminosity due to the low density of high-energy photons [5]. A source of high-energy, solid-density photon beams also enables the generation of neutral collimated ultradense electron-positron jets, opening a unique portal to novel relativistic laboratory astrophysics studies [6–9]. Moreover, energetic solid-density electron and photon beams make it possible to access important unexplored regimes in high-density beam physics [10,11]. Furthermore, intense sources of high-energy photons have broad applications in industry, medicine, and materials science [12–15].

The growing interest in intense high-energy photon sources has recently stimulated several proposals to further increase the attainable photon energy and flux. These proposals include high-power laser-plasma interactions [16–29], plasma instabilities [30], QED cascades [31,32], multiple colliding laser pulses [33,34], and beamstrahlung [35–37]. A number of experiments, where the generated photon beam properties could be accurately measured and tuned, were also successfully performed [38–45]. In those schemes, however, the achievable density remains less than $\sim 10^{24}$ m^{-3}.

Here we introduce a novel concept for an ultraintense gamma-ray source based on the interaction of a single high-current ultrarelativistic electron beam with multiple submicrometer-thick conducting foils (see Fig. 1). By using fully 3D particle-in-cell (PIC) simulations, we show that (i) an ultrarelativistic (10 GeV), dense

---

Published by the American Physical Society under the terms of the Creative Commons Attribution 4.0 International license. Further distribution of this work must maintain attribution to the author(s) and the published article's title, journal citation, and DOI. Open access publication funded by the Max Planck Society.

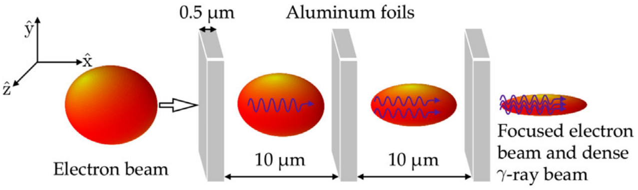

FIG. 1. Schematic setup. An ultrarelativistic electron beam sequentially collides with aluminum foils. At each beam-foil collision, a strong transverse force which focuses the electron beam and leads to copious gamma-ray emission is induced.

(4.7×10^{27} m^{-3}) electron beam can be radially focused up to 4.5×10^{29} m^{-3}, i.e., beyond the 1.8×10^{29} m^{-3} electron density of solid aluminum; (ii) electron beam focusing is accompanied by intense synchrotron photon emission with more than 30% of the electron beam energy eventually converted into a 2.8×10^{29} m^{-3} peak density collimated gamma-ray beam (with a maximum density of 8.5×10^{29} m^{-3} achieved in the course of the interaction); (iii) when the electron beam density exceeds the foil electron density, the beam self-fields expel the target electrons and create an electron-depleted channel through the foil. The fields experienced by the beam electrons inside the plasma channel are so high that the quantum parameter $\chi \approx \gamma|\boldsymbol{f}_\perp|/eF_{\rm cr}$ exceeds unity [46,47]. Here $\boldsymbol{f}_\perp = q(\boldsymbol{E}_\perp + \boldsymbol{\beta} \times \boldsymbol{B})$ is the Lorentz force transverse to the beam velocity, γ the beam relativistic factor, $q = -e$ the electron charge, $F_{\rm cr} = m_e^2 c^3/e\hbar \approx 1.3 \times 10^{18}$ V/m the QED critical field [4,46,47]. This opens up the possibility of laserless strong-field QED investigations with only one ultrarelativistic electron beam [48].

We start by considering the free propagation of an electron beam in vacuum. The electric $\boldsymbol{E}$ and magnetic $\boldsymbol{B}$ self-fields of a cold electron beam in vacuum are related by $\boldsymbol{B} = \boldsymbol{\beta} \times \boldsymbol{E}$ [49], where $\boldsymbol{\beta} = \boldsymbol{v}/c$ is the normalized beam velocity (Gaussian units are employed for equations). Thus, $\boldsymbol{f}_\perp = q\boldsymbol{E}_\perp/\gamma^2$ is strongly suppressed for large γ, and the beam propagates almost ballistically over relatively long distances in vacuum.

When a beam collides with a conductor, it can be subject to strong near-field coherent transition radiation (CTR), which alters the nearly perfect cancellation of the electric and magnetic terms in the Lorentz force. Electromagnetic boundary conditions require that the electric field component tangential to the surface of a perfect conductor must be continuous and zero at the conductor surface, whereas the tangential magnetic field can be discontinuous and remains large [49]. Thus, when an electron beam encounters a conductor, the magnetic term of the Lorentz force, which drives beam focusing, can overcome the electric term, which drives beam expansion. Effectively, when the beam length is smaller than its transverse size, this process can be visualized as a beam colliding with its image charge (see below and Supplemental Material [50] for details on the near-field CTR fields, which include Refs. [51–56]). Notice that a large $\boldsymbol{f}_\perp$ naturally results in intense emission of radiation. For instance, in the classical regime the radiated power (mean photon energy) is proportional to $\gamma^2 \boldsymbol{f}_\perp^2$ ($\gamma^2 \boldsymbol{f}_\perp$) [47,49].

For modeling, we consider an ultrarelativistic cold electron beam with cylindrical symmetry around its propagation axis x. The description is simplified by employing cylindrical coordinates with $r = \sqrt{y^2 + z^2}$, $\theta = \arctan(z/y)$, and x being the radial, azimuthal and vertical components, respectively. We assume that cylindrical symmetry is preserved throughout the interaction. Hence, fields are independent of θ, the azimuthal electric field E_θ and the radial B_r and vertical B_x components of the magnetic field are zero. Here beam and conductor fields are denoted by the superscript b and c, respectively. For an ultrarelativistic charge distribution $\rho(x,r,t) = \rho_0 e^{-r^2/2\sigma_\perp^2} e^{-(x-x_0-vt)^2/2\sigma_\parallel^2}$ with N_e electrons, initial position x_0, velocity v along x, and peak charge density $\rho_0 = qN_e/(2\pi)^{3/2}\sigma_\perp^2\sigma_\parallel$, $E_r^b \gg E_x^b \approx 0$,

$$E_r^b(x,r,t) = \frac{2qN_e}{\sqrt{2\pi}\sigma_\parallel r}\left(1 - e^{-r^2/2\sigma_\perp^2}\right) e^{-(x-x_0-vt)^2/2\sigma_\parallel^2}, \quad (1)$$

and $B_\theta^b(x,r,t) = \beta E_r^b(x,r,t)$, provide an approximate solution to Maxwell equations up to terms of order $1/\gamma^2$ around the beam [48]. To evaluate $E_r^c(x,r,t)$ and $B_\theta^c(x,r,t)$, we consider a flat perfectly conducting foil with front surface at $x = 0$. When the electron beam is outside the conductor, the method of images can be employed for determining $E_r^c(x,r,t)$ and $B_\theta^c(x,r,t)$ in $x < 0$ [57]. This method cannot be applied when the beam enters the foil, because the image would be located in $x < 0$, where conductor fields must satisfy source-free Maxwell equations. However, when $\sigma_\perp \gg \sigma_\parallel$ one can approximate $E_r^c(x,r,t)$ and $B_\theta^c(x,r,t)$ with the image charge fields. This "reflected-field" approximation holds because CTR, which is emitted with transverse size $\sigma_\perp$ and typical wavelength $\sigma_\parallel$, undergoes weak diffraction over a Rayleigh length of approximately $\sigma_\perp^2/\sigma_\parallel \gg \sigma_\parallel$ from the boundary. The opposite limit $\sigma_\perp \ll \sigma_\parallel$, corresponds to the magnetostatic approximation, yielding a vanishing B_θ^c and a surface-localized E_r^c (see Supplemental Material [50]). Note that beam focusing in the $\sigma_\perp \ll \sigma_\parallel$ limit has been demonstrated in accelerators [58–62].

The electron beam to radiated energy conversion efficiency η can be calculated from $E_r = E_r^b + E_r^c$ and $B_\theta = B_\theta^b + B_\theta^c$, where Eq. (1) is employed for the beam and image charge fields. The average energy radiated per particle per unit time is conveniently approximated as [47] $\dot{\varepsilon}_\gamma = 2\alpha m_e c^2 \chi^2/3\tau_c[1 + 4.8(1+\chi)\ln(1+1.7\chi) + 2.44\chi^2]^{2/3}$, where $\alpha = e^2/\hbar c$ is the fine-structure constant, $\tau_c = \hbar/m_e c^2$ is the Compton time, and $\chi \approx \gamma|E_r - B_\theta|/F_{\rm cr}$. Thus,

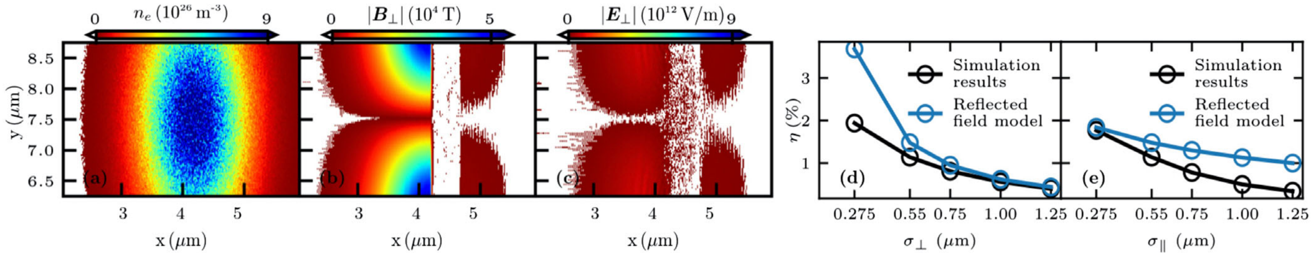

FIG. 2. (a) Electron beam density, (b) transverse magnetic field, and (c) transverse electric field in the collision with a 0.5 μm-thick aluminum foil. For comparison, the peak magnetic and electric beam self-fields are 3.1×10^4 T, and 9.4×10^{12} V/m, respectively. (d) Electron beam to radiation energy conversion efficiency η as a function of $\sigma_\perp$ in the collision with one foil. The electron beam has 2 nC charge, 10 GeV energy, and $\sigma_\parallel = 0.55$ μm. Black circles: 3D PIC simulations results; blue circles: reflected-field model predictions. (e) Same as in panel (d) but for $\sigma_\perp = 0.55$ μm and as a function of $\sigma_\parallel$.

$$\eta = \frac{2\pi \int_{-\infty}^{+\infty} dt \int_{-\infty}^{0} dx \int_{0}^{+\infty} dr r \rho(x, r, t) \dot{\varepsilon}_\gamma[\chi(x, r, t)]}{\gamma m_e c^2 q N_e}. \quad (2)$$

In Eq. (2) we have assumed that all electrons have the same initial momentum and energy $\gamma m_e c^2$. Furthermore, we have neglected the change in γ during the beam-foil interaction. The triple integral in Eq. (2) can be carried out numerically.

Figure 2 shows the results of 3D PIC simulations of a cold electron beam colliding with one 0.5 μm-thick aluminum foil. The electron beam has 2 nC charge, 10 GeV energy, and Gaussian spatial distribution with $\sigma_\parallel = 0.55$ μm, $\sigma_\perp = 1.25$ μm, and 9.2×10^{26} m^{-3} density. Figure 2(a) displays a snapshot of the electron beam density when the beam center has reached the front surface of the foil. Figures 2(b) and 2(c) show the transverse magnetic $\boldsymbol{B}_\perp$ and electric field $\boldsymbol{E}_\perp$, respectively. While $\boldsymbol{B}_\perp$ is amplified and its peak value nearly doubles with respect to the beam self-field (3.1×10^4 T), $\boldsymbol{E}_\perp$ is suppressed and much smaller than the beam self-field (9.4×10^{12} V/m).

Figure 2(d) [Fig. 2(e)] plots η during single electron beam-foil collision with the same parameters as above but for $\sigma_\parallel = 0.55$ μm ($\sigma_\perp = 0.55$ μm) and $\sigma_\perp$ ($\sigma_\parallel$) ranging from 0.275 to 1.25 μm. Black circles and blue circles correspond to 3D PIC simulation and reflected-field model results, respectively. These simulations confirm that the mechanism of beam focusing and photon emission is robust and effective. Indeed, as shown in the Supplemental Material [50], dense collimated photon beams can already be generated with the electron beam parameters attainable at existing accelerator facilities such as FACET-II [63].

Figures 2(d)–2(e) show that simulation results approach the prediction of the reflected-field model with increasing (decreasing) $\sigma_\perp$ ($\sigma_\parallel$). For beam density smaller than the foil electron density, simulations indicate that foil thickness is irrelevant provided that collisions and plasma instabilities remain negligible. By contrast, foil thickness is important when the electron beam density exceeds the conductor density [48]. Note that synchrotron photon emission also occurs when the beam exits the foil, as E_r is suppressed at the rear foil surface and B_θ grows gradually during the beam exit [64]. However, for $\sigma_\perp \gtrsim \sigma_\parallel$, the contribution of the rear surface to the radiated energy is subdominant, and is neglected in our model.

The above considerations suggest that the focusing and radiative effects can be substantially enhanced by colliding the self-focused beam with further foils. In fact, the increased beam density results in stronger self-fields, thereby amplifying both self-focusing and photon emission at successive collisions (see Figs. 3–4). Note that, for efficient self-focusing, the distance between two consecutive foils needs to be sufficiently large to allow beam self-field restoration around its propagation axis ($r \lesssim \sigma_\perp$). This requires that the travelled distance is much larger than $\sigma_\perp$. Furthermore, the interfoil distance needs to be short enough to prevent beam expansion. This can be estimated by considering the effect of $|\boldsymbol{f}_\perp| \approx |2qB_\theta|$ calculated at $x \approx x_0 + vt$ and $r \approx \sigma_\perp$, i.e., where focusing is stronger. For $\sigma_\perp \gtrsim \sigma_\parallel$, CTR extends approximately over a distance $\sigma_\perp^2/\sigma_\parallel$, which is larger than the beam length $\sigma_\parallel$. Thus, $|\boldsymbol{f}_\perp|$ lasts for approximately $\sigma_\parallel/c$, and the deflection angle is $\vartheta \approx |\boldsymbol{f}_\perp|\sigma_\parallel/\gamma m_e c^2$. Hence, to prevent defocusing the interfoil distance must be much smaller than $\sigma_\perp/\vartheta$. Also, for effective focusing, ϑ must be much larger than the beam angular spread $\Delta\vartheta_{p_\perp/p_\parallel} \approx \epsilon_n/\gamma\sigma_\perp$, where ϵ_n is the normalized beam emittance.

In our multifoil 3D PIC simulations, the electron beam has 2 nC charge, Gaussian spatial and momentum distributions with $\sigma_\parallel = \sigma_\perp = 0.55$ μm, 10 GeV mean energy, 212 MeV FWHM energy spread, and 3 mm-mrad normalized emittance ($\vartheta \approx 2$ mrad with these parameters). Comparable parameters are expected at the advanced stage of FACET-II by employing a plasma lens [63,65]. The beam collides with 20 consecutive aluminum foils with 0.5 μm thickness, 10 μm interfoil distance, and 1.8×10^{29} m^{-3} initial electron density. The computational box size is 6.6 μm$(x) \times 8.8$ μm$(y) \times 8.8$ μm(z) with $528(x) \times 352(y) \times 352(z)$ grid points, 4 particles-per-cell (ppc) for beam electrons and 8 ppc for foil electrons and

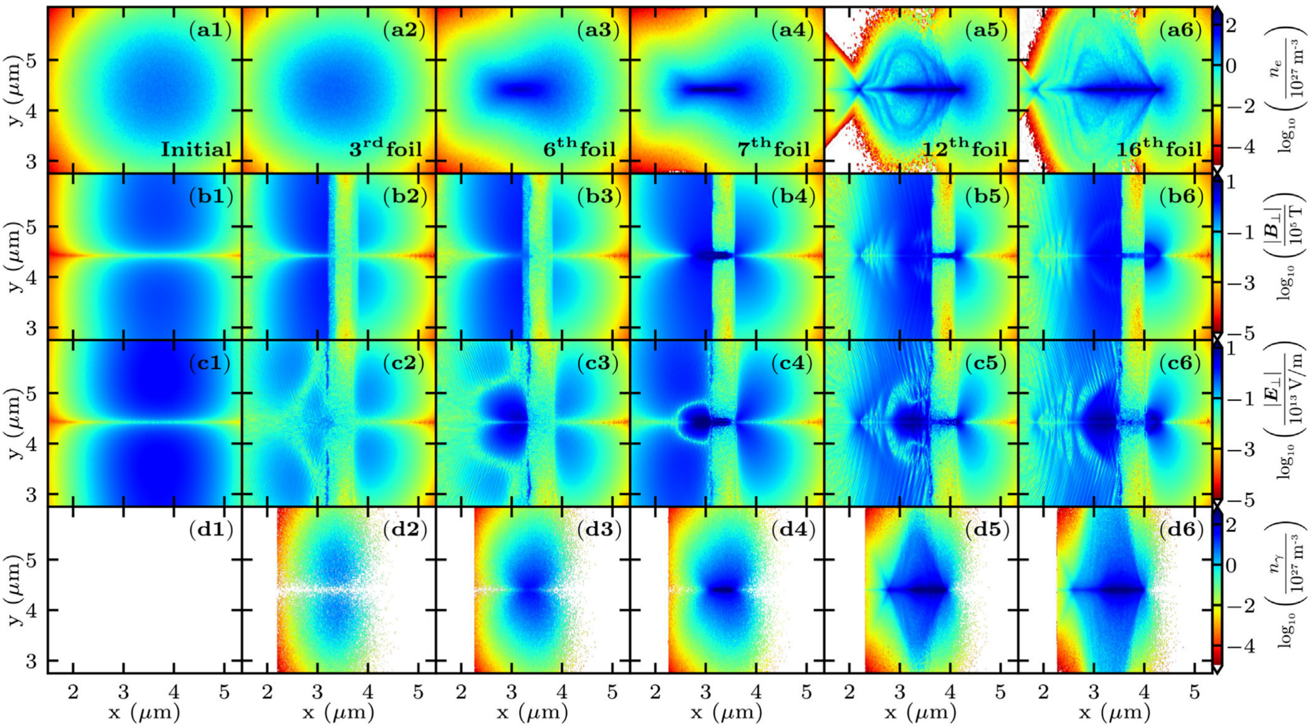

FIG. 3. Beam evolution. First column, initial electron beam density (a1), its magnetic (b1) and electric (c1) fields, and the initial photon density (d1). Second to sixth column, same quantities as in the first column but at the 3rd (a2)–(d2), the 6th (a3)–(d3), the 7th (a4)–(d4), the 12th (a5)–(d5), and the 16th (a6)–(d6) beam-foil interaction, respectively.

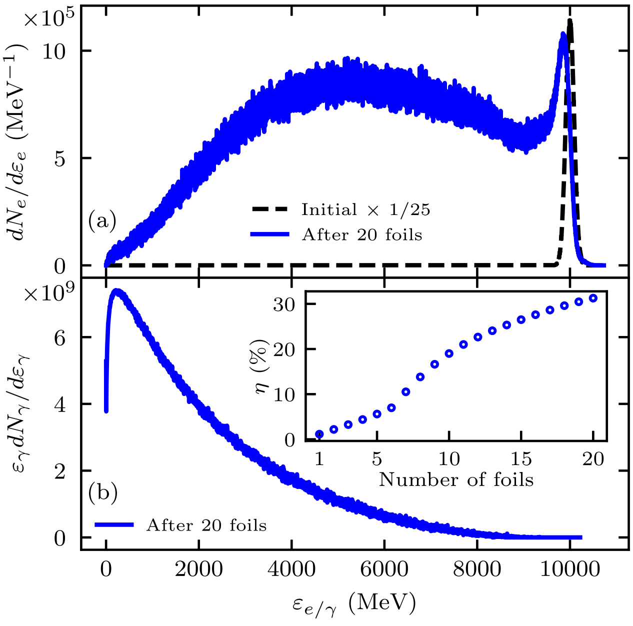

FIG. 4. (a) Initial (black dashed line) and final (blue line) electron beam energy distribution. (b) Final photon spectrum. The inset displays η as a function of the number of foils crossed by the electron beam.

ions were used. The moving window technique was employed to follow the beam evolution. Simulations were independently performed with Smilei [66,67] and CALDER [68] PIC codes with good agreement. The initial self-consistent beam fields, the effect of field and collisional ionization and binary Coulomb collisions were included. Synchrotron and bremsstrahlung emission, and multiphoton Breit-Wheeler and Bethe-Heitler pair production were implemented with state-of-the-art Monte Carlo methods [48,67,69,70]. Consistent with the submicrometer foil thickness, simulations showed that collisional processes are negligible.

Figure 3 displays snapshots of the electron and gamma-ray beam evolution (see Supplemental Material [50] for a movie). Until the 6th foil, the beam interacts with the field "reflected" by each foil. This leads the beam to self-focus and gradually become denser (see the first to third column of Fig. 3). The electron beam density rises from its initial value of 4.7×10^{27} to 8.2×10^{28} m^{-3} after the 6th foil, while the maximum photon density and χ are 2.9×10^{28} m^{-3} and 0.8, respectively [see Fig. 3(a3)–3(d3)]. During (immediately after) the interaction with the 7th foil, the electron beam density reaches 3.8×10^{29} m^{-3} (4.5×10^{29} m^{-3}), which exceeds the electron foil density of 1.8×10^{29} m^{-3}. Hence, the foil is unable to reflect the fields of the beam, and a channel where foil electrons are expelled is created [see Fig. 3(b4)–3(c4)].

Here χ and the photon beam density rise up to 3 and 4.1×10^{29} m^{-3}, respectively. The overall maximum gamma-ray density of 8.5×10^{29} m^{-3} is reached immediately after electron beam interaction with the 8th foil. Moreover, a fraction of approximately 10^{-4} photons with energies $> 2m_e c^2$ convert into $e^- e^+$ pairs via the multiphoton Breit-Wheeler process. Electron beam density stops increasing when it becomes larger than the foil electron density. In the following beam-foil collisions, the electron beam density profile undergoes longitudinal modulations, the reflected field strength being dependent on the longitudinal position and stronger around the rear part of the beam [Fig. 3(a5)–3(a6)].

Figure 4(a) plots the initial (black dashed line) and final (blue line) electron beam energy distribution after the interaction with 20 consecutive foils. The broad distribution around approximately 5 GeV results from intense synchrotron emission occurring in the central and rear parts of the electron beam. The residual peak around the initial electron beam energy is indicative of the small synchrotron and collisional energy losses in the front part of the beam, which experiences only weak amplitude CTR. Figure 4(b) reports the final photon spectrum and the conversion efficiency η (inset) as a function of the number of crossed foils. The increase in η at the 7th foil is due to the extremely high beam density and, consequently, to the ultrastrong fields induced inside the foil. After colliding with 20 foils, more than 30% of the electron beam energy is converted into a collimated (5 mrad rms photon energy angular distribution), 4 fs FWHM duration, 2.8×10^{29} m^{-3} peak density gamma-ray pulse.

In summary, we have introduced a new scheme to efficiently produce extremely dense gamma-ray beams from the interaction of a high-current ultrarelativistic electron beam with a sequence of thin foils. This scheme also provides a promising route for producing solid-density ultrarelativistic electron beams and for exploring strong-field QED processes with a single electron beam, that is, without the need of an external powerful laser drive. In fact, following a methodology analogous to that employed with intense laser pulses [43–45], the field experienced *in situ* by the electron beam and the ensuing strong-field QED effects can be inferred by measuring particle angular distributions, spectra, and photon and pair yields along with CTR [71–74].

This work was performed in the framework of the E-305 Collaboration. E-305 is a SLAC experiment whose aims include the generation of bright gamma rays, in particular, in electron beam-solid interaction. Based on the findings of this work, the E-332 experiment on solid-density gamma-ray pulse generation in electron beam-multifoil interaction has been developed and approved, and will be carried out at SLAC. This article comprises parts of the Ph.D. thesis work of Archana Sampath, submitted to the Heidelberg University, Germany. The work at LOA was supported by the European Research Council (ERC) under the European Unions Horizon 2020 research and innovation programme (Grant Agreement No. 715807). We acknowledge GENCI for granting us access to the supercomputer Irene under the Grant No. A0080510786 to run CALDER simulations. The work at SLAC was supported by U.S. DOE FES Grant No. FWP100331. UCLA was supported by U.S. Department of Energy Grant No. DE-SC001006 and NSF Grant No. 1734315.

---

[*] matteo.tamburini@mpi-hd.mpg.de

[1] G. A. Mourou, T. Tajima, and S. V. Bulanov, Optics in the relativistic regime, Rev. Mod. Phys. **78**, 309 (2006).

[2] M. Marklund and P. K. Shukla, Nonlinear collective effects in photon-photon and photon-plasma interactions, Rev. Mod. Phys. **78**, 591 (2006).

[3] R. Ruffini, G. Vereshchagin, and S.-S. Xue, Electron-positron pairs in physics and astrophysics: From heavy nuclei to black holes, Phys. Rep. **487**, 1 (2010).

[4] A. Di Piazza, C. Müller, K. Z. Hatsagortsyan, and C. H. Keitel, Extremely high-intensity laser interactions with fundamental quantum systems, Rev. Mod. Phys. **84**, 1177 (2012).

[5] V. I. Telnov, Problems in obtaining $\gamma\gamma$ and γe colliding beams at linear colliders, Nucl. Instrum. Methods Phys. Res., Sect. A **294**, 72 (1990).

[6] G. Sarri *et al.*, Generation of neutral and high-density electron-positron pair plasmas in the laboratory, Nat. Commun. **6**, 6747 (2015).

[7] H. Chen, F. Fiuza, A. Link, A. Hazi, M. Hill, D. Hoarty, S. James, S. Kerr, D. D. Meyerhofer, J. Myatt, J. Park, Y. Sentoku, and G. J. Williams, Scaling the Yield of Laser-Driven Electron-Positron Jets to Laboratory Astrophysical Applications, Phys. Rev. Lett. **114**, 215001 (2015).

[8] M. Lobet, C. Ruyer, A. Debayle, E. d'Humières, M. Grech, M. Lemoine, and L. Gremillet, Ultrafast Synchrotron-Enhanced Thermalization of Laser-Driven Colliding Pair Plasmas, Phys. Rev. Lett. **115**, 215003 (2015).

[9] C. D. Arrowsmith, N. Shukla, N. Charitonidis, R. Boni, H. Chen, T. Davenne, D. H. Froula, B. T. Huffman, Y. Kadi, B. Reville, S. Richardson, S. Sarkar, J. L. Shaw, L. O. Silva, R. M. G. M. Trines, R. Bingham, and G. Gregori, Generating ultra-dense pair beams using 400 GeV/c protons, arXiv:2011.04398.

[10] F. Del Gaudio, R. Fonseca, L. O. Silva, and T. Grismayer, Plasma Wakes Driven by Photon Bursts Via Compton Scattering, Phys. Rev. Lett. **125**, 265001 (2020).

[11] X. Xu, D. B. Cesar, S. Corde, V. Yakimenko, M. J. Hogan, C. Joshi, A. Marinelli, and W. B. Mori, Generation of terawatt, attosecond pulses from relativistic transition radiation, arXiv:2007.12736.

[12] D. H. Bilderback, P. Elleaume, and E. Weckert, Review of third and next generation synchrotron light sources, J. Phys. B **38**, S773 (2005).

[13] J. Ullrich, A. Rudenko, and R. Moshammer, Free-electron lasers: New avenues in molecular physics and photochemistry, Annu. Rev. Phys. Chem. **63**, 635 (2012).

[14] S. Corde, K. T. Phuoc, G. Lambert, R. Fitour, V. Malka, A. Rousse, A. Beck, and E. Lefebvre, Femtosecond x rays from laser-plasma accelerators, Rev. Mod. Phys. **85**, 1 (2013).

[15] http://www.lightsources.org/.

[16] C. P. Ridgers, C. S. Brady, R. Duclous, J. G. Kirk, K. Bennett, T. D. Arber, A. P. L. Robinson, and A. R. Bell, Dense Electron-Positron Plasmas and Ultraintense γ Rays from Laser-Irradiated Solids, Phys. Rev. Lett. **108**, 165006 (2012).

[17] T. Nakamura, J. K. Koga, T. Z. Esirkepov, M. Kando, G. Korn, and S. V. Bulanov, High-Power γ-Ray Flash Generation in Ultraintense Laser-Plasma Interactions, Phys. Rev. Lett. **108**, 195001 (2012).

[18] L. L. Ji, A. Pukhov, E. N. Nerush, I. Yu. Kostyukov, B. F. Shen, and K. U. Akli, Energy partition, γ-ray emission, and radiation reaction in the near-quantum electrodynamical regime of laser-plasma interaction, Phys. Plasmas **21**, 023109 (2014).

[19] J.-X. Li, K. Z. Hatsagortsyan, B. J. Galow, and C. H. Keitel, Attosecond Gamma-Ray Pulses Via Nonlinear Compton Scattering in the Radiation-Dominated Regime, Phys. Rev. Lett. **115**, 204801 (2015).

[20] X.-L. Zhu, Y. Yin, T.-P. Yu, F.-Q. Shao, Z.-Y. Ge, W.-Q. Wang, and J.-J. Liu, Enhanced electron trapping and γ ray emission by ultra-intense laser irradiating a near-critical-density plasma filled gold cone, New J. Phys. **17**, 053039 (2015).

[21] D. J. Stark, T. Toncian, and A. V. Arefiev, Enhanced Multi-MeV Photon Emission by a Laser-Driven Electron Beam in a Self-Generated Magnetic Field, Phys. Rev. Lett. **116**, 185003 (2016).

[22] H. X. Chang, B. Qiao, T. W. Huang, Z. Xu, C. T. Zhou, Y. Q. Gu, X. Q. Yan, M. Zepf, and X. T. He, Brilliant petawatt gamma-ray pulse generation in quantum electrodynamic laser-plasma interaction, Sci. Rep. **7**, 45031 (2017).

[23] W.-M. Wang, Z.-M. Sheng, P. Gibbon, L.-M. Chen, Yu.-T. Li, and J. Zhang, Collimated ultrabright gamma rays from electron wiggling along a petawatt laser-irradiated wire in the QED regime, Proc. Natl. Acad. Sci. U.S.A. **115**, 9911 (2018).

[24] T. W. Huang, C. M. Kim, C. T. Zhou, C. M. Ryu, K. Nakajima, S. C. Ruan, and C. H. Nam, Tabletop laser-driven gamma-ray source with nanostructured double-layer target, Plasma Phys. Controlled Fusion **60**, 115006 (2018).

[25] T. W. Huang, C. M. Kim, C. T. Zhou, M. H. Cho, K. Nakajima, C. M. Ryu, S. C. Ruan, and C. H. Nam, Highly efficient laser-driven Compton gamma-ray source, New J. Phys. **21**, 013008 (2019).

[26] M. Vranic, T. Grismayer, S. Meuren, R. A. Fonseca, and L. O. Silva, Are we ready to transfer optical light to gamma-rays?, Phys. Plasmas **26**, 053103 (2019).

[27] M. Jirka, O. Klimo, Y.-J. Gu, and S. Weber, Enhanced photon emission from a double-layer target at moderate laser intensities, Sci. Rep. **10**, 8887 (2020).

[28] J. Ferri, S. Corde, A. Döpp, A. Lifschitz, A. Doche, C. Thaury, K. Ta Phuoc, B. Mahieu, I. A. Andriyash, V. Malka, and X. Davoine, High-Brilliance Betatron γ-Ray Source Powered by Laser-Accelerated Electrons, Phys. Rev. Lett. **120**, 254802 (2018).

[29] X.-L. Zhu, M. Chen, S.-M. Weng, T.-P. Yu, W.-M. Wang, F. He, Z.-M. Sheng, P. McKenna, D. A. Jaroszynski, and J. Zhang, Extremely brilliant GeV γ-rays from a two-stage laser-plasma accelerator, Sci. Adv. **6**, eaaz7240 (2020).

[30] A. Benedetti, M. Tamburini, and C. H. Keitel, Giant collimated gamma-ray flashes, Nat. Photonics **12**, 319 (2018).

[31] M. Jirka, O. Klimo, S. V. Bulanov, T. Z. Esirkepov, E. Gelfer, S. S. Bulanov, S. Weber, and G. Korn, Electron dynamics and γ and $e^{-}e^{+}$ production by colliding laser pulses, Phys. Rev. E **93**, 023207 (2016).

[32] M. Tamburini, A. Di Piazza, and C. H. Keitel, Laser-pulse-shape control of seeded QED cascades, Sci. Rep. **7**, 5694 (2017).

[33] A. Gonoskov, A. Bashinov, S. Bastrakov, E. Efimenko, A. Ilderton, A. Kim, M. Marklund, I. Meyerov, A. Muraviev, and A. Sergeev, Ultrabright GeV Photon Source Via Controlled Electromagnetic Cascades in Laser-Dipole Waves, Phys. Rev. X **7**, 041003 (2017).

[34] J. Magnusson, A. Gonoskov, M. Marklund, T. Z. Esirkepov, J. K. Koga, K. Kondo, M. Kando, S. V. Bulanov, G. Korn, and S. S. Bulanov, Laser-Particle Collider for Multi-GeV Photon Production, Phys. Rev. Lett. **122**, 254801 (2019).

[35] V. Yakimenko, S. Meuren, F. Del Gaudio, C. Baumann, A. Fedotov, F. Fiuza, T. Grismayer, M. J. Hogan, A. Pukhov, L. O. Silva, and G. White, Prospect of Studying Non-perturbative QED with Beam-Beam Collisions, Phys. Rev. Lett. **122**, 190404 (2019).

[36] F. Del Gaudio, T. Grismayer, R. A. Fonseca, W. B. Mori, and L. O. Silva, Bright γ rays source and nonlinear Breit-Wheeler pairs in the collision of high density particle beams, Phys. Rev. Accel. Beams **22**, 023402 (2019).

[37] M. Tamburini and S. Meuren, Efficient High-Energy Photon Production in the supercritical QED regime, arXiv:1912.07508.

[38] H.-P. Schlenvoigt, K. Haupt, A. Debus, F. Budde, O. Jäckel, S. Pfotenhauer, H. Schwoerer, E. Rohwer, J. G. Gallacher, E. Brunetti, R. P. Shanks, S. M. Wiggins, and D. A. Jaroszynski, A compact synchrotron radiation source driven by a laser-plasma wakefield accelerator, Nat. Phys. **4**, 130 (2008).

[39] S. Kneip *et al.*, Bright spatially coherent synchrotron x-rays from a table-top source, Nat. Phys. **6**, 980 (2010).

[40] S. Cipiccia *et al.*, Gamma-rays from harmonically resonant betatron oscillations in a plasma wake, Nat. Phys. **7**, 867 (2011).

[41] K. T. Phuoc, S. Corde, C. Thaury, V. Malka, A. Tafzi, J. P. Goddet, R. C. Shah, S. Sebban, and A. Rousse, All-optical Compton gamma-ray source, Nat. Photonics **6**, 308 (2012).

[42] G. Sarri, D. J. Corvan, W. Schumaker, J. M. Cole, A. Di Piazza, H. Ahmed, C. Harvey, C. H. Keitel, K. Krushelnick, S. P. D. Mangles, Z. Najmudin, D. Symes, A. G. R. Thomas, M. Yeung, Z. Zhao, and M. Zepf, Ultrahigh Brilliance Multi-MeV γ-Ray Beams from Nonlinear Relativistic Thomson Scattering, Phys. Rev. Lett. **113**, 224801 (2014).

[43] W. Yan, C. Fruhling, G. Golovin, D. Haden, J. Luo, P. Zhang, B. Zhao, J. Zhang, C. Liu, M. Chen, S. Chen, S. Banerjee, and D. Umstadter, High-order multiphoton Thomson scattering, Nat. Photonics **11**, 514 (2017).

[44] J. M. Cole *et al.*, Experimental Evidence of Radiation Reaction in the Collision of a High-Intensity Laser Pulse with a Laser-Wakefield Accelerated Electron Beam, Phys. Rev. X **8**, 011020 (2018).
[45] K. Poder *et al.*, Experimental Signatures of the Quantum Nature of Radiation Reaction in the Field of an Ultraintense Laser, Phys. Rev. X **8**, 031004 (2018).
[46] V. I. Ritus, Quantum effects of the interaction of elementary particles with an intense electromagnetic field, J. Russ. Laser Res. **6**, 497 (1985).
[47] V. N. Baier, V. M. Katkov, and V. M. Strakhovenko, *Electromagnetic Processes at High Energies in Oriented Single Crystals* (World Scientific, Singapore, 1998).
[48] A. Sampath, Ph.D. thesis, Ruprecht-Karls-Universität, Heidelberg, 2020.
[49] J. D. Jackson, *Classical Electrodynamics*, 3rd ed. (John Wiley and Sons, Inc., 1998).
[50] See Supplemental Material at http://link.aps.org/supplemental/10.1103/PhysRevLett.126.064801 for (i) modeling of the near-field CTR; (ii) PIC simulations at presently achievable beam densities; (iii) a movie of the electron and gamma beam evolution in the interaction with 20 consecutive foils.
[51] V. Ginzburg and V. N. Tsytovich, *Transition Radiation and Transition Scattering* (Adam Hilger, Bristol, UK, 1990).
[52] I. S. Gradshteyn, I. M. Ryzhik, A. Jeffrey, and D. Zwillinger, *Table of Integrals, Series, and Products* (Academic Press, Burlington, USA, 2007).
[53] V. A. Verzilov, Transition radiation in the pre-wave zone, Phys. Lett. A **273**, 135 (2000).
[54] J. E. Harvey, Fourier treatment of near-field scalar diffraction theory, Am.J. Phys. **47**, 974 (1979).
[55] M. Castellano and V. A. Verzilov, Spatial resolution in optical transition radiation beam diagnostics, Phys. Rev. ST Accel. Beams **1**, 062801 (1998).
[56] A. F. Lifschitz, X. Davoine, E. Lefebvre, J. Faure, C. Rechatin, and V. Malka, Particle-in-cell modelling of laser–plasma interaction using fourier decomposition, J. Comput. Phys. **228**, 1803 (2009).
[57] P. Hammond, Electric and magnetic images, Proc IEE Part C Monographs **107**, 306 (1960).
[58] R. J. Adler, Image-field focusing of intense ultra-relativistic electron beams in vacuum, Part. Accel. **12**, 39 (1982), http://cdsweb.cern.ch/record/1107997/files/.
[59] S. Humphries, Equilibria for foil-focused relativistic electron beams, Part. Accel. **13**, 249 (1983), http://cds.cern.ch/record/1108004/files/.
[60] S. Humphries and C. B. Ekdahl, Image charge focusing of relativistic electron beams, J. Appl. Phys. **63**, 583 (1988).
[61] S. Humphries, C. Ekdahl, and D. M. Woodall, Image current guiding of a relativistic electron beam in a foil focusing system, Appl. Phys. Lett. **54**, 2195 (1989).
[62] R. F. Fernsler, R. F. Hubbard, and S. P. Slinker, Foil focusing of electron beams, J. Appl. Phys. **68**, 5985 (1990).
[63] V. Yakimenko, L. Alsberg, E. Bong, G. Bouchard, C. Clarke, C. Emma, S. Green, C. Hast, M. J. Hogan, J. Seabury, N. Lipkowitz, B. O'Shea, D. Storey, G. White, and G. Yocky, FACET-II facility for advanced accelerator experimental tests, Phys. Rev. Accel. Beams **22**, 101301 (2019).
[64] N. J. Carron, Fields of particles and beams exiting a conductor, Prog. Electromagn. Res. **28**, 147 (2000).
[65] C. E. Doss, E. Adli, R. Ariniello, J. Cary, S. Corde, B. Hidding, M. J. Hogan, K. Hunt-Stone, C. Joshi, K. A. Marsh, J. B. Rosenzweig, N. Vafaei-Najafabadi, V. Yakimenko, and M. Litos, Laser-ionized, beam-driven, underdense, passive thin plasma lens, Phys. Rev. Accel. Beams **22**, 111001 (2019).
[66] J. Derouillat, A. Beck, F. Prez, T. Vinci, M. Chiaramello, A. Grassi, M. Fl, G. Bouchard, I. Plotnikov, N. Aunai, J. Dargent, C. Riconda, and M. Grech, Smilei: A collaborative, open-source, multi-purpose particle-in-cell code for plasma simulation, Comput. Phys. Commun. **222**, 351 (2018).
[67] Smilei particle-in-cell code, https://smileipic.github.io/Smilei/.
[68] E. Lefebvre *et al.*, Electron and photon production from relativistic laser-plasma interactions, Nucl. Fusion **43**, 629 (2003).
[69] M. Lobet, E. d'Humières, M. Grech, C. Ruyer, X. Davoine, and L. Gremillet, Modeling of radiative and quantum electrodynamics effects in PIC simulations of ultra-relativistic laser-plasma interaction, J. Phys. Conf. Ser. **688**, 012058 (2016).
[70] B. Martinez, M. Lobet, R. Duclous, E. d'Humières, and L. Gremillet, High-energy radiation and pair production by Coulomb processes in particle-in-cell simulations, Phys. Plasmas **26**, 103109 (2019).
[71] J. van Tilborg, C. B. Schroeder, C. V. Filip, C. Tóth, C. G. R. Geddes, G. Fubiani, R. Huber, R. A. Kaindl, E. Esarey, and W. P. Leemans, Temporal Characterization of Femtosecond Laser-Plasma-Accelerated Electron Bunches Using Terahertz Radiation, Phys. Rev. Lett. **96**, 014801 (2006).
[72] Y. Glinec, J. Faure, A. Norlin, A. Pukhov, and V. Malka, Observation of Fine Structures in Laser-Driven Electron Beams Using Coherent Transition Radiation, Phys. Rev. Lett. **98**, 194801 (2007).
[73] T. J. Maxwell, C. Behrens, Y. Ding, A. S. Fisher, J. Frisch, Z. Huang, and H. Loos, Coherent-Radiation Spectroscopy of Few-Femtosecond Electron Bunches Using a Middle-Infrared Prism Spectrometer, Phys. Rev. Lett. **111**, 184801 (2013).
[74] O. Lundh, C. Rechatin, J. Lim, V. Malka, and J. Faure, Experimental Measurements of Electron-Bunch Trains in a Laser-Plasma Accelerator, Phys. Rev. Lett. **110**, 065005 (2013).

PHYSICAL REVIEW RESEARCH **2**, 023123 (2020)

Editors' Suggestion

Probing ultrafast magnetic-field generation by current filamentation instability in femtosecond relativistic laser-matter interactions

G. Raj,[1,*,†] O. Kononenko,[1,*,‡] M. F. Gilljohann,[2,3] A. Doche,[1] X. Davoine,[4] C. Caizergues,[1] Y.-Y. Chang,[5]
J. P. Couperus Cabadağ,[5] A. Debus,[5] H. Ding,[2,3] M. Förster,[2,3] J.-P. Goddet,[1] T. Heinemann,[6,7,8] T. Kluge,[5] T. Kurz,[5,9]
R. Pausch,[5] P. Rousseau,[1] P. San Miguel Claveria,[1] S. Schöbel,[5,9] A. Siciak,[1] K. Steiniger,[5] A. Tafzi,[1] S. Yu,[1] B. Hidding,[7,8]
A. Martinez de la Ossa,[6] A. Irman,[5] S. Karsch,[2,3] A. Döpp,[2,3] U. Schramm,[5,9] L. Gremillet,[4] and S. Corde[1,§]

[1]*LOA, ENSTA Paris, CNRS, Ecole Polytechnique, Institut Polytechnique de Paris, 91762 Palaiseau, France*
[2]*Ludwig-Maximilians-Universität München, Am Coulombwall 1, 85748 Garching, Germany*
[3]*Max Planck Institut für Quantenoptik, Hans-Kopfermann-Str. 1, Garching 85748, Germany*
[4]*CEA, DAM, DIF, 91297 Arpajon, France*
[5]*Helmholtz-Zentrum Dresden - Rossendorf, Institute of Radiation Physics, Bautzner Landstrasse 400, 01328 Dresden, Germany*
[6]*Deutsches Elektronen-Synchrotron DESY, 22607 Hamburg, Germany*
[7]*Scottish Universities Physics Alliance, Department of Physics, University of Strathclyde, Glasgow G4 0NG, United Kingdom*
[8]*Cockcroft Institute, Sci-Tech Daresbury, Keckwick Lane, Daresbury, Cheshire WA4 4AD, United Kingdom*
[9]*Technische Universität Dresden, 01062 Dresden, Germany*

(Received 28 July 2019; revised manuscript received 22 December 2019; accepted 7 April 2020;
published 4 May 2020)

The current filamentation instability is a key phenomenon underpinning various processes in astrophysics, laboratory laser-plasma, and beam-plasma experiments. Here we show that the ultrafast dynamics of this instability can be explored in the context of relativistic laser-solid interactions through deflectometry by low-emittance, highly relativistic electron bunches from a laser wakefield accelerator. We present experimental measurements of the femtosecond timescale generation of strong magnetic-field fluctuations, with a measured line-integrated B field of 2.70 ± 0.39 kT μm. Three-dimensional, fully relativistic particle-in-cell simulations demonstrate that such fluctuations originate from the current filamentation instability arising at submicron scales around the irradiated target surface, and that they grow to amplitudes strong enough to broaden the angular distribution of the probe electron bunch a few tens of femtoseconds after the laser pulse maximum. Our results open a branch of physics experiments investigating the femtosecond dynamics of laser-driven plasma instabilities by means of synchronized, wakefield-accelerated electron beams.

DOI: 10.1103/PhysRevResearch.2.023123

I. INTRODUCTION

The Weibel-type current filamentation instability (CFI) [1,2] has been extensively investigated in past decades owing to its recognized importance in an increasing variety of plasma environments. Induced by temperature anisotropies or relative drifts between the plasma constituents [3–6], it gives rise to kinetic-scale, current filaments surrounded by toroidal magnetic fields, through which the charged particles are progressively isotropized [3,7,8]. This instability is widely thought to underpin the physics of relativistic outflows in powerful astrophysical objects (e.g., gamma-ray bursts, pulsar winds, active galactic nuclei), especially as the source of the collisionless shock waves held responsible for generating nonthermal high-energy particles and radiations [9–13]. Moreover, it is expected to operate in magnetic reconnection scenarios [14], and has been invoked as a possible generation mechanism for cosmological magnetic fields [15].

On the laboratory side, the CFI stands as a key process in intense laser-plasma interactions. In the case of overdense plasmas irradiated at relativistic laser intensities ($I_0\lambda_0^2 \gtrsim 10^{18}\ \mathrm{W\,cm^{-2}\,\mu m^2}$, where I_0 and λ_0 are the laser intensity and wavelength, respectively), it arises from the counterstreaming of the forward-directed, laser-accelerated fast electrons and the current-neutralizing, cold plasma electrons [16–19]. The resulting magnetic fluctuations may grow fast enough to cause significant scattering and deceleration of the fast electrons [20–23]. These effects are generally considered detrimental to fast-electron-based applications, e.g., the fast ignition approach to inertial confinement fusion [19] or target normal sheath ion acceleration [24–26]. Still, they can also be triggered purposefully in laboratory astrophysics experiments addressing the physics of collisionless shocks, whether involving relativistic laser-solid interactions [27,28], laser-driven interpenetrating plasma flows [29,30], or electron beam-plasma interactions [31,32].

---

[*] These authors have contributed equally to this work.
[†] Corresponding author: gaurav.raj@polytechnique.edu
[‡] Corresponding author: olena.kononenko@polytechnique.edu
[§] Corresponding author: sebastien.corde@polytechnique.edu

Published by the American Physical Society under the terms of the Creative Commons Attribution 4.0 International license. Further distribution of this work must maintain attribution to the author(s) and the published article's title, journal citation, and DOI.

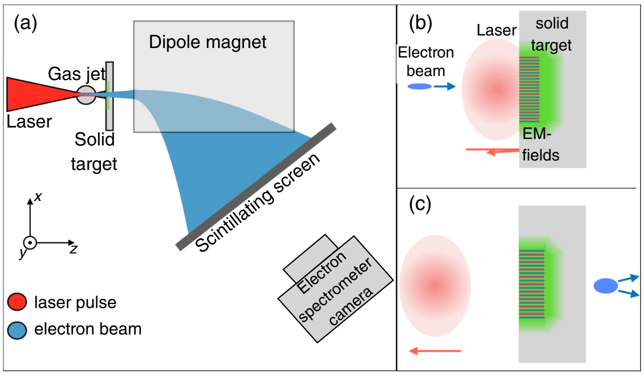

FIG. 1. Schematic of the experimental setup: (a) A laser pulse accelerates a relativistic electron beam from a supersonic gas jet, and is subsequently reflected off a solid foil target placed at the exit of the gas jet. The electron beam passes through the foil and is sent toward an electron spectrometer. (b), (c) When traveling across the foil, the beam electrons are scattered by the electromagnetic fluctuations driven by the laser pulse.

Experimental evidence for the development of the CFI in relativistic laser-driven plasmas has been mainly provided through characterization of the spatial profiles of the fast electron [33–36] or ion [24–26,37,38] beams exiting the target. *In situ* measurements of the magnetic-field fluctuations at the irradiated target surface have been performed using optical polarimetry [39,40], yet this technique cannot access the volumetric distribution of the fields, and the data obtained so far could not capture their femtosecond timescale dynamics. Probing plasma electromagnetic fields by an ultrashort electron beam was previously exploited to image plasma wakefields in a laser wakefield accelerator (LWFA) [41] or large-scale inductively generated magnetic fields in target normal sheath acceleration [42].

In this paper, we demonstrate that the physics of the CFI developing at femtosecond timescales in the interaction of ultrashort, moderately relativistic laser pulses with solid targets can be explored by electron deflectometry using a 100-MeV-range probe electron bunch, produced by a laser wakefield accelerator [43–47]. Our measurements of the line-integrated magnetic field agree well with detailed three-dimensional (3D) fully relativistic particle-in-cell (PIC) simulations, and taken together, they indicate that the kT-level, submicron-scale magnetic fluctuations indeed result from a Weibel-type CFI excited at the target surface. In our experimental setup, the laser pulse driving the LWFA is the same one that induces the electromagnetic fluctuations in a neighboring foil target (see Fig. 1). This ensures a well-controlled time delay between the electron bunch and the laser pump, and therefore probing of the field fluctuations a few tens of femtoseconds only after the on-target laser pulse maximum. Their line-integrated field strength is then inferred from the angular broadening induced upon the electron bunch and successfully compared to the numerical modeling.

II. EXPERIMENTAL RESULTS

The experiment was performed at Laboratoire d'Optique Appliquée with the "Salle Jaune" Ti:sapphire laser system, delivering laser pulses with 30-fs full width at half-maximum (FWHM) duration and up to 1.5-J energy on target. The laser pulse had a 810-nm central wavelength and was linearly polarized along the horizontal x axis. Corrected using adaptive optics, it was focused at the entrance of a 3-mm exit diameter gas jet target by a $f/16$ off-axis parabola to a 20-μm FWHM spot size in vacuum, yielding a normalized peak vector potential of $a_0 \simeq 1.5$ when accounting for the experimental intensity distribution in the focal plane. The supersonic gas jet used for the LWFA consisted of a mixture of 99% hydrogen and 1% nitrogen, enabling well-controlled electron acceleration through ionization injection [48–51]. Due to relativistic self-focusing and self-steepening in the LWFA stage, the laser field strength is expected to be enhanced to $a_0 \gtrsim 3$ [52]. After exiting the gas jet, the laser pulse and the electron beam impinged on a thin Mylar or aluminium foil, located at a variable position along the propagation axis. The electron beam transmitted through the foil was characterized by an electron spectrometer comprising a 10-cm-long, 1.0-T dipole magnet deflecting electrons depending on their energy along the horizontal x axis, and a scintillating screen imaged onto a 16-bit camera [see Fig. 1(a)]. The spectrometer also recorded angular information along the nondispersive vertical y axis (perpendicular to laser polarization), but the large distance (about 35 cm) between the foil and the scintillating screen prevented submicron-scale structures of the beam profile close to the target from being resolved.

The LWFA was operated in the highly nonlinear regime [53], and the electrons from the inner shells of the nitrogen dopant were ionized within the blowout cavity by the high-intensity part of the laser pulse. This resulted in continuous injection as the laser propagated through the gas, and therefore in electron beams with a broad energy spectrum extending beyond 200 MeV [Fig. 2(a) (top)], a 50–100 pC charge (above 100 MeV) and a 2–4 mrad FWHM divergence. The longitudinal separation between the electron beam and the laser pulse was on the order of the plasma wavelength ($\sim 10\ \mu$m for an electron plasma density of $\sim 10^{19}\ \mathrm{cm}^{-3}$). After exiting the gas jet, the peak intensity of the diffracting laser pulse decreased with the propagation distance.

Figure 2(a) displays typical electron energy-angle spectra recorded during the experiment. The top panel shows the reference spectrum from the LWFA (no solid target). When a 13-μm-thick Mylar foil is placed 0.42 mm from the gas jet exit, the beam divergence is significantly increased [Fig. 2(a), middle], as also demonstrated in Fig. 2(c). The beam divergence, which is seen to scale as $1/\gamma$ (γ the electron relativistic factor), is strongly reduced when the jet-foil distance is increased to 2.61 mm [Fig. 2(a), bottom], corresponding to a decrease in the laser intensity on the solid target surface. Additional experimental data (see Supplemental Material [54]) shows that the beam divergence is still significantly affected at a jet-foil distance of $\sim$2.5 mm when using higher on-target laser energy (2.5 J). Multiple scattering of beam electrons in the foil due to elastic collisions cannot account for this behavior since it should cause a negligible increase in the divergence in 13-μm-thick Mylar (scattering angle of 0.38 mrad for 150 MeV electrons) and be independent of the foil position.

Figure 2(b) plots the variations in the electron beam divergence with the jet-foil distance (in the range from 0.25

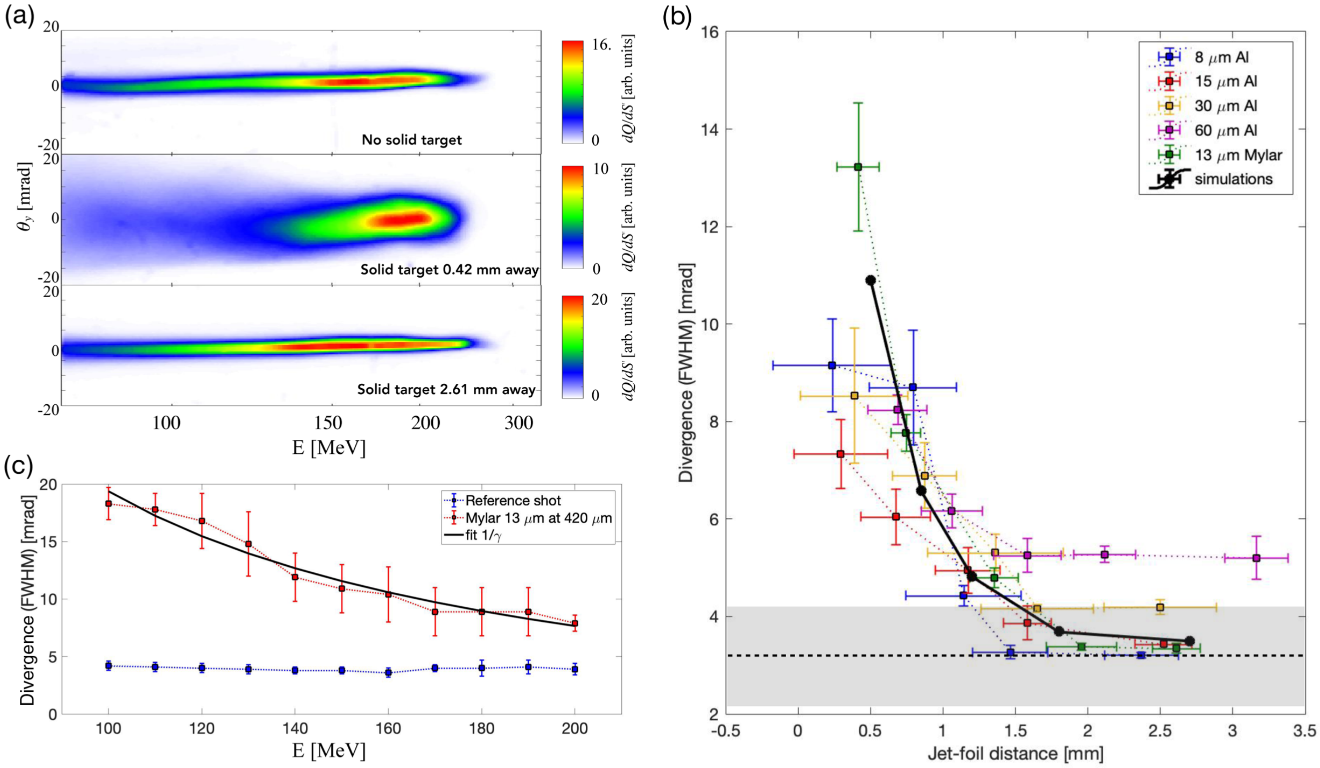

FIG. 2. Experimental results. (a) Typical electron spectra for the reference case (no solid target, top), and for distances of 0.42 mm (middle) and 2.61 mm (bottom) between the 13-μm-thick Mylar foil and the gas jet exit. (b) Angular divergence (FWHM) of the 150-MeV beam electrons as a function of the distance between the gas jet exit and the solid foil: 8 μm Al (blue), 15 μm Al (red), 30 μm Al (yellow), and 60 μm Al (magenta), as well as the 13-μm-thick Mylar foil (green). The gray area represents the divergence of the reference shots (no solid target) together with its variation during the experiments. The black solid line corresponds to 3D PIC simulation results. (c) Angular divergence (FWHM) of the beam electrons as a function of their energy: reference shots (blue), shot of Fig. 2(a) middle (red, 13-μm-thick Mylar foil at a distance of 0.42 mm), and $1/\gamma$ fit (black).

to 3.2 mm) as measured with different targets (13-μm-thick Mylar and 8- to 60-μm-thick Al). Significant variation in the laser peak intensity at the solid target surface due to laser self-focusing and self-steepening in the laser wakefield-accelerator results in relatively large shot-to-shot fluctuations. These could be strongly reduced with independent control of LWFA- and CFI-driving laser pulses. For each target type, the beam divergence is seen to decrease monotonically with the jet-foil distance. Increasing the Al foil thickness only entails detectable changes at large distances ($\gtrsim$1.5 mm) due to stronger multiple scattering. These data indicate that the angular broadening of the electron beam takes place in the vicinity of the irradiated target surface. 3D simulation results, discussed below and plotted as a black solid line, provide a satisfactory match with the measurements.

As a result, our data provide a direct measurement of the integrated Lorentz force experienced by the beam in the solid foil, expressed as an equivalent line-integrated magnetic field

$$B_{x,\mathrm{int}} = \sqrt{\left\langle \left(\int B_x dz \right)^2 \right\rangle_{n_b}},$$

where the average is weighed by the transverse profile of the electron beam. This field induces a spread $\sigma_{p_y} = eB_{x,\mathrm{int}}$ in the transverse momentum distribution of the electron beam, and therefore contributes to a total divergence $\theta_y^2 = \theta_{y,\mathrm{ref}}^2 + \theta_{y,\mathrm{sc}}^2 + \theta_{y,\mathrm{B}}^2$. Here, $\theta_{y,\mathrm{ref}}$ is the original divergence of the LWFA-generated beam, $\theta_{y,\mathrm{sc}}$ is the contribution from the multiple scattering, and $\theta_{y,\mathrm{B}} \simeq \sigma_{p_y}/p_z = ecB_{x,\mathrm{int}}/E$ is the contribution from the integrated equivalent magnetic field, with E the electron energy. From the experimentally measured divergence, $\theta_y = 13.23 \pm 1.31$ mrad (FWHM), of the 150-MeV energy electrons passing through the 13-μm-thick Mylar foil at a 0.42-mm distance, one infers an integrated equivalent magnetic field of $B_{x,\mathrm{int}} = 2.70 \pm 0.39$ kT μm.

III. SIMULATION RESULTS

In order to identify the physical mechanism behind the electromagnetic field generation around the target surface, 2D and 3D PIC simulations have been performed using the code CALDER [55–58]. These fully relativistic simulations describe both the laser-foil and subsequent beam-plasma interactions, including the effects of binary Coulomb collisions, impact ionization, and field ionization. The laser is modeled as a planar wave with a Gaussian temporal profile and a 20-fs FWHM pulse duration. Its field strength on target is estimated to drop from $a_0 = 2.3$ to 0.7 when the jet-foil distance is increased from 0.5 to 2.7 mm (assuming 1 Joule of laser energy and 15 μm FWHM spot size at the gas jet exit).

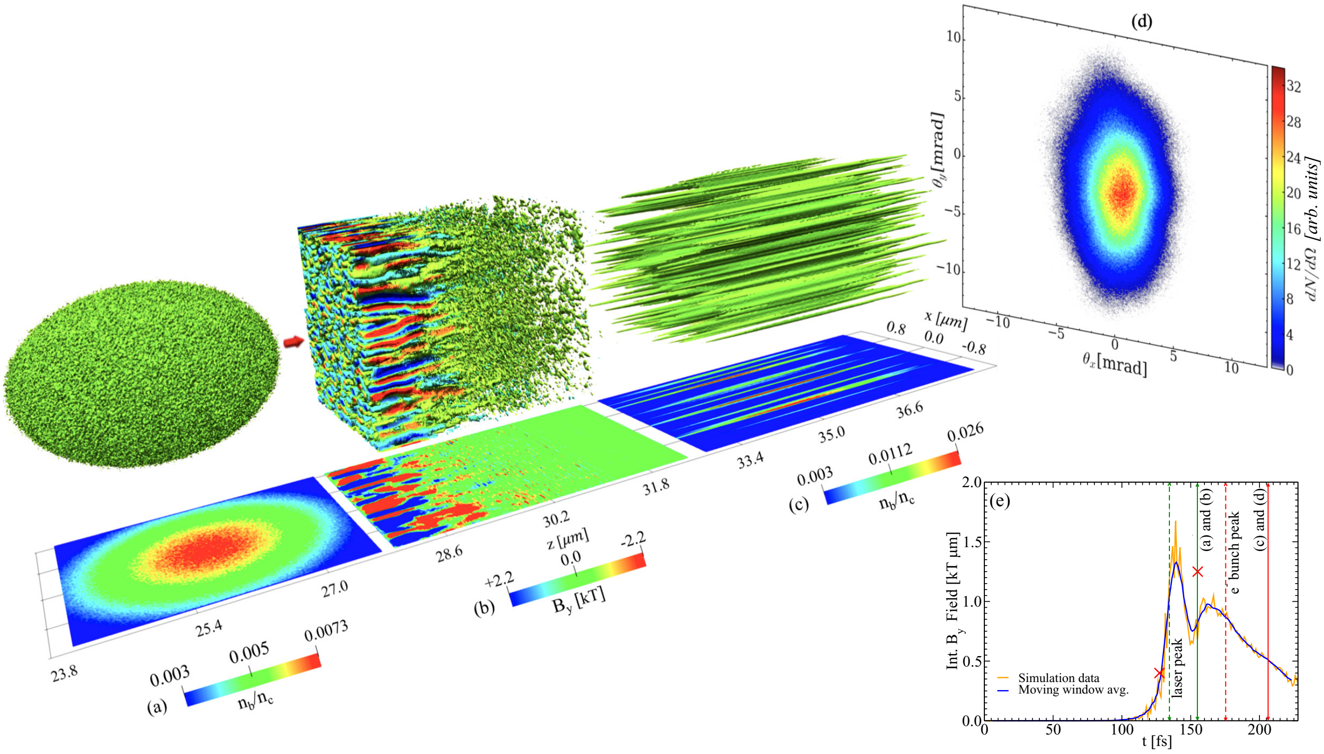

FIG. 3. 3D PIC simulation snapshots showing isosurfaces and slices at $y = 0$ of (a) the electron bunch before entering the Al foil, (b) the B_y component of the magnetic field generated due to laser-solid interaction, (c) the electron bunch after exiting the Al foil. The angular distribution of the final electron bunch is shown in (d), and (e) represents the temporal evolution of the z-integrated B_y field obtained from 2D simulations using the same parameters as in the 3D simulation. In (e), the vertical lines indicate the time of arrival at the foil front surface of the peak of the laser pulse (dashed green) and of the electron beam (dashed red), and the time at which (a), (b) or (c), (d) snapshots are taken (respectively, green and red solid lines). Red crosses in (e) show the instantaneous values of $B_{y,\text{int}}$ from the 3D simulation, and the blue curve is a moving window average of the 2D simulation data (orange).

The electron beam is initialized with a 150-MeV energy, a 1-μm root-mean-square (RMS) transverse size, a 1.6-μm RMS bunch length, a 50-pC total charge, and a 11-μm peak-to-peak separation with the laser pulse. The target consists of a 8-μm-thick, solid-density, neutral plasma of electrons and Al^{3+} ions. On its front side is added a linearly ramped preplasma of 0.8-μm length to take account of an imperfect laser contrast (see Supplemental Material [54] for a discussion of the weak effect of the preplasma length on the resulting integrated B field). The 3D domain size is $L_x \times L_y \times L_z = 2.1 \times 2.1 \times 45\ \mu\text{m}^3$ with a cell size in each direction of $\Delta x = \Delta y = \Delta z = \lambda_0/64$, while for the 2D simulations, the domain size is $L_x \times L_z = 2.1 \times 45\ \mu\text{m}^2$ with a cell size $\Delta x = \Delta z = \lambda_0/64$. 50 macroparticles per cell for each species are used in all simulations.

Figure 3 shows results from the 3D PIC simulation for a 0.5-mm jet-foil distance. While several mechanisms may give rise to strong electromagnetic fluctuations in the vicinity of the foil surface (e.g., parametric decay of laser-driven surface oscillations or Rayleigh-Taylor–type instability [59,60]), the Weibel-type CFI appears to be the dominant process under our experimental conditions (see Supplemental Material [54]). The resulting fluctuations, of mainly magnetic nature, exhibit a characteristic filamentary pattern with a ∼0.4-μm transverse periodicity, and extending to a ∼1-μm depth [Fig. 3(b)]. The time evolution of the z-integrated magnetic field during and after the laser irradiation is presented in Fig. 3(e), showing that the beam electrons experience fully grown magnetic fields as soon as they enter the target. Their (θ_x, θ_y) angular distribution after transiting through the target is displayed in Fig. 3(d): the beam divergence along the vertical (y) direction is measured to be $\theta_y \simeq 10$ mrad (FWHM), much larger than its initial value ($\simeq 0.1$ mrad) in the simulation. Moreover, these magnetic deflections translate into strong transverse modulations in the beam profile [compare Figs. 3(a) and 3(c)]. The asymmetry between the horizontal (x) and vertical (y) divergences originates from the stronger laser-induced electron heating along the laser polarization axis (x); this excites current modulations preferentially along the cold (y) axis, hence leading to $B_{x,\text{int}} > B_{y,\text{int}}$ and to a larger vertical divergence. The effect of the head-on interaction between the reflected laser and the electron beam was found to be negligible when examining the beam angular distribution prior and after its collision with the reflected pulse, but before entering the solid target (see Supplemental Material [54]).

That a moderately relativistic laser pulse can generate kT-range magnetic fluctuations in a metal foil within a few 10 fs only is not an obvious result. Interestingly, a self-consistent modeling of field ionization turns out to be necessary for a quantitative reproduction of the measurements. This was

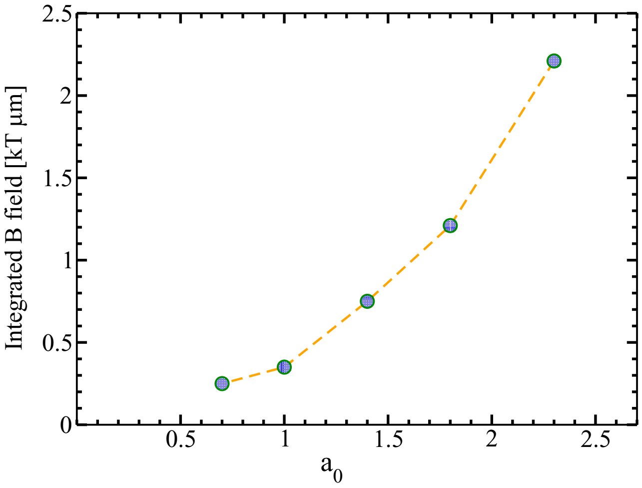

FIG. 4. Parameter scan using 3D PIC simulations, showing the variation in the line-integrated magnetic field ($B_{x,\mathrm{int}}$) as experienced by 150-MeV electrons passing through a 8-μm-thick Al foil, with the laser strength a_0 (the change of which corresponds to a varying jet-foil distance in the experiment).

found by running additional 2D simulations in which either field [56] or collisional [57] ionization was deactivated. The major change arose when disabling field ionization, leading to a ∼5× drop in the B-field strength (see Supplemental Material [54]). Such mitigation of the CFI is ascribed to a decrease in both the background electron density and the forward momentum flux of the hot electrons driving the instability. This result is in line with a recent simulation study [61] which predicted the enhancement of the CFI by field ionization.

To further compare the simulation results with the experimental observations, and quantify the sensitivity of the CFI-induced magnetic fluctuations to the laser-driven intensity, we plot in Fig. 4 the results of a parametric scan where a_0 is varied from 2.3 to 0.7, corresponding to a jet-foil distance ranging from 0.5 to 2.7 mm. The integrated magnetic field experienced by the electron beam is seen to monotonically drop (down to $B_{x,\mathrm{int}} \approx 0.25$ kT μm at $a_0 = 0.7$) as the laser strength is reduced (or, equivalently, the foil is moved away from the gas jet).

IV. CONCLUSION

To conclude, we have evidenced the generation of submicron-scale magnetic fields by the CFI excited during femtosecond ultraintense laser-solid interactions, and demonstrated, both experimentally and numerically, the potential of low-emittance LWFA-driven electron beams to probe these fields. Supported by PIC simulations, our measurements indicate that B fields of 2.70 ± 0.39 kT μm line-integrated strength build up at the front surface of a solid Al target irradiated by a ∼20 fs, $\sim 10^{19}$ W cm^{-2} laser pulse. Simulations show that the ultrafast CFI growth is furthered by field ionization. These results pave the way for measurements of the CFI dynamics at femtosecond timescales, by generating the probe electron beam from an auxiliary laser pulse with controlled delay. They are also of prime interest for staged plasma-based accelerators [62], including novel hybrid schemes, which aim to miniaturize beam-driven plasma wakefield accelerators (PWFA) [63,64] and achieve unprecedented beam quality by using relativistic electron drive beams from a LWFA [65–70], and separating the LWFA and PWFA by a thin foil. This study highlights the need to mitigate the CFI (e.g., by depleting the laser pulse energy before it hits the solid target) so as to avoid degrading the quality of the electron beam driving the subsequent acceleration stage.

ACKNOWLEDGMENTS

This work was supported by the European Research Council (ERC) under the European Union’s Horizon 2020 research and innovation programme (Miniature beam-driven Plasma Accelerators project, Grant Agreement No. 715807). H.D., A.D., M.F., M.F.G., and S.K. were supported by DFG (Deutsche Forschungsgemeinschaft), project name ’EXC 158: Munich-Centre for Advanced Photonics (MAP)’ and project number 24819222 through the Cluster of Excellence Munich Centre for Advanced Photonics (MAP EXC 158). Numerical simulations were performed using HPC resources from PRACE (Partnership for Advanced Computing in Europe) (Grant No. 2017174175) and GENCI-TGCC (Grand Équipement National de Calcul Intensif) (Grants No. 2018-A0040507594 and No. 2019-A0060510786) with the IRENE supercomputer.

---

[1] E. S. Weibel, Phys. Rev. Lett. **2**, 83 (1959).
[2] B. D. Fried, Phys. Fluids **2**, 337 (1959).
[3] R. C. Davidson, D. A. Hammer, I. Haber, and C. E. Wagner, Phys. Fluids **15**, 317 (1972).
[4] A. Bret, L. Gremillet, and M. E. Dieckmann, Phys. Plasmas **17**, 120501 (2010).
[5] A. Achterberg and J. Wiersma, Astron. Astrophys. **475**, 1 (2007).
[6] C. Zhang, C.-K. Huang, K. A. Marsh, C. E. Clayton, W. B. Mori, and C. Joshi, Sci. Adv. **5**, eaax4545 (2019).
[7] A. Achterberg, J. Wiersma, and C. A. Norman, Astron. Astrophys. **475**, 19 (2007).
[8] C. Ruyer, L. Gremillet, A. Debayle, and G. Bonnaud, Phys. Plasmas **22**, 032102 (2015).
[9] M. V. Medvedev and A. Loeb, Astrophys. J. **526**, 697 (1999).
[10] A. Spitkovsky, Astrophys. J. Lett. **682**, L5 (2008).
[11] T. N. Kato and H. Takabe, Astrophys. J. Lett. **681**, L93 (2008).
[12] A. Marcowith, A. Bret, A. Bykov, M. E. Dieckman, L. O’C Drury, B. Lembège, M. Lemoine, G. Morlino, G. Murphy, G. Pelletier, I. Plotnikov, B. Reville, M. Riquelme, L. Sironi, and A. Stockem Novo, Rep. Prog. Phys. **79**, 046901 (2016).
[13] M. Lemoine, L. Gremillet, G. Pelletier, and A. Vanthieghem, Phys. Rev. Lett. **123**, 035101 (2019).

[14] M. Swisdak, Y.-H. Liu, and J. F. Drake, Astrophys. J. **680**, 999 (2008).

[15] R. Schlickeiser and P. K. Shukla, Astrophys. J. Lett. **599**, L57 (2003).

[16] Y. Sentoku, K. Mima, S. Kojima, and H. Ruhl, Phys. Plasmas **7**, 689 (2000).

[17] L. O. Silva, R. A. Fonseca, J. W. Tonge, W. B. Mori, and J. M. Dawson, Phys. Plasmas **9**, 2458 (2002).

[18] C. Ren, M. Tzoufras, J. Tonge, W. B. Mori, F. S. Tsung, M. Fiore, R. A. Fonseca, L. O. Silva, J.-C. Adam, and A. Heron, Phys. Plasmas **13**, 056308 (2006).

[19] A. P. L. Robinson, D. J. Strozzi, J. R. Davies, L. Gremillet, J. J. Honrubia, T. Johzaki, R. J. Kingham, M. Sherlock, and A. A. Solodov, Nucl. Fusion **54**, 054003 (2014).

[20] Y. Sentoku, K. Mima, P. Kaw, and K. Nishikawa, Phys. Rev. Lett. **90**, 155001 (2003).

[21] B. Chrisman, Y. Sentoku, and A. J. Kemp, Phys. Plasmas **15**, 056309 (2008).

[22] J. C. Adam, A. Héron, and G. Laval, Phys. Rev. Lett. **97**, 205006 (2006).

[23] A. Debayle, J. J. Honrubia, E. d'Humières, and V. T. Tikhonchuk, Phys. Rev. E **82**, 036405 (2010).

[24] J. Fuchs, T. E. Cowan, P. Audebert, H. Ruhl, L. Gremillet, A. Kemp, M. Allen, A. Blazevic, J.-C. Gauthier, M. Geissel, M. Hegelich, S. Karsch, P. Parks, M. Roth, Y. Sentoku, R. Stephens, and E. M. Campbell, Phys. Rev. Lett. **91**, 255002 (2003).

[25] S. Göde, C. Rödel, K. Zeil, R. Mishra, M. Gauthier, F.-E. Brack, T. Kluge, M. J. MacDonald, J. Metzkes, L. Obst, M. Rehwald, C. Ruyer, H.-P. Schlenvoigt, W. Schumaker, P. Sommer, T. E. Cowan, U. Schramm, S. Glenzer, and F. Fiuza, Phys. Rev. Lett. **118**, 194801 (2017).

[26] G. G. Scott, C. M. Brenner, V. Bagnoud, R. J. Clarke, B. Gonzalez-Izquierdo, J. S. Green, R. I. Heathcote, H. W. Powell, D. R. Rusby, B. Zielbauer, P. McKenna, and D. Neely, New J. Phys. **19**, 043010 (2017).

[27] F. Fiuza, R. A. Fonseca, J. Tonge, W. B. Mori, and L. O. Silva, Phys. Rev. Lett. **108**, 235004 (2012).

[28] C. Ruyer, L. Gremillet, and G. Bonnaud, Phys. Plasmas **22**, 082107 (2015).

[29] W. Fox, G. Fiksel, A. Bhattacharjee, P.-Y. Chang, K. Germaschewski, S. X. Hu, and P. M. Nilson, Phys. Rev. Lett. **111**, 225002 (2013).

[30] C. M. Huntington, F. Fiuza, J. S. Ross, A. B. Zylstra, R. P. Drake, D. H. Froula, G. Gregori, N. L. Kugland, C. C. Kuranz, M. C. Levy, C. K. Li, J. Meinecke, T. Morita, R. Petrasso, C. Plechaty, B. A. Remington, D. D. Ryutov, Y. Sakawa, A. Spitkovsky, H. Takabe, and H.-S. Park, Nat. Phys. **11**, 173 (2015).

[31] B. Allen, V. Yakimenko, M. Babzien, M. Fedurin, K. Kusche, and P. Muggli, Phys. Rev. Lett. **109**, 185007 (2012).

[32] A. Benedetti, M. Tamburini, and C. H. Keitel, Nat. Photonics **12**, 319 (2018).

[33] M. Tatarakis, F. N. Beg, E. L. Clark, A. E. Dangor, R. D. Edwards, R. G. Evans, T. J. Goldsack, K. W. D. Ledingham, P. A. Norreys, M. A. Sinclair, M.-S. Wei, M. Zepf, and K. Krushelnick, Phys. Rev. Lett. **90**, 175001 (2003).

[34] M. S. Wei, F. N. Beg, E. L. Clark, A. E. Dangor, R. G. Evans, A. Gopal, K. W. D. Ledingham, P. McKenna, P. A. Norreys, M. Tatarakis, M. Zepf, and K. Krushelnick, Phys. Rev. E **70**, 056412 (2004).

[35] R. Jung, J. Osterholz, K. Löwenbrück, S. Kiselev, G. Pretzler, A. Pukhov, O. Willi, S. Kar, M. Borghesi, W. Nazarov, S. Karsch, R. Clarke, and D. Neely, Phys. Rev. Lett. **94**, 195001 (2005).

[36] M. Manclossi, J. J. Santos, D. Batani, J. Faure, A. Debayle, V. T. Tikhonchuk, and V. Malka, Phys. Rev. Lett. **96**, 125002 (2006).

[37] J. Metzkes, T. Kluge, K. Zeil, M. Bussmann, S. D. Kraft, T. E. Cowan, and U. Schramm, New J. Phys. **16**, 023008 (2014).

[38] M. King, N. Butler, R. Wilson, R. Capdessus, R. Gray, H. W. Powell, R. Dance, H. Padda, B. Gonzalez-Izquierdo, D. Rusby, N. Dover, G. S. Hicks, O. Ettlinger, C. Scullion, D. Carroll, Z. Najmudin, M. Borghesi, D. Neely, and P. Mckenna, High Power Laser Sci. Eng. **7**, e14 (2019).

[39] S. Mondal, V. Narayanan, W. J. Ding, A. D. Lad, B. Hao, S. Ahmad, W. M. Wang, Z. M. Sheng, S. Sengupta, P. Kaw, A. Das, and G. R. Kumar, Proc. Natl. Acad. Sci. USA **109**, 8011 (2012).

[40] G. Chatterjee, K. M. Schoeffler, P. Kumar Singh, A. Adak, A. D. Lad, S. Sengupta, P. Kaw, L. O. Silva, A. Das, and G. R. Kumar, Nat. Commun. **8**, 15970 (2017).

[41] C. J. Zhang, J. F. Hua, Y. Wan, C.-H. Pai, B. Guo, J. Zhang, Y. Ma, F. Li, Y. P. Wu, H.-H. Chu, Y. Q. Gu, X. L. Xu, W. B. Mori, C. Joshi, J. Wang, and W. Lu, Phys. Rev. Lett. **119**, 064801 (2017).

[42] W. Schumaker, N. Nakanii, C. McGuffey, C. Zulick, V. Chyvkov, F. Dollar, H. Habara, G. Kalintchenko, A. Maksimchuk, K. A. Tanaka, A. G. R. Thomas, V. Yanovsky, and K. Krushelnick, Phys. Rev. Lett. **110**, 015003 (2013).

[43] T. Tajima and J. M. Dawson, Phys. Rev. Lett. **43**, 267 (1979).

[44] J. Faure, Y. Glinec, A. Pukhov, S. Kiselev, S. Gordienko, E. Lefebvre, J.-P. Rousseau, F. Burgy, and V. Malka, Nature (London) **431**, 541 (2004).

[45] C. G. R. Geddes, C. Toth, J. van Tilborg, E. Esarey, C. B. Schroeder, D. Bruhwiler, C. Nieter, J. Cary, and W. P. Leemans, Nature (London) **431**, 538 (2004).

[46] S. P. D. Mangles, C. D. Murphy, Z. Najmudin, A. G. R. Thomas, J. L. Collier, A. E. Dangor, E. J. Divall, P. S. Foster, J. G. Gallacher, C. J. Hooker, D. A. Jaroszynski, A. J. Langley, W. B. Mori, P. A. Norreys, F. S. Tsung, R. Viskup, B. R. Walton, and Krushelnick, Nature (London) **431**, 535 (2004).

[47] A. J. Gonsalves, K. Nakamura, J. Daniels, C. Benedetti, C. Pieronek, T. C. H. de Raadt, S. Steinke, J. H. Bin, S. S. Bulanov, J. van Tilborg, C. G. R. Geddes, C. B. Schroeder, C. Tóth, E. Esarey, K. Swanson, L. Fan-Chiang, G. Bagdasarov, N. Bobrova, V. Gasilov *et al.*, Phys. Rev. Lett. **122**, 084801 (2019).

[48] T. P. Rowlands-Rees, C. Kamperidis, S. Kneip, A. J. Gonsalves, S. P. D. Mangles, J. G. Gallacher, E. Brunetti, T. Ibbotson, C. D. Murphy, P. S. Foster, M. J. V. Streeter, F. Budde, P. A. Norreys, D. A. Jaroszynski, K. Krushelnick, Z. Najmudin, and S. M. Hooker, Phys. Rev. Lett. **100**, 105005 (2008).

[49] A. Pak, K. A. Marsh, S. F. Martins, W. Lu, W. B. Mori, and C. Joshi, Phys. Rev. Lett. **104**, 025003 (2010).

[50] C. McGuffey, A. G. R. Thomas, W. Schumaker, T. Matsuoka, V. Chvykov, F. J. Dollar, G. Kalintchenko, V. Yanovsky, A. Maksimchuk, K. Krushelnick, V. Y. Bychenkov, I. V. Glazyrin, and A. V. Karpeev, Phys. Rev. Lett. **104**, 025004 (2010).

[51] A. Döpp, B. Mahieu, A. Lifschitz, C. Thaury, A. Doche, E. Guillaume, G. Grittani, O. Lundh, M. Hansson, J. Gautier, M. Kozlova, J. P. Goddet, P. Rousseau, A. Tafzi, V. Malka,

A. Rousse, S. Corde, and K. Ta Phuoc, Light: Sci. Appl. **6**, e17086 (2017).

[52] S. Corde, C. Thaury, A. Lifschitz, G. Lambert, K. Ta Phuoc, X. Davoine, R. Lehe, D. Douillet, A. Rousse, and V. Malka, Nat. Commun. **4**, 1501 (2013).

[53] E. Esarey, C. B. Schroeder, and W. P. Leemans, Rev. Mod. Phys. **81**, 1229 (2009).

[54] See Supplemental Material at http://link.aps.org/supplemental/10.1103/PhysRevResearch.2.023123 for additional experimental data with higher laser energy, and regarding preplasma length, magnetic-field generation mechanisms, and effects of reflected laser and field ionization.

[55] E. Lefebvre, N. Cochet, S. Fritzler, V. Malka, M.-M. Aléonard, J.-F. Chemin, S. Darbon, L. Disdier, J. Faure, A. Fedotoff, O. Landoas, G. Malka, V. Méot, P. Morel, M. Rabec LeGloahec, A. Rouyer, C. Rubbelynck, V. Tikhonchuk, R. Wrobel *et al.*, Nucl. Fusion **43**, 629 (2003).

[56] R. Nuter, L. Gremillet, E. Lefebvre, A. Lévy, T. Ceccotti, and P. Martin, Phys. Plasmas **18**, 033107 (2011).

[57] F. Pérez, L. Gremillet, A. Decoster, M. Drouin, and E. Lefebvre, Phys. Plasmas **19**, 083104 (2012).

[58] M. Lobet, E. d'Humières, M. Grech, C. Ruyer, X. Davoine, and L. Gremillet, J. Phys.: Conf. Ser. **688**, 012058 (2016).

[59] A. Macchi, F. Cornolti, and F. Pegoraro, Phys. Plasmas **9**, 1704 (2002).

[60] T. Kluge, J. Metzkes, K. Zeil, M. Bussmann, U. Schramm, and T. E. Cowan, Phys. Plasmas **22**, 064502 (2015).

[61] Y. Lang, X. H. Yang, H. Xu, Z. Jin, and H. B. Zhuo, Plasma Phys. Control. Fusion **60**, 075002 (2018).

[62] S. Steinke, J. van Tilborg, C. Benedetti, C. G. R. Geddes, C. B. Schroeder, J. Daniels, K. K. Swanson, A. Gonsalves, K. P. Nakamura, N. Matlis, B. Shaw, E. Esarey, and W. Leemans, Nature (London) **530**, 190 (2016).

[63] P. Chen, J. M. Dawson, R. W. Huff, and T. Katsouleas, Phys. Rev. Lett. **54**, 693 (1985).

[64] M. Litos, E. Adli, W. An, C. I. Clarke, C. E. Clayton, S. Corde, J. P. Delahaye, R. J. England, A. S. Fisher, J. Frederico, S. Gessner, S. Z. Green, M. J. Hogan, C. Joshi, W. Lu, K. A. Marsh, W. B. Mori, P. Muggli, N. Vafaei-Najafabadi, D. Walz *et al.*, Nature (London) **515**, 92 (2014).

[65] B. Hidding, T. Königstein, J. Osterholz, S. Karsch, O. Willi, and G. Pretzler, Phys. Rev. Lett. **104**, 195002 (2010).

[66] S. Chou, J. Xu, K. Khrennikov, D. E. Cardenas, J. Wenz, M. Heigoldt, L. Hofmann, L. Veisz, and S. Karsch, Phys. Rev. Lett. **117**, 144801 (2016).

[67] J. Ferri, S. Corde, A. Döpp, A. Lifschitz, A. Doche, C. Thaury, K. Ta Phuoc, B. Mahieu, I. A. Andriyash, V. Malka, and X. Davoine, Phys. Rev. Lett. **120**, 254802 (2018).

[68] M. F. Gilljohann, H. Ding, A. Döpp, J. Götzfried, S. Schindler, G. Schilling, S. Corde, A. Debus, T. Heinemann, B. Hidding, S. M. Hooker, A. Irman, O. Kononenko, T. Kurz, A. Martinez de la Ossa, U. Schramm, and S. Karsch, Phys. Rev. X **9**, 011046 (2019).

[69] A. Martinez de la Ossa, R. W. Assmann, M. Bussmann, S. Corde, J. P. Couperus Cabadag, A. Debus, A. Döpp, A. Ferran Pousa, M. F. Gilljohann, T. Heinemann, B. Hidding, A. Irman, S. Karsch, O. Kononenko, T. Kurz, J. Osterhoff, R. Pausch, S. Schöbel, and U. Schramm, Philos. Trans. R. Soc. A **377**, 20180175 (2019).

[70] T. Kurz, T. Heinemann, M. F. Gilljohann, Y. Y. Chang, J. P. C. Cabadağ, A. Debus, O. Kononenko, R. Pausch, S. Schöbel, R. W. Assmann, M. Bussmann, H. Ding, J. Götzfried, A. Köhler, G. Raj, S. Schindler, K. Steiniger, O. Zarini, S. Corde, A. Döpp *et al.*, arXiv:1909.06676.

BIBLIOGRAPHY

[1] Michael Benedikt, Alain Blondel, Patrick Janot, Michelangelo Mangano, and Frank Zimmermann. Future Circular Colliders succeeding the LHC. *Nature Phys.*, 16:402–407. 6 p, 2020, doi:10.1038/s41567-020-0856-2. 11

[2] Y. Fukuda, T. Hayakawa, E. Ichihara, K. Inoue, Ishihara, et al. Evidence for oscillation of atmospheric neutrinos. *Phys. Rev. Lett.*, 81:1562–1567, Aug 1998, doi:10.1103/PhysRevLett.81.1562. 11

[3] T. Tajima and J. M. Dawson. Laser electron accelerator. *Phys. Rev. Lett.*, 43:267–270, Jul 1979, doi:10.1103/PhysRevLett.43.267. 11, 18

[4] V. Yakimenko et al. FACET-II facility for advanced accelerator experimental tests. *Phys. Rev. Accel. Beams*, 22(10):101301, 2019, doi:10.1103/PhysRevAccelBeams.22.101301. 12, 108

[5] A. Bret, L. Gremillet, and M. E. Dieckmann. Multidimensional electron beam-plasma instabilities in the relativistic regime. *Physics of Plasmas*, 17(12):120501, 2010, doi:10.1063/1.3514586. 13, 69, 71, 75, 77, 92

[6] Rhon Keinigs and Michael E. Jones. Two-dimensional dynamics of the plasma wakefield accelerator. *The Physics of Fluids*, 30(1):252–263, 1987, doi:10.1063/1.866183. 13, 25

[7] S. Chatrchyan, V. Khachatryan, A.M. Sirunyan, et al. Observation of a new boson at a mass of 125 gev with the cms experiment at the lhc. *Physics Letters B*, 716(1):30–61, 2012, doi:https://doi.org/10.1016/j.physletb.2012.08.021. 18

[8] G. Aad, T. Abajyan, B. Abbott, et al. Observation of a new particle in the search for the standard model higgs boson with the atlas detector at the lhc. *Physics Letters B*, 716(1):1–29, 2012, doi:https://doi.org/10.1016/j.physletb.2012.08.020. 18

[9] Jie Yang, Riccardo Dettori, J. Pedro F. Nunes, Nanna H. List, Elisa Biasin, Martin Centurion, Zhijiang Chen, Amy A. Cordones, Daniel P. Deponte, Tony F. Heinz, Michael E. Kozina, Kathryn Ledbetter, Ming-Fu Lin, Aaron M. Lindenberg, Mianzhen Mo, Anders Nilsson, Xiaozhe Shen, Thomas J. A. Wolf, Davide Donadio, Kelly J. Gaffney, Todd J. Martinez, and Xijie Wang. Direct observation of ultrafast hydrogen bond strengthening in liquid water. *Nature*, 596(7873):531–535, 2021, doi:10.1038/s41586-021-03793-9. 18

[10] Pisin Chen, J. M. Dawson, Robert W. Huff, and T. Katsouleas. Acceleration of electrons by the interaction of a bunched electron beam with a plasma. *Phys. Rev. Lett.*, 54:693–696, Feb 1985, doi:10.1103/PhysRevLett.54.693. 18

[11] V Malka. Plasma wake accelerators: introduction and historical overview. *arXiv preprint arXiv:1705.09584*, 2017. 19

[12] A. Modena, Z. Najmudin, A. E. Dangor, C. E. Clayton, K. A. Marsh, C. Joshi, V. Malka, C. B. Darrow, C. Danson, D. Neely, and F. N. Walsh. Electron acceleration from the breaking of relativistic plasma waves. *Nature*, 377(6550):606–608, 1995, doi:10.1038/377606a0. 19

[13] Donna Strickland and Gerard Mourou. Compression of amplified chirped optical pulses. *Optics Communications*, 56(3):219–221, 1985, doi:https://doi.org/10.1016/0030-4018(85)90120-8. 19, 124

[14] J. Faure, Y. Glinec, A. Pukhov, S. Kiselev, S. Gordienko, E. Lefebvre, J. P. Rousseau, F. Burgy, and V. Malka. A laser–plasma accelerator producing monoenergetic electron beams. *Nature*, 431(7008):541–544, 2004, doi:10.1038/nature02963. 20

[15] C. G. R. Geddes, Cs. Toth, J. van Tilborg, E. Esarey, C. B. Schroeder, D. Bruhwiler, C. Nieter, J. Cary, and W. P. Leemans. High-quality electron beams from a laser wakefield accelerator using plasma-channel guiding. *Nature*, 431(7008):538–541, 2004, doi:10.1038/nature02900. 20

[16] S. P. D. Mangles, C. D. Murphy, Z. Najmudin, A. G. R. Thomas, J. L. Collier, A. E. Dangor, E. J. Divall, P. S. Foster, J. G. Gallacher, C. J. Hooker, D. A. Jaroszynski, A. J. Langley, W. B. Mori, P. A. Norreys, F. S. Tsung, R. Viskup, B. R. Walton, and K. Krushelnick. Monoenergetic beams of relativistic electrons from intense laser–plasma interactions. *Nature*, 431(7008):535–538, 2004, doi:10.1038/nature02939. 20

[17] J. B. Rosenzweig, D. B. Cline, B. Cole, H. Figueroa, W. Gai, R. Konecny, J. Norem, P. Schoessow, and J. Simpson. Experimental observation of plasma wake-field acceleration. *Phys. Rev. Lett.*, 61:98–101, Jul 1988, doi:10.1103/PhysRevLett.61.98. 20

[18] Ian Blumenfeld, Christopher E. Clayton, Franz-Josef Decker, Mark J. Hogan, Chengkun Huang, Rasmus Ischebeck, Richard Iverson, Chandrashekhar Joshi, Thomas Katsouleas, Neil Kirby, Wei Lu, Kenneth A. Marsh, Warren B. Mori, Patric Muggli, Erdem Oz, Robert H. Siemann, Dieter Walz, and Miaomiao Zhou. Energy doubling of 42 gev electrons in a metre-scale plasma wakefield accelerator. *Nature*, 445(7129):741–744, 2007, doi:10.1038/nature05538. 20

[19] J. B. Rosenzweig. Nonlinear plasma dynamics in the plasma wake-field accelerator. *Phys. Rev. Lett.*, 58:555–558, Feb 1987, doi:10.1103/PhysRevLett.58.555. 20

[20] W. Lu, C. Huang, M. Zhou, M. Tzoufras, F. S. Tsung, W. B. Mori, and T. Katsouleas. A nonlinear theory for multidimensional relativistic plasma wave wakefields. *Physics of Plasmas*, 13(5):056709, 2006, doi:10.1063/1.2203364. 20, 28, 115

[21] J. B. Rosenzweig, B. Breizman, T. Katsouleas, and J. J. Su. Acceleration and focusing of electrons in two-dimensional nonlinear plasma wake fields. *Phys. Rev. A*, 44:R6189–R6192, Nov 1991, doi:10.1103/PhysRevA.44.R6189. 20

[22] J. B. Rosenzweig, N. Barov, M. C. Thompson, and R. B. Yoder. Energy loss of a high charge bunched electron beam in plasma: Simulations, scaling, and accelerating wakefields. *Phys. Rev. ST Accel. Beams*, 7:061302, Jun 2004, doi:10.1103/PhysRevSTAB.7.061302. 20, 115

[23] C. E. Clayton, E. Adli, J. Allen, W. An, C. I. Clarke, S. Corde, J. Frederico, S. Gessner, S. Z. Green, M. J. Hogan, C. Joshi, M. Litos, W. Lu, K. A. Marsh, W. B. Mori, N. Vafaei-Najafabadi, X. Xu, and V. Yakimenko. Self-mapping the longitudinal field structure of a nonlinear plasma accelerator cavity. *Nature Communications*, 7(1):12483, 2016, doi:10.1038/ncomms12483. 20

[24] M Litos, E Adli, J M Allen, W An, C I Clarke, S Corde, C E Clayton, J Frederico, S J Gessner, S Z Green, M J Hogan, C Joshi, W Lu, K A Marsh, W B Mori, M Schmeltz, N Vafaei-Najafabadi, and V Yakimenko. 9 GeV energy gain in a beam-driven plasma wakefield accelerator. *Plasma Physics and Controlled Fusion*, 58(3):034017, feb 2016, doi:10.1088/0741-3335/58/3/034017. 20

[25] M. Tzoufras, W. Lu, F. S. Tsung, C. Huang, W. B. Mori, T. Katsouleas, J. Vieira, R. A. Fonseca, and L. O. Silva. Beam loading in the nonlinear regime of plasma-based acceleration. *Phys. Rev. Lett.*, 101:145002, Sep 2008, doi:10.1103/PhysRevLett.101.145002. 20, 29

[26] S. Schröder, C. A. Lindstrøm, S. Bohlen, G. Boyle, R. D'Arcy, S. Diederichs, M. J. Garland, P. Gonzalez, A. Knetsch, V. Libov, P. Niknejadi, Kris Põder, L. Schaper, B. Schmidt, B. Sheeran, G. Tauscher, S. Wesch, J. Zemella, M. Zeng, and J. Osterhoff. High-resolution sampling of beam-driven plasma wakefields. *Nature Communications*, 11(1):5984, 2020, doi:10.1038/s41467-020-19811-9. 20, 29

[27] C. A. Lindstrøm, J. M. Garland, S. Schröder, L. Boulton, G. Boyle, J. Chappell, R. D'Arcy, P. Gonzalez, A. Knetsch, V. Libov, G. Loisch, A. Martinez de la Ossa, P. Niknejadi, K. Põder, L. Schaper, B. Schmidt, B. Sheeran, S. Wesch, J. Wood, and J. Osterhoff. Energy-spread preservation and high efficiency in a plasma-wakefield accelerator. *Phys. Rev. Lett.*, 126:014801, Jan 2021, doi:10.1103/PhysRevLett.126.014801. 20, 29

[28] Naveen Kumar, Alexander Pukhov, and Konstantin Lotov. Self-modulation instability of a long proton bunch in plasmas. *Phys. Rev. Lett.*, 104:255003, Jun 2010, doi:10.1103/PhysRevLett.104.255003. 20

[29] E. Adli, A. Ahuja, O. Apsimon, R. Apsimon, A. M. Bachmann, D. Barrientos, F. Batsch, J. Bauche, V. K. Berglyd Olsen, M. Bernardini, T. Bohl, C. Bracco, F. Braunmüller, G. Burt, B. Buttenschön, A. Caldwell, M. Cascella, J. Chappell, E. Chevallay, M. Chung, D. Cooke, H. Damerau, L. Deacon, L. H. Deubner, A. Dexter, S. Doebert, J. Farmer, V. N. Fedosseev, R. Fiorito, R. A. Fonseca, F. Friebel, L. Garolfi, S. Gessner, I. Gorgisyan, A. A. Gorn, E. Granados, O. Grulke, E. Gschwendtner, J. Hansen, A. Helm, J. R. Henderson, M. Hüther, M. Ibison, L. Jensen, S. Jolly, F. Keeble, S. Y. Kim, F. Kraus, Y. Li, S. Liu, N. Lopes, K. V. Lotov, L. Maricalva Brun, M. Martyanov, S. Mazzoni, D. Medina Godoy, V. A. Minakov, J. Mitchell, J. C. Molendijk, J. T. Moody, M. Moreira, P. Muggli, E. Öz,

C. Pasquino, A. Pardons, F. Peña Asmus, K. Pepitone, A. Perera, A. Petrenko, S. Pitman, A. Pukhov, S. Rey, K. Rieger, H. Ruhl, J. S. Schmidt, I. A. Shalimova, P. Sherwood, L. O. Silva, L. Soby, A. P. Sosedkin, R. Speroni, R. I. Spitsyn, P. V. Tuev, M. Turner, F. Velotti, L. Verra, V. A. Verzilov, J. Vieira, C. P. Welsch, B. Williamson, M. Wing, B. Woolley, and G. Xia. Acceleration of electrons in the plasma wakefield of a proton bunch. *Nature*, 561(7723):363–367, 2018, doi:10.1038/s41586-018-0485-4. 20

[30] Wentao Wang, Ke Feng, Lintong Ke, Changhai Yu, Yi Xu, Rong Qi, Yu Chen, Zhiyong Qin, Zhijun Zhang, Ming Fang, Jiaqi Liu, Kangnan Jiang, Hao Wang, Cheng Wang, Xiaojun Yang, Fenxiang Wu, Yuxin Leng, Jiansheng Liu, Ruxin Li, and Zhizhan Xu. Free-electron lasing at 27 nanometres based on a laser wakefield accelerator. *Nature*, 595(7868):516–520, 2021, doi:10.1038/s41586-021-03678-x. 21, 140

[31] A. J. Gonsalves, K. Nakamura, J. Daniels, C. Benedetti, C. Pieronek, T. C. H. de Raadt, S. Steinke, J. H. Bin, S. S. Bulanov, J. van Tilborg, C. G. R. Geddes, C. B. Schroeder, Cs. Tóth, E. Esarey, K. Swanson, L. Fan-Chiang, G. Bagdasarov, N. Bobrova, V. Gasilov, G. Korn, P. Sasorov, and W. P. Leemans. Petawatt laser guiding and electron beam acceleration to 8 gev in a laser-heated capillary discharge waveguide. *Phys. Rev. Lett.*, 122:084801, Feb 2019, doi:10.1103/PhysRevLett.122.084801. 22

[32] Kosta Oubrerie, Adrien Leblanc, Olena Kononenko, Ronan Lahaye, Igor A. Andriyash, Julien Gautier, Jean-Philippe Goddet, Lorenzo Martelli, Amar Tafzi, Kim Ta Phuoc, Slava Smartsev, and Cedric Thaury. Controlled acceleration of gev electron beams in an all-optical plasma waveguide, 2021. 22, 140

[33] C. S. Hue, G. J. Cao, I. A. Andriyash, A. Knetsch, M. J. Hogan, E. Adli, S. Gessner, and S. Corde. Efficiency and beam quality for positron acceleration in loaded plasma wakefields. *Phys. Rev. Research*, 3:043063, Oct 2021, doi:10.1103/PhysRevResearch.3.043063. 22

[34] T. Kurz, T. Heinemann, M. F. Gilljohann, Y. Y. Chang, J. P. Couperus Cabadağ, A. Debus, O. Kononenko, R. Pausch, S. Schöbel, R. W. Assmann, M. Bussmann, H. Ding, J. Götzfried, A. Köhler, G. Raj, S. Schindler, K. Steiniger, O. Zarini, S. Corde, A. Döpp, B. Hidding, S. Karsch, U. Schramm, A. Martinez de la Ossa, and A. Irman. Demonstration of a compact plasma accelerator powered by laser-accelerated electron beams. *Nature Communications*, 12(1):2895, 2021, doi:10.1038/s41467-021-23000-7. 22, 119

[35] Alberto Martinez de la Ossa, Ralph Assmann, R. Bussmann, S. Corde, Jurjen Couperus Cabadağ, A. Debus, Andreas Doepp, Ángel Ferran Pousa, M. Gilljohann, Thomas Heinemann, B. Hidding, Arie Irman, Stefan Karsch, Olena Kononenko, Thomas Kurz, Jens Osterhoff, Richard Pausch, and U. Schramm. Hybrid lwfa | pwfa staging as a beam energy and brightness transformer : Conceptual design and simulations, 03 2019. 22

[36] M. F. Gilljohann, H. Ding, A. Döpp, J. Götzfried, S. Schindler, G. Schilling, S. Corde, A. Debus, T. Heinemann, B. Hidding, S. M. Hooker, A. Irman, O. Kononenko, T. Kurz, A. Martinez de la Ossa, U. Schramm, and S. Karsch. Direct observation of plasma waves and dynamics induced by laser-accelerated electron beams. *Phys. Rev. X*, 9:011046, Mar 2019, doi:10.1103/PhysRevX.9.011046. 22, 111, 119

[37] John M. Dawson. Nonlinear electron oscillations in a cold plasma. *Phys. Rev.*, 113:383–387, Jan 1959, doi:10.1103/PhysRev.113.383. 27

[38] S. Gordienko and A. Pukhov. Scalings for ultrarelativistic laser plasmas and quasimonoenergetic electrons. *Physics of Plasmas*, 12(4):043109, 2005, doi:10.1063/1.1884126. 27

[39] K. V. Lotov. Blowout regimes of plasma wakefield acceleration. *Phys. Rev. E*, 69:046405, Apr 2004, doi:10.1103/PhysRevE.69.046405. 27

[40] W. Lu, C. Huang, M. Zhou, W. B. Mori, and T. Katsouleas. Nonlinear theory for relativistic plasma wakefields in the blowout regime. *Phys. Rev. Lett.*, 96:165002, Apr 2006, doi:10.1103/PhysRevLett.96.165002. 27, 31

[41] W. K. H. Panofsky and W. A. Wenzel. Some considerations concerning the transverse deflection of charged particles in radio-frequency fields. *Review of Scientific Instruments*, 27(11):967–967, 1956, doi:10.1063/1.1715427. 28

[42] S. Lee, T. Katsouleas, R. G. Hemker, E. S. Dodd, and W. B. Mori. Plasma-wakefield acceleration of a positron beam. *Phys. Rev. E*, 64:045501, Sep 2001, doi:10.1103/PhysRevE.64.045501. 29

[43] S. Corde, E. Adli, J. M. Allen, W. An, C. I. Clarke, C. E. Clayton, J. P. Delahaye, J. Frederico, S. Gessner, S. Z. Green, M. J. Hogan, C. Joshi, N. Lipkowitz, M. Litos, W. Lu, K. A. Marsh, W. B. Mori, M. Schmeltz, N. Vafaei-Najafabadi, D. Walz, V. Yakimenko, and G. Yocky. Multi-gigaelectronvolt acceleration of positrons in a self-loaded plasma wakefield. *Nature*, 524(7566):442–445, 2015, doi:10.1038/nature14890. 29

[44] Joel Frederico. *Theory and measurements of emittance preservation in plasma wakefield acceleration*. PhD thesis, Stanford University, 2016. 30

[45] *Beam Optics and Focusing Systems without Space Charge: Sections 3.1 - 3.5*, chapter 3, pages 51–103. John Wiley and Sons, Ltd, 2008. 31

[46] P. San Miguel Claveria, E. Adli, L. D. Amorim, W. An, C. E. Clayton, S. Corde, S. Gessner, M.J. Hogan, C. Joshi, O. Kononenko, M. Litos, W. Lu, K.A. Marsh, W.B. Mori, B. O'Shea, G. Raj, D. Storey, N. Vafaei-Najafabadi, G. White, Xinlu Xu, and V. Yakimenko. Betatron radiation and emittance growth in plasma wakefield accelerators. *Philosophical Transactions of the Royal Society A: Mathematical, Physical and Engineering Sciences*, 2019, doi:10.1098/rsta.2018.0173. 33, 37, 41, 43, 44, 46, 137

[47] M. Tzoufras, W. Lu, F. S. Tsung, C. Huang, W. B. Mori, T. Katsouleas, J. Vieira, R. A. Fonseca, and L. O. Silva. Beam loading by electrons in nonlinear plasma wakes. *Physics of Plasmas*, 16(5):056705, 2009, doi:10.1063/1.3118628. 32

[48] F.-J. Decker, C. Adolphsen, W.J. Corbett, P. Emma, I. Hsu, H. Moshammer, J.T. Seeman, and W.L. Spence. Dispersion and betatron matching into the linac. In *Conference Record of the 1991 IEEE Particle Accelerator Conference*, pages 905–907 vol.2, 1991. 32

[49] Weiming An, Viktor K. Decyk, Warren B. Mori, and Thomas M. Antonsen. An improved iteration loop for the three dimensional quasi-static particle-in-cell algorithm: Quickpic. *Journal of Computational Physics*, 250:165–177, 2013, doi:https://doi.org/10.1016/j.jcp.2013.05.020. 33, 40, 147

[50] C. Huang, V.K. Decyk, C. Ren, M. Zhou, W. Lu, W.B. Mori, J.H. Cooley, T.M. Antonsen, and T. Katsouleas. Quickpic: A highly efficient particle-in-cell code for modeling wakefield acceleration in plasmas. *Journal of Computational Physics*, 217(2):658–679, 2006, doi:https://doi.org/10.1016/j.jcp.2006.01.039. 33, 40

[51] R. Ariniello, C. E. Doss, K. Hunt-Stone, J. R. Cary, and M. D. Litos. Transverse beam dynamics in a plasma density ramp. *Phys. Rev. Accel. Beams*, 22:041304, Apr 2019, doi:10.1103/PhysRevAccelBeams.22.041304. 34, 98

[52] X. L. Xu, J. F. Hua, Y. P. Wu, C. J. Zhang, F. Li, Y. Wan, C.-H. Pai, W. Lu, W. An, P. Yu, M. J. Hogan, C. Joshi, and W. B. Mori. Physics of phase space matching for staging plasma and traditional accelerator components using longitudinally tailored plasma profiles. *Phys. Rev. Lett.*, 116:124801, Mar 2016, doi:10.1103/PhysRevLett.116.124801. 34, 98

[53] David H. Whittum, William M. Sharp, Simon S. Yu, Martin Lampe, and Glenn Joyce. Electron-hose instability in the ion-focused regime. *Phys. Rev. Lett.*, 67:991–994, Aug 1991, doi:10.1103/PhysRevLett.67.991. 34

[54] C. Huang, W. Lu, M. Zhou, C. E. Clayton, C. Joshi, W. B. Mori, P. Muggli, S. Deng, E. Oz, T. Katsouleas, M. J. Hogan, I. Blumenfeld, F. J. Decker, R. Ischebeck, R. H. Iverson, N. A. Kirby, and D. Walz. Hosing instability in the blow-out regime for plasma-wakefield acceleration. *Phys. Rev. Lett.*, 99:255001, Dec 2007, doi:10.1103/PhysRevLett.99.255001. 34, 35

[55] T. J. Mehrling, R. A. Fonseca, A. Martinez de la Ossa, and J. Vieira. Mitigation of the hose instability in plasma-wakefield accelerators. *Phys. Rev. Lett.*, 118:174801, Apr 2017, doi:10.1103/PhysRevLett.118.174801. 34

[56] John David Jackson. *Classical electrodynamics; 2nd ed.* Wiley, New York, NY, 1975. 35, 41, 63

[57] S. Corde, K. Ta Phuoc, G. Lambert, R. Fitour, V. Malka, A. Rousse, A. Beck, and E. Lefebvre. Femtosecond x rays from laser-plasma accelerators. *Rev. Mod. Phys.*, 85:1–48, Jan 2013, doi:10.1103/RevModPhys.85.1. 35, 36, 37

[58] Shuoqin Wang, C. E. Clayton, B. E. Blue, E. S. Dodd, K. A. Marsh, W. B. Mori, C. Joshi, S. Lee, P. Muggli, T. Katsouleas, F. J. Decker, M. J. Hogan, R. H. Iverson, P. Raimondi, D. Walz, R. Siemann, and R. Assmann. X-ray emission from betatron motion in a plasma wiggler. *Phys. Rev. Lett.*, 88:135004, Mar 2002, doi:10.1103/PhysRevLett.88.135004. 36

[59] S. Fourmaux, S. Corde, K. Ta Phuoc, P. Lassonde, G. Lebrun, S. Payeur, F. Martin, S. Sebban, V. Malka, A. Rousse, and J. C. Kieffer. Single shot phase contrast imaging using laser-produced betatron x-ray beams. *Opt. Lett.*, 36(13):2426–2428, Jul 2011, doi:10.1364/OL.36.002426. 37

[60] S. Corde, C. Thaury, A. Lifschitz, G. Lambert, K. Ta Phuoc, X. Davoine, R. Lehe, D. Douillet, A. Rousse, and V. Malka. Observation of longitudinal and transverse self-injections in laser-plasma accelerators. *Nature Communications*, 4(1):1501, 2013, doi:10.1038/ncomms2528. 37

[61] Kim Ta Phuoc, Sebastien Corde, Rahul Shah, Felicie Albert, Romuald Fitour, Jean-Philippe Rousseau, Fréderic Burgy, Brigitte Mercier, and Antoine Rousse. Imaging electron trajectories in a laser-wakefield cavity using betatron x-ray radiation. *Phys. Rev. Lett.*, 97:225002, Nov 2006, doi:10.1103/PhysRevLett.97.225002. 37

[62] A. Curcio, M. Anania, F. Bisesto, E. Chiadroni, A. Cianchi, M. Ferrario, F. Filippi, D. Giulietti, A. Marocchino, M. Petrarca, V. Shpakov, and A. Zigler. Trace-space reconstruction of low-emittance electron beams through betatron radiation in laser-plasma accelerators. *Phys. Rev. Accel. Beams*, 20:012801, Jan 2017, doi:10.1103/PhysRevAccelBeams.20.012801. 37

[63] Michaela Kozlova, Igor Andriyash, Julien Gautier, Stephane Sebban, Slava Smartsev, Noemie Jourdain, Uddhab Chulagain, Yasmina Azamoum, Amar Tafzi, Jean-Philippe Goddet, Kosta Oubrerie, Cedric Thaury, Antoine Rousse, and Kim Ta Phuoc. Hard x rays from laser-wakefield accelerators in density tailored plasmas. *Phys. Rev. X*, 10:011061, Mar 2020, doi:10.1103/PhysRevX.10.011061. 37

[64] J. Ferri, S. Corde, A. Döpp, A. Lifschitz, A. Doche, C. Thaury, K. Ta Phuoc, B. Mahieu, I. A. Andriyash, V. Malka, and X. Davoine. High-brilliance betatron γ-ray source powered by laser-accelerated electrons. *Phys. Rev. Lett.*, 120:254802, Jun 2018, doi:10.1103/PhysRevLett.120.254802. 37

[65] B. Williamson, G. Xia, S. Gessner, A. Petrenko, J. Farmer, and A. Pukhov. Betatron radiation diagnostics for AWAKE Run 2. *Nucl. Instrum. Meth. A*, 971:164076, 2020, doi:10.1016/j.nima.2020.164076. 37

[66] https://portal.slac.stanford.edu/sites/ard-public/facet/Pages/FACET II.aspx. 39

[67] S. Li, C. Clarke, R. England, Joel Frederico, S. Gessner, Mark Hogan, R. Jobe, Michael Litos, D. Walz, P. Muggli, Weiming An, and Christopher Clayton. Results from plasma wakefield experiments at facet. 01 2011. 39

[68] C Joshi, E Adli, W An, C E Clayton, S Corde, S Gessner, M J Hogan, M Litos, W Lu, K A Marsh, W B Mori, N Vafaei-Najafabadi, B O'shea, Xinlu Xu, G White, and V Yakimenko. Plasma wakefield acceleration experiments at FACET II. *Plasma Physics and Controlled Fusion*, 60(3):034001, jan 2018, doi:10.1088/1361-6587/aaa2e3. 39, 49

[69] R. Weingartner, S. Raith, A. Popp, S. Chou, J. Wenz, K. Khrennikov, M. Heigoldt, A. R. Maier, N. Kajumba, M. Fuchs, B. Zeitler, F. Krausz, S. Karsch, and F. Grüner. Ultralow emittance electron beams from a laser-wakefield accelerator. *Phys. Rev. ST Accel. Beams*, 15:111302, Nov 2012, doi:10.1103/PhysRevSTAB.15.111302. 43

[70] T. J. Mehrling, C. Benedetti, C. B. Schroeder, A. Martinez de la Ossa, J. Osterhoff, E. Esarey, and W. P. Leemans. Accurate modeling of the hose instability in plasma

wakefield accelerators. *Physics of Plasmas*, 25(5):056703, 2018, doi:10.1063/1.5017960. 46

[71] E. Adli, S.J. Gessner, S. Corde, M.J. Hogan, and H.H. Bjerke. Cherenkov light-based beam profiling for ultrarelativistic electron beams. *Nuclear Instruments and Methods in Physics Research Section A: Accelerators, Spectrometers, Detectors and Associated Equipment*, 783:35–42, 2015, doi:https://doi.org/10.1016/j.nima.2015.02.003. 49

[72] Technical Design Report for the FACET-II Project at SLAC National Accelerator Laboratory, 8 2016. 49, 61, 110

[73] Julian Schwinger. On gauge invariance and vacuum polarization. *Phys. Rev.*, 82:664–679, Jun 1951, doi:10.1103/PhysRev.82.664. 49

[74] Bernhard Hidding et al. First Measurements of Trojan Horse Injection in a Plasma Wakefield Accelerator. In *8th International Particle Accelerator Conference*, 5 2017. 51

[75] Y. Glinec, J. Faure, A. Guemnie-Tafo, V. Malka, H. Monard, J. P. Larbre, V. De Waele, J. L. Marignier, and M. Mostafavi. Absolute calibration for a broad range single shot electron spectrometer. *Review of Scientific Instruments*, 77(10):103301, 2006, doi:10.1063/1.2360988. 52

[76] S. Agostinelli, J. Allison, K. Amako, J. Apostolakis, H. Araujo, P. Arce, M. Asai, D. Axen, S. Banerjee, G. Barrand, et al. Geant4—a simulation toolkit. *Nuclear Instruments and Methods in Physics Research Section A: Accelerators, Spectrometers, Detectors and Associated Equipment*, 506(3):250–303, 2003, doi:https://doi.org/10.1016/S0168-9002(03)01368-8. 52

[77] T. Radcliffe, G. Barnea, B. Wowk, R. Rajapakshe, and S. Shalev. Monte carlo optimization of metal/phosphor screens at megavoltage energies. *Medical Physics*, 20(4):1161–1169, 1993, doi:https://doi.org/10.1118/1.596970. 55

[78] P. A. Ross. A new method of spectroscopy for faint x-radiations. *J. Opt. Soc. Am.*, 16(6):433–437, Jun 1928, doi:10.1364/JOSA.16.000433. 56

[79] K. Ta Phuoc, S. Corde, C. Thaury, V. Malka, A. Tafzi, J. P. Goddet, R. C. Shah, S. Sebban, and A. Rousse. All-optical compton gamma-ray source. *Nature Photonics*, 6(5):308–311, 2012, doi:10.1038/nphoton.2012.82. 57

[80] C. Chiuderi and M. Velli. *Basics of Plasma Astrophysics*. 2015. 69

[81] Martin Lemoine, Laurent Gremillet, Guy Pelletier, and Arno Vanthieghem. Physics of weibel-mediated relativistic collisionless shocks. *Phys. Rev. Lett.*, 123:035101, Jul 2019, doi:10.1103/PhysRevLett.123.035101. 69

[82] Arno Vanthieghem, Martin Lemoine, Illya Plotnikov, Anna Grassi, Mickael Grech, Laurent Gremillet, and Guy Pelletier. Physics and phenomenology of weakly magnetized, relativistic astrophysical shock waves. *Galaxies*, 8(2), 2020, doi:10.3390/galaxies8020033. 69

[83] Marian Karlický. ELECTRON BEAM-PLASMA INTERACTION AND THE RETURN-CURRENT FORMATION. *The Astrophysical Journal*, 690(1):189–197, dec 2008, doi:10.1088/0004-637x/690/1/189. 69

[84] M. Lazar, R. Schlickeiser, R. Wielebinski, and S. Poedts. COSMOLOGICAL EFFECTS OF WEIBEL-TYPE INSTABILITIES. *The Astrophysical Journal*, 693(2):1133–1141, mar 2009, doi:10.1088/0004-637x/693/2/1133. 69

[85] L. O. Silva, R. A. Fonseca, J. W. Tonge, J. M. Dawson, W. B. Mori, and M. V. Medvedev. Interpenetrating plasma shells: Near-equipartition magnetic field generation and non-thermal particle acceleration. *The Astrophysical Journal*, 596(1):L121–L124, sep 2003, doi:10.1086/379156. 69

[86] Andrew J. Levan and Peter G. Jonker. Electromagnetic counterparts of gravitational wave sources at the very large telescope. *Nature Reviews Physics*, 2(9):455–457, 2020, doi:10.1038/s42254-020-0216-2. 69

[87] Irving Langmuir. Scattering of electrons in ionized gases. *Phys. Rev.*, 26:585–613, Nov 1925, doi:10.1103/PhysRev.26.585. 70

[88] J. R. Pierce. Possible fluctuations in electron streams due to ions. *Journal of Applied Physics*, 19(3):231–236, 1948, doi:10.1063/1.1715050. 70

[89] D. Bohm and E. P. Gross. Theory of plasma oscillations. a. origin of medium-like behavior. *Phys. Rev.*, 75:1851–1864, Jun 1949, doi:10.1103/PhysRev.75.1851. 70, 71, 74

[90] Burton D. Fried. Mechanism for instability of transverse plasma waves. *The Physics of Fluids*, 2(3):337–337, 1959, doi:10.1063/1.1705933. 70

[91] Erich S. Weibel. Spontaneously growing transverse waves in a plasma due to an anisotropic velocity distribution. *Phys. Rev. Lett.*, 2:83–84, Feb 1959, doi:10.1103/PhysRevLett.2.83. 70

[92] S. A. Bludman, K. M. Watson, and M. N. Rosenbluth. Statistical mechanics of relativistic streams. ii. *The Physics of Fluids*, 3(5):747–757, 1960, doi:10.1063/1.1706121. 70

[93] Lester E. Thode and R. N. Sudan. Plasma heating by relativistic electron beams. i. two-stream instability. *The Physics of Fluids*, 18(11):1552–1563, 1975, doi:10.1063/1.861053. 71

[94] Roswell Lee and Martin Lampe. Electromagnetic instabilities, filamentation, and focusing of relativistic electron beams. *Phys. Rev. Lett.*, 31:1390–1393, Dec 1973, doi:10.1103/PhysRevLett.31.1390. 71

[95] A. Bret, M.-C. Firpo, and C. Deutsch. Collective electromagnetic modes for beam-plasma interaction in the whole k space. *Phys. Rev. E*, 70:046401, Oct 2004, doi:10.1103/PhysRevE.70.046401. 71, 77

[96] A. Bret, M.-C. Firpo, and C. Deutsch. Electromagnetic instabilities for relativistic beam-plasma interaction in whole k space: Nonrelativistic beam and plasma temperature effects. *Phys. Rev. E*, 72:016403, Jul 2005, doi:10.1103/PhysRevE.72.016403. 71

[97] Max Tabak, James Hammer, Michael E. Glinsky, William L. Kruer, Scott C. Wilks, John Woodworth, E. Michael Campbell, Michael D. Perry, and Rodney J. Mason. Ignition and high gain with ultrapowerful lasers*. *Physics of Plasmas*, 1(5):1626–1634, 1994, doi:10.1063/1.870664. 71

[98] C. Ren, M. Tzoufras, J. Tonge, W. B. Mori, F. S. Tsung, M. Fiore, R. A. Fonseca, L. O. Silva, J.-C. Adam, and A. Heron. A global simulation for laser-driven mev electrons in 50-um-diameter fast ignition targets. *Physics of Plasmas*, 13(5):056308, 2006, doi:10.1063/1.2173617. 71

[99] C. A. Kapetanakos, D. A. Hammer, C. D. Striffler, and R. C. Davidson. Destructive instabilities in hollow intense relativistic electron beams. *Phys. Rev. Lett.*, 30:1303–1306, Jun 1973, doi:10.1103/PhysRevLett.30.1303. 71

[100] C. A. Kapetanakos. Filamentation of intense relativistic electron beams propagating in dense plasmas. *Applied Physics Letters*, 25(9):484–486, 1974, doi:10.1063/1.1655558. 71

[101] C. A. Kapetanakos, W. M. Black, and K. R. Chu. Plasma heating by a rotating relativistic electron beam. *Phys. Rev. Lett.*, 34:1156–1159, May 1975, doi:10.1103/PhysRevLett.34.1156. 71

[102] B. Allen, V. Yakimenko, M. Babzien, M. Fedurin, K. Kusche, and P. Muggli. Experimental study of current filamentation instability. *Phys. Rev. Lett.*, 109:185007, Nov 2012, doi:10.1103/PhysRevLett.109.185007. 71, 110

[103] Michael E. Jones, Don S. Lemons, and Michael A. Mostrom. Space-time evolution of the beam-plasma instability. *The Physics of Fluids*, 26(10):2784–2786, 1983, doi:10.1063/1.864044. 71, 80, 84

[104] A. Bers and M. N. Rosenbluth. *Space-Time Evolution of Plasma Instabilities - Absolute and Convective*, volume 1. North-Holland Physics Publishing, Amsterdam, 1983. 72, 80, 84

[105] V B Pathak, T Grismayer, A Stockem, R A Fonseca, and L O Silva. Spatial-temporal evolution of the current filamentation instability. *New Journal of Physics*, 17(4):043049, apr 2015, doi:10.1088/1367-2630/17/4/043049. 72, 76, 80, 84, 92, 99, 100

[106] C. D. Decker, W. B. Mori, T. Katsouleas, and D. E. Hinkel. Spatial temporal theory of raman forward scattering. *Physics of Plasmas*, 3(4):1360–1372, 1996, doi:10.1063/1.871728. 72, 84, 99, 100

[107] T. M. O'Neil and J. H. Winfrey. Nonlinear interaction of a small cold beam and a plasma. part ii. *The Physics of Fluids*, 15(8):1514–1522, 1972, doi:10.1063/1.1694117. 74

[108] L.D. Landau. 61 - on the vibrations of the electronic plasma. In D. TER HAAR, editor, *Collected Papers of L.D. Landau*, pages 445–460. Pergamon, 1965. 75

[109] Ronald C. Davidson, David A. Hammer, Irving Haber, and Carl E. Wagner. Nonlinear development of electromagnetic instabilities in anisotropic plasmas. *The Physics of Fluids*, 15(2):317–333, 1972, doi:10.1063/1.1693910. 76

[110] E. V. Rostomian. Space-time evolution of beam-plasma instabilities. *Physics of Plasmas*, 7(5):1595–1600, 2000, doi:10.1063/1.873980. 81, 82

[111] P. San Miguel Claveria, X. Davoine, J. R. Peterson, M. Gilljohann, I. Andriyash, R. Ariniello, H. Ekerfelt, C. Emma, J. Faure, S. Gessner, M. Hogan, C. Joshi, C. H. Keitel, A. Knetsch, O. Kononenko, M. Litos, Y. Mankovska, K. Marsh, A. Matheron, Z. Nie, B. O'Shea, D. Storey, N. Vafaei-Najafabadi, Y. Wu, X. Xu, J. Yan, C. Zhang, M. Tamburini, F. Fiuza, L. Gremillet, and S. Corde. Spatiotemporal dynamics of ultra-relativistic beam-plasma instabilities. *arXiv*:2106.11625 [physics.plasm ph]. 82, 86, 88, 89, 90, 96, 137

[112] N. Shukla, J. Vieira, P. Muggli, G. Sarri, R. Fonseca, and L. O. Silva. Conditions for the onset of the current filamentation instability in the laboratory. *Journal of Plasma Physics*, 84(3):905840302, 2018, doi:10.1017/S0022377818000314. 87, 92

[113] N Shukla, S F Martins, P Muggli, J Vieira, and L O Silva. Interaction of ultra relativistic e-e+ fireball beam with plasma. *New Journal of Physics*, 22(1):013030, jan 2020, doi:10.1088/1367-2630/ab60f0. 87

[114] Brian Allen, Ashkan Seyedi, Joana Martins, Luís O. Silva, Vitaly Yakimenko, Mikhail Fedurin, Karl Kusche, Marcus Babzien, Chengkun Huang, Warren Mori, and Patric Muggli. Simulation of current filamentation instability for an accelerator beam in a capillary plasma. *AIP Conference Proceedings*, 1299(1):516–521, 2010, doi:10.1063/1.3520377. 87

[115] P. Muggli, S. F. Martins, N. Shukla, J. Vieira, and L. O. Silva. Interaction of ultra relativistic e- e+ fireball beam with plasma, 2018. 87

[116] A. Bret, M.-C. Firpo, and C. Deutsch. Characterization of the initial filamentation of a relativistic electron beam passing through a plasma. *Phys. Rev. Lett.*, 94:115002, Mar 2005, doi:10.1103/PhysRevLett.94.115002. 92

[117] J. R. Peterson, S. Glenzer, and F. Fiuza. Magnetic field amplification by a nonlinear electron streaming instability. *Phys. Rev. Lett.*, 126:215101, May 2021, doi:10.1103/PhysRevLett.126.215101. 92

[118] L. Gremillet, D. Bénisti, E. Lefebvre, and A. Bret. Linear and nonlinear development of oblique beam-plasma instabilities in the relativistic kinetic regime. *Physics of Plasmas*, 14(4):040704, 2007, doi:10.1063/1.2714509. 100

[119] Alberto Benedetti, Matteo Tamburini, and Christoph H. Keitel. Giant collimated gamma-ray flashes. *Nature Photonics*, 12(6):319–323, 2018, doi:10.1038/s41566-018-0139-y. 107

[120] Kim Molvig. Filamentary instability of a relativistic electron beam. *Phys. Rev. Lett.*, 35:1504–1507, Dec 1975, doi:10.1103/PhysRevLett.35.1504. 107

[121] Laurent Gremillet, Guy Bonnaud, and François Amiranoff. Filamented transport of laser-generated relativistic electrons penetrating a solid target. *Physics of Plasmas*, 9(3):941–948, 2002, doi:10.1063/1.1432994. 107

[122] Archana Sampath, Xavier Davoine, Sébastien Corde, Laurent Gremillet, Max Gilljohann, Maitreyi Sangal, Christoph H. Keitel, Robert Ariniello, John Cary, Henrik Ekerfelt, Claudio Emma, Frederico Fiuza, Hiroki Fujii, Mark Hogan, Chan Joshi, Alexander Knetsch, Olena Kononenko, Valentina Lee, Mike Litos, Kenneth Marsh, Zan Nie, Brendan O'Shea, J. Ryan Peterson, Pablo San Miguel Claveria, Doug Storey, Yipeng Wu, Xinlu Xu, Chaojie Zhang, and Matteo Tamburini. Extremely dense gamma-ray pulses in electron beam-multifoil collisions. *Phys. Rev. Lett.*, 126:064801, Feb 2021, doi:10.1103/PhysRevLett.126.064801. 108, 141

[123] G. Raj, O. Kononenko, M. F. Gilljohann, A. Doche, X. Davoine, C. Caizergues, Y.-Y. Chang, J. P. Couperus Cabadağ, A. Debus, H. Ding, M. Förster, J.-P. Goddet, T. Heinemann, T. Kluge, T. Kurz, R. Pausch, P. Rousseau, P. San Miguel Claveria, S. Schöbel, A. Siciak, K. Steiniger, A. Tafzi, S. Yu, B. Hidding, A. Martinez de la Ossa, A. Irman, S. Karsch, A. Döpp, U. Schramm, L. Gremillet, and S. Corde. Probing ultrafast magnetic-field generation by current filamentation instability in femtosecond relativistic laser-matter interactions. *Phys. Rev. Research*, 2:023123, May 2020, doi:10.1103/PhysRevResearch.2.023123. 119, 120, 121, 135, 140

[124] C. Thaury, F. Quéré, J. P. Geindre, A. Levy, T. Ceccotti, P. Monot, M. Bougeard, F. Réau, P. d'Oliveira, P. Audebert, R. Marjoribanks, and Ph. Martin. Plasma mirrors for ultrahigh-intensity optics. *Nature Physics*, 3(6):424–429, 2007, doi:10.1038/nphys595. 120

[125] G G Scott, C M Brenner, V Bagnoud, R J Clarke, B Gonzalez-Izquierdo, J S Green, R I Heathcote, H W Powell, D R Rusby, B Zielbauer, P McKenna, and D Neely. Diagnosis of weibel instability evolution in the rear surface density scale lengths of laser solid interactions via proton acceleration. *New Journal of Physics*, 19(4):043010, apr 2017, doi:10.1088/1367-2630/aa652c. 121

[126] C. Ruyer, S. Bolaños, B. Albertazzi, S. N. Chen, P. Antici, J. Böker, V. Dervieux, L. Lancia, M. Nakatsutsumi, L. Romagnani, R. Shepherd, M. Swantusch, M. Borghesi, O. Willi, H. Pépin, M. Starodubtsev, M. Grech, C. Riconda, L. Gremillet, and J. Fuchs. Growth of concomitant laser-driven collisionless and resistive electron filamentation instabilities over large spatiotemporal scales. *Nature Physics*, 16(9):983–988, 2020, doi:10.1038/s41567-020-0913-x. 122

[127] Sudipta Mondal, V. Narayanan, Wen Jun Ding, Amit D. Lad, Biao Hao, Saima Ahmad, Wei Min Wang, Zheng Ming Sheng, Sudip Sengupta, Predhiman Kaw, Amita Das, and G. Ravindra Kumar. Direct observation of turbulent magnetic fields in hot, dense laser produced plasmas. *Proceedings of the National Academy of Sciences*, 109(21):8011–8015, 2012, doi:10.1073/pnas.1200753109. 122

[128] Gourab Chatterjee, Prashant Kumar Singh, A. P. L. Robinson, D. Blackman, N. Booth, O. Culfa, R. J. Dance, L. A. Gizzi, R. J. Gray, J. S. Green, P. Koester, G. Ravindra Kumar, L. Labate, Amit D. Lad, K. L. Lancaster, J. Pasley, N. C. Woolsey, and P. P. Rajeev. Micron-scale mapping of megagauss magnetic fields using optical polarimetry to probe hot electron transport in petawatt-class laser-solid interactions. *Scientific Reports*, 7(1):8347, 2017, doi:10.1038/s41598-017-08619-1. 122

[129] W. L. Kruer and Kent Estabrook. Jxb heating by very intense laser light. *The Physics of Fluids*, 28(1):430–432, 1985, doi:10.1063/1.865171. 122

[130] Matteo Passoni, Luca Bertagna, and Alessandro Zani. Target normal sheath acceleration: theory, comparison with experiments and future perspectives. 12(4):045012, apr 2010, doi:10.1088/1367-2630/12/4/045012. 123

[131] M. Nakatsutsumi, Y. Sentoku, A. Korzhimanov, S. N. Chen, S. Buffechoux, A. Kon, B. Atherton, P. Audebert, M. Geissel, L. Hurd, M. Kimmel, P. Rambo, M. Schollmeier, J. Schwarz, M. Starodubtsev, L. Gremillet, R. Kodama, and J. Fuchs. Self-generated surface magnetic fields inhibit laser-driven sheath acceleration of high-energy protons. *Nature Communications*, 9(1):280, 2018, doi:10.1038/s41467-017-02436-w. 123, 124

[132] B. Albertazzi, S. N. Chen, P. Antici, J. Böker, M. Borghesi, J. Breil, V. Dervieux, J. L. Feugeas, L. Lancia, M. Nakatsutsumi, Ph. Nicolaï, L. Romagnagni, R. Shepherd, Y. Sentoku, M. Starodubtsev, M. Swantusch, V. T. Tikhonchuk, O. Willi, E. d'Humières, H. Pépin, and J. Fuchs. Dynamics and structure of self-generated magnetics fields on solids following high contrast, high intensity laser irradiation. *Physics of Plasmas*, 22(12):123108, 2015, doi:10.1063/1.4936095. 123, 131

[133] Subhendu Kahaly, S. Mondal, G. Ravindra Kumar, S. Sengupta, A. Das, and P. K. Kaw. Polarimetric detection of laser induced ultrashort magnetic pulses in overdense plasma. *Physics of Plasmas*, 16(4):043114, 2009, doi:10.1063/1.3118586. 123

[134] B. Albertazzi, E. d'Humières, L. Lancia, V. Dervieux, P. Antici, J. Böcker, J. Bonlie, J. Breil, B. Cauble, S. N. Chen, J. L. Feugeas, M. Nakatsutsumi, P. Nicolaï, L. Romagnani, R. Shepherd, Y. Sentoku, M. Swantusch, V. T. Tikhonchuk, M. Borghesi, O. Willi, H. Pépin, and J. Fuchs. A compact broadband ion beam focusing device based on laser-driven megagauss thermoelectric magnetic fields. *Review of Scientific Instruments*, 86(4):043502, 2015, doi:10.1063/1.4917273. 123

[135] W. Schumaker, N. Nakanii, C. McGuffey, C. Zulick, V. Chyvkov, F. Dollar, H. Habara, G. Kalintchenko, A. Maksimchuk, K. A. Tanaka, A. G. R. Thomas, V. Yanovsky, and K. Krushelnick. Ultrafast electron radiography of magnetic fields in high-intensity laser-solid interactions. *Phys. Rev. Lett.*, 110:015003, Jan 2013, doi:10.1103/PhysRevLett.110.015003. 123, 129, 131

[136] D. N. Nikogosyan. Beta barium borate (bbo). *Applied Physics A*, 52(6):359–368, 1991, doi:10.1007/BF00323647. 126

[137] Julius Huijts, Igor A. Andriyash, Lucas Rovige, Aline Vernier, and Jérôme Faure. Identifying observable carrier-envelope phase effects in laser wakefield acceleration with near-single-cycle pulses. *Physics of Plasmas*, 28(4):043101, 2021, doi:10.1063/5.0037925. 127

[138] A. Popp, J. Vieira, J. Osterhoff, Zs. Major, R. Hörlein, M. Fuchs, R. Weingartner, T. P. Rowlands-Rees, M. Marti, R. A. Fonseca, S. F. Martins, L. O. Silva, S. M. Hooker, F. Krausz, F. Grüner, and S. Karsch. All-optical steering of laser-wakefield-accelerated electron beams. *Phys. Rev. Lett.*, 105:215001, Nov 2010, doi:10.1103/PhysRevLett.105.215001. 127

[139] C. A. Lindstrøm, E. Adli, G. Boyle, R. Corsini, A. E. Dyson, W. Farabolini, S. M. Hooker, M. Meisel, J. Osterhoff, J.-H. Röckemann, L. Schaper, and K. N. Sjobak. Emittance preservation in an aberration-free active plasma lens. *Phys. Rev. Lett.*, 121:194801, Nov 2018, doi:10.1103/PhysRevLett.121.194801. 131

[140] R. J. Shalloo, S. J. D. Dann, J. N. Gruse, C. I. D. Underwood, A. F. Antoine, C. Arran, M. Backhouse, C. D. Baird, M. D. Balcazar, N. Bourgeois, J. A. Cardarelli, P. Hatfield, J. Kang, K. Krushelnick, S. P. D. Mangles, C. D. Murphy, N. Lu, J. Osterhoff, K. Põder, P. P. Rajeev, C. P. Ridgers, S. Rozario, M. P. Selwood, A. J. Shahani, D. R. Symes, A. G. R. Thomas, C. Thornton, Z. Najmudin, and M. J. V. Streeter. Automation and control of laser wakefield accelerators using bayesian optimization. *Nature Communications*, 11(1):6355, 2020, doi:10.1038/s41467-020-20245-6. 139

[141] C. Emma, A. Edelen, M. J. Hogan, B. O'Shea, G. White, and V. Yakimenko. Machine learning-based longitudinal phase space prediction of particle accelerators. *Phys. Rev. Accel. Beams*, 21:112802, Nov 2018, doi:10.1103/PhysRevAccelBeams.21.112802. 139

[142] Thomas R. Preston, Sam M. Vinko, Orlando Ciricosta, Hyun-Kyung Chung, Richard W. Lee, and Justin S. Wark. The effects of ionization potential depression on the spectra emitted by hot dense aluminium plasmas. *High Energy Density Physics*, 9(2):258–263, 2013, doi:https://doi.org/10.1016/j.hedp.2012.12.014. 141

[143] V. Yakimenko, S. Meuren, F. Del Gaudio, C. Baumann, A. Fedotov, F. Fiuza, T. Grismayer, M. J. Hogan, A. Pukhov, L. O. Silva, and G. White. Prospect of studying nonperturbative qed with beam-beam collisions. *Phys. Rev. Lett.*, 122:190404, May 2019, doi:10.1103/PhysRevLett.122.190404. 141

[144] J. L. Vay. Simulation of plasma accelerators with the particle-in-cell method, 2020. 145, 146, 147

[145] John M. Dawson. Particle simulation of plasmas. *Rev. Mod. Phys.*, 55:403–447, Apr 1983, doi:10.1103/RevModPhys.55.403. 145

[146] Carey Huang, Weiming An, V Decyk, W Lu, W. Mori, Frank Tsung, Michail Tzoufras, S Morshed, T Antonsen, Bowei Feng, T Katsouleas, Ricardo Fonseca, S Martins, J. Vieira, L Silva, E Esarey, C Geddes, Wim Leemans, Estelle Cormier-Michel, and Kevin Paul. Recent results and future challenges for large scale particle-in-cell simulations of plasma-based accelerator concepts. *Journal of Physics: Conference Series*, 180:012005, 08 2009, doi:10.1088/1742-6596/180/1/012005. 145

[147] Langdon A. Bruce. Birdsall, Charles K. *Plasma physics via computer simulation*. Adam Hilger ; IOP, Bristol; Philadelphia; New York; Philadelphia, 1991. 145

[148] E Lefebvre, N Cochet, S Fritzler, V Malka, M.-M Al onard, J.-F Chemin, S Darbon, L Disdier, J Faure, A Fedotoff, O Landoas, G Malka, V M ot, P Morel, M. Rabec Le Gloahec, A Rouyer, Ch Rubbelynck, V Tikhonchuk, R Wrobel, P Audebert, and C Rousseaux. Electron and photon production from relativistic laser–plasma interactions. *Nuclear Fusion*, 43(7):629–633, jul 2003, doi:10.1088/0029-5515/43/7/317. 146

[149] Brendan B Godfrey. Numerical cherenkov instabilities in electromagnetic particle codes. *Journal of Computational Physics*, 15(4):504–521, 1974, doi:https://doi.org/10.1016/0021-9991(74)90076-X. 146

[150] Remi Lehe, Manuel Kirchen, Brendan B. Godfrey, Andreas R. Maier, and Jean-Luc Vay. Elimination of numerical cherenkov instability in flowing-plasma particle-in-cell simulations by using galilean coordinates. *Phys. Rev. E*, 94:053305, Nov 2016, doi:10.1103/PhysRevE.94.053305. 146

[151] http://www-hpc.cea.fr/fr/complexe/tgcc-joliotcurie.htm. 146

[152] https://idre.ucla.edu/hoffman2. 147

ECOLE
DOCTORALE

Titre : Rayonnement bétatron dans l’accélération á champ de sillage plasma piloté par faisceau et instabilités faisceau-plasma ultra-relativistes.

Mots clés : interaction faisceau-plasma, rayonnement gamma, instabilités plasma

Résumé : Une grande variété de processus physiques peut survenir dans l’interaction d’un faisceau de particules relativistes avec des plasmas. Dans la plupart de ces processus, la réponse collective du plasma à la charge et au courant du faisceau peut agir comme un mécanisme efficace pour transformer l’énergie du faisceau en champs électromagnétiques de grande amplitude. Avoir une bonne compréhension de ces mécanismes permet d’une part de développer de nouvelles techniques expérimentales basées sur ces champs, et d’autre part d’améliorer les modèles astrophysiques où des mécanismes similaires jouent un rôle important. Ce manuscrit se concentre sur deux de ces processus et les expériences programmées à l’installation de l’accélérateur FACET-II : l’excitation de l’onde de sillage plasma et les instabilités faisceau-plasma.

La technique d’accélération par champ de sillage piloté par faisceau est aujourd’hui l’une des alternatives les plus prometteuses aux accélérateurs conventionnels. Avec des gradients d’accélération jusqu’à quatre ordres de grandeur plus importants que dans une cavité RF, cette technique pourrait réduire considérablement la taille et le coût des accélérateurs de particules à haute énergie. Pourtant, plusieurs étapes expérimentales doivent être franchies pour démontrer que le concept PWFA peut fonctionner au niveau requis de reproductibilité et de contrôle et qualité du faisceau pour des applications sociétales, industrielles et de physique de hautes energies. Dans ce manuscrit, nous proposons via des simulations une nouvelle méthode non destructive basée sur le rayonnement pour diagnostiquer des dynamiques transverses du faisceau dans une onde de sillage non linéaire qui sont préjudiciables à la qualité du faisceau accéléré.

Les instabilités faisceau-plasma sont souvent étudiées dans des systèmes non bornés. Dans la limite ultra-relativiste, la soi-disant ”instabilité oblique” est censée médier le stade précoce de l’interaction. Dans ce manuscrit, les effets des frontières du système sur les modes obliques instables sont étudiés, à savoir une nouvelle théorie spatio-temporelle est développée. Les répercussions sur les systèmes expérimentaux visant à étudier ces processus sont discutées. Enfin, une plate-forme laser pour étudier les instabilités de filamentation plasma est présentée avec des résultats expérimentaux.

Title : Betatron radiation in beam-driven plasma wakefield acceleration and ultra-relativistic beam-plasma instabilities.

Keywords : beam-plasma interaction, plasma wakefield acceleration, plasma instabilities

Abstract : A large variety of physical processes can arise in the interaction of a relativistic particle beam with plasmas. In most of these processes the collective plasma response to the beam’s charge and current can act as efficient mechanisms to transform the beam energy into large amplitude electromagnetic fields. Having a good understanding of these mechanisms allows on the one hand to develop new experimental techniques based on these fields, and on the other hand to improve the astrophysical models where similar mechanisms play an important role. This manuscript focuses on two of those processes and the programmed experiments at the FACET-II accelerator facility: plasma wakefield excitation and beam-plasma instabilities.

The beam-driven plasma wakefield acceleration technique is now-a-days one of the most promising alternatives to conventional accelerators. With acceleration gradients up to four orders of magnitude larger than in an RF-cavity, this technique could significantly reduce the size and cost of high energy particle accelerators. Yet, several experimental milestones need to be achieved to demonstrate that the PWFA concept can perform at the required level of reproducibility and beam control and quality for societal, industrial and high energy physics applications. In this manuscript we propose via simulations a new non-destructive radiation-based method to diagnose beam transverse dynamics in a non-linear PWFA stage that can be detrimental for the accelerated beam quality.

The beam-plasma instabilities are often studied in unbounded systems. In the ultra-relativistic limit, the so-called ”oblique instability” is though to mediate the early stage of the interaction. In this manuscript the effects of the system boundaries on the oblique unstable modes are studied, namely a novel spatiotemporal theory is developed. Repercussion on experimental systems aiming to study these processes are discussed. Finally, a laser-based platform to study plasma streaming instabilities is presented together with experimental results.

Institut Polytechnique de Paris
91120 Palaiseau, France